**Dissertation**
submitted to the
Combined Faculty of Natural Sciences and Mathematics
of the Ruperta Carola University Heidelberg, Germany
for the degree of
Doctor of Natural Sciences

Presented by

M.Sc. Laura Hartmann
Born in: Schweinfurt
Oral Examination: 19.05.2021

# Photon versus carbon ion radiotherapy –

# combining radiotherapy with immune checkpoint blockade in the EO771 breast cancer model

Referees: Prof. Dr. Martin Müller

Prof. Dr. Stefan Eichmüller

## Publications based on this study

Parts of this thesis have been published previously in: Hartmann L*, Schröter P*, Osen W, Baumann D, Offringa R, Moustafa M, Will R, Debus J, Brons S, Rieken S*, Eichmüller S*. *Photon versus carbon ion irradiation: immunomodulatory effects exerted on murine tumor cell lines.* Scientific Reports. (2020) 10(1):21517. * contributed equally

Schröter P, Hartmann L, Osen W, Baumann D, Offringa R, Eisel D, Debus J, Eichmüller SB*, Rieken S*. *Radiation-induced alterations in immunogenicity of a murine pancreatic ductal adenocarcinoma cell line*. Scientific Reports. (2020) 10(1):686. * contributed equally

## Presentations based on this study

Hartmann L, Schröter P, Osen W, Rieken S, Eichmüller SB
*Photon versus carbon ion irradiation – impact on immune modulation and establishment of an abscopal breast cancer tumor model*
Cancer Immunotherapy Meeting (CIMT) 2019, Mainz, Germany

Hartmann L, Schröter P, Daffinger S, Osen W, Debus J, Rieken S, Eichmüller SB
*Photon versus carbon ion irradiation – effects on immune modulation*
25. Jahrestagung der Deutschen Gesellschaft für Radioonkologie (DEGRO) 2019, Münster, Germany

Schröter P, Hartmann L, Daffinger S, Osen W, Debus J, Rieken S, Eichmüller SB
*Radioimmunbiologische Charakterisierung der murinen Pankreaskarzinomzelllinie PDA30364*
25. Jahrestagung der Deutschen Gesellschaft für Radioonkologie (DEGRO) 2019, Münster, Germany

Hartmann L, Osen W, Rieken S, Eichmüller SB
*Carbon ion irradiation – impact on immunomodulation and establishment of an abscopal tumor model*
DKFZ Poster Presentation 2019 – awarded with best poster presentation award

# Table of contents

# Abstract

Carbon ion radiation is characterized by favorable physical and biological properties when compared to classical photon radiation. While photon radiation has been shown to act as an *in situ* vaccine inducing immunological cell death, little is known about the immunomodulatory capacity of carbon ion radiation. Thus, the aim of this study was to compare the immunomodulatory potential of photon versus carbon ion radiation.

In the first part of this thesis, cytotoxic and immunomodulatory effects of photon and carbon ion radiation on the murine breast cancer cell line EO771 were analyzed *in vitro*. In clonogenic survival assays, biologically equivalent doses of 0.12, 1.11, 3.08, 8.0 Gy carbon ions corresponding to 1, 3, 5, and 10 Gy photons in the EO771 cell line were defined. Applying these doses, photon and carbon ion radiation induced comparable radiogenic effects *in vitro*. Thus, irradiation elicited a dose-dependent cytotoxicity as increasing doses reduced proliferation, initiated a transient G2/M cell cycle arrest, and induced apoptosis and cell death. Likewise, a dose-dependent enhanced expression of the immunomodulatory molecules PD-L1, CD73, and MHC class I molecules (H2-$K^b$ and H2 $D^b$), both on the mRNA and protein level, as well as increased secretion of the danger signal HMGB1 were observed. Furthermore, both radiation types made tumor cells more sensitive to CTL-mediated killing in a dose-dependent manner, while the CTLs' IFN γ response levels remained constant.

In the second part of this thesis, a bilateral tumor model was established as radiotherapy (RT) of a primary tumor can induce antitumor immune responses that might even induce the regression of distant metastases (abscopal effect). In fact, therapeutic effects on both local (irradiated, tumor #1) and distant (non-irradiated, tumor #2) tumors could be monitored in this tumor model. As abscopal effects only rarely occur, most likely due to radiation-induced immunosuppression, RT was combined with immune checkpoint blockade against PD-L1 or CTLA-4. Both photon and carbon ion RT alone could control local tumor growth to limited extent, while growth of distant tumors was not affected. Interestingly, photon RT appeared slightly superior to carbon ion RT when used as monotherapy. Combination of RT with anti-PD-L1 antibodies further enhanced antitumor effects on tumor #1, but had only a marginal impact on tumor #2. Remarkably, RT plus anti-CTLA-4 checkpoint blockade showed superior therapeutic efficacies on both tumor #1 and tumor #2 leading to complete responses in up to 80% of mice. Using combination therapy with anti-CTLA-4 antibodies, a side-by-side comparison of photon vs. carbon ion RT proved to be equally effective.

In tumor #1, photon and carbon ion RT plus anti-CTLA-4 therapy was associated with decreased frequencies of Tregs and $CD4^+$CTLA-$4^+$ T cells, decreased infiltration by $CD4^+$ and $CD8^+$ T cells expressing the immune checkpoint molecules PD-1 and LAG-3, and high numbers of $CD8^+CD73^+$ T cells. Overall, these observations point towards an activated and functional phenotype of T cells in the tumor microenvironment. In tumor #2, combination therapy resulted in decreased Treg and increased $CD8^+$ T cell infiltration, however due to high variations between single tumors within a group, no significant differences were observed in expression levels of the other markers investigated. Finally, 100% of mice showing complete responses after photon RT plus anti-CTLA-4 therapy rejected a secondary tumor engraftment. Moreover, splenocytes of these mice released INF-γ in response to EO771 tumor cells, but not to other tumor cell lines, demonstrating the establishment of tumor-specific memory immune responses.

Taken together, this thesis shows that photon and carbon ion radiation induce comparable cytotoxic and immunomodulatory effects when using biologically equivalent doses. Due to the outstanding antitumor effects on local and distant tumors, both radiation types provide great potential for clinical cancer management when applied in combination with immune checkpoint

blockade. However, based on its favorable physical and biological properties allowing precise irradiation of tumors, while sparing normal tissue, carbon ion RT appears as preferable treatment option.

# Zusammenfassung

Die Kohlenstoffionenstrahlung zeichnet sich im Vergleich zur klassischen Photonenstrahlung durch vorteilhafte physikalische und biologische Eigenschaften aus. Zwar ist bekannt, dass Photonenbestrahlung als *in-situ* Vakzine wirkt und immunologischen Zelltod hervorruft - die immunmodulatorischen Auswirkungen der Kohlenstoffionenbestrahlung sind dagegen bisher kaum untersucht. Ziel dieser Arbeit war es daher, das immunmodulatorische Potential der Photonen- und der Kohlenstoffionenstrahlung zu vergleichen.

Im ersten Teil dieser Arbeit wurden zytotoxische und immunmodulatorische Effekte von Photonen- gegenüber Kohlenstoffionenstrahlung auf die murine Brustkrebszelllinie EO771 *in vitro* untersucht. Mittels klonogener Assays wurden biologisch äquivalente Dosen von 0,12, 1,11, 3,08, 8,0 Gy Kohlenstoffionen definiert, welche Photonendosen von 1, 3, 5 und 10 Gy für die EO771 Zelllinie entsprechen. Bei Anwendung dieser Strahlendosen induzierten Photonen- und Kohlenstoffionenstrahlung vergleichbare radiogene Effekte *in vitro*. Beide Bestrahlungsarten lösten eine dosisabhängige Zytotoxizität aus, denn zunehmende Bestrahlungsdosen bewirkten eine verringerte Proliferation sowie einen transienten G2/M-Zellzyklusarrest und lösten Apoptose und Zelltod aus. Zudem bewirkte Bestrahlung eine dosisabhängige, verstärkte Expression der immunmodulatorischen Moleküle PD-L1, CD73 und MHC-Klasse-I Moleküle (H2-$K^b$ und H2-$D^b$) sowohl auf mRNA- als auch auf Proteinebene, sowie eine erhöhte Sekretion des *Danger Signal*-Moleküls HMGB1. Beide Strahlungsarten sensitivierten zudem in dosisabhängiger Weise Tumorzellen für eine CTL-vermittelte Zytolyse, ohne das IFN-γ-Sekretions-Verhalten der CTLs zu beeinflussen.

Da die Bestrahlung eines Primärtumors unter Umständen auch Antitumor-Immunantworten auslösen kann, die gegen Fernmetastasen gerichtet sind und deren Regression induzieren (abskopaler Effekt), wurde zur Untersuchung dieses Phänomens im zweiten Teil dieser Arbeit ein bilaterales Tumormodel etabliert. Somit konnte die therapeutische Wirkung einer Radiotherapie (RT) auf lokale (bestrahlt, Tumor #1) Tumore sowie auf Tumore außerhalb des Bestrahlungsfeldes (nicht bestrahlt, Tumor #2) untersucht werden. Da abskopale Effekte vermutlich aufgrund strahleninduzierter immunsuppressiver Effekte relativ selten auftreten, wurde die RT mit einer Immun-Checkpoint-Blockade gegen PD-L1 und CTLA-4 kombiniert. Sowohl die Monotherapie mit Photonen- als auch mit Kohlenstoffionenbestrahlung konnte das Wachstum von Tumor #1 in gewissem Maße eindämmen, während das Wachstum von Tumor #2 nicht beeinflusst wurde. Als Monotherapie zeigte sich interessanterweise die RT mit Photonen gegenüber der RT mit Kohlenstoffionen leicht überlegen. Die Kombination der RT mit anti-PD-L1-Antikörpern verstärkte die Antitumorwirkung gegen Tumor #1, hatte jedoch nur einen geringen Einfluss auf Tumor #2. Bemerkenswerterweise zeigte die RT plus anti-CTLA-4 Checkpoint-Blockade eine überlegene therapeutische Wirksamkeit sowohl gegen Tumor #1 als auch gegen Tumor #2, was zu einer kompletten Remission bei bis zu 80% der Mäuse führte. Bei Anwendung der kombinierten Radiotherapie mit anti-CTLA-4-Antikörpern erwies sich die RT mit Photonen und Kohlenstoffionen als gleich wirksam.

In Tumor #1 war die Photonen- und Kohlenstoffionen-RT plus anti-CTLA-4-Therapie mit einer verringerten Tumorinfiltration von Tregs und $CD4^+CTLA\text{-}4^+$ T Zellen, einer verringerten Infiltration mit $CD4^+$ und $CD8^+$ T Zellen, die die Immun-Checkpoint-Moleküle PD-1 und LAG-3 exprimierten, sowie einem hohen Anteil CD73-exprimierender $CD8^+$ T Zellen verbunden. Insgesamt deuten diese Beobachtungen auf einen aktivierten und funktionellen Phänotyp der T Zellen im Tumormikromilieu hin. Im Tumor #2 führte die Kombinationstherapie zu einer verringerten Treg-Infiltration und einer erhöhten Infiltration mit $CD8^+$ T-Zellen. Aufgrund der starken Schwankungen in der Marker-Expression zwischen einzelnen Tumoren innerhalb einer Gruppe, konnten für die weiteren untersuchten Marker keine signifikante Unterschiede

in der Expression ermittelt werden. Schließlich zeigten 100% der Mäuse, die nach Photonen-RT plus anti-CTLA-4-Therapie eine komplette Remission aufgewiesen hatten, eine effektive Abstoßung sekundär übertragener EO771 Tumorzellen. Darüber hinaus sekretierten Splenozyten dieser Mäuse nach Stimulation mit EO771 Tumorzellen, jedoch nicht mit anderen Tumorzelllinien, INF-γ, was auf die Gegenwart tumorspezifischer Gedächtnis-Immunzellen hinweist.

Zusammengefasst konnte diese Arbeit zeigen, dass die Photonen- und Kohlenstoffionenstrahlung bei Verwendung von biologisch äquivalenten Dosen vergleichbare radiogene Effekte *in vitro* und *in vivo* hervorrufen. Aufgrund ihrer hervorragenden Antitumorwirkung auf lokale und distale Tumoren bietet die Kombinationstherapie beider Strahlenarten mit einer Immun-Checkpoint-Blockade ein großes Potenzial für die erfolgreiche Krebsbehandlung. Aufgrund der günstigen physikalischen und biologischen Eigenschaften, die eine präzisere Bestrahlung von Tumoren ermöglichen und gleichzeitig normales Gewebe schonen, scheint die RT mit Kohlenstoffionen die bevorzugte Behandlungsart zu sein.

# List of tables

# List of figures

# List of abbreviations

| | |
|---|---|
| $^{12}C$ ion | carbon ion |
| 3D-CRT | three-dimensional conformal radiation therapy |
| 7-AAD | 7-amino-actinomycin D |
| ACT | adoptive cell therapy |
| aCTLA-4 | anti-CTLA-4 |
| ADC | antibody-drug conjugates |
| ADCC | antibody-dependent cellular cytotoxicity |
| ADP | adenosine diphosphate |
| AMP | adenosine monophosphate |
| APAF1 | apoptotic protease-activating factor 1 |
| aPD-L1 | anti-PD-L1 |
| ATM | ataxia-telangiectasia mutated |
| ATP | adenosine triphosphate |
| ATR | kinase and ataxia-telangiectasia and RAD3-related |
| BAK | BCL-2 antagonist/killer |
| BAX | BCL-2-associated X protein |
| BCL-2 | B-cell lymphoma 2 |
| BCR | B cell receptor |
| BED | biologically equivalent dose |
| BiTE | bi-specific T cell engager |
| CAF | cancer-associated fibroblast |
| cAMP | cyclic AMP |
| CAR | chimeric antigen receptor |
| CD | cluster of differentiation |
| CDC | complement-dependent cytotoxicity |
| CDK | cyclin-dependent kinase |
| cDNA | complementary DNA |
| CHK | checkpoint kinase |
| CIRT | carbon ion radiothearpy |
| CSF1 | colony stimulating factor 1 |
| CT | computed tomography |
| CTL | cytotoxic T lymphocyte |
| CTLA-4 | cytotoxic T-lymphocyte-associated protein 4 |
| CXCL | C-X-C motif ligand |
| CXCR | C-X-C motif receptor |
| DAMP | danger-associated molecular pattern |
| DC | dendritic cell |
| DEG | differentially expressed gene |
| DFS | disease-free survival |
| DFS | disease-free survival |
| DISC | death-inducing signaling complex |
| DNA | deoxyribonucleic acid |
| DSB | double-strand break |
| E:T ratio | effector to target cell ratio |
| EBRT | external beam radiotherapy |
| ECM | extracelllular matrix |

| | |
|---|---|
| EGFR | epidermal growth factor receptor |
| ELISA | enzyme-linked immunosorbent assay |
| ELISpot | enzyme-linked immune absorbent spot |
| EMT | epithelial mesenchymal transition |
| ER | estrogen receptor |
| ES | enrichment score |
| FACS | fluorescence activated cell sorting |
| FADD | fas-associated death domain |
| FCS | fetal calf serum |
| FDA | food and drug administration |
| FEN1 | flap endonuclease 1 |
| FMO | fluorescence minus one |
| FSC | forward scatter |
| GITR | glucocorticoid-induced TNFR-related protein |
| GM-CSF | granulocyte-macrophage colony-stimulating factor |
| gp100 | glycoprotein 100 |
| GyE | Gray equivalent |
| HBSS | hanks' balanced salt solution |
| HBV | hepatitis B virus |
| HDR | homology-directed repair |
| HER2 | human epidermal growth factor receptor 2 |
| HIF-1α | hypoxia-inducible factor 1-alpha |
| HIT | Heidelberg Ion Beam Therapy Center |
| HIV | human immunodeficiency virus |
| HMGB1 | high mobility group box 1 |
| HPV | human papillomavirus |
| HR | hormone receptor |
| HSP | heat shock protein |
| i.p. | intraperitoneal |
| ICB | immune checkpoint inhibition |
| ICD | immunogenic cell death |
| IDO | indoleamine 2,3-dioxygenase-1 |
| IFN | interferon |
| IGRT | image-guided radiation therapy |
| IHC | immunohistochemistry |
| IL | interleukin |
| IMRT | Intensity-modulated radiation therapy |
| iNOS | inducible nitric-oxide synthase |
| iPSC | induced pluripotent stem cells |
| IRF1 | interferon regulatory factor 1 |
| KEGG | Kyoto Encyclopedia of Genes and Genomes |
| KIR | killer-cell immunoglobulin-like receptors |
| LAG-3 | lymphocyte-activation gene 3 |
| LCIS | lobular carcinoma *in situ* |
| LET | linear energy transfer |
| LPS | lipopolysaccharide |
| LQM | linear-quadratic model |
| Luci | luciferase |

| | |
|---|---|
| mAb | monoclonal antibody |
| MAGE | melanoma-associated antigen |
| MALT | mucosa-associated lymphoid tissue |
| MART-1 | melanoma-associated antigen recognized by T cells 1 |
| MDSC | myeloid-derived suppressor cell |
| MFI | median fluorescence intensity |
| MHC | major histocompatibility protein |
| M-MDSC | monocytic myeloid-derived suppressor cell |
| MOMP | mitochondrial outer membrane permeabilization |
| MRI | magnetic resonance imaging |
| MST | median survival time |
| MuLV | murine leukemia virus |
| NHEJ | non-homologous end joining |
| NIRS | National Institute of Radiological Sciences |
| NK cell | natural killer cell |
| NO | nitric oxide |
| NT5E | 5'-nucleotidase ecto |
| NY-ESO-1 | New York esophageal squamous cell carcinoma 1 |
| OD | optical density |
| OS | overall survival |
| OV | oncolytic virus |
| OVA | ovalbumin |
| PAMP | pathogen-associated molecular pattern |
| PBS | phosphate buffered saline |
| PCNA | proliferating cell nuclear antigen |
| PD-1 | programmed cell death protein 1 |
| PD-L1 | programmed cell death ligand 1 |
| PE | plating efficacy |
| PFS | progression-free survival |
| PI | propidium iodide |
| PMN-MDSC | polymorphonuclear myeloid-derived suppressor cell |
| PR | progesterone receptor |
| PRR | pathogen recognition receptor |
| PVDF | polyvinylidenfluorid |
| RBE | relative biological effectiveness |
| RCD | regulated cell death |
| RNS | reactive nitrogen species |
| ROS | reactive oxygen species |
| RT | room temperature |
| RT | radiotherapy |
| s.c. | subcutaneous |
| SBRT | stereotactic body radiation therapy |
| SF | surviving fraction |
| SNV | single nucleotide variant |
| SSB | single-strand break |
| SSC | side scatter |
| TAA | tumor-associated antigen |
| TAM | tumor-associated macrophage |

| | |
|---|---|
| TAN | tumor-associated neutrophils |
| TCR | T cell receptor |
| TGF-β | transforming growth factor beta |
| Th1 | type 1 T helper |
| Th2 | type 2 T helper |
| TIGIT | T cell immunoglobulin and immunoreceptor tyrosine-based inhibitory motif |
| TIL | tumor-infiltrating lymphocyte |
| TIM-3 | T-cell immunoglobulin domain and mucin domain-3 |
| TLR | Toll-like receptor |
| TME | tumor microenvironment |
| TNBC | triple-negative breast cancer |
| TNF | Tumor necrosis factor |
| TNFR | tumor necrosis factor receptor |
| TRAIL | TNF-related apoptosis-inducing ligand |
| Treg | regulatory T cell |
| T-VEC | talimogene laherparepvec |
| TYR | tyrosinase |
| V(D)J | variable, (diversity), joining |
| VEGF | vascular endothelial growth factor |

# 1 Introduction

## 1.1 Cancer

The development of cancer is characterized by a complex interplay of cellular malfunctions that can affect almost any type of normal tissue within the body including epithelial, mesenchymal and hematopoietic tissues. All cancers can originate from a single cell that aberrantly proliferates due to somatic mutations and genetic alterations such as chromosomal rearrangements. Consequently, every cancerous disease is unique and finding successful therapy options suiting individual cancers is challenging [1]. With a rapidly growing and aging population worldwide, cancer incidence and mortality is continuously increasing and in developed countries like Germany, cancer is already nowadays the leading cause of death in people younger than 70 [2]. While only a small proportion of cancer cases are due to genetic predisposition, the majority of cancer cases result from environmental factors, such as tobacco, alcohol, diet, obesity, UV light, or viral infections [3].
Although the onset and development of cancer is diverse, Hanahan and Weinberg defined ten common hallmarks promoting cancer growth (Figure 1.1). Thus, cancer cells receive sustained proliferative signaling from oncoproteins such as RAS, MYC, and RAF, while tumor suppressor genes such as *pRb* and *p53* are silenced or mutated impairing the function of the respective proteins. Furthermore, tumor cells are resistant to programmed cell death and gain replicative immortality via telomere maintenance. To ensure the supply with nutrients within the tumor mass, the formation of new blood vessels by angiogenesis is induced, which in turn facilitates the invasion and metastasis formation into distant tissues through epithelial mesenchymal transition (EMT). Moreover, tumor cells depend on genome instability and mutational load for aberrant growth and benefit from tumor-promoting inflammatory signals. Finally, cancer cells adapt their cellular metabolism to constant neoplastic proliferation and develop mechanisms to evade immune destruction in particular from T cells, natural killer (NK) cells, and macrophages [4].

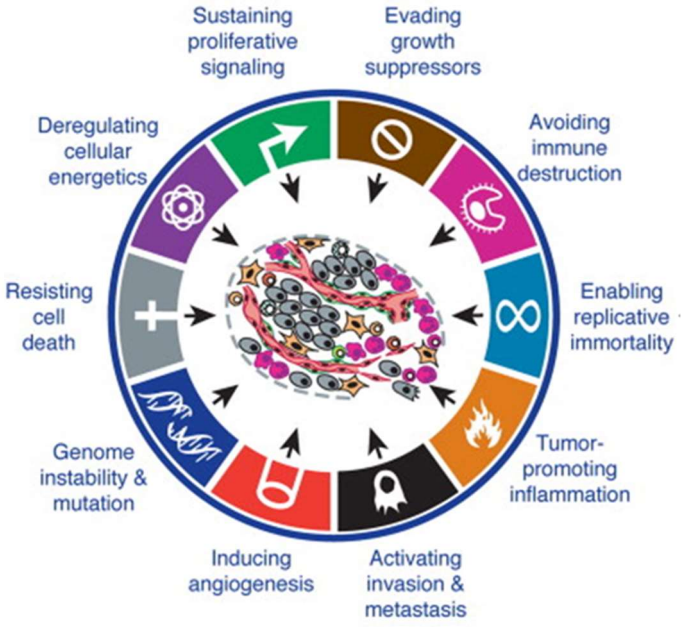


**Figure 1.1 The hallmarks of cancer.** The figure illustrates a summary of cellular malfunctions promoting tumor development and growth as defined by Hanahan and Weinberg. Picture was adapted from [4].

## 1.2 Tumor immunology

### 1.2.1 Principles of the immune system

The immune system is one of the most complex networks in the body consisting of a variety of lymphatic organs, immune cells, and signaling proteins. The core task of the immune system is to discriminate between self and non-self components defending the body from foreign invaders like bacteria, viruses and toxic substances, while sparing the host's own tissue. Classically, the immune system is divided into the innate and adaptive immune system, which jointly orchestrate an immune response. While the innate immune system is the first line of defense that initiates an immune response, the adaptive immune system is the second line of defense finally clearing a pathogen [5].

The innate immune system provides an immediate recognition of non-self structures. First, anatomical barriers like the skin and mucous membranes inhibit pathogen entry. When a pathogen has still entered the host, an inflammatory response is initiated by the cells of the innate immune system. Thus, pattern recognition receptors (PRR) expressed by monocytes, macrophages, dendritic cells (DCs) or neutrophils recognize evolutionary conserved molecular patterns on foreign invaders, called pathogen-associated molecular patterns (PAMPs). A well-known PAMP is lipopolysaccharide (LPS), a membrane structure of Gram-negative bacteria, which is bound by the PRR Toll-like receptor 4 (TLR4). In response to ligand binding to PRRs, particularly macrophages and DCs initiate phagocytosis and antigen presentation and trigger inflammatory pathways activating and recruiting the adaptive immune system [6]. Further operators of the innate immune system are NK cells, which are lymphocytes that are inactivated as long as stimulation of activating and inhibitory receptors are balanced. Ligands for activating receptors are frequently upregulated in virus-infected cells and when NK cells receive sustained signaling via activating receptors killing of infected cells is initiated. A well-known activating receptor expressed on NK cells is FcγRIII (CD16), which binds the Fc region of an antibody enabling the killing of opsonized cells by antibody-dependent cellular cytotoxicity (ADCC). Moreover, when NK cells cannot detect major histocompatibility complex (MHC) molecules and thus lack an inhibitory signal, the balance is interrupted and NK cells become activated [7]. The mediators described so far are part of the cellular innate immunity. In addition, the complement system represents the humoral arm of the innate immune system. It consists of a number of serum proteins which induce pro-inflammatory molecules, targeted lysis and opsonization of targets for phagocytosis [8].

While the innate immune system is relatively inflexible and limited in its repertoire, adaptive immune cells can react to a particular pathogen and generate a highly specific immune response. The mediators of adaptive immune responses are B and T cells. B cells, which are part of the humoral immune system, generate antibodies neutralizing pathogens or opsonizing cells for phagocytosis and ADCC. T cells can be divided into $CD4^+$ and $CD8^+$ T cells. While $CD4^+$ T cells have regulatory impact on various immune cells, $CD8^+$ cytotoxic lymphocytes (CTLs) are directly eliminating pathogens and aberrant cells. Each B and T cell expresses a single, antigen-specific B cell receptor (BCR) and T cell receptor (TCR), respectively. BCRs are membrane-bound immunoglobulins consisting of two heavy and two light chains, while TCRs of classical T cells consist of an α and a β chain and TCRs of non-classical T cells of a γ and a δ chain. In contrast to the innate immune system, where PRRs are germ-line encoded, the abundant repertoire of BCRs and TCRs originate from somatic recombination of a few hundred germline-encoded gene elements that are rearranged to millions of different antigen receptors [5]. Thus, TCRs and BCRs are randomly assembled by variable (V), diversity (D), and, joining (J) gene elements in a process called V(D)J recombination. Independent of a

foreign antigen, V(D)J recombination creates a huge variety of B cell and T cells clones, which further mature and clonally expand after antigen encounter, with the result that adaptive immune responses develop slightly delayed compared to innate immune responses. Besides specificity, the formation of an immunological memory is a hallmark of adaptive immune responses. During a second encounter, a foreign structure can be eliminated more quickly and efficiently by memory B and T cells [9].
Both B and T cells develop from pluripotent stem cells. The primary lymphoid organ for B cells is the bone marrow, whereas T cell development occurs in the thymus. In the thymus, several quality control steps take place. Thus, TCRs with a low affinity to self-MHC molecules are eliminated, as binding of TCRs to MHC molecules presenting foreign structures is pivotal for T cell activation. Details of T cell activation will be further described in section 1.2.3. Moreover, to avoid autoimmunity, T cells expressing TCRs recognizing MHC-restricted epitopes of autologous origin are deleted by apoptosis. Lymph nodes, the spleen, and mucosa-associated lymphoid tissue (MALT) represent secondary lymphoid tissues, where mature B and T cell clones become activated and proliferate after antigen encounter [5].

### 1.2.2 Cancer immunosurveillance

Besides the defense of pathogens, recent evidence suggests that the immune system plays an important role in controlling and eliminating tumor cells that are recognized as foreign. The immune-mediated prevention of tumor outgrowth is called tumor immunosurveillance and was already proposed by Burnet and Thomas in the late 1950s [10]. Although controversially discussed over the past decades, numerous observations have corroborated the concept of tumor immunosurveillance meanwhile. In early mouse models, the antigenic potential of tumor cells was shown. Thus, mice vaccinated with irradiated tumor cells were protected from a challenge with the same tumor cell line, but not from a different tumor cell line [11]. Moreover, immunodeficient mice that lack specific immune cell types and cytokines show a higher risk of developing chemically-induced and spontaneous tumors. For instance, $Rag2^{-/-}$ $Stat1^{-/-}$ mice, which are deficient for B, T and NKT cells as well as type I and II interferon (IFN) signaling, spontaneously develop intestinal adenomas as well as breast and colon carcinomas [12]. Likewise, in humans the prevalence of cancer increases when patients are immunodeficient due to human immunodeficiency virus (HIV) infections or immune suppression during organ transplantations [13, 14]. Furthermore, among cancer patients there is a positive correlation between disease-free survival (DFS) and the density of tumor infiltration lymphocytes (TILs), while the presence of regulatory T cells (Tregs) within the tumor microenvironment is associated with poorer prognosis [15, 16]. Finally, tumor cells evolve mechanisms to avoid recognition by the immune system indicating coherence between developing tumors and the arising immune response [17].
Immune evasion may also explain why patients having a functional immune system still develop tumors. In the course of tumor development, cancer immunoediting occurs, which consists of three phases: elimination, equilibrium, and escape (Figure 1.2). During the elimination phase, pro-inflammatory immune responses predominate thereby controlling tumor growth. Thus, cells of the innate and adaptive immune system are jointly involved in tumor cell killing and pro-inflammatory cytokines like interferon IFN-γ, IFN-α/β, interleukin (IL)-12, and tumor necrosis factor (TNF) predominate in the tumor microenvironment (TME). This may lead to complete tumor clearance. However, when tumors are not completely eradicated, they enter the equilibrium phase, in which tumor cells undergo genetic and epigenetic changes causing tumor dormancy, where pro- and antitumor signals are balanced. Consequently, the outgrowth of a tumor is prevented, but antitumor immune responses are not strong enough to further

eliminate the tumor. The equilibrium phase is primarily maintained by cells of the adaptive immune system, especially activated $CD4^+$ and $CD8^+$ effector T cells, as well as the presence of IFN-γ and IL-12 in the TME. Finally, under the constant selective pressure of the immune system, tumor cells develop escape mechanisms resulting in the outgrowth of tumors. In this state, immunosuppressive cytokines like IL-6, IL-10, and transforming growth factor beta (TGF-β) accumulate in the TME. Consequently, the function of pro-inflammatory immune cells like CTLs and NK cells is impaired, whereas immunosuppressive immune cells including Tregs and myeloid-derived suppressor cells (MDSCs) become activated. Furthermore, the expression of immune checkpoint molecules, such as cytotoxic T-lymphocyte-associated protein 4 (CTLA-4), programmed cell death protein 1 (PD-1), and programmed cell death ligand 1 (PD-L1), is induced causing T cell exhaustion and death (see also section 1.2.4.1). Moreover, the metabolism of tumor-infiltrating immune cells is affected. Hence, expression of the cytosolic enzyme indoleamine 2,3-dioxygenase (IDO1) is upregulated catabolizing and thus depleting tryptophane, which is essential for T cell an NK cell function. Finally, tumors frequently downregulate the expression of MHC class I molecules to escape from recognition by T cells [18-21].

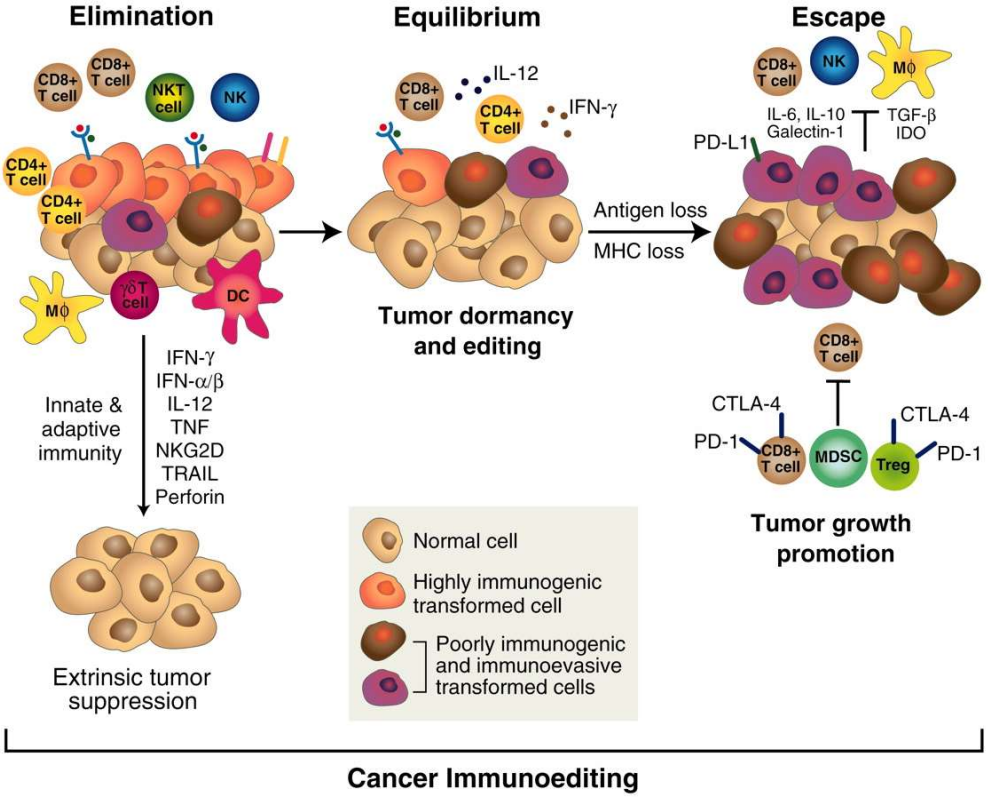


**Figure 1.2: The three phases of cancer immunoediting: elimination, equilibrium, and escape**. During the elimination phase, pro-inflammatory immune responses of the innate and adaptive immune system predominate leading to tumor cell clearance. In the equilibrium phase, tumors undergo genetic and epigenetic changes to evade from the immune system leading to tumor dormancy and a balance of pro-inflammatory and anti-inflammatory signals. The escape phase is associated with immunosuppressive immune cells and cytokines within the tumor microenvironment promoting the outgrowth of tumors. CTLA-4: cytotoxic T lymphocyte antigen 4, DC: dendritic cell, IDO: Indoleamine 2,3-dioxygenase, IFN: interferon, IL: interleukin, MDSC: myeloid-derived suppressor cell, MHC: major histocompatibility complex, Mφ: macrophage, NK: natural killer cell, NKG2D: natural killer group 2D, PD-(L)1: programmed cell death (ligand) 1, TGF-β: transforming growth factor beta, TNF: tumor necrosis factor, TRAIL: tumor necrosis factor related apoptosis inducing ligand, Treg: regulatory T cell. Picture was adapted from [18]

### 1.2.3 The cancer immunity cycle

Due to genetic and cellular changes, tumor cells can be recognized as foreign and defended by the immune system, similar to pathogens like bacteria and viruses. In the first step, tumor-associated antigens (TAA) are released and taken up by professional antigen presenting cells (APCs), in particular by DCs. A number of TAAs, which are not or only weakly expressed in normal cells, are shared between different patients. Tissue-specific differentiation antigens are only expressed in certain healthy cells, such as tyrosinase (TYR), glycoprotein 100 (gp100), and melanoma-associated antigen recognized by T cells 1 (MART 1) in melanocytes, but are commonly overexpressed in melanoma cells. Moreover, not only overexpression of differentiation antigens can elicit an immune response, but also other antigens have been shown to be immunogenic when overexpressed, including the apoptosis protein survivin and the growth factor receptor human epidermal growth factor 2 (HER2) [22]. The expression of cancer-testis antigens is limited to germline cells under normal physiological conditions, while many carcinomas express immunogenic antigens like the New York esophageal squamous cell carcinoma 1 (NY-ESO-1) antigen and antigens of the melanoma-associated antigen (MAGE) family [23]. In virus-associated cancers, oncoviral proteins like the E6 and E7 proteins from human papillomaviruses (HPV) can be recognized by the immune system. Finally, in contrast to shared antigens, neoantigens are derived from nonsynonymous mutations resulting in altered tumor proteins that are tumor-specific [24].
Upon antigen uptake, DCs process exogenous proteins to short peptides, which are further presented on MHC class I and MHC class II molecules to prime antigen-specific T cells in the lymph nodes. Generally, exogenous proteins are presented on MHC class II molecules of APCs to prime naïve $CD4^+$ T cells, while peptide epitopes of endogenous proteins are presented to $CD8^+$ T cells on MHC class I molecules in all nucleated cells. A unique feature of DCs is cross-presentation, which enables epitope presentation of exogenous antigen on MHC class I molecules to prime naïve $CD8^+$ T cells. Beside MHC/peptide binding, co-stimulation by interaction of CD28 (T cells) and CD80/CD86 (DCs) as well as through cytokines such as IL-2, IL-12, and IFN-γ is necessary for effective T cell activation [25]. Activated T cells traffic to and infiltrate the tumor, where tumor epitopes presented on MHC class I molecules of the tumor are recognized by antigen-specific TCRs leading to the killing of cancer cells and further antigen release [26].

### 1.2.4 Tumor microenvironment

The TME not only consists of tumor cells, but a complex structure of blood vessels, immune cells, cancer-associated fibroblasts (CAFs), secreted factors, and extracellular matrix proteins, which are interconnected in tumor development and progression. In the following, the phenotype and function of the most frequent stromal cell types will be described.

#### 1.2.4.1 T cells

T cells play the leading role in effective antitumor immune responses, especially $CD8^+$ T cells, which directly kill aberrant tumor cells by delivering the cytotoxic granules perforin and granzyme B to the tumor cells by synaptic exocytosis or indirectly by secreting cytokines like IFN-γ or TNF [27]. The abundance of $CD8^+$ T cells in the tumor and the circulation was correlated with a better prognosis for various cancer entities including colorectal cancer, breast cancer, and lung cancer [15, 28-30]. The role of $CD4^+$ T cells in the TME was payed less attention to, but increasing evidence points towards their importance in orchestrating antitumor immune responses. The main function of $CD4^+$ T cells is to support $CD8^+$ T cells by secreting pro-inflammatory cytokines like IL-2 and IFN-γ, stimulating APCs that in turn prime $CD8^+$ CTLs,

preventing activation-induced cell death, and supporting memory formation (classical T helper function) [31]. Some preclinical studies showed that $CD4^+$ T cells might also exert direct cytotoxic functions against the tumor similar to CTLs [32, 33]. Furthermore, recent studies showed the pivotal role of $CD4^+$ T cells in generating immune responses against neoantigens [34, 35]. Thus, when cancer patients were vaccinated with personalized neoantigen vaccines, tumor-specific immune responses were rather driven by $CD4^+$ T cells than $CD8^+$ T cells [36, 37]. Depending on the cytokine production and effector functions, $CD4^+$ T cells are classified into different subtypes, including T helper 1 (Th1), T helper 2 (Th2), T helper 17 (Th17) cells, as well as Tregs. Classically, Th1 and Th17 were reported to be involved in antitumor immune responses, while Th2 cells and Tregs were associated with tumor progression. However, regarding Th17 and Th2 cells also contrary functions have been shown. Th1 cells produce the pro-inflammatory cytokines IL-12, IFN-γ, TNF-α, and IL-2 fostering T cell effector functions [38]. Th17 cells secreting IL-17 on the one hand stimulate effector T cells, but on the other hand promote apoptosis and create an immunosuppressive milieu [39]. Similarly, Th2 cells suppress immune responses and promote tumor growth by IL-10 secretion and driving angiogenesis, but also induce antitumor activity by secreting IL-4 and attracting eosinophils to the tumor [40]. Finally, Tregs are the mediators of numerous suppressive mechanisms. First, Tregs secrete suppressive cytokines IL-10, TGF-β, and IL-35 inhibiting T cell functions. Furthermore, Tregs can directly lyse effector T cells by secreting perforin and granzymes. Moreover, Tregs affect T cell metabolism by converting adenosine triphosphate (ATP) to adenosine via the CD73/CD39 axis and withdraw IL-2 from conventional T cells. Finally, Tregs can suppress the function of APCs rendering APCs unable to active T cells [41].
The phenotype and functional state of T cells can be defined through the expression profile of a variety of receptors, with co-stimulatory receptors pointing towards an activated state of a T cell and inhibitory immune checkpoint molecules implying an exhausted state.

**Co-stimulatory receptors.** Besides CD27 and CD28, which are constitutively expressed on resting lymphocytes, other co-stimulatory receptors are induced after $CD4^+$ and $CD8^+$ T cell activation delivering stimulatory signals [42]. Moreover, some of these inducible receptors may be expressed constitutively on Tregs and ligand binding can decrease their suppressive activity [43]. Various co-stimulatory receptors are currently investigated, also for agonistic therapy approaches (see section 1.3.2). (1) 4-1BB (CD137) stimulation can enhance CTL cytotoxicity by upregulation of cytolytic granule proteins, protect from activation induced cell death (AICD), and prevent apoptosis by expression of B-cell lymphoma 2 (BCL-2) family proteins [44]. Furthermore, 4-1BB expression was shown to correlate with tumor reactivity of T cells [45]. Agonistic stimulation of Tregs drives their expansion without affecting their suppressive activity, whereas $CD4^+$ and $CD8^+$ T cells become less prone to Treg inhibition upon stimulation of 4-1BB [46, 47]. (2) OX-40 is a member of the tumor necrosis factor receptor (TNFR) superfamily and can positively affect T cell function by pro-inflammatory cytokine production, upregulation of anti-apoptotic proteins, and promoting T cell memory [48]. OX-40 is constitutively expressed on Tregs and ligand binding to OX-40L abrogates their suppressive functions [49]. (3) Glucocorticoid induced TNF-receptor related protein (GITR) is highly expressed on Tregs, but is rapidly activated also in $CD4^+$ and $CD8^+$ T cells upon activation. Similar to 4-1BB and OX-40, GITR was shown to prevent AICD, to support T cell proliferation and cytokine production, and to reduce suppression by Tregs [50].

**Immune checkpoint molecules**. Efficient anticancer immune responses are often suppressed by cell intrinsic or suppressive signals from the TME. To prevent autoimmunity, T cells have developed negative feedback signals, which are also activated in anticancer immune responses. Thus, upon T cell activation so-called immune checkpoint molecules are expressed, which impair T cell functions such as proliferation, cytotoxic activity, and cytokine production. Numerous immune checkpoint molecules have been identified as they offer an excellent therapeutic target reversing immunosuppression [51] (immunotherapies targeting immune checkpoint molecules will be described in section 1.3.2). (1) CTLA-4 binds the B7 ligands CD80/CD86 expressed on APCs with a higher affinity compared to CD28 thereby inhibiting T cell functions. Moreover, CTLA-4 expressed on Tregs can remove CD80/CD86 from APCs via trans-endocytosis reducing their ability to further activate T cells [52]. (2) PD-1 is transiently upregulated after T cell activation and binding to its receptors PD-L1 and PD-L2 impairs T cell effector functions. Indeed, PD-1 is a suppressive molecule, but its expression might be a biomarker for the presence of tumor-reactive $CD8^+$ CTLs [53]. Regarding the prognostic value of PD-1 expression, contrary results have been reported. While a high expression of PD-1 was associated with poor prognosis for cervical cancer and epithelial-originated cancer, it was correlated with better prognosis in colorectal cancer and head and neck squamous cell carcinoma (HNSCC) patients [54-57]. (3) Lymphocyte activation gene-3 (LAG-3) shares similarities with the CD4 receptor, but binds MHC class II molecules with a higher affinity causing a tolerogenic DC maturation. LAG-3 is pivotal for the suppressive functions of Tregs, but was also shown to be expressed on $CD4^+$ and $CD8^+$ T cells [58, 59]. (4) CD73 (also known as 5'-nucleotidase ecto (NT5E)) is a surface enzyme expressed on immune cells including naïve T cells and in particular Tregs as well as tumor cells. Together with CD39, CD73 catalyzes the conversion of ATP to adenosine. Thus, CD39 degrades ATP and adenosine diphosphate (ADP) to adenosine monophosphate (AMP), while CD73 converts AMP to adenosine [60]. Extracellular adenosine further suppresses effector T cells by limiting proliferation, activation, cytotoxicity, and cytokine release and in addition promotes the suppressive functions and proliferation of Tregs. In this way, adenosine can facilitate tumor growth and metastasis formation [61]. (5) T-cell immunoglobulin domain and mucin domain-3 (TIM-3) was originally identified as a Th1 cell marker, whose blockade induced macrophage activation and autoimmune reactions in a mouse model [62]. In addition, TIM-3 is expressed on CTLs and Tregs [63]. Upon binding of its receptor galectin-9, which is expressed on Tregs and tumor cells, T cell responses become dysfunctional and cell death can be induced [64]. Moreover, TIM-3 can bind and thereby inactive the danger signal high mobility group box 1 (HMGB1), which is associated with T cell priming [65]. Expression of TIM-3 on T cells has been correlated with poor clinical outcome, which seems even worse when co-expressed with PD-1 [66, 67]. (6) T cell immunoglobulin and immunoreceptor tyrosine-based inhibitory motif (TIGIT) binds to molecules of the nectin family, which mediate cell adhesion and lymphocyte migration, and negatively regulates various steps of the cancer immunity cycle. Thus, TIGIT expression can reduce antigen presentation and thus T cell activation, promote the secretion of immunosuppressive IL-10, and also directly suppress T cell effector functions [68, 69].
Of note, effects of co-stimulatory receptors and immune checkpoint molecules have been described in detail for T cells, however they can also affect other immune cell types like myeloid cells, NK cells and APCs.

#### 1.2.4.2 Natural killer cells

NK cells were initially discovered as lymphocytes autonomously lysing mouse Moloney leukemia cells without prior sensitization [70]. NK cells become activated when inhibitory receptors are deprived of their signals or activating receptors are stimulated, thus leading to the imbalance towards activating signals. Inhibitory receptors mainly include MHC class I-binding receptors, such as NKG2A and various killer-cell immunoglobulin-like receptors (KIRs). As tumor cells commonly downregulate MHC class I surface expression during the tumor escape phase, NK cells become activated when the inhibitory signal is missing [71]. Activating receptors receive signals from different stress-related molecules and tumor cell ligands. For instance, FcγRIII (CD16) binds the Fc part of antibodies initiating cytolysis of tumor cells by ADCC. Another important activating receptor is NKG2D, which binds ligands like MHC class I polypeptide–related sequence A and B (MICA/B) expressed by tumor cells. NK cell activation results in direct granule-mediated lysis of target cells, the secretion of the immunostimulatory cytokines IFN-γ and TNF-α, as well as the upregulation of the apoptosis receptors FasL and TNF-related apoptosis-inducing ligand (TRAIL) [72]. A high number of NK cells correlates with favorable clinical outcome in cancer patients [73]. However, similar to T cells, NK cells are delicate to the suppressive TME. Thus, NK cells are subjected to immunosuppressive cytokines and an impaired metabolism due to nutrient and oxygen deprivation. Moreover, NK cells upregulate immune checkpoint molecules like PD-1, LAG-3, and CD73 resulting in NK cell exhaustion [71, 74].

#### 1.2.4.3 Dendritic cells

DCs are of major importance for presenting cancer antigen-derived epitopes to T cells and thus, priming antitumor immune responses. However, in the suppressive TME, DCs frequently become dysfunctional and might even contribute to tumorigenesis. Thus, hypoxia and increasing levels of adenosine prevent efficient T cell activation by DCs. Moreover, IL-10 downregulates MHC class I molecule, CD80 and CD86 expression on DCs and limits the secretion of IL-12 by DCs, which further impairs the activation of T cells. In addition, factors like vascular endothelial growth factor (VEGF), TGF-β, IL-1β, and prostaglandins may lead to differentiation of DCs into immunosuppressive tumor-associated macrophages (TAMs) or MDSCs. Likewise, Tregs have a suppressive impact on DCs by downregulating co-stimulatory molecules and stimulating IDO production, which further results in the expression of PD-L1 [75, 76].

#### 1.2.4.4 Tumor-associated macrophages

TAMs are myeloid immune cells that particularly in breast cancer can account for up to 50% of the cells in the TME and are often associated with poor prognosis. Depending on the environmental signals, TAMs can be roughly divided into pro-inflammatory M1-like (classically activated) and anti-inflammatory M2-like (alternatively activated) TAMs. Of note, not only these two extreme phenotypes exist, but also a spectrum of intermediate states [77, 78]. Macrophages are recruited to tumors predominantly by CC chemokines (e.g. CCL2, CCL11, CCL16) secreted by the TME or recruit further macrophages by secreting CCL2 themselves. M1-like macrophages are activated by factors like IFN-γ, granulocyte-macrophage colony-stimulating factor (GM-CSF), as well as LPS and are predominant during early development of a tumor. M1-like macrophages are associated with Th1 cell responses, contribute to tissue destruction by producing reactive oxygen and nitrogen species (ROS/RNS) and secreting pro-inflammatory cytokines like IL-1β, IL-6, and TNF-α. In later stages of tumor development, TAMs are frequently polarized into M2-like macrophages in response to colony stimulating factor 1

(CSF-1), IL-4, IL-13, or IL-10 and are associated with Th2 cell responses [79, 80]. M2-like TAMs promote tumor growth in various ways. Thus, the suppressive cytokines TGF-β and IL-10 are secreted impairing effector functions of T cells and inducing Tregs [81]. Furthermore, expression of arginase 1 and IDO1 induce the production of immunosuppressive metabolites causing the metabolic starvation of T cells [82, 83]. Finally, M2-like macrophages are associated with the promotion of neovascularization, tumor migration, invasion and metastasis [80].

#### 1.2.4.5 Myeloid-derived suppressor cells

MDSCs are a subset of poorly differentiated myeloid cells that only accumulate under pathological conditions. Two types of MDSCs have been identified: (1) polymorphonuclear MDSCs (PMN-MDSCs), which show phenotypical similarity to neutrophils and (2) monocytic MDSCs (M-MDSCs) resembling monocytes [84]. MDSCs suppress T cell functions via pleiotropic mechanisms. Thus, MDSCs induce Treg differentiation by secretion of IL-10 and TGF-β or recruit Tregs to the TME via CCL3, CCL4 and CCL5 [85, 86]. Moreover, MDSCs upregulate arginase 1, which deprives L-arginase from T cells and produce ROS and nitric oxide (NO) reducing T cell proliferation [87]. In addition, NO downregulates adhesion molecules expressed on T cells impairing T cell homing, whereas the expression of PD-L1 and FasL on MDSCs lead to T cell exhaustion and apoptosis, respectively [86, 88]. Finally, the hypoxic TME can further drive the differentiation of M-MDSCs to TAMs [89]. A meta-analysis of 16 studies with 1864 patients of different cancer entities (e.g. breast, rectal, colorectal cancer) showed that accumulation of MDSCs is associated with poor prognosis as indicated by a shorter overall survival (OS) and DFS [90].

#### 1.2.4.6 Tumor-associated neutrophils

Another immune cell type of the myeloid lineage are neutrophils. Neutrophils are the most frequent white blood cells in the circulation and are mainly recruited to the tumor via C-X-C motif chemokine receptor 2 (CXCR2) and IL17 [91, 92]. Similar to macrophages, different polarization states and functions have been proposed for tumor-associated neutrophils (TANs) dependent on TGF-β, with N1 being anti-tumorigenic and N2 being pro-tumorigenic [93]. Regarding the role of neutrophils in tumor progression, TANs are associated with the release of ROS, the secretion of anti-inflammatory cytokines, and the release of enzymes favoring metastasis formation [94]. A high neutrophil-to-lymphocyte ratio is associated with poor prognosis in prostate cancer, gastric cancer, and pancreatic cancer [95-97].

#### 1.2.4.7 Cancer-associated fibroblasts

In normal tissues, fibroblasts are the main component of connective tissue and play a pivotal role in wound healing. In the TME, normal fibroblasts can be activated to CAFs by physiological stress like ROS, DNA damage, inflammatory cytokines like IL-1, IL-6, and TNF-α, physical changes in the extracellular matrix (ECM), as well as contact signaling through Notch. A major pro-tumorigenic mechanism of CAFs is the remodeling of the ECM contributing to cancer cell migration, evasion, and metastasis formation. Moreover, they activate TGF-β and produce IL-6, CXCR12, and CCL2 thereby inhibiting T cell functions, while the release of VEGF can drive *de novo* synthesis of vasculature [98].

## 1.3 Cancer immunotherapy

Cancer immunotherapy has revolutionized the management of metastatic cancer leading to the development of numerous immunotherapeutic approaches. While monotherapy with several immunotherapies yielded impressive results in clinical trials, there is a trend towards combining different immunotherapeutic approaches to increase the therapeutic efficacy. In the following, the currently most relevant immunotherapies will be described.

### 1.3.1 Tumor-targeting monoclonal antibodies

Tumor-targeting monoclonal antibodies (mAbs) selectively target surface molecules on cancer cells or trophic factors delivered by the tumor stroma. Clinically, tumor-targeting mAbs are the most abundant class of immunotherapeutic drugs, which exert antitumor functions via a variety of mechanisms. First, mAbs like cetuximab and trastuzumab can bind to growth factor receptors EGFR and HER2, respectively, thereby blocking the signal transduction required for tumor cell survival and proliferation. Second, mAbs can exert agonistic functions activating pro-apoptotic receptors like TRAILR2 on tumor cells. Furthermore, Fc receptor-binding mAbs can activate the immune system by opsonization for NK-cell mediated ADCC, complement-dependent cytotoxicity (CDC), or antibody-dependent cellular phagocytosis of the tumor cell [99]. Next, antibody-drug conjugates (ADCs) are antibodies armed with a small cytotoxic drug to increase therapeutic efficacy. Clinically investigated cytotoxic drugs include chemotherapeutic agents inhibiting microtubules formation or inducing DNA damage. Thus, the FDA-approved ADC trastuzumab emtansine is a HER2-targeting antibody linked to the microtubule inhibitor mertansine [100]. Finally, bi-specific T cell engagers (BiTEs) are composed of two single-chain antibodies; one targeting a TAA and one binding T cells via the constant component of the CD3 complex. In this way, T cells can be guided to the tumor in an MHC-independent manner. Blinatumomab, an anti-CD19/anti-CD3 BiTE, achieved promising results in clinical trials [101]. Due to the immunostimulatory effects, BiTEs could also be classified as immunomodulatory agents.

### 1.3.2 Immunomodulatory monoclonal antibodies

In contrast to tumor-targeting mAbs, immunomodulatory mAbs are targeting immune cells or immunomodulatory factors, with the main goal to induce a *de novo* immune response against the tumor or restore the activity of exhausted immune cells. This can be achieved by activation of co-stimulatory receptors, neutralizing immunosuppressive factors in the TME, or inhibiting suppressive immune receptors and ligands [102]. Regarding activation of co-stimulatory receptors, agonistic mAbs targeting 4-1BB yielded promising results in preclinical trials. Thus, using the agonistic mAb CTX-471 large tumors could be controlled, whereas other immunomodulatory mAbs proved to be inefficient [103]. Moreover, two candidates are currently tested in clinical trials showing preliminary antitumor activity [104]. Further promising targets include OX40, CD40, and GITR, which are currently tested in clinical trials often in combination therapies [105-109]. A soluble factor suppressing T cell responses is TGF-β rendering it an attractive target for neutralizing mAbs [110].

Immunomodulatory mAbs targeting suppressive immune receptors and ligands, also called immune checkpoint blockade (ICB), are clinically most relevant due to the induction of robust and durable responses in various solid tumors [111-113]. The first FDA-approved checkpoint-blocking antibody ipilimumab targeting CTLA-4 was the first systemic immunotherapy approach that yielded prolonged OS of metastatic melanoma patients, with survival rates of 20% ten years after treatment [114]. However, the therapeutic efficacy is accompanied by

immune-related adverse events like vitiligo, diarrhea, and rashes [113]. Furthermore, the PD-L1/PD-1 axis can be targeted by checkpoint-inhibiting antibodies. A clinical trial comparing the PD-1-blocking antibody pembrolizumab with ipilimumab in advanced melanoma showed favorable DFS and response rates as well as lower rates of severe adverse events in patients treated with pembrolizumab [115]. Similar results were shown in a phase III clinical trial with nivolumab (anti-PD-1 antibody) either as monotherapy or in combination with ipilimumab [111, 116]. Indeed, checkpoint-blocking antibodies have revolutionized the management of cancer, but still a great number of patients does not respond to checkpoint blocking therapy. Various determinants for predicting the responsiveness to ICB have been found. Thus, responsiveness to IFN-γ, an intact antigen presentation machinery, and a high mutational burden have been associated with a response to ICB. Moreover, the magnitude of $CD8^+$ T cell numbers is positively correlated with therapeutic efficacy [117].

Both anti-CTLA-4 and anti-PD-1/PD-L1-blocking antibodies result in the activation of the immune system, however at different stages of the immune response and with different mode of actions (Figure 1.3). CTLA-4-blocking antibodies target the early phase of an immune response targeting the interaction between T cells and APCs during T cell activation. Moreover, CTLA-4 is constitutively expressed on Tregs and on activated conventional T cells. When anti-CTLA-4 is blocked by immune checkpoint inhibitors, suppressive mechanisms are abolished, leading to the activation of conventional T cells and depletion of Tregs [52]. PD-1/PD-L1 blocking antibodies intervene in a later stage of the immune response targeting the interaction of T cells and tumor cells and thus, the T cell effector phase. Similar to CTLA-4, PD-1 is expressed on activated T cells and binding to its ligands PD-L1 and PD-L2, which are expressed on tumor cells or other immune cells, impairs T cell functions, which can be restored with PD-1/PD-L1-blocking antibodies [118].

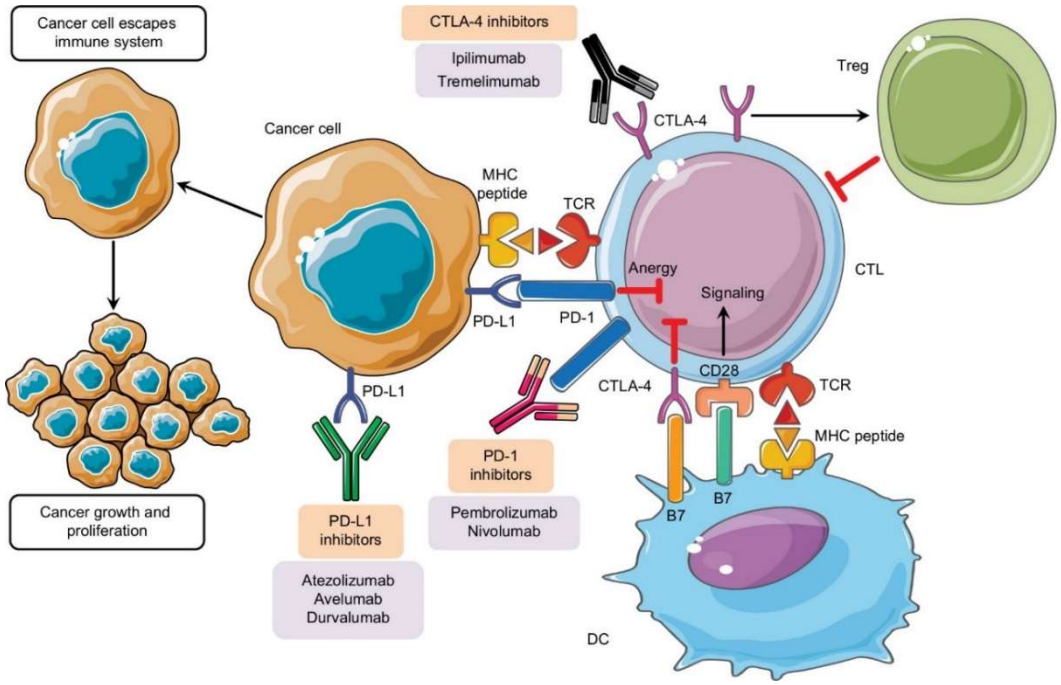


**Figure 1.3: Mechanisms of immune checkpoint blockade.** CTLA-4 expressed on T cells binds B7 ligands expressed on DCs delivering inhibitory signals to the T cell. Expression of CTLA-4 on Tregs enhances their suppressive function. Binding of PD-1 (activated T cells) to its ligand PD-L1 (tumor cell) leads to T cell anergy. Inhibitory signals can be restored by blocking CTLA-4, PD-1, and PD-L1 with monoclonal antibodies. CTL: cytotoxic T lymphocyte, CTLA-4: cytotoxic T-lymphocyte antigen 4, DC: dendritic cell, MHC: major histocompatibility complex, PD-(L)1: programmed cell death (ligand) 1, TCR: T cell receptor, Treg: regulatory T cell. Picture was taken from [118].

Beside immune checkpoint blockade of CTLA-4 and PD-1/PD-L1, targeting of other immune checkpoint molecules yielded promising preclinical results and is currently under clinical investigation. Thus, a soluble LAG-3 protein called IMP321 was tested in several phase I/II clinical trials in combination with chemotherapy or peptide vaccination showing good tolerability and induction of immune responses as well as antitumor activity. Binding of IMP321 to MHC class II blocks intrinsic LAG-3 signaling and simultaneously matures DCs, which can further activate antitumor immune responses [119-121]. Supported by promising preclinical trials [122-124], a number of anti-CD73 mAbs and small molecule inhibitors are currently tested in clinical trials (NCT03611556, NCT02754141, NCT04148937). However, no results have been published yet. Moreover, therapies targeting TIM-3 and TIGIT are under preclinical [125, 126] and clinical investigation (NCT03680508, NCT04354246).

### 1.3.3 Adoptive cell transfer

Adoptive cell transfer (ACT) is one of the first immunotherapies that obtained objective response rates of up to 50% in metastatic melanoma patients. In this approach, autologous circulating or tumor-infiltrating lymphocytes are isolated and expanded to large numbers *ex vivo* and are then re-infused into the patient. Patients are usually pre-conditioned by nonmyeloablative lymphodepletion that depletes endogenous immunosuppressive cells, provides space and prevents competition with endogenous lymphocytes for cytokines. Furthermore, administration of IL-2 assist proliferation of transferred T cells *in vivo* [127-129]. Of note, *in vitro* lysis of autologous tumor cells by expanded TILs, correlates with a significantly better response of patients after ACT [130]. In a retrospective study with 402 melanoma patients, generation of viable TILs was feasible in 94% of cases and tumor-specific TILs were identified in 67% of patients [131].

Recent developments of ACT strategies aim at the selection and modification of TILs to improve the therapeutic efficacy. One candidate for selection is 4-1BB, which has been proposed as a marker for tumor-specific T cells [132]. In preclinical mouse models, expansion of T cells in the presence of an agonistic anti-4-1BB antibody improved expansion rates and antitumor function of $CD8^+$ T cells [133]. Likewise, addition of anti-CTLA-4 antibody in the initial phase of TIL culture increased tumor recognition *in vitro* compared to standard TIL cultures [134]. Furthermore, T cell clones specifically targeting neoepitopes derived from somatic mutations are promising candidates for ACT, as neoepitopes are characterized by their tumor-specificity as well as their insusceptibility to central tolerance mechanisms [135]. The drawback of neoepitope-based T cell therapies is the elaborate identification of patient-specific neoepitopes [136]. Yet, with whole-sequencing techniques and peptide-MHC-binding algorithms advancing quickly, a neoepitope-based individualized T cell therapy might be feasible. Notably, neoepitope-specific T cells cannot only be expanded from the TME, but also from patient's peripheral blood, even in patients with tumors showing a low mutational burden [137, 138].

Finally, T cells genetically engineered to target tumor antigens are used for ACT. Two strategies employing different mode of actions are currently applied in clinical trials. Thus, T cells are transduced with functional TCRs targeting epitopes presented by MHC molecules. Upon activation, mechanisms occurring in natural T cell activation are involved. In contrast, chimeric antigen receptor (CAR)-T cells contain an artificial receptor composed of an antigen-targeting single-chain variable fragment (scFv), an extracellular hinge region, a transmembrane domain, and an intracellular T cell signaling domain. The latter endows CAR-T cells with full functionality through co-stimulatory signals like CD3ζ chain, CD28, and 4-1BB. While TCR-transduced T cells can target a variety of antigens processed as peptides

including intracellular proteins, CAR-T cells can only bind surface molecules. The advantageous of CAR-T cells is that they act independent of MHC class I expression and recognize also antigens other than peptides [139]. CAR-T cell therapy achieved outstanding results in hematological malignancies, whereas therapeutic efficacy is solid tumors is still limited. Recent research focuses on the reduction of cytokine release syndromes and on-target off-tumor toxicities, the prevention of CAR-T cell exhaustion, and improved therapy for solid tumors [140].

### 1.3.4 Vaccination strategies

Vaccination strategies can be divided into prophylactic and therapeutic vaccination. Prophylactic cancer vaccines aim to prevent the formation of cancer. However, as cancer is a very heterogeneous disease, it is difficult to identify antigens suitable to prevent cancer across the population. To date, the only FDA-approved prophylactic cancer vaccine prevents infections with HPV, which is the leading cause of cervical cancer and can be involved in the development of anal, vaginal, penile and oropharyngeal cancer [141]. While the first generation of HPV vaccines protect from two to four high-risk HPV types causing 70% of cervical cancers, the second generation provides immunity against nine high-risk HPV types involved in 90% of cervical cancer cases [142]. More than 10 years after the introduction of the HPV vaccine, studies show an up to 90% efficacy of the vaccine and evidence of herd immunity [143]. Moreover, vaccination against hepatitis B virus (HBV), which was initially not developed as a prophylactic cancer vaccine, reduced the incidence of liver cancer [144]. Recent studies focus on the development of prophylactic vaccines in non-virally induced cancers. Thus, in a mouse model induced pluripotent stem cell (iPSC) vaccines prevented tumor growth by targeting shared antigens between iPSCs and tumor cells [145].

In contrast to prophylactic vaccines, therapeutic vaccines are used to treat an existing cancerous lesion. Therapeutic vaccination is considered an active form of immunotherapy, as TAAs are delivered to the patient's DCs, which can further active tumor-reactive T cell responses to elicit a comprehensive antitumor immune response. TAAs commonly investigated for vaccination strategies include cancer-testis, overexpressed, differentiation, and viral antigens. For therapeutically effective vaccination, the immunogenicity of the antigen as well as sufficient delivery of antigen to DCs is crucial and various strategies have been developed [146]. (1) Antigens can be delivered via peptides. While short peptides, with a length of 8-12 amino acids, exogenously bind to MHC molecules of all nucleated cells, synthetic long peptides (25-30 amino acids) are processed by APCs via physiological pathways. The latter lead to the activation of both $CD4^+$ and $CD8^+$ T cells, which makes synthetic long peptides more efficient in inducing immune responses compared to short peptides [147]. (2) DNA- and mRNA-based vaccines encode the TAA sequence, which can be administered in vectors or naked. From these, TAAs are directly translated or APCs are transformed to express the protein. mRNA-based vaccines have the advantage that they do not have to reach the nucleus and are more inflammatory compared to DNA-based vaccine [147, 148]. (3) For DC-vaccines, DCs are matured from autologous monocytes, loaded with peptide or nucleic acid of a TAA *ex vivo,* and reinfused into the patient. However, this personalized approach is very elaborative and the physiological maturation and activation of DCs *ex vivo* is challenging [149].

Although extensively investigated, the efficacy of therapeutic vaccines still lags behind other immunotherapies. Consequently, vaccination is combined with checkpoint inhibitors to counteract the immunosuppressive TME and vaccinations against tumor-specific antigens like neoantigens are tested [146].

### 1.3.5 Oncolytic viruses

Oncolytic viruses (OVs) are non-pathogenic or attenuated viruses that selectively target and kill tumor cells through pleiotropic mechanisms. Thus, due to molecular changes occurring in tumor cells (described in section 1.1), they get more susceptible to viral infection and replication which ultimately causes tumor cell lysis and viral spread [150]. Moreover, some OV strains target and lyse tumor blood vessels impairing tumor perfusion and proliferation of tumor cells. Furthermore, recent evidence suggests that OVs can function as *in situ* vaccines inducing a systemic immune response. Thus, during oncolysis, endogenous danger signals, pro-inflammatory cytokines and TAA are released priming an antitumor immune response. The therapeutic effect of OVs can further be enhanced by introducing a therapeutic transgene into the viral genome [151, 152]. These transgenes may deliver pro-apoptotic, anti-angiogenic or immunostimulatory functions [153-155]. The only FDA-approved OV talimogene laherparepvec (T-VEC) is a herpes simplex virus expressing GM-CSF, which is locally expressed within the tumor after viral infection and can recruit and activate APCs to elicit a systemic immune response. In a phase II trial, 16% of stage IIIB and IV melanoma patients showed durable responses [156, 157]. In preclinical models, a variety of immunomodulators have been investigated including cytokines, checkpoint inhibiting antibodies, and BiTEs [155, 158, 159]. Furthermore, OVs may have a natural tropism for tumor cells, but can also be retargeted to a specific antigen overexpressed in cancer, such as HER2, via a scFv [160].

### 1.3.6 Other immunotherapies

Beside the already described immunotherapies, a variety of other immunotherapeutic approaches exists. Cytokines are small proteins that are pivotal for the regulation of almost all physiological functions including pro- and anti-inflammatory processes. As one of the first immunotherapies, treatment with recombinant IFN-α and IL-2 represent a milestone of cancer immunotherapy. However, due to low efficacy, short half-life, and high toxicity, monotherapy with cytokines nowadays plays a less important role. Recent developments rather focus on new targets, inhibition of suppressive cytokines, favorable delivery and bioavailability as well as combination with other immunotherapies [161]. PRRs are the first sensors of foreign invaders leading to the activation of the innate immune system. Likewise, in cancer immunotherapy PRR agonists are used to initiate an antitumor immune response by activating APCs and reprogramming the immunosuppressive TME [162]. Moreover, immunotherapeutic approaches may target the immunosuppressive metabolism of immune cells. Hence, inhibitors of CD73, which together with CD39 converts ATP to immunosuppressive adenosine, and IDO1, a regulator of tryptophan catabolism, are investigated in clinical trials [163, 164]. Another interesting approach concerns the reprogramming of pro-tumoral M2-like macrophages to anti-tumoral M1-like macrophages using TLR agonists, IFN-γ, or monoclonal antibodies against CD40 [165]. Finally, several DNA-damaging reagents have been shown to induce immunogenic cell death (ICD) which is characterized by the release of damage-associated molecular patterns (DAMPs) that lead to the activation of the immune system. ICD is not only initiated by various chemotherapeutical drugs, but also radiotherapy (RT) has been shown to be a potent initiator of ICD stimulating the immune system [166].

## 1.4 Radiotherapy

Radiation is pivotal for both the diagnosis and treatment of cancer. Thus, radiation is essential in medical imaging and diagnostics of tumors using techniques like ultrasonography, computed tomography (CT), and magnetic resonance imaging (MRI) [167, 168]. For cancer management, ionizing radiation is directly used to destroy malignant cells as a physical therapy called radiotherapy. During RT, ionizing radiation passes through a tissue depositing energy to the cells, which leads to tumor cell killing or the induction of lethal DNA damage. In around 50% of all cancer cases, RT is applied in the course of the treatment as curative, neoadjuvant, adjuvant, or palliative therapy. Curative approaches intend to cure the cancer, neoadjuvant approaches aim to shrink tumor lesions before surgery, adjuvant approaches are supposed to destroy residing tumors cells after surgery, whereas palliative approaches aim to reduce the tumor burden and relieve patients from symptoms in incurable cancers. Furthermore, RT is frequently combined with other therapeutic approaches including surgery, chemotherapy and immunotherapy [169].

### 1.4.1 External beam radiotherapy

External beam radiotherapy (EBRT), in which high-energy rays are directed to the tumor from outside the body, is most widely used in cancer therapy. The ultimate goal of EBRT is to target the whole tumor mass, while sparing the surrounding normal tissue. However, as normal tissue cannot be protected completely, the total irradiation dose is frequently fractionated into small doses, typically 1.8 – 2 Gy per day, which are applied over a period of several weeks. Fractionation allows normal cells to repair sublethal DNA damage, whereas DNA repair mechanisms are often dysfunctional in cancer cells making them more susceptible to lethal DNA damage. Different fractionation regimes are currently used in the clinics. Hyperfractionation uses higher frequencies of lower doses within the same period of conventional therapy schedules. In contrast, hypofractionation delivers higher doses in a reduced number of fractions. Finally, accelerated fractionation reduces the period of therapy by applying more than one fraction per day [170, 171].

During the last decades, major advances in irradiation technologies allow irradiation with accurate and precise targeting of tumor tissue [172]. Three-dimensional conformal radiation therapy (3D-CRT) combines imaging, especially CT, and RT. Thus, with development of more sophisticated imaging techniques and treatment planning software, three-dimensional tumor structures can be precisely reconstructed and irradiated from different angles. For intensity-modulated radiation therapy (IMRT), an advancement of 3D-CRT, the irradiation beam can be divided into small irradiation fields with individual intensities. This allows regulation of the dose distribution guiding high doses to the tumor, while avoiding critical organs [173]. Image-guided radiation therapy (IGRT) monitors the exact position of the tumor before each fraction. This allows dose escalation, the control of organ motion and the reduction of safety margins (adjacent normal tissue) by around 1.5 cm [174, 175]. Stereotactic body radiation therapy (SBRT) uses very high doses in a single or few fractions precisely delivered to the tumor. For instance, in stage I non-small-cell lung cancer (NSCLS) patients, 60-66 Gy in three fractions were well tolerated and studies showed local control rates of 80% to 100%. Ablative SBRT is primarily indicated for nonmetastatic primary tumors and oligometastasis [176].

### 1.4.2 Photon vs. carbon ion radiation

#### 1.4.2.1 Physical differences

While EBRT is classically performed with photons, particle therapy has gained attention in recent years. Photons and particles, such as protons and carbon ions, have distinct physical properties. Photons are very small light particles that move through space in form of electromagnetic waves, such as x-rays or gamma rays, whereas proton irradiation uses charged nuclei of hydrogen atoms. Carbon ion radiotherapy (CIRT), also called heavy ion RT, uses positively charged carbon nuclei, which are even more massive compared to protons. For RT, photons beams are usually generated in linear accelerators, while particles are accelerated in synchrotrons to up to 70% of the speed of light. At the same time, this means that photon therapy can be implemented quite easily in the clinical practice and thus, is the standard radiation type used for RT. In contrast, carbon ion therapy needs a sophisticated and expensive facility so that carbon ion therapy is nowadays limited to a couple of centers worldwide, including the Heidelberg Ion Beam Therapy Center (HIT) and the National Institute of Radiological Sciences (NIRS) in Japan [177, 178].
The physical differences between photons, protons and carbon ions result in differences in the physical dose distribution of the irradiation beam within a tissue or water (Figure 1.4). Photon beams show a build-up effect in the first centimeters, which is followed by an exponential decrease of the relative dose as the beam travels through a tissue. Consequently, if a tumor is located deep within the body, only a proportion of the initial dose will reach the tumor. At the same time, adjacent normal tissue located in front and behind the tumor will be affected by the photon beam as well. In contrast, proton and carbon ions beams are characterized by an inverted depth-dose profile, where the maximal dose is released at the end of the beam track, the so-called Bragg peak. This dose distribution renders particle beams ideal for cancer therapy, as tumors can be precisely irradiated allowing dose escalation and treatment of deeply located tumors. As the Bragg peak is quite narrow, it is spread out via multiple beam scans to cover the whole tumor. This comes along with an increase of the dose in the plateau phase, which is located in front of the Bragg peak. Similar to 3D-CRT and IMRT, intensity controlled raster scanning techniques generate a carbon ion beam conforming to tumor shape [179].

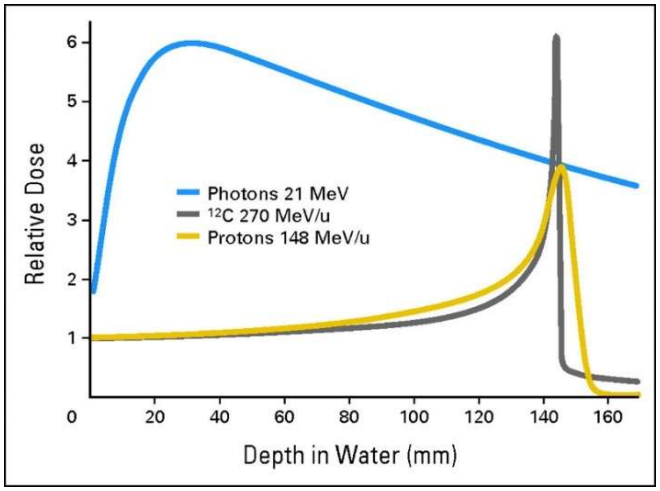


**Figure 1.4: Depth-dose profiles photons, protons and carbon ions**. Relationship between relative dose and depth in water. Protons and carbon ions show characteristic Bragg peak. Picture was taken from [177].

#### 1.4.2.2 Biological differences

A parameter influencing the biological effectiveness of irradiation is the linear energy transfer (LET), which describes the amount of energy deposited to a material per unit distance along the track of an ionizing particle. The LET increases with particle size meaning that photon radiation is considered a low LET radiation compared to carbon ion radiation. As higher LETs are associated with higher relative biological effectiveness (RBE), carbon ion irradiation obtains higher biological efficiency compared to photon irradiation [177].
On the cellular level, carbon ion radiation is associated with several advantages. First, carbon ion irradiation induces a higher degree of irreparable DNA damage ultimately causing cell death. Thus, photon irradiation mainly induces single-strand breaks (SSBs), which can be repaired efficiently. If double-strand breaks (DSBs) are induced upon photon irradiation, they are dispersed and can rapidly and efficiently be repaired by non-homologous end joining (NHEJ) or homology-directed repair (HDR). After carbon ion irradiation, around 70% of DNA damage are DSBs, which are clustered and thus harder to repair [178, 179]. Hence, small DNA fragments emerge, which cannot be recognized by the machinery of NHEJ [180]. Second, photon irradiation is highly dependent on oxygen. Thus, photons only indirectly induce DNA damage by producing free radicals from water, which in turn cause DNA damage [181]. Consequently, tumors not responding to photon irradiation are commonly hypoxic tumors such as pancreatic cancer and head and neck cancer [182]. In contrast, carbon ion irradiation can directly induce DNA damage, as the charge of carbon ions is most likely great enough to be cytotoxic independent of oxygen, which is of great benefit regarding hypoxic tumor regions with poor blood supply [183, 184]. Third, carbon ion irradiation induces cell death independent of the cell cycle phase thereby being destructive also in slowly growing tumors. On the contrary, cells in G0 and S phase are radioresistant to photon irradiation, most likely due to the presence of the HR machinery in S phase [178, 179]. Finally, preclinical trials indicate that carbon ion irradiation might be more efficient in suppressing metastasis formation [185, 186]. Thus, carbon ion irradiation might be more destructive to cancer stem cells (CSCs) compared to photon irradiation thereby diminishing the outgrowth of metastases [187]. Furthermore, in a recent preclinical study, tumor recurrence after photon and carbon ion therapy was assessed. Interestingly, recurrent tumors after photon irradiation, but not carbon ion irradiation, were more aggressive as indicated by enhanced microvessel formation and increased expression of genes associated with metastases [188].

#### 1.4.2.3 Clinical indication for carbon ion radiotherapy

Overall, preclinical studies suggest that CIRT might be ideal for cancer treatment due to the superior physical and biological effects compared to classical photon therapy. As very precise irradiation is feasible with CIRT, hypofractionation regimes are practicable reducing treatment time and costs. However, as CIRT can still be considered a rather new therapy approach and application is limited to a few centers worldwide due to the extensive costs for building and maintenance, there are a number of clinical trials ongoing clarifying the therapeutic potential of CIRT [189]. Overall, CIRT is particularly meaningful for tumor entities that are insensitive to photon irradiation or tumors that are surrounded by organs at risk, including intracranial tumors like high-grade glioma. In a phase I/II clinical trial, malignant glioma patients were treated with photon therapy plus chemotherapy and a boost of carbon ion therapy with eight fractions of 16.8 to 24.8 Gray equivalent (GyE). Particularly in patients treated with a high-dose carbon ion boost, progression-free survival (PFS) and median survival time (MST) could be increased to 14 and 26 month compared to 4 and 7 month for patients receiving a low dose boost [190]. Moreover, CIRT is well-suited for the treatment of skull base chordoma due to the proximity to

organs at risk. A study by Schulz-Ertner *et al*. showed good efficacy and tolerability of CIRT (60-70 GyE in 20 fractions) with local control rates and OS of 70% and 88.5%, respectively, after 5 years [191]. In order to directly compare the effect of particle therapy with protons and carbon ions in skull base chondrosarcoma patients, a prospective, randomized phase III clinical trial has been initiated. The overall aim is to show that carbon ion therapy (experimental treatment) might be as effective as proton therapy (standard therapy) [192]. Moreover, there are also clinical trials comparing the effect of photon, proton and carbon ion therapy. Hence, the PINNOCHIO trial (NCT01795300) at HIT in Heidelberg compares four arms in skull base meningioma patients: conventional fractionated radiation as active comparator (57.6 Gy in 32 fractions à 1.8 Gy), hypofractionated photon therapy (45 Gy in 15 fractions à 3 Gy), proton therapy (45 GyE in 15 fractions à 3 Gy), and CIRT (45 GyE in 15 fractions à 3 Gy). Apart from the above mentioned tumor entities, CIRT is applied and tested in numerous tumors including head and neck tumors, lung tumors, gastrointestinal tumors, genitourinary tumors, gynecological tumors, sarcomas and pediatric tumors [193].

### 1.4.3 Cytotoxic effects of radiotherapy

#### 1.4.3.1 Cell cycle arrest

The primary effect of ionizing radiation is the induction of DNA damage in form of SSBs and DSBs leading to cell cycle arrest, which allows DNA repair or initiation of cell death. Upon irradiation, ataxia-telangiectasia mutated (ATM) kinase and ataxia-telangiectasia and RAD3-related (ATR) kinase are detecting DNA damage resulting in the phosphorylation and activation of downstream proteins regulating cell cycle arrest, including checkpoint kinase-1 and -2 (CHK1 and CHK2) [194]. Thus, phosphorylation of cell division cycle 25 (CDC25) phosphatase by CHK1 and CHK2 causes the degradation of CDC25, which cannot further activate cyclin-dependent kinase 1 (CDK1) and CDK2 leading to a cell cycle arrest at the G1 or G2 checkpoint [195]. Moreover, ATM, CHK1, and CHK2 directly phosphorylate and stabilize p53, which is bound to the ubiquitin ligase mouse double minute 2 homolog (MDM2) protein and subjected to proteasomal degradation under normal conditions. p53 is key player in determining the fate of a cell after irradiation. On the one hand, p53, functioning as a transcription factor after activation, can induce cell cycle arrest. Thus, p53 promotes the transcription and activation of the CDK-inhibitor p21, which in turn inhibits CDK4 and CDK6 leading to a G1 and G2 cell cycle arrest. On the other hand, extensive DNA damage prolongs p53 signaling favoring apoptosis [196, 197].

#### 1.4.3.2 DNA repair of radiation-induced DNA damage

After cell cycle arrest, DNA repair mechanisms are initiated. Overall, SSBs can be more easily repaired compared to DSBs. Damaged bases are excised by the base excision repair (BER) pathway resulting in SSBs, which are sensed by poly-ADP-ribose polymerase (PARP), an important protein recruiting further repair proteins. SSBs are then replaced by single strand break repair (SSBR), which operates in two different mechanisms: short-patch and long-patch SSBR. In short-patch SSBR, single nucleotides are inserted by DNA polymerase β and ligated by DNA ligase III. In contrast, long-patch SSBR is more complex including the removal and replacement of several nucleotides by proliferating cell nuclear antigen (PCNA), polymerase δ/ϵ, flap endonuclease 1 (FEN1), and DNA ligase I [198].
Two major pathways repair irradiation-induced DSBs: NHEJ and HR. The NHEJ pathway operates predominantly upon irradiation-induced DNA damage and throughout the complete cell cycle. NHEJ can accurately ligate DNA ends with complementary overhangs, however

irradiation frequently produces ends that cannot be ligated and are thus processed by error-prone mechanisms [199]. During one step of NHEJ, histone H2AX becomes phosphorylated, which is frequently used as a biomarker for irradiation-induced DNA damage [200]. While HR is more accurate than NHEJ, it is only functioning in late S phase and G2 phase, as HR requires an identical copy of DNA, which is used as a template [201]. In case of successful DNA repair, the cell will continue with its cell cycle, whereas cell death will be induced, if DNA repair fails.

#### 1.4.3.3 Cell death

**Mitotic catastrophe.** Severe DNA damage or failure of mitotic checkpoints can interrupt the regular course of mitoses leading to mitotic catastrophe, which results in premature mitosis before S and G2 phase are completed. The exact mechanisms underlying the initiation of mitotic catastrophe is unclear, but p53 is most likely involved and knockout of proteins associated with cell cycle control, including ATM, CHK1, and p21, enhance mitotic catastrophe. Afterwards, senescence or mitotic death, a form of regulated cell death (RCD) associated with the intrinsic apoptosis pathway, may follow. Cell death may not only occur directly during the first cell division after irradiation, but also after subsequent cell divisions with a delay of up to six days. As aberrant mitosis leads to atypical chromosomal segregation and cell division, cells undergoing mitotic catastrophe are of giant size bearing aberrant nuclear morphology, multiple nuclei or several micronuclei. Thus, cells that not directly enter mitotic cell death may become tetraploid due to improper cytokinesis becoming apparent by cell swelling. p53 wild type cells will enter apoptosis in the next G1 phase, whereas p53 mutant cells may undergo further cell divisions before cell death [202, 203].

**Apoptosis.** When cells undergo apoptosis after irradiation, the intrinsic (mitochondrial) apoptosis pathway is predominantly activated. The intrinsic apoptosis pathway is tightly regulated by members of the BCL-2 family exerting both pro- and anti-apoptotic functions. When nuclear p53 accumulates, the expression of pro-apoptotic BCL-2 genes is enhanced causing the activation of two key mediators of apoptosis, BCL-2-associated X protein (BAX) and BCL-2 antagonist/killer (BAK). Both BAX and BAK can initiate mitochondrial outer membrane permeabilization (MOMP), a process in which pores are introduced into the mitochondrial outer membrane and which is a point of no-return in apoptosis. Consequently, the intermembrane space proteins cytochrome c and SMAC are released. While cytochrome c builds the apoptosome together with apoptotic protease-activating factor 1 (APAF1), SMAC neutralizes caspase-inhibitory proteins. Both mechanisms turn pro-caspase-9 into caspase-9, which stimulates the activation of caspase 3, 6, and 7 executing the controlled degradation of a cell [204, 205]. Moreover, apoptosis can be initiated by irradiation-induced ROS stimulating the release of cytochrome c by mitochondria or disturbing the mitochondrial membrane potential by causing the release of $Ca^{2+}$ [206, 207]. Under specific conditions, irradiation can induce the extrinsic apoptosis pathway, which involves signaling through death receptors of the TNFR super family including Fas, TNFR1, TRAILR1 and its ligands FasL and TRAIL1. Both death receptors and ligands can be transactivated by p53 in response to irradiation. Receptor-ligand binding initiates trimerization and clustering of death receptors leading to the recruitment of Fas-associated death domain (FADD) and pro-caspase-8, which make up the death-inducing signaling complex (DISC). Finally, caspase-8 activates the executioner caspases 3 and 7, which conduct apoptosis in the same manner as in the intrinsic pathway [208, 209].

**Senescence**. Alternative to apoptosis, irradiated cells can enter senescence, a state in which cells are not proliferating, but remain viable and metabolically active, resist apoptosis, and secrete factors that may promote tumor growth and evasion. Moreover, senescence might only represent a temporal growth-arrest to cope with the irradiation-induced cytotoxicity. Stimuli, like survivin, CDK1, and CDC2, may trigger regrowth of senescent cells that might exhibit stem-like features and increased proliferation, migration, and invasion [210].

**Immunogenic cell death.** In recent years, increasing evidence suggests that irradiation not only induces cell death, but also at the same time may activate the immune system and thus induce ICD. Of note, while necrosis was classically considered immunogenic and apoptosis immunologically silent, also apoptosis has been shown to elicit immunogenic responses [211].

### 1.4.4 Irradiation-induced immune responses

#### 1.4.4.1 Immunostimulatory effects

Following irradiation, various immunostimulatory effects eliciting an antitumor immune response are activated affecting (I) T cell priming, (II) leukocyte infiltration, (III) the composition of the TME, and (IV) immunomodulation of tumor cells (Figure 1.5) [212]. In this section, irradiation-induced immunostimulatory effects will be described, however also immunosuppressive effects are induced, which will be discussed in section 1.4.4.2.

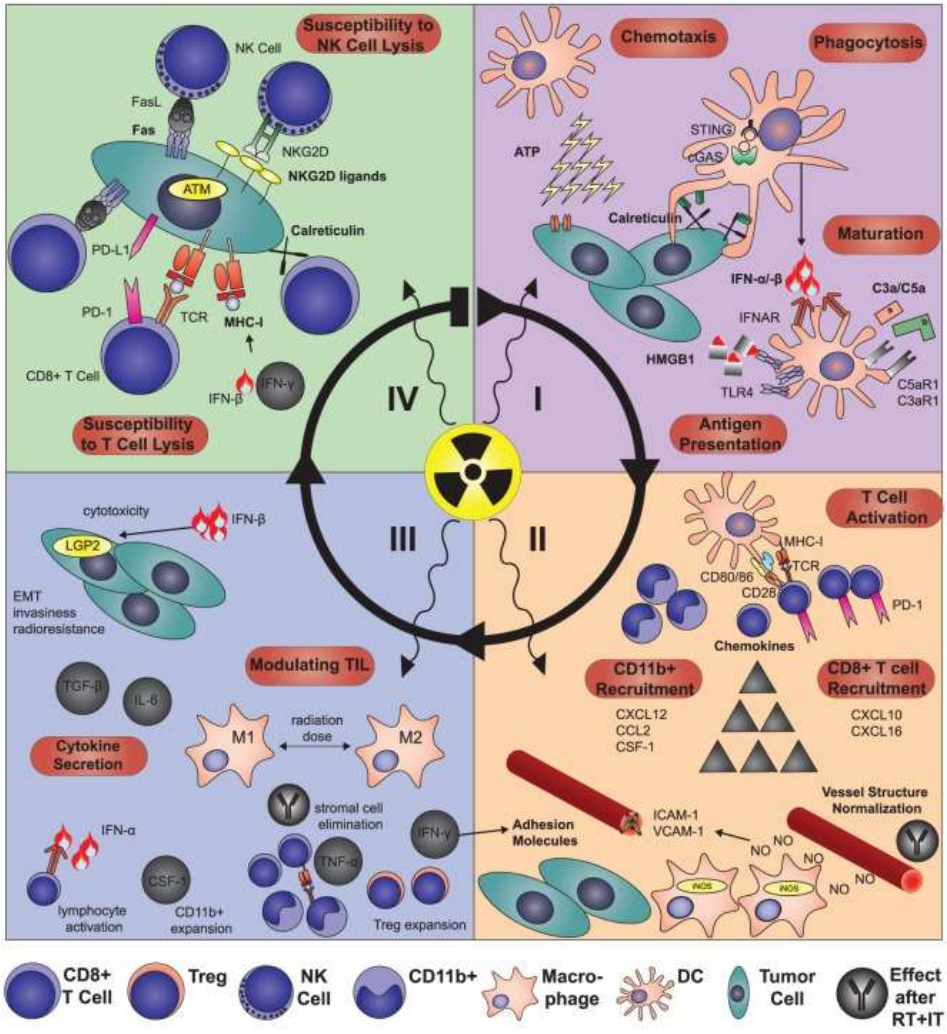

**Figure 1.5: Immunostimulatory effects of irradiation.** Irradiation elicits pro-inflammatory immune responses by affecting (I) T cell priming, (II) leukocyte infiltration, (III) the composition of the TME, and (IV) immunomodulation of tumor cells. During T cell priming, danger signals are released promoting maturation and activation of DCs. Leukocyte infiltration is facilitated by normalization of the tumor vasculature, as well as the upregulation of adhesion molecules and chemokines. The composition of the TME is altered as irradiation induces a burst of cytokines. Moreover, low-dose irradiation favors the polarization of macrophages into the M1-like phenotype. Immunogenicity of tumors cells is enhanced due to the upregulation of MHC class I molecules, apoptosis receptors, and activating NK receptors. ATM: ataxia teleangiectasia mutated, ATP: adenosine triphosphate, cGAS: cyclic GMP-AMP synthase, CCL: C-C motif chemokine ligand, CSF-1: colony stimulating factor-1, CXCL: C-X-C motif chemokine ligand, DC: dendritic cell, EMT: epithelial-mesenchymal transition, HMGB1: high mobility group box 1, IFN: interferon, IL: interleukin, iNOS: nitric oxide synthase 2, LGP2: laboratories of genetics and physiology 2, M1: M1-like macrophage, M2: M2-like macrophage, MHC-I: major histocompatibility complex I, NK: natural killer cell, NKG2D: killer cell lectin-like receptor K1, NO: nitric oxide, PD-(L)1: programmed cell death (ligand) 1, STING: transmembrane protein 173, TCR: T cell receptor, TGF-β: transforming growth-factor beta: TIL: tumor-infiltrating lymphocyte, TLR: toll-like receptor, TME: tumor microenvironment, TNF: tumor necrosis factor, TNFR: tumor necrosis factor receptor, Treg: regulatory T cell. Picture taken from [212].

**I. T cell priming**. Irradiation can favor T cell priming by inducing the release of tumor antigens, which can be uptaken and cross-presented by DCs priming tumor-specific immune responses in the draining lymph nodes [213]. Moreover, the radiation-induced release of DAMPs facilitates various stages of T cell priming. Thus, extracellular ATP supports the recruitment of DCs into the TME, whereas translocation of calreticulin to the cell surface, whose expression is confined to the endoplasmic reticulum under normal conditions, enhances phagocytosis of tumor cells by APCs [214-216]. Moreover, DC migration and maturation are mediated by increased cytoplasmic translocation and extracellular secretion of the nuclear chromatin-binding protein HMGB1 [217, 218]. Finally, irradiation induces cytosolic double-stranded DNA (dsDNA), which is a known activator of the cGAS-STING pathway causing the expression of type I IFNs promoting DC maturation and activation of further leukocytes [219].

**II. Leukocyte infiltration.** Tumors are characterized by an aberrant tumor vasculature of heterogenic, permeable, and disorganized blood vessel networks with diminished functionality [220]. Low dose irradiation can normalize these aberrant vessel structures promoting the infiltration of $CD8^+$ T cells primed in the lymph nodes. Thus, upon low dose irradiation, the expression of inducible nitric oxide synthases (iNOS) by M1-like macrophages can convey vascular normalization [221]. Moreover, adhesion molecules play a pivotal role in leukocyte recruitment. Irradiation induces the expression of intercellular adhesion molecule 1 (ICAM-1) and vascular cell adhesion molecule in (VCAM-1) in lymphatic endothelial cells mediating increased adherence of T cells and promoting leukocyte transmigration [222]. Finally, irradiation upregulates the release of chemokines such as C-X-C motif ligand 10 (CXCL10) and CXCL16, which attract effector T cells and NK cells to the TME [223, 224].

**III. Composition of the tumor microenvironment.** Following irradiation, a magnitude of pro- and anti-inflammatory cytokines is released into the TME. On the part of pro-inflammatory cytokines, type I IFNs (IFN α/β) and type II IFNs (IFN-γ) are of utmost importance. Type I IFNs promote the cross-presenting capacity of DCs and expand tumor-specific T cells. Importantly, in IFNAR1 knockout mice response to RT is diminished highlighting the crucial role of radiation-induced IFN signaling [225]. Moreover, type I IFN show direct effects on tumor cells decreasing their proliferative capacity, altering the cell cycle, and upregulating apoptosis markers as well as MHC class I molecules [226]. While type I IFN are produced via the cGAS/STING pathway after irradiation in response to dsDNA, type II IFNs are mainly secreted activated $CD8^+$ T cells. Thus, intratumoral IFN-γ levels are decreased by 90%, when $CD8^+$ T cells are depleted [227]. Similar to type I IFNs, irradiation-induced IFN-γ is associated with the upregulation of chemokines and MHC class I molecules [228]. Besides changing the leukocyte composition in

the TME via increased leukocyte infiltration, irradiation can also directly affect the phenotype of tumor-resident macrophages. Thus, low dose-irradiation has been shown to polarize TAMs towards an M1-like phenotype by cell-intrinsic mechanisms potentiating the therapeutic effect of ACT [221]. Moreover, irradiation mediates antigen presentation by stromal $CD11b^+$ myeloid cells rendering them susceptible to CTL-mediated killing [229].

**IV. Immunomodulation of tumor cells.** Finally, irradiation ha a direct impact on tumor cells increasing their immunogenicity and susceptibility to leukocyte-mediated killing. As mentioned before, irradiation induces an IFN-dependent upregulation of MHC class I surface expression. Furthermore, irradiation increases the peptide repertoire that can be presented by MHC class I molecules. Thus, intracellular peptide levels are increased as existing proteins are degraded, *de novo* protein translation is enhanced, and unique novel peptides are produced. All these events are associated with increased CTL-mediated tumor cell killing *in vitro* and *in vivo* [230]. In addition, the upregulation of the death receptors Fas and TRAILR on tumors cell can trigger the extrinsic apoptosis pathway stimulated after receptor-ligand binding by T cells and NK cells [209, 231]. Surface expression of calreticulin not only facilitates phagocytosis of tumors by DCs, but also increases the susceptibility to CTL-mediated lysis [232]. Finally, irradiation enhances the expression of NK receptors like NKG2D providing an activating signal triggering NK cell-mediated cytotoxicity [212].

#### 1.4.4.2 Immunosuppressive effects

Besides the immunostimulatory effects, RT has been shown to upregulate immunosuppressive pathways as well. Indeed, irradiation induces the extracellular release of ATP triggering the recruitment of DCs [216]. However, in the immunosuppressive TME, increased ATP levels are rapidly catabolized to adenosine by CD39 and CD73 limiting effector T cell functions and promoting the suppressive capacity of Tregs [61]. Accordingly, upregulation of CD73 in pancreatic cancer cells was associated with radioresistance [233]. Moreover, the checkpoint molecule TIM-3 is upregulated upon irradiation. Consequently, increased levels of TIM-3 can catch away the danger signal HMGB1 limiting its functions in T cell priming [65, 234].
Indeed, irradiation can destruct tumor vasculature [221]. However, at the same time, hypoxia may be induced and hypoxia-inducible factor 1-alpha (HIF-1α), a crucial regulator of angiogenesis, accumulates in the TME in response to irradiation enhancing radioresistance of endothelial cells and thus limiting vascular destruction [235]. Moreover, binding of HIF-1α to a transcriptionally active hypoxia-response element that is in proximity to the PD-L1 promoter mediates the expression of PD-L1 in MDSCs, macrophages, and DCs [88]. In DCs, HIF-1α can further inhibit IL-12 production limiting Th1 immune responses, while HIF-1α depletion reconstituted IL-12 and downregulated IL-10 expression [236]. Notably, gene expression analysis showed that HIF-1α upregulation was correlated with both pro-inflammatory and anti-inflammatory immune signatures, but the immunosuppressive signatures seemed to prevail [237]. Finally, HIF-1α can induce VEGF expression promoting neovascularization [235, 238]. Similar to HIF-1α, VEGF also directly exerts immunosuppressive functions. Aside from TIM-3, the expression of the checkpoint molecules CTLA-4, PD-1, LAG-3, and GITR is induced on T cells promoting immunosuppression [234]. The upregulation of these inhibitory receptors might be a direct consequence of increased VEGF-A expression upon irradiation [239, 240]. Furthermore, VEGF receptors are highly expressed on Tregs and ligand binding stimulates Treg proliferation, while VEGF-A suppresses myeloid cell differentiation fostering immunosuppressive MDSCs [241, 242].

In addition, irradiation mediates the expression of immunosuppressive chemokines and cytokines. Thus, irradiation-induced release of the chemokines CCL2 and CXCL12 attracts suppressive myeloid cells to the tumor [243, 244]. Moreover, the cytokine CSF-1 is upregulated upon irradiation and can either stimulate the differentiation of monocytes into TAMs or directly promote the infiltration, proliferation, and polarization of M2-like TAMs [245, 246]. Furthermore, M2-like macrophages were found to be more resistant to irradiation leading to higher proportions of M2-like TAMs in the TME [247]. Likewise, Tregs are comparably radioresistant [248]. Another crucial cytokine determining the fate of antitumor immune responses after RT is TGF-β. Blocking of TGF-β was shown to increase the therapeutic efficacy of RT on the irradiated tumor and non-irradiated metastases in poorly immunogenic tumors due to the generation of a $CD8^+$ T cell response [249]. TGF-β activation exerts pleiotropic immunosuppressive functions. Regarding its effects on T cells, TGF-β mediates the differentiation of naïve $CD4^+$ T cells to Tregs, suppresses the effector functions of $CD8^+$ T cells, and induces the expression of CD39 and CD73 on $CD4^+$ and $CD8^+$ T cells. In the myeloid compartment, TGF-β promotes the polarization of TAMs and TANs to M2-like and N2-like phenotypes, respectively [250]. Regarding the expression of immunomodulatory surface receptors on tumor cells, especially PD-L1 was shown to be upregulated upon irradiation, suppressing T cell function via the PD-1/PD-L1 axis [251].

#### 1.4.4.3 Abscopal effects

Already in the 1950s, local irradiation of a primary tumor was observed to induce therapeutic effects on distant metastases, indicating that RT might have further mechanisms of action beside DNA damage [252]. Nowadays, knowing that ICD can act as an *in situ* vaccine it is generally accepted that this so-called abscopal effect is mediated by the activation of the immune system. Thus, irradiation-induced antitumor immune responses cannot only be directed against the primary tumor, but possibly also against distant metastases. Indeed, abscopal effects have been described for several tumor entities including melanoma, renal cell carcinoma, and breast cancer, however a review from 2016 reports only 46 cases of abscopal effects from 1969 to 2014 [253-256]. This highlights the impact of immunosuppressive effects induced by irradiation inhibiting the occurrence of abscopal effects. A recent study further suggest that autophagy might inhibit abscopal responses as dsDNA fragments released after MOMP are cleared by autophagy and can consequently not stimulate antitumor immune responses [257]. Similarly, doses above 12-18 Gy were shown to induce the DNA exonuclease 3' repair exonuclease 1 (TREX1), which inhibits immune activation by clearing dsDNA [258].

## 1.5 Combination of immunotherapy and radiotherapy

With immunotherapies advancing in recent years, a combination of RT and immunotherapies might counteract immune suppression and boost the therapeutic effect on both primary and distant tumors. Various preclinical studies corroborate this theory. One of the first studies showing regression of abscopal tumors after combined RT with 2-6 Gy plus immunotherapy with FMS-like tyrosine kinase receptor 3 ligand (FLT3L) was performed by Demaria *et al*. Briefly, mice were implanted with two 67NR (mammary carcinoma) tumors and only after the combination therapy delayed tumor growth of the non-irradiated tumor site was observed. Furthermore, they showed that the effect was tumor-specific and T cell-dependent, as an abscopal tumor with a different cancer cell line was not affected and experiments with nude mice did not evoke abscopal effects [259]. Since then, several pre-clinical studies corroborated these findings in different tumor models including MC38 colon adenocarcinoma, B16F10

melanoma, and 4T1 mammary carcinoma. Notably, the radiation schemes in these studies varied applying 3 x 8 Gy, 20 Gy, and 12 x 2 Gy in the MC38, B16F10, and 4T1 model, respectively. Moreover, different immunotherapy schedules were applied in these studies using single or dual immune checkpoint blockade either before, concurrent with or after RT [260-262]. This highlights a major challenge of radioimmunotherapy approaches as optimal treatment regimens remain to be elucidated, especially in clinical applications [263]. Still, preclinical data provide some evidence for the design of radioimmunotherapy approaches. Dewan *et al.* compared single dose RT (20 Gy) with fractionated RT (3 x 8 Gy and 5 x 6 Gy) plus anit-CTLA-4 checkpoint blockade in two mouse models, in which only fractionated RT regimens induced abscopal effects [264]. Regarding the timing of the administration of immunotherapies, survival of mice was only significantly prolonged when anti-PD-L1 therapy was administered concurrently with the first or last fraction, but not when it was administered sequentially one week after the last fraction [265].
First clinical evidence for abscopal effects after radioimmunotherapy were provided by a phase I/II clinical trial applying 35 Gy in ten fractions over two weeks to one metastatic site and immunotherapy with GM-CSF daily for two weeks starting in the second week of RT. In 41 patients with different tumor entities, an abscopal response in 26.8% of patients was observed [266]. Moreover, in a phase I trial treating metastatic melanoma patients with RT plus ipilimumab, 13.6% of patients showed complete responses, whereas other studies with ipilimumab monotherapy report CR rates of 1.4-2.2%. Notably, in this trial ipilimumab was administered concurrently, while a phase I clinical trial in which ipilimumab was administered after RT showed comparable results to ipilimumab monotherapy, corroborating preclinical data [212, 265]. As results might differ between tumor entities and tumor stages, numerous clinical trials are currently evaluating the combination of RT with immunotherapy. While in the majority of clinical trials a combination to RT with anti-PD-1/PD-L1 and anti-CTLA-4 antibodies is investigated, other trials include immunotherapy with the cytokines GM-CSF or IL-2, TGF-β-blocking agents, TLR agonists, or cancer vaccines [263]. Finally, patient-specific immune monitoring could contribute to the design of an appropriate treatment schedule. When RT was combined with chemotherapy, frequencies of circulating T cells decreased, while expression of PD-1 on $CD4^+$ T cells was increased. This observation point towards a possible benefit from additional immunotherapy to restore immune responses [267].

## 1.6 The EO771 breast cancer model

EO771 tumors cells were first isolated from a spontaneous medullary breast adenocarcinoma in a female C57BL/6 mouse in 1951 [268]. Although EO771 cells are frequently used as a transplantable, syngeneic and non-metastatic breast cancer model, the molecular characterization of EO771 cells remains ambiguous. Overall, breast cancer can be classified into four different molecular subtypes, which is determined by the receptor status of the tumor and is an important indicator for successful therapy. Using immunohistochemistry the two hormone receptors (HR) progesterone receptor (PR) and estrogen receptor (ER) as well as the growth receptor HER2 are analyzed. The luminal A subtype, the most common and least aggressive subtype, is $HR^+$ and $HER2^-$. Luminal B tumors are $HR^+$, possibly $HER2^+$, and are characterized by highly proliferating cells as determined by expression of Ki67. Compared to luminal A tumors, prognosis for luminal B tumors is worse, with a survival rate of 92.5% and 90.3% at four years, respectively. HER2-positive breast cancers express high levels of HER2, while being negative for hormone receptors. The four-year survival rate accounts four 82.7%.

Triple-negative breast cancer (TNBC), also basal-like cancer, shows the poorest outcome (77.0%) and is negative for any of the receptors ($HR^-$, $HER2^-$) [269, 270].
Johnstone *et al.* suggest that EO771 cells have a predominant TNBC phenotype as indicated by immunohistochemistry (IHC) stainings negative for ERβ, PR, and HER2 receptors and only diffuse cytoplasmic, but not nuclear, staining for ERα protein. Moreover, EO771 cells were shown to express the TNBC marker epidermal growth factor receptor (EGFR). However, gene expression profiles were not enriched in basal-like gene signatures and despite the lack of HRs, EO771 cells were sensitive to hormone therapy with tamoxifen *in vivo*, but not *in vitro* [271]. In a more recent study, EO771 cells were classified as luminal B breast cancer. Hence, both on the transcriptome and protein level, EO771 cells were shown to express ERβ, PR and HER2 receptors [272]. The driver-mutation promoting tumorigenesis in EO771 cells is unknown. Regarding the 30 most commonly mutated genes in human breast cancer, EO771 is carries homozygous mutations in *trp53, spen, tbl1xr1*, and *kras* genes as well as heterozygous mutations in *map2k4* and *med23* genes. Moreover, an amplification of the *myc* and *pvt1* locus and a homozygous deletion of *cdkn2b* have been described [273].

## 1.7 Aim of the study

Carbon ion RT has emerged as a promising therapeutic approach for cancer management due to its favorable physical and biological properties compared to classical photon radiation. However, while it has been well described in literature that photon radiation may act as an *in situ* vaccine inducing pro-inflammatory immune responses, capable of mediating even regression of distant tumors (abscopal effect), little is known when it comes to the immunomodulatory capacity of carbon ion radiation. Consequently, the primary goal of this thesis was to elucidate the therapeutic and immunomodulatory potential of carbon ion irradiation in direct comparison to classical photon radiation. For this purpose, the breast cancer cell line EO771 was used, for which irradiation-induced effects have only been poorly characterized so far.

In the first part of the project, the aim was to compare cytotoxic and immunomodulatory effects induced by photon versus carbon ion irradiation on EO771 cells *in vitro*. To gain a broad overview, EO771 cells were irradiated with graded doses, ranging from low to high dose irradiation, using biologically equivalent doses of photons and carbon ions.

In the second part of the project, the overall goal was to characterize therapeutic and immunomodulatory effects on local and distant tumor sites induced after radiotherapy. Importantly, radiotherapy was combined with immune checkpoint blockade to counteract the suppressive TME. For this purpose, the aim was to

1. establish an abscopal tumor model in which mice bear contralateral tumors
2. establish a new system for local photon irradiation of murine tumors, in which the second contralateral tumor is shielded
3. identify an optimal treatment schedule for combined radiotherapy plus immune checkpoint blockade against PD-L1 or CTLA-4
4. characterize therapeutic effects, determine immune cell profiles in both tumors, and investigate the formation of tumor-specific memory immune responses after photon irradiation plus checkpoint blockade as a reference.
5. compare the effects of photon and carbon ion irradiation *in vivo* in terms of the aforementioned properties.

# 2 Materials and Methods

## 2.1 Materials

### 2.1.1 General instrumentation

Table 2-1: General instrumentation

| Instrument | Manufacturer |
|---|---|
| 7300 Real Time PCR System | Applied Biosystems, Foster City, USA |
| Aesclap Isis Clipper | B. Braun, Melsungen, Germany |
| BD FACS LSRFortessa Flow Cytometer | Becton Dickinson, Franklin Lakes, USA |
| BD FACSCanto II Flow Cytometer | Becton Dickinson, Franklin Lakes, USA |
| Biological Safety Cabinet, Hera Safe | Heraeus, Hanau, Germany |
| CASY Cell Counter | OLS OMNI Life Science, Bremen, Germany |
| CB 150 Incubator | BINDER, Tuttlingen, Germany |
| Centrifuge 5415 R | Eppendorf, Hamburg, Germany |
| Centrifuge 5810 R | Eppendorf, Hamburg, German |
| CLARIOstar Plus Microplate Reader | BMG Labtech, Ortenberg, Germany |
| CTL ELISpot Reader System | Cellular Techn. Ltd, Shaker Heights, USA |
| Faxitron MultiRad225 | Faxitron Bioptics, LLC, Tucson, USA |
| Gammacell 1000 Elite | Best Theratronics, Ottawa, Canada |
| Gammacell 40 Exactor | Best Theratronics, Ottawa, Canada |
| Gel Documentation System | Bio-Rad Laboratories, Hercules, USA |
| gentleMACS™ Dissociator | Miltenyi Biotec, Bergisch Gladbach, Germany |
| Innova 4230 Refrigerated Benchtop Incubator | New Brunswick Scientific, Edison, USA |
| Megafuge 2.0R | Heraeus, Hanau, Germany |
| Microscope Olympus CK40 | Leica Camera, Wetzlar, Germany |
| Mini Laboratory Centrifuge | neoLab Migge, Heidelberg, Germany |
| Mithras LB 940 | Berthold Technologies, Bad Wildbad, Germany |
| Multipipette E3x | Eppendorf, Hamburg, Germany |
| Nalgene Mr. Forsty Freezing Container | Thermo Fischer Scientific, Waltham, USA |
| NanoDrop 2000 Spectrophotometer | Thermo Fischer Scientific, Waltham, USA |
| pH Meter 766 Calimatic | Knick, Berlin, Germany |
| PIPETBOY acu 2 | INTEGRA Biosciences, Biebertal, Germany |
| PIPETMAN Pipettes (P2, P10, P20, P100, P200, P1000) | Gilson, Middleton, USA |
| Qubit$^{MT}$ 4 Fluorometer | Thermo Fischer Scientific, Waltham, USA |
| RS PRO 150mm Digital Caliper 0.0005 in, 0.01 mm | RS Components, Corby, United Kingdom |
| Thermomixer Comfort | Eppendorf, Hamburg, Germany |
| Ultraviolet Sterilizing PCR Workstation | Peqlab Biotechnologie, Erlangen, Germany |
| Veriti 96-Well Thermal Cycler | Applied Biosystems, Foster City, USA |
| Vortex-Genie 2 | Scientific Industries, New York, USA |

### 2.1.2 General consumables

Table 2-2: General consumables

| Material | Manufacturer |
|---|---|
| 5 ml Polysterene Round-Botton Tube with Cell-Strainer Cap | Corning, New York, USA |
| BD Discardit II Disposable Syringe (5, 10 ml) | Becton Dickinson, Franklin Lakes, USA |
| BD Mircolance 3 Needle (25G, 27G) | Becton Dickinson, Franklin Lakes, USA |
| Bepanthen Augen- und Nasensalbe | Bayer, Leverkusen, Germany |
| CASY Cups | OLS OMNI Life Science, Bremen, Germany |
| CASYton | OLS OMNI Life Science, Bremen, Germany |
| C-Chip™ Disposable Counting Chamber | NanoEnTek Inc, Waltham, USA |
| CELLSTAR® Cell Culture Flask (25, 75, 175 $cm^2$) | Greiner Bio-One, Kremsmünster, Austria |
| Centrifuge tube PP with Screw Cap PE (15, 50 ml) | nerbe plus, Winsen, Germany |
| Costar® Reagent Reservoir (50 ml) | Corning, New York, USA |
| Costar® Serological Pipette (5, 10, 25, 50, 100 ml) | Corning, New York, USA |
| Cryo.s™ Cryogenic Vial | Greiner Bio-One, Kremsmünster, Austria |
| CulturPlate-96, White, Opaque 96-well Microplate | Perkin Elmer, Waltham, USA |
| EASYstrainer™ (40, 70 µm) | Greiner Bio-One, Kremsmünster, Austria |
| Eppendorf Combitips advanced (0.1, 1, 5, 25 ml) | Eppendorf, Hamburg, Germany |
| Eppendorf Safe-Lock Tubes (0.5, 1.5, 2, 5 ml) | Eppendorf, Hamburg, Germany |
| Eppendorf Safe-Lock Tubes, PCR clean (1.5, 2 ml) | Eppendorf, Hamburg, Germany |
| Feather Disposable Scalpel | Feather, Osaka, Japan |
| Inject®-F Syringe (1 ml) | B. Braun, Melsungen, Germany |
| MicroAmp Optical 96-Well Reaction Plate | Applied Biosystems, Foster City, USA |
| MicroAmp Optical Adhesive Film | Applied Biosytems, Foster City, USA |
| MultiScreenHTS-IP, 0,45 µm, white, sterile | Merck KGaD, Darmstadt, Germany |
| PCR Strip Tube | Greiner, Frickenhausen, German |
| Pipette Filter Tips (10, 20, 100, 200, 1250 µl) | nerbe plus, Winsen, Germany |
| Pipette Tips PP Refill System (10, 200, 1000 µl) | nerbe plus, Winsen, Germany |
| Plastic Serum Pipette | Greiner Bio-One, Kremsmünster, Austria |
| Tissue Culture Test Plate (6, 12, 24, 96 Wells) | TPP, Trasadingen, Switzerland |
| Tissue Culture Test Plate (96F, 96U) | TPP, Trasadingen, Switzerland |

### 2.1.3 Chemicals and reagents

#### 2.1.3.1 Chemicals

Table 2-3: Chemicals

| Chemical | Manufacturer |
|---|---|
| 6x Orange DNA Loading Dye | Thermo Fisher Scientific, Waltham, USA |
| Agarose | Sigma-Aldrich, Saint Louis, USA |
| Ethanol Absolute (Analytical Reagent Grade) | VWR, Radnor Township, USA |
| Ethidium Bromide Solution 0.025% | Carl Roth, Karlsruhe, Germany |
| Ethylenediaminetetraacetic Acid (EDTA) | Acros Organics, Geel, Belgium |
| Mehylene Blue | Sigma-Aldrich, Saint Louis, USA |
| Quick-Load® 100 bp DNA Ladder | New England Biolabs, Ipswich, USA |

| | |
|---|---|
| Tris | Sigma-Aldrich, Saint Louis, USA |
| Tween 20 | Gerbu Biotechnik, Geiberg, Germany |
| Water, sterile, RNase- and DNAse-free | Sigma-Aldrich, Saint Louis, USA |

### 2.1.3.2 Reagents for cell culture

Table 2-4: Reagents for cell culture

| Reagent | Manufacturer |
|---|---|
| 2-Mercaptoethanol | Sigma-Aldrich, Saint Louis, USA |
| ACK Lysing Buffer | Thermo Fisher Scientific, Waltham, USA |
| Concanavalin A (conA) | Sigma-Aldrich, Saint Louis, US |
| Dimethyl sulfoxide (DMSO), Cell Culture Grade | AppliChem, Darmstadt, Germany |
| DPBS, no Calcium, no Magnesium | Thermo Fisher Scientific, Waltham, USA |
| Dynabeads® Mouse T-Activator CD3/CD28 | Thermo Fisher Scientific, Waltham, USA |
| Fetal Calf Serum (FCS) | Biochrom, Darmstadt, Germany |
| Geneticin Selective Antibiotic (G418 Sulfate) | Thermo Fisher Scientific, Waltham, USA |
| HEPES Solution | Sigma-Aldrich, St. Louis, USA |
| L-Glutamine (200 mM) | Thermo Fisher Scientific, Waltham, USA |
| Methyl α-D-Mannopyranoside (αMM) | Sigma-Aldrich, Saint Louis, USA |
| Minimum Essential Medium Eagle (MEM) | Sigma-Aldrich, St. Louis, USA |
| Mouse IFN gamma Recombinant Protein Carrier-Free | eBioscience, Waltham, USA |
| Penicillin-Streptomycin | Sigma-Aldrich, St. Louis, USA |
| Puromycin Dihydrochloride dissolved | Thermo Fisher Scientific, Waltham, USA |
| RPMI 1640 Medium, GlutaMAX™ Supplement | Thermo Fisher Scientific, Waltham, USA |
| Sodium Pyruvate | Sigma-Aldrich, St. Louis, USA |
| Trypan Blue | Biochem, Berlin, Germany |
| Trypsin-EDTA (0.25%), Phenol Red | Thermo Fisher Scientific, Waltham, USA |

### 2.1.3.3 Reagents for flow cytometry

Table 2-5: Reagents for flow cytometry

| Reagent | Manufacturer |
|---|---|
| ArC™ Amine Reactive Compensation Bead Kit | Thermo Fisher Scientific, Waltham, USA |
| CountBright™ Absolute Counting Beads | Thermo Fisher Scientific, Waltham, USA |
| Foxp3/Transcription Factor Staining Buffer Set | eBioscience, Waltham, USA |
| LIVE/DEAD® Fixable Blue Dead Cell Stain Kit | Thermo Fisher Scientific, Waltham, USA |
| LIVE/DEAD® Fixable Yellow Dead Cell Stain Kit | Thermo Fisher Scientific, Waltham, USA |
| Normal Syrian Hamster Serum | Jackson Laboratory, Bar Harbor, USA |
| OneComp eBeads | eBioscience, Waltham, USA |
| Propidium Iodide (PI) | Sigma-Aldrich, Saint Louis, USA |
| Purified Rat Anti-Mouse CD16/CD3 | Becton Dickinson, Franklin Lakes, USA |
| Rat serum | GeneTex, Irvine, USA |
| RNAse A | AppliChem, Darmstadt, Germany |

#### 2.1.3.4 Reagents for luciferase-based cytotoxicity assay

Table 2-6: Reagents for luciferase-based cytotoxicity assay

| Reagent | Manufacturer |
|---|---|
| D-Luciferin Firefly | Biosynth AG, Staad, Switzerland |
| Luciferase Assay B2 Buffer | Unpublished composition, kindly provided by Prof. Dr. Michael Boutros |
| Luciferase Assay BL Buffer | Unpublished composition, kindly provided by Prof. Dr. Michael Boutros |
| Magnesium Sulfate ($MgSO_4$) | neoLab Migge GmbH, Heidelberg, Germany |
| Triton X-100 | GERBU Biotechnik GmbH, Heidelberg, Germany |

#### 2.1.3.5 Reagents for IFN-γ ELISpot assay

Table 2-7: Reagents for IFN-γ ELISpot assay

| Reagent | Manufacturer |
|---|---|
| Alkaline Phosphatase Streptavidin | Becton Dickinson, Franklin Lakes, USA |
| BCIP/NBT Liquid Substrate System | Sigma, Saint Louis, USA |
| Biotin Rat Anti-Mouse IFN-γ Antibody | Becton Dickinson, Franklin Lakes, USA |
| Purified Rat Anti-Mouse IFN-γ Antibody | Becton Dickinson, Franklin Lakes, USA |

#### 2.1.3.6 Reagents for digestions of tumor tissue

Collagenase D, DNase I and TLCK were dissolved in HBSS and stored at – 80 °C.

Table 2-8: Reagents for digestion of tumor tissue

| Reagent | Manufacturer |
|---|---|
| Collagenase D | Hoffmann-La Roche, Basel, Switzerland |
| Deoxyribonuclease I (DNAse I) from Bovine Pancreas | Sigma-Aldrich, St. Louis, USA |
| Hanks' Balanced Salt solution (HBSS) | Sigma-Aldrich, St. Louis, USA |
| HEPES buffer solution | Sigma-Aldrich, St. Louis, USA |
| Nα-Tosyl-L-lysine chloromethyl ketone hydrochloride (TLCK) | Sigma-Aldrich, St. Louis, USA |

### 2.1.4 Cell lines and culture medium

#### 2.1.4.1 Cell lines

All cell lines used in this thesis are of mouse origin. The respective culture medium for each cell line is listed in Table 2-10.

Table 2-9: Cell lines

| Cell line | Cell type | Modification | Source |
|---|---|---|---|
| 4T1 | breast cancer | none | AG Wiemann, DKFZ, Heidelberg |
| B16F10 | melanoma | none | ATCC, Manassas, USA |
| E.G7 | T-cell lymphoma | OVA | DKFZ, Heidelberg, Germany |
| EL-4 | T-cell lymphoma | none | DKFZ, Heidelberg, Germany |
| EO771 | breast cancer | none | Tebu-Bio, Offenbach, Germany |
| EO771/Luci | breast cancer | Luciferase | generated by D. Eisel |
| EO771/Luci/OVA | breast cancer | Luciferase/OVA | generated by D. Eisel |
| EO771/OVA | breast cancer | OVA | generated by D. Eisel |
| OVA-specific CTLs ($OVA_{257-264}$; Kb) | T cell line | none | generated by W. Osen |
| RMA | T-cell lymphoma | none | DKFZ, Heidelberg, Germany |

### 2.1.4.2 Culture media

Table 2-10: Culture media

| Cell line | Medium | Supplements |
|---|---|---|
| 4T1, B16F10, EL-4, RMA | RPMI 1640 Medium, GlutaMAX™ Supplement | 10% FCS<br>100 U/ml Penicillin<br>100 µg/ml Streptomycin |
| E.G7 | RPMI 1640 Medium, GlutaMAX™ Supplement | 10% FCS<br>100 U/ml Penicillin<br>100 µg/ml Streptomycin<br>0.8 mg/ml G418 |
| EO771 | RPMI 1640 Medium, GlutaMAX™ Supplement | 10% FCS<br>10 mM HEPES<br>100 U/ml Penicillin<br>100 µg/ml Streptomycin |
| EO771/Luci | RPMI 1640 Medium, GlutaMAX™ Supplement | 10% FCS<br>10 mM HEPES<br>100 U/ml Penicillin<br>100 µg/ml Streptomycin<br>1 µg/ml Puromycin |
| EO771/Luci/OVA | RPMI 1640 Medium, GlutaMAX™ Supplement | 10% FCS<br>10 mM HEPES<br>100 U/ml Penicillin<br>100 µg/ml Streptomycin<br>1 mg/ml G418<br>1 µg/ml Puromycin |

| | | |
|---|---|---|
| EO771/OVA | RPMI 1640 Medium, GlutaMAX™ Supplement | 10% FCS<br>10 mM HEPES<br>100 U/ml Penicillin<br>100 µg/ml Streptomycin<br>1 mg/ml G418 |
| OVA-specific CTLs ($OVA_{257-264}$; Kb) | Minimum Essential Medium Eagle | 10% FCS<br>2 mM L-Glutamine<br>50 µM 2-Mercaptoethanol<br>12.5 mM Methyl α-D-Mannopyranoside<br>12.5 ml ConA culture supernatant<br>100 U/ml Penicillin<br>100 µg/ml Streptomycin |

### 2.1.5 Primers for quantitative real-time polymerase chain reaction (qPCR)

All primers are targeting mouse genes. They were purchased at Sigma-Aldrich (St. Louis, USA). Lyophilized primers were resolved in $ddH_2O$ (RNAse-, DNAse-free) to a stock concentration of 100 µM and stored at -20 °C.

Table 2-11: Primers for qPCR

| Target | Primer name | Sequence (5'-3') | Product size [bp] | Efficiency [%] | Source |
|---|---|---|---|---|---|
| Cd274 (Pdl1) | PD-L1_fwd<br>PD-L1_rev | TCGCCTGCAGATAGTTCCC<br>TGACGTTGCTGCCATACTCC | 133 | 94.6 | designed by P. Schröter |
| H2-D1 | MHC-I (H2-D1)_fwd<br>MHC-I (H2-D1)_rev | GTGCTGCAGAGCATTACAAGG<br>TGCCTTTGGGGAATCTGTGC | 110 | 90.6 | |
| H2-K1 | MHC-I (H2-K1)_fwd<br>MHC-I (H2-K1)_rev | TGAGAAGGAGAAACACAGGTGG<br>GTCACCAAGTCCACTCCAGG | 151 | 91.6 | |
| Nt5e (Cd73) | CD73_fwd<br>CD73_rev | GCATTCCTGAAGATGCGACC<br>ATCGTTCTCCCGAGTTCCTG | 91 | 100.7 | |
| gp-70-1 | Gp-70-1 fwd<br>Gp-70-1 rev | AAAGTGACACATGCCCACAA<br>CCCCAAGAGGCACAATAGAA | 110 | 75.5 | Scrimieri *et al.,* 2013 [274] |
| gp-70-2 | Gp-70-2 fwd<br>Gp-70-2 rev | TGACCTTGTCCGAAGTGACC<br>TAGGACCCATCGCTTGTCTT | 103 | 86.3 | Scrimieri *et al.,* 2013 [274] |
| Actb (HK) | bactin_fw61<br>bactin_rev62 | ACCCTAAGGCCAACCGTGA<br>ATGGCGTGAGGGAGAGCATA | 193 | 91.28 | designed by D. Eisel |
| Hprt (HK) | HPRT_qPCR_FP25<br>HPRT_qPCR_RP26 | AGTACAGCCCCAAAATGGTTAAG<br>CTTAGGCTTTGTATTTGGCTTTTC | 203 | 95.29 | Zhu *et al*., 2014 [275] |
| Ppia (HK) | Ppia_fw79<br>Ppia_rev80 | GAGCTGTTTGCAGACAAAGTTC<br>CCCTGGCACATGAATCCTGG | 125 | 95.62 | PrimerBank ID 6679438c1 |
| Rpl19 (HK) | Rpl19_fw69<br>Rpl19_rev70 | TACCGGGAATCCAAGAAGATTGA<br>AGGATGCGCTTGTTTTTGAAC | 89 | 98.13 | PrimerBank ID 226958656c3 |
| Tgfb1 (HK) | TGFβ1_fw49<br>TGFβ1_rev50 | AAGTTGGCATGGTAGCCCTT<br>GCCCTGGATACCAACTATTGC | 128 | 93.8 | Shaul *et al.,* 2010 [276] |

Pdl1: programmed cell death 1 ligand; H2-D1/K1: H-2 class I histocompatibility antigen, D-B/K-B alpha chain; Nt5e: 5'-Nucleotidase Ecto; Actb: Beta-actin; Hprt: Hypoxanthine-guanine phosphoribosyltransferase; Ppia: Peptidylprolyl Isomerase A; Rpl19: ribosomal protein L19; Tgfb1: Transforming Growth Factor Beta 1; HK: housekeeping gene

### 2.1.6 Antibodies

#### 2.1.6.1 Antibodies for flow cytometry

All flow cytometry antibodies (Table 2-12) used in this study are directed against mouse antigens. Corresponding isotype antibodies are listed in Table 2-13.

Table 2-12: Antibodies for flow cytometry

| Antigen | Coupled to | Manufacturer | Index | Index isotype |
|---|---|---|---|---|
| CD11b | PerCp-Cy5.5 | BioLegend | 101 | 100 |
| CD11c | APC/Cy7 | BioLegend | 252 | 257 |
| CD127 | FITC | BioLegend | 239 | 141 |
| CD137 | APC | BioLegend | 247 | 257 |
| CD152 | PerCp-Cy5.5 | BioLegend | 232 | 168 |
| CD184 | BV711 | BioLegend | 222 | 223 |
| CD19 | BV785 | BioLegend | 253 | 258 |
| CD206 | PE/Cy7 | BioLegend | 201 | 87 |
| CD223 | BV785 | BioLegend | 243 | 248 |
| CD25 | APC/Cy7 | BioLegend | 238 | 259 |
| CD273 | APC | BD Biosciences | 220 | 221 |
| CD274 | PE | BioLegend | 213 | 214 |
| CD274 | BV785 | BioLegend | 224 | 225 |
| CD279 | BV605 | BioLegend | 237 | 111 |
| CD3 | PerCp-Cy3.3 | BioLegend | 44 | 100 |
| CD335 | BV711 | BioLegend | 249 | 250 |
| CD4 | V450 | BD Biosciences | 110 | 148 |
| CD44 | BV711 | BioLegend | 241 | 223 |
| CD45 | PE | BD Biosciences | 53 | 158 |
| CD62L | PerCp-Cy5.5 | BioLegend | 246 | 251 |
| CD69 | AF700 | BioLegend | 242 | 255 |
| CD73 | APC/Fire750 | BioLegend | 218 | 219 |
| CD8 | PE/Cy7 | BioLegend | 89 | 87 |
| F4/80 | BV421 | BioLegend | 159 | 160 |
| FoxP3 | APC | Invitrogen | 240 | 146 |
| Gr-1 | AF488 | BioLegend | 202 | 203 |
| H-2Db | PerCp-Cy5.5 | BioLegend | 144 | 150 |
| H-2Kb | BUV395 | BD Biosciences | 215 | 216 |
| H-2Kb | PE/Cy7 | BioLegend | 217 | 205 |
| H-2Kb | FITC | BioLegend | 143 | 151 |
| H-2Kb SIINFEKL | PE | BioLegend | 206 | 207 |

| | | | | |
|---|---|---|---|---|
| I-A[b] | AF647 | BioLegend | 104 | 103 |
| iNos | AF488 | Invitrogen | 229 | 245 |
| NK1.1 | BV711 | BioLegend | 275 | 276 |
| OX-40 | FITC | Invitrogen | 244 | 197 |

Table 2-13: Isotype control antibodies for flow cytometry

| Index | Antigen | Coupled to | Manufacturer |
|---|---|---|---|
| 87 | Isotype Ctrl. | PE/Cy7 | BioLegend |
| 93 | Isotype Ctrl. | AF700 | BioLegend |
| 100 | Isotype Ctrl. | PerCp-Cy5.5 | BioLegend |
| 104 | Isotype Ctrl. | AF647 | BioLegend |
| 111 | Isotype Ctrl. | BV605 | BioLegend |
| 141 | Isotype Ctrl. | FITC | BioLegend |
| 146 | Isotype Ctrl. | APC | Invitrogen |
| 148 | Isotype Ctrl. | V450 | BD Biosciences |
| 150 | Isotype Ctrl. | PerCp-Cy5.5 | BioLegend |
| 151 | Isotype Ctrl. | FITC | BioLegend |
| 158 | Isotype Ctrl. | PE | BD Biosciences |
| 160 | Isotype Ctrl. | BV421 | BioLegend |
| 168 | Isotype Ctrl. | PerCp-Cy5.5 | BioLegend |
| 197 | Isotype Ctrl. | FITC | Invitrogen |
| 203 | Isotype Ctrl. | AF488 | BioLegend |
| 205 | Isotype Ctrl. | PE/Cy7 | BioLegend |
| 207 | Isotype Ctrl. | PE | BioLegend |
| 214 | Isotype Ctrl. | PE | BioLegend |
| 216 | Isotype Ctrl. | BUV395 | BD Biosciences |
| 219 | Isotype Ctrl. | APC/Fire750 | BioLegend |
| 221 | Isotype Ctrl. | APC | BD Biosciences |
| 223 | Isotype Ctrl. | BV411 | BioLegend |
| 223 | Isotype Ctrl. | BV711 | BioLegend |
| 225 | Isotype Ctrl. | BV785 | BioLegend |
| 245 | Isotype Ctrl. | AF488 | Invitrogen |
| 248 | Isotype Ctrl. | BV785 | BioLegend |
| 250 | Isotype Ctrl. | BV711 | BioLegend |
| 251 | Isotype Ctrl. | PerCp-Cy5.5 | BioLegend |
| 254 | Isotype Ctrl. | APC/Cy7 | BioLegend |
| 255 | Isotype Ctrl. | AF700 | BioLegend |
| 257 | Isotype Ctrl. | APC | BioLegend |
| 257 | Isotype Ctrl. | APC/Cy7 | BioLegend |
| 258 | Isotype Ctrl. | BV785 | BioLegend |
| 259 | Isotype Ctrl. | APC/Cy7 | BD Biosciences |

#### 2.1.6.2 Antibodies for immune checkpoint inhibition

Table 2-14: Antibodies for immune checkpoint inhibition

| Antibody | Clone | Manufacturer |
|---|---|---|
| InVivoMAb anti-mouse CTLA-4 (CD152) | 9H10 | Bio X Cell, West Lebanon, USA |
| InVivoMAb anti-mouse PD-L1 | B7/H1 | Bio X Cell, West Lebanon, USA |
| InVivoMAb polyclonal Syrian hamster IgG | N/A | Bio X Cell, West Lebanon, USA |
| InVivoMAb rat IgG2b isotype control | LTF-2 | Bio X Cell, West Lebanon, USA |

### 2.1.7 Drugs for anesthesia of mice

Table 2-15: Drugs for anesthesia of mice

| Drug | Manufacturer |
|---|---|
| ANTISEDAN® (atipamezole hydrochloride), 5 mg/ml | Zoetis, Parsippany-Troy Hills, USA |
| Dorbene vet (medetomidin hydrochloride), 1 mg/ml | Zoetis, Parsippany-Troy Hills, USA |
| Flumazenil Kabi 0,1 mg/ml | Fresenius Kabi, Bad Homburg, Germany |
| Isofluran CP 1 ml/ml, 250 ml | CP Pharma, Burgdorf, Germany |
| Midazolam-ratiopharm® 15 mg/3 ml Injektionslösung | Ratiopharm, Ulm, Germany |
| NaCl 0.9% | B. Braun, Melsungen, Germany |

### 2.1.8 Kits

Table 2-16: Kits

| Kit | Manufacturer |
|---|---|
| RNeasy Mini Kit | Qiagen, Hilden, Germany |
| Tumor Dissociation Kit, mouse | Miltenyi Biotec, Bergisch Gladbach Germany |
| Transcriptor First Strand cDNA Synthesis Kit | Hoffmann-La Roche, Basel, Switzerland |
| Colorimetric Cell Viability Kit III (XTT) | PromoCell, Heidelberg, Germany |
| HMGB1 ELISA | IBL International GmbH, Hamburg, Germany |
| FITC Annexin V Apoptosis Detection Kit with 7-AAD | BioLegend, San Diego, USA |
| miRNeasy Mni Kit | Qiagen, Hilden, Germany |
| Power SYBR™ Green PCR Master Mix | Thermo Fisher Scientific, Waltham, USA |
| Qubit™ RNA BR Assay Kit | Thermo Fisher Scientific, Waltham, USA |
| RNase-Free DNase Set | Qiagen, Hilden, Germany |

### 2.1.9 Software

Table 2-17: Software

| Software | Manufacturer |
|---|---|
| BD FACSDiva v8.0.1 Software | Becton Dickinson, Franklin Lakes, USA |
| Clonogenic Survival CALculator V1.60j | Christian Schwager, DKFZ, Heidelberg, Germany |
| DAVID Bioinformatic Resources 6.8 | Laboratory of Human Retrovirology and Immunoinformatics (LHRI), Frederick, USA |

| | |
|---|---|
| EndNote X9 | Thomson Reuters, Toronto, Canada |
| Enrichr | Ma'ayan Laboratory, New York, USA |
| FlowJo V10 | Becton Dickinson, Franklin Lakes, USA |
| GraphPad Prism 7 | GraphPad Software, San Diego, USA |
| ImmunoSpot® Software | Cellular Techn. Ltd, Shaker Heights, USA |
| MARS Data Analysis Software | BMG Labtech, Ortenberg, Germany |
| Microsoft Office 2010 | Microsoft, Redmont, USA |
| MikroWin Software | Berthold Technologies, Bad Wildbad, Germany |
| R | The R Development Core Team, GNU |
| R Studio | R studio, Boston, USA |
| SigmaPlot 14.0 | Systat Software, Inc, San Jose, USA |

## 2.2 Methods

### 2.2.1 Cell culture

Cell lines and culture media used in this study are found in Table 2-9 and Table 2-10, respectively. Cells were handled under sterile conditions and cultivated in a humidified atmosphere at 37 °C and 5% $CO_2$. For cell culture maintenance, tumor cells were passaged by trypsination three times a week. Cell numbers were determined using a Neubauer hemocytometer or a CASY cell counter according to manufacturer's instructions.
Ovalbumin (OVA)-specific $CD8^+$ CTLs, recognizing the epitope $OVA_{257-264}$ (SIINFEKL), were kept in 24-well plates and restimulated every week. To this end, spleens from syngeneic C57BL/6 mice were aseptically removed, transferred to PBS and passed through a 70 µm cell strainer to obtain single cells. After centrifugation (300 x g, 5 min), splenocytes were resuspended in 4 ml ACK lysing buffer and incubated for 3-5 min. Having washed the cells with 40 ml PBS, pellets were resuspended in CTL medium, adjusted to 5 x $10^7$ cells/ml and irradiated with 33 Gy using a Gammacell® 1000 Elite irradiator (Caesium-137 source). EG.7 cells (suspension cells) were harvested, adjusted to 2 x $10^6$ cells/ml and irradiated with 200 Gy. Finally, OVA-specific CTLs were titrated and 5 x $10^6$ irradiated splenocytes (feeder cells), 2 x $10^5$ irradiated E.G7 cells (stimulators) and CTL medium were added to a final volume of 2 ml. Cell culture supernatants were regularly tested for contaminations with mycoplasma.

### 2.2.2 Irradiation of tumor cells *in vitro*

Photon irradiation of tumor cells was performed with a Gammacell® 40 Extractor (Caesium-137 source), which showed a dose rate of 0.91 Gy/min. The exact dose rate was determined every three months by the Department of Medical Physics in Radiation Oncology at the DKFZ. For *in vitro* studies with photon irradiation, EO771 cells were seeded 10-12 h before irradiation and irradiated with 1, 3, 5, and 10 Gy if not indicated otherwise.
Carbon ion irradiation was performed at the HIT with a horizontal beamline using the raster scanning technique. Irradiation doses were delivered within an 8 mm wide extended Bragg peak (dose average linear energy transfer (LET), 103 keV/µm) adjusted with a 30 mm wide acrylic absorber. Plans for carbon ion irradiation were calculated by Dr. Stephan Brons (Department of Radiation Oncology, HIT, Heidelberg). Cell monolayers were positioned in the middle of the extended Bragg peak. For carbon ion irradiation of EO771 cells, 0.12, 1.11, 3.08, and 8 Gy were determined as biologically equivalent doses (BED) to 1, 3, 5, and 10 Gy photon irradiation by a clonogenic survival assay (section 2.2.3).

### 2.2.3 Clonogenic survival assay

EO771 were irradiated with 1, 2, 3, and 5 Gy photons and 0.5, 1, 2, and 4 Gy carbon ions, respectively. After 18 h of incubation, cells were harvested and seeded into 96-wells plates by limiting dilutions in triplicates. Therefore, cells were diluted to 1 x $10^4$ cells/ml followed by dilutions of 1:2000 or 1:1000 to receive 1 cell or 2 cells per well, when seeding 200 µl. After 10-14 days of incubation, cells were fixed with 70% ethanol for 10 min and stained with 0.1% methylene blue for 5-10 min. Having rinsed the plates with distilled water, plates were dried for at least 1 day. Using an inverted microscope, wells with colonies consisting of more than 50 cells were defined as positive wells. Plating efficacy (PE) and surviving fraction (SF) were determined using equation (1) and (2). Survival curves were fitted with a linear quadratic model (LQM) as described in equation (3) using SigmaPlot 14. Based on the survival curves of photon- and carbon ion-irradiated cells, RBEs were calculated with equation (4).

(1) $PE = \frac{1}{N} * \ln(\frac{96}{n-})$

(2) $SF = \frac{PE\ (treatment)}{PE\ (control)}$

(3) $\ln(SF) = -\alpha D - \beta D^2$

(4) $RBE = \frac{D_p}{D_c}$

*PE = plating efficacy*
*N = cells seeded per well*
*n- = negative wells*
*SF = surviving fraction*
*D = dose*
*a = linear constant*
*β = quadratic constant*
*RBE = relative biological effectiveness*
*$D_p$ = absorbed dose of photon radiation*
*$D_c$ = absorbed dose of carbon ion radiation*

Results were validated using the software Clonogenic Survival CALculator (CS-Cal) V1.60j implemented by Christian Schwager (Department of Clinical Cooperation Unit Translational Radiation Oncology, DKFZ, Heidelberg). Cs-Cal fits photon survival curves with a LQM, while it fits carbon ion survival curves with a linear model.

### 2.2.4 Cell viability assay

Directly after irradiation, 5000 cells/well were seeded in 200 µl in a 96-well plate in quintuplicates. As a blank control, only culture medium was added to five wells. After 12, 36, 60, and 84 h, the medium was replaced with 200 µl fresh medium. Cell viability was determined using the Colorimetric Cell Viability Kit III (XTT). Reaction solution was prepared by mixing XTT reagent solution and the activation solution (1:200). Then, 50 µl reaction solution were added per well and incubated for 3 h. The colorimetric reaction was detected by measuring the optical density (OD) at a wavelength of 450 nm and a background wavelength of 630 nm, which was subtracted from the $OD_{450}$ value. Finally, the mean OD of the blank control (medium) was subtracted from the OD values of the samples.

### 2.2.5 Cell cycle analysis

12, 36, 60, and 84 h after irradiation, cells were harvested, washed twice with PBS, resuspended in ice cold 70% EtOH to a cell concentration of 1 x $10^6$ cells/ml and stored at 4 °C. Then, 5 x $10^5$ – 1 x $10^6$ cells were washed twice in PBS and centrifuged at 300 x g for 5 min. Pellets were resuspended in 200 µl RNase A solution (stock: 1mg/ml diluted in TE-buffer; working solution 100 µg/ml diluted in PBS) an incubated for 10 min at RT. DNA was stained with 5 – 10 µl propidium iodide (PI) solution (1 mg/ml in $H_2O$) an incubated overnight (RT, protected from light). Samples were analyzed with a BD FACSCanto II Flow Cytometer with low flow rate and not exceeding 400 events/s. Based on the DNA content, cell cycle stages (sub G1-, G0/G1-, S-, G2/M – phase) were determined using FlowJo V10.

### 2.2.6 Apoptosis assay

12, 36, 60, and 84 h after irradiation, supernatants containing dead cells were collected and pooled with adherent cells that were harvested by trypsination. 2.5 x $10^5$ – 1 x $10^6$ cells were stained for apoptotic/necrotic cells using the FITC Annexin V Apoptosis Detection Kit with 7-AAD according to manufacturer's instructions. Samples were acquired with a BD FACSCanto II Flow Cytometer and analyzed with FlowJo V10.

### 2.2.7 RNA isolation and quantification

Following irradiation, cells were harvested after 12, 24, and 36 h, washed with PBS and cell pellets were snap frozen in liquid nitrogen and stored at -80 °C. Total RNA was isolated using the RNeasy Mini Kit according to manufacturer's instructions. RNA concentration was determined using Qubit™ RNA BR Assay Kit according to manufacturer's instructions. Eluted RNA was stored at -80 °C.

### 2.2.8 cDNA synthesis

RNA was reverse transcribed using the Transcriptor First Strand cDNA Synthesis Kit. Briefly, reagents of step 1 (Table 2-18) were mixed and incubated at 65 °C for 10 min in a Veriti 96-Well Thermal Cycler to ensure denaturation of RNA secondary structures. Having kept the samples on ice for 5 min, reagents of step 2 were added and samples were incubated at 50 °C for 60 min followed by an incubation at 85 °C for 5 min. cDNA samples were stored at – 20°C.

Table 2-18: Pipetting scheme for cDNA synthesis

| | Reagent | Final conc. | Volume |
|---|---|---|---|
| **Step 1** | RNA | 500 ng | x µl |
| | Anchored-oligo(dT)$_{18}$ Primer | 2.5 µM | 1 µl |
| | $H_2O$, PCR grade | | (12 – x) µl |
| | Total volume | | 13 µl |
| **Step 2** | Reaction mix from step 1 | | 13 µl |
| | RT Reaction Buffer | 8 mM MgCl2 | 4 µl |
| | Protector RNase Inhibitor | 20 U | 0.5 µl |
| | Deoxynucleotide Mix | 1 mM each | 2 µl |
| | Reverse Transcriptase | 10 U | 0.5 µl |
| | Total volume | | 20 µl |

### 2.2.9 Quantitative real-time polymerase chain reaction (qPCR)

Forward and reverse primers (Table 2-11), Power SYBR™ Green PCR Master Mix and $H_2O$ (RNase/DNase-free) were mixed as shown in Table 2-19 and added to a MicroAmp™ Optical reaction plate in triplicates. Then, 2 µl of cDNA (diluted 1:5 in $H_2O$) were pipetted to the reaction mix. The plate was run in a 7300 Real Time PCR System with the conditions listed in Table 2-20.

Melting curves were made when primers were tested for the first time. The relative fold gene expression was calculated with the $2^{-\Delta\Delta Ct}$ method and standard deviation (SD) was calculated using error propagation formulas.

Primer efficiency was determined by serial dilutions of the cDNA template. Ct values were plotted as a standard curve and the slope of this standard curve was used to calculate the primer efficiency with the following formula:

$$\text{Efficiency [\%]} = 10^{-1/\text{slope}} * 100$$

Table 2-19: Pipetting scheme for qPCR reaction mix

| Reagent | Volume |
|---|---|
| Power SYBR™ Green PCR Master Mix (2x) | 10 µl |
| RNase/DNase-free $H_2O$ | 7.2 µl |
| Forward primer (10 µM) | 0.4 µl |
| Reverse primer (10 µM) | 0.4 µl |
| Total volume | 18 µl |

Table 2-20: Thermal cycling parameters for qPCR

| Step | Cycles | Temperature | Time |
|---|---|---|---|
| Pre-incubation | 1 x | 50 °C<br>95 °C | 2 min<br>2 min |
| Denaturation<br>Annealing<br>Extension | 40 x | 95 °C<br>60 °C<br>72 °C | 15 s<br>60 s<br>30 s |
| Melting curve (optional) | 1 x | 98 °C<br>60 °C<br>95 °C<br>60 °C | 15 s<br>60 s<br>15 s<br>15 s |

### 2.2.10 Flow Cytometry of tumor cell lines

12 and 36 h after irradiation, cells were harvested, 1 x $10^6$ cells per well were transferred to a 96U-bottom plate and washed twice in 200 µl PBS (centrifugation for 2 min at 2000 rpm and 4°C). For live/dead discrimination, cells were resuspended in 100 µl LIVE/DEAD™ Fixable Yellow Dead Cell Stain Kit, which was diluted 1:1000 in PBS before. After incubation for 30 min at 4 °C, cells were washed twice in 200 µl FACS buffer (PBS + 3% FCS) and stained with fluorochrome-coupled antibodies (Table 2-12) diluted in FACS buffer, for 30 min at 4 °C. For each treatment condition, fluorescence minus one (FMO) controls were prepared, in which the antibody for an epitope was replaced by the corresponding isotype control antibody (Table 2-13). Finally, samples were washed twice in FACS buffer, acquired with a BD FACSCanto II Flow Cytometer and analyzed with FlowJo V10 software. Compensation was done with OneComp eBeads™ Compensation Beads (fluorochrome-coupled antibodies) and ArC™ Amine Reactive Compensation Bead Kit (live/dead dye) according to manufacturer's instructions. Delta median fluorescence intensity (ΔMFI) was calculated, by subtracting the MFI of FMO controls from the MFI of stained samples for each irradiation dose.

### 2.2.11 HMGB1 ELISA

Cell culture supernatants of irradiated EO771 cells were collected, centrifuged at 1000 x g for 10 min and 4 °C, and stored at –80 °C. Cells were harvested and counted. Extracellular HMGB1 was detected using the HMGB1 ELISA Kit according to Manufacturer's instructions in duplicates. Absorbance was measured with a CLARIOstar Plus Microplate Reader. The standard curve was fitted by a four parameter logistic curve. As also bovine HMGB1, naturally occurring in FCS, is detected, HMGB1 concentration of control wells with medium only was subtracted from samples. HMGB1 concentration was normalized to cell counts.

### 2.2.12 Luciferase-based cytotoxicity assay

Having incubated irradiated EO771/Luci/OVA cells for 12 h, tumor cells were harvested and 5 x $10^3$ cells per well were added to a white, opaque 96-well plate in 100 µl in quadruplicates. OVA-specific CTLs were added at an effector to target cell ratio of 1:5 or 1:10 (final volume 200 µl) and co-cultures were incubated for 16 – 20 h. Optimal CTL numbers were determined in a previous assay, in which CTL numbers were titrated. For development, cells were washed with PBS and lysed with 20 µl lysis reagent, as listed in Table 2-21, for 15 min. Then, 100 µl assay buffer (Table 2-22) were added and the luminescence was directly measured at a Mithras LB 940 Multimode Microplate Reader collecting light for 0.2 s/well.

Table 2-21: Lysis reagent for luciferase-based cytotoxicity assay

| Reagent | Volume |
|---|---|
| Buffer BL | 19.1 µl |
| $MgSO_4$ (1 M) | 0.3 µl |
| Triton X-100 (10%) | 0.6 µl |
| Total volume | 20 µl |

Table 2-22: Assay buffer for luciferase-based cytotoxicity assay

| Reagent | Volume |
|---|---|
| Buffer BL | 88.7 µl |
| Buffer B2 | 10 µl |
| D-Luciferin | 1.3 µl |
| Total volume | 100 µl |

The relative luminescence units (RLU) are proportional to the amount of live cells attached to the wells. Percentage cytolysis was calculated using the mean RLU of quadruplicates with the following formula:

Cytolysis [%]: $\frac{RLU\ (wo\ CTLs) - RLU\ (with\ CTLs)}{RLU\ (wo\ CTLs)}$ x 100

The SD was calculated using error propagation formulas. Finally, the cytolysis of irradiated samples was compared to the untreated control using a t-test calculated with an R code considering error propagation created by Prof. Dr. Annette Kopp-Schneider (Biostatistics Department, DKFZ, Heidelberg).

### 2.2.13 IFN-γ ELISpot assay

The polyvinylidenfluorid (PVDF) membrane of a MultiScreenHTS-IP ELISpot plate was pre-wet with 50 µl of 80% ethanol for 2 min, washed twice with PBS and coated with 1 µg/ml rat anti-mouse IFNγ capture antibody diluted in PBS (100 µl per well) overnight at 4 °C. The next day, unbound antibody was removed, plates washed twice with PBS, and blocked with 200 µl of EO771 culture medium for at least 1 h at 37 °C. Having incubated irradiated EO771/Luci/OVA cells for 12 h, tumor cells were harvested, blocking medium was discarded from the ELISpot plate and 5 x $10^4$ tumor cells in 100 µl culture medium were added per well in triplicates. OVA-specific CTLs were harvested and 400 or 800 CTLs were added to a final volume of 200 µl. Optimal CTL numbers were determined in a previous assay, in which CTLs

were used in graded numbers. Having incubated the co-culture for 16-20 h at 37 °C, wells were washed five times with PBS containing 0.5% Tween 20 and once with PBS. Then, 1 µg/ml biotinylated rat anti-mouse IFN-γ antibody was diluted in PBS and 100 µl were added to each well for 1 h at 4 °C. Excess antibody was removed by washing plates four times with PBS followed by incubation of wells with 100 µl avidin-conjugated alkaline phosphatase (stock diluted 1:500 in PBS) for 30 min at RT. Again, plates were washed four times with PBS and developed by adding 100 µl BCIP/NBT substrate to each well for 1 – 3 min. The colorimetric reaction was stopped by rinsing the plate with distilled water. After the membrane had dried completely, the plate was analyzed with the CTL ELISpot Reader System. Thus, spots were automatically counted and quality control was done with the ImmunoSpot® Software.

### 2.2.14 RNA and small RNA sequencing

EO771 cells were irradiated with 5 Gy photons and 3.08 Gy carbon ions, respectively. 24 h after irradiations cells pellets were frozen in liquid nitrogen and stored at -80°C. For isolation of both total RNA and miRNA, the miRNeasy Mini Kit was used according to manufacturer's instructions including an on column DNA digest using the RNase-Free DNase Set. RNA concentration was determined using Qubit™ RNA BR Assay Kit according to manufacturer's instructions. Sample purity was checked with a NanoDrop Spectrophotometer.
Next generation sequencing of RNA (mRNA and long non-coding RNA) and small RNA were performed by GENEWIZ (Leipzig Germany) using Illumina® NovaSeq™ and Illumina HighSeq® platforms, respectively. Samples were analyzed by GENEWIZ including trimming, mapping, and differential gene expression. Genes were considered differentially expressed if the $\log_2$ fold change was greater than 1 and adjusted p values (Benjamini-Hochberg adjusted) below 0.05. For functional annotation, the DAVID Bioinformatics Sources 6.8 tool was used applying pathway analysis with the Kyoto Encyclopedia of Genes and Genomes (KEGG) and BioCarta tool.

### 2.2.15 Animals

Female C57BL/6J mice (6-8 weeks old) were ordered from Janvier Labs (Le Genest-Saint-Isle, France) and kept for at least 9 days in the animal facilities of DKFZ before starting an experiment. Mice were maintained in groups of maximum six mice in individually ventilated cages at 25 °C. Mice received water and food *ad libitum*. Animal care was provided by the center for preclinical research at the DKFZ. Animal experiments were approved by the District Government in Karlsruhe, Germany (approval ID 35-9185.81/G-209/18).

### 2.2.16 Tumor growth experiments

For subcutaneous (s.c.) tumor cell implantation in mice, EO771 cells (70-80% confluent) were harvested, washed three times in PBS, resuspended to desired cell concentrations in PBS, and stored on ice until implantation. Having shaved the injection side, 100 µl cell suspension was injected s.c. using a 27 G hypodermic needle. Tumor #1 was implanted on the right hind leg, while tumor #2 was implanted into the left flank on the contralateral side. Tumor volume was monitored by measuring the largest and smallest tumor diameter with a caliper every 2-3 days. Tumor volume was calculated as follows:

$V\ [mm^3]$ = largest diameter [mm] x (smallest diameter [mm])$^2$ / 2

When tumors were established, mice were assigned to treatment groups stratified by tumor volume of both tumors. As termination criteria largest diameter >15 mm, tumor ulceration, signs of severe illness such as apathy, respiratory distress, or weight loss over 20% were defined. When one of these criteria was met, mice were sacrificed by cervical dislocation or gradual $CO_2$ exposition.

### 2.2.17 Photon irradiation of murine s.c. tumors

Photon irradiation of s.c. mouse tumors was performed using a Faxitron MultiRad225 irradiator. To allow local irradiation of tumor #1, a mouse irradiation device was constructed in collaboration with Armin Runz, while the dosimetry for this device was measured by Dr. Peter Häring and Clemens Lang (all from the Department of Medical Physics in Radiation Oncology, DKFZ, Heidelberg). Applying the irradiation device, always one mouse was positioned in a way that tumor #1 (implanted at the hind leg) was centered vertically beneath the x-ray source. The body of the mouse (including tumor #2) was covered with a lead shield, which had a 13-mm-wide orbital opening through which tumor #1 was irradiated. With 200 kV, 17.8 mA, and a copper filter, there was a dose rate of 5.57 Gy/min at tumor #1 when the irradiation device was positioned in shelf 6 of the irradiator. The leakage beneath the shield accounted for approximately 1.5%. During irradiation, tumor-bearing mice were drugged with an antagonizing anesthesia consisting of components shown in Table 2-23.

Table 2-23: Components of antagonizing anesthesia for mice

| | Drugs | Stock conc. | Dose | For 1 mouse (20 g, 100 µl) |
|---|---|---|---|---|
| **Anesthesia mix** | Medetomidin hydrochl. | 1 mg/ml | 0.25 mg/kg | 5 µl |
| | Midazolam | 5 mg/ml | 2.5 mg/kg | 10 µl |
| | NaCl solution (0.9%) | | | 85 µl |
| | Total volume | | | 100 µl |
| **Antagonist mix** | Atipamezole hydrochl. | 5 mg/ml | 1.25 mg/kg | 5 µl |
| | Flumazenil | 0.1 mg/ml | 0.25 mg/ml | 50 µl |
| | NaCl solution (0.9%) | | | 45 µl |
| | Total volume | | | 100 µl |

Mice were injected i.p. with 100 µl anesthesia mix per 20 g body weight. When mice had fallen asleep after approximately 5-10 min, they were irradiated with 5 Gy (54 s) and afterwards anesthesia was antagonized by injecting 100 µl of antagonist mix per 20 g body weight s.c. into the nuchal fold. Antagonization took approximately 2 min. During the time a mouse was in anesthesia, the eyes of the mouse were covered with ophthalmic ointment and mouse cages were placed on heating pads.

### 2.2.18 Carbon ion irradiation of murine s.c. tumors

As for *in vitro* experiments, carbon ion RT of murine tumors was performed at HIT with a horizontal beamline using the raster scanning technique. Irradiation doses were delivered within a 20 mm wide extended Bragg peak (dose average linear energy transfer (LET), 103 keV/µm) adjusted with a 30 mm wide acrylic absorber. As before, the plan for irradiation was calculated by Dr. Stephan Brons. Mice were anesthetized with isoflurane and positioned in the radiation field using a holder that was previously designed by Dr. Mahmoud Moustafa

(Department of Radiation Oncology, Heidelberg University Hospital, Heidelberg). The holder leads isoflurane to each mouse and allows the fixation and irradiation of six mice in parallel. Before starting irradiation of mice, a filter was irradiated to ensure correct positioning of tumors in the irradiation field.

### 2.2.19 Treatment with immune checkpoint inhibitors

Tumor-bearing mice were treated with antibodies against the immune checkpoint molecules CTLA-4 and PD-L1 by i.p injection (100 µg antibody in 100 µl; diluted in PBS). Antibody concentrations and injected volumes per mouse are found in Table 2-24.

Table 2-24: Composition of antibodies for immune checkpoint inhibition

| Antibody | concentration | µl for 100 µg (1 mouse) | µl PBS (1 mouse) |
|---|---|---|---|
| InVivoMAb anti-mouse CTLA-4 | 7.57 mg/ml | 13.2 µl | 86.8 µl |
| InVivoMAb anti-mouse PD-L1 | 6.76 mg/ml | 14.8 µl | 85.2 µl |
| InVivoMAb polyclonal Syrian hamster IgG (IgG control for CTLA-4) | 7.11 mg/ml | 14.1 µl | 85.9 µl |
| InVivoMAb rat IgG2b isotype control (IgG control for PD-L1) | 7.62 mg/ml | 13.1 µl | 86.1µl |

### 2.2.20 Tumor digestion and isolation of tumor infiltrating lymphocytes

Subcutaneous tumors were removed, collected in HBSS and minced into small pieces with a pair of scissors. Tumor digestion was performed in 0.5 mg/ml collagenase D, 10 µg/ml DNAse I, 0.1 µg/ml TLCK and 10 mM HEPES buffer diluted in HBSS and incubated for 1 h at 37 °C and shaking at 200 rpm. Digested tumors were plunged through a 70 µm cell strainer and collected in PBS. Single cell suspensions were centrifuged at 500 x g for 10 min before cell pellets were incubated in 4 ml ACK lysing buffer for 3-5 min. Having stopped the erythrocyte lysis by adding 30-40 ml PBS, cells were centrifuged at 300 x g for 10 min. Cells pellets were resuspended in FACS buffer (PBS + 3% FCS) and further stained for flow cytometry analysis.

### 2.2.21 Flow cytometry of tumor tissue

Single cells suspensions from digested tumor samples were added to a 96U-bottom plate and centrifuged (2 min at 2000 rpm and 4°C). For blocking of Fc receptors, cells were incubated in 100 µl of a mixture containing rat anti-mouse CD16/CD32 (50 µg/ml), normal Syrian hamster serum (1:100) and rat serum (1:100) diluted in FACS buffer (PBS + 3% FCS) for 20 min at 4 °C. Then, cells were washed twice in 200 µl PBS followed by live/dead staining with LIVE/DEAD® Fixable Yellow/Blue Dead Cell Stain Kit diluted 1:1000 in PBS for 30 min at 4 °C. Cells were washed twice in 200 µl FACS buffer and stained with fluorochrome-coupled antibodies or corresponding isotype control antibodies (Table 2-12 and Table 2-12) diluted in FACS buffer, for 30 min at 4 °C. After washing the cells twice in 200 µl FACS buffer, cells were fixed/permeabilized in Foxp3/Transcription Factor Staining Buffer Set. Thus, one part concentrate was mixed with three parts diluent and 200 µl were added to the samples for 30 min at 4 °C. Cells were washed twice in 200 µl permeabilization buffer (diluted 1:10 in distilled $H_2O$), resuspended in permeabilization buffer and kept at 4 °C overnight. For intracellular staining of proteins, 100 µl of fluorochrome-conjugated antibody (diluted 1:100 in

permeabilization buffer) were added to the cells for 30 min at 4 °C. Compensation was done with OneComp eBeads™ Compensation Beads (fluorochrome-coupled antibodies) and ArC™ Amine Reactive Compensation Bead Kit (live/dead dye) according to manufacturer's instructions. Samples were acquired at a BD FACS LSRFortessa Flow Cytometer within 2-4 days and analyzed with FlowJo V10.

### 2.2.22 Protein expression analysis of tumor tissue with ScioCD

*The following protocol described by Sciomics GmbH (Neckargemünd, Germany) was applied:*

Tumour tissue samples were directly snap frozen after harvesting and stored at -80° C until further processing. At Sciomics GmbH, proteins were extracted with scioExtract buffer (Sciomics) using the extraction SOPs. The bulk protein concentration was determined by BCA assay. The samples were labelled at an adjusted protein concentration for two hours with scioDye 1 and scioDye 2. After two hours the reaction was stopped and the buffer exchanged to PBS. All labelled protein samples were stored at -20° C until use. The 6 samples were analysed in a dual-colour approach using a reference based design on 6 scioCD antibody microarrays (Sciomics) targeting different CD surface markers and cytokines/chemokines. Each antibody is represented on the array in eight replicates. The arrays were blocked with scioBlock (Sciomics) on a Hybstation 4800 (Tecan, Austria) and afterwards the samples were incubated competitively using a dual-color approach. After incubation for three hours, the slides were thoroughly washed with 1x PBSTT, rinsed with 0.1 x PBS as well as with water and subsequently dried with nitrogen. Slide scanning was conducted using a Powerscanner (Tecan, Austria) with identical instrument laser power and constant PMT settings. Spot segmentation was performed with GenePix Pro 6.0 (Molecular Devices, Union City, CA, USA). Acquired raw data were analysed using the linear models for microarray data (LIMMA) package of R-Bioconductor after uploading the median signal intensities. For normalization, a specialized invariant Lowess method was applied. For analysis of the samples a one-factorial linear model was fitted with LIMMA resulting in a two sided t-test or F-test based on moderated statistics. All presented p values were adjusted for multiple testing by controlling the false discovery rate according to Benjamini and Hochberg. Proteins were defined as differential for $|logFC| > 0.505$ and an adjusted p value $< 0.05$. Differences in protein abundance between different samples or sample groups are presented as log-fold changes (logFC) calculated for the basis 2. In a study comparing samples versus control a logFC = 1 means that the sample group had on average a $2^1 = 2$ fold higher signal as the control group. logFC = −1 stands for $2^{-1} = 1/2$ of the signal in the sample as compared to the control group.
Using the significantly upregulated proteins identified by ScioCD, pathways were predicted with enrichr [277, 278].

### 2.2.23 Tumor re-challenge and analysis of tumor-specific memory immune responses

Mice showing a complete response after treatment were re-challenged with 4 x $10^5$ EO771 cells injected into the right flank of the mice. Naïve mice were used as controls and tumor growth of all mice was monitored. After 14 days, spleens were aseptically removed and single cell suspensions were prepared (section 2.2.1) and resuspended in T cell medium containing culture supernatant of conA-stimulated rat spleen cells as IL-2 source. EO771, B16F10, and RMA cells were harvested in T cell medium and irradiated with 250 Gy. IFN-γ secretion was detected by IFN-γ ELISpot assays as described above (section 2.2.13). Splenocytes and irradiated target cells were co-cultured in effector to target cell ratios of 20:1, 10:1 and 5:1. Moreover, splenocytes were cultured with the H2-$K^b$-restricted peptide KSPWFTTL, which is

the epitope of the murine leukemia virus (MuLV) recognized by CTLs [274, 279]. As a positive control, splenocytes were stimulated with Dynabeads® Mouse T-Activator CD3/CD28 according to manufacturer's instructions.

### 2.2.24 Statistical analysis

If not indicated otherwise in the method description, statistical analysis was calculated using GraphPad Prism 7.05. The respective statistical test is stated in the figure legend. Levels of significance are defined as follows:* $p \leq 0.05$, ** $p \leq 0.01$; *** $p \leq 0.001$: **** $p \leq 0.0001$).

# 3 Results

## 3.1 Cytotoxic effects of photon and carbon ion irradiation on EO771 cells

### 3.1.1 Clonogenic survival and proliferation after irradiation

For a start, the impact of photon and carbon ion radiation on clonogenic survival of EO771 cells was compared. To this end, EO771 cells were irradiated with increasing doses of photons or carbon ions, the capacity to form colonies was determined, and survival curves were fitted using a LQM (Figure 3.1a).

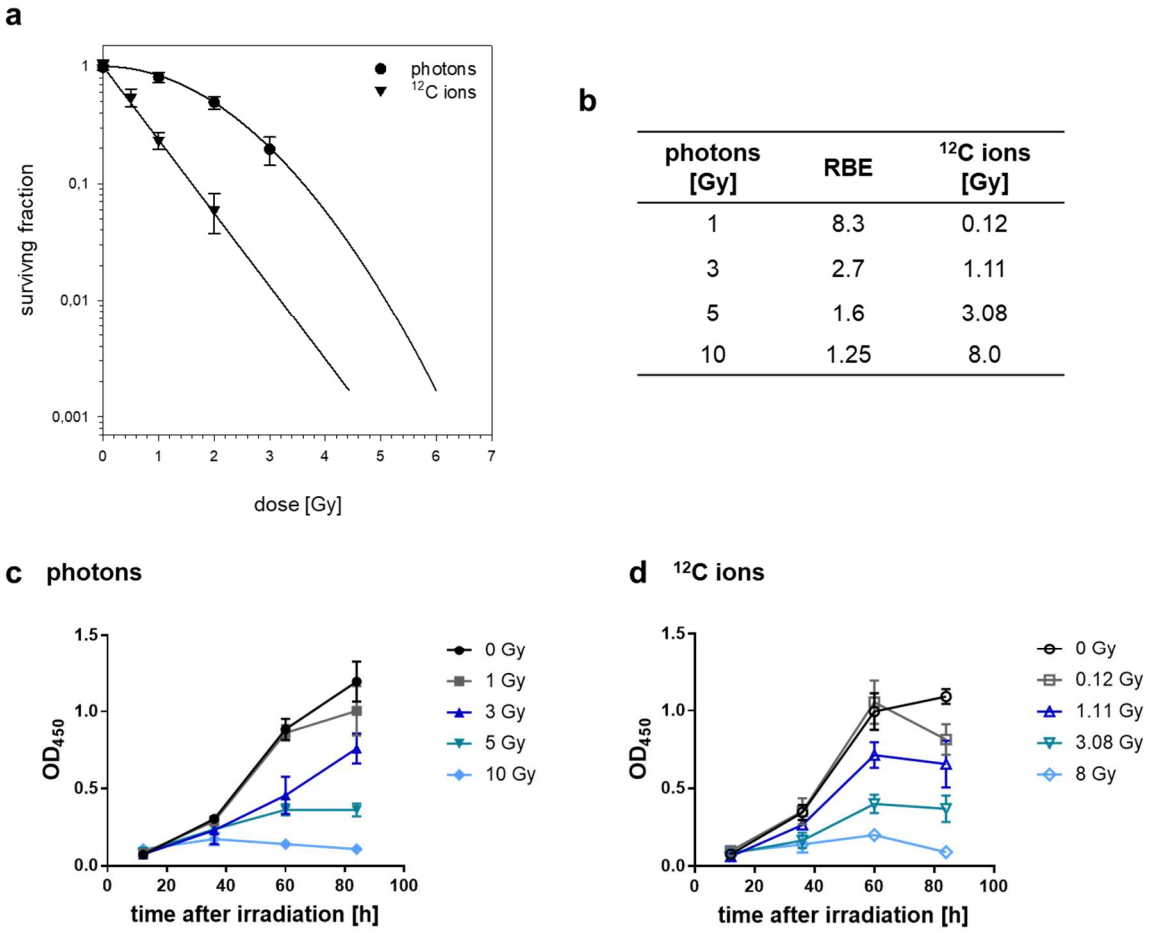


| photons [Gy] | RBE | $^{12}$C ions [Gy] |
|---|---|---|
| 1 | 8.3 | 0.12 |
| 3 | 2.7 | 1.11 |
| 5 | 1.6 | 3.08 |
| 10 | 1.25 | 8.0 |

**Figure 3.1: Clonogenic survival and proliferation of EO771 cells irradited with photons or carbon ions.** **(a)** Survival curves after irradiation with graded doses of photons or carbon ions. Surviving fractions were calculated based on the capacity of irradiated cells to form colonies and survival curves were fitted by a linear quadratic model (LQM). Mean values ± SD of triplicates seeded with 1 or 2 cells (n = 6) within the same experiment are shown. **(b)** Physical doses of carbon ions biologically equivalent to 1, 3, 5 and 10 Gy photons when applying dose-dependent relative biological effectiveness (RBE). **(c)** and **(d)** Proliferation after irradiation of EO771 cells with graded doses of photons or biologically equivalent doses of carbon ions using a XTT proliferation assay. Cell viability is depicted as optical density at a wavelength of 450 nm ($OD_{450}$), which correaltes with the activity of mitochondrial enzymes that are only active in viable cells. Mean values ± SD of quintuplicates are shown.

After photon irradiation, survival curves showed a distinct shoulder at the beginning of the curve, where lower doses were applied, while higher doses resulted in an almost exponential course of the curve. Thus, abrogation of clonogenicity was less efficient in the lower dose range, but increased with higher doses. In contrast, a steeper dose-response relationship was observed after carbon ion irradiation, where the survival curve was exponential also in the lower dosing range, which already efficiently affected clonogenic survival.
Throughout the study, the aim was to characterize cytotoxic and immunomodulatory effects of photon and carbon irradiation over a dosing range including low, intermediate and high irradiation doses. For this purpose, photon doses of 1, 3, 5, and 10 Gy were chosen and biologically equivalent doses (BEDs) of carbon ions were determined based on surviving fractions of the survival curves. Due to the different shapes of the survival curves, the relative biological effectiveness (RBE) between photons and carbon ions was dose-dependent ranging from 8.3 to 1.25 Gy and resulted in biologically equivalent carbon ion doses of 0.12, 1.11. 3.08 and 8.0 Gy (Figure 3.1b). These RBE-matched physical doses of photons and carbon ions were further used throughout the study.
Then, the effect of irradiation on proliferation of EO771 cells was assessed. Regarding photon irradiation first, a clear dosing effect was observed. While irradiation with 1 Gy photons hardly affected proliferation, higher doses increasingly impaired cell growth (Figure 3.1c). After irradiation with 10 Gy photons, there was no noticeable proliferation observed, but cells were still mitotically active. When using BED of carbon ions, the impact on proliferation followed a similar pattern validating that the BEDs determined by clonogenic survival assays have a comparable cytotoxic effect on EO771 cells (Figure 3.1d).

### 3.1.2 Irradiation-induced apoptosis and cell death

To further investigate the cytotoxic impact of photon and carbon ion radiation, irradiation-induced apoptosis and cell death were analyzed by flow cytometric analysis of Annexin V and 7-AAD. To this end, both adherent cells and supernatants containing dead cells were pooled and analyzed. In Figure 3.2a, the gating strategy for EO771 cells after 60 h without irradiation or photon irradiation with 5 Gy is exemplified. In all flow cytometric *in vitro* analyses within this study, cells were first gated according to size and granularity (FSC-A vs. SSC-A), followed by discrimination of singlets and doublets (FSC–A vs. FSC-H). Of note, tumor cells underwent distinct morphological changes after irradiation (Supplementary Figure 5.1) Thus, when EO771 cells were irradiated with doses greater than 3 Gy photons, a swelling of cells was observed as shown by an increase of size and granularity 36 – 84 h after irradiation. The same effect occurred after irradiation of cells with BEDs of carbon ions (not shown). For the analysis of apoptotic and necrotic cells, single cells were further analyzed by staining with Annexin V and 7-AAD. Double negative cells represent viable cells, Annexin $V^+$ 7-$AAD^-$ early apoptotic cells and double positive cells late apoptotic/necrotic cells.
Overall, the impact of photon and carbon ion irradiation on the induction of early and late apoptosis in EO771 cells was comparable (Figure 3.2b and c). Thus, for both radiation types no major cytotoxic effects were observed 12 h after irradiation. At the 36 h time point, only for cells irradiated with doses equal or greater than 5 Gy photons and 3.08 Gy carbon ions, respectively, a distinct population of late apoptotic/necrotic cells was observed, while the proportion of early apoptotic cells only increased marginally compared to unirradiated cells. 60 h after irradiation, apoptosis and necrosis were in addition observed in cells irradiated with 3 Gy photons or 1.11 Gy carbon ions with approximately 75% being viable cells compared to over 90% viable cells among untreated cells. With increasing doses, the proportion of viable cells further decreased to 15 – 18% for cells irradiated with 10 Gy photons or 8 Gy carbon ions.

Compared to the previous time point, the proportion of early apoptotic cells clearly increased, while the proportion of late apoptotic/necrotic cells remained similar. Finally, 84 h after irradiation, no further changes were observed, except for cells irradiated with 5 Gy photons or 3.08 Gy carbon ions, where the proportion of early apoptotic cells was greater than 60 h after irradiation.

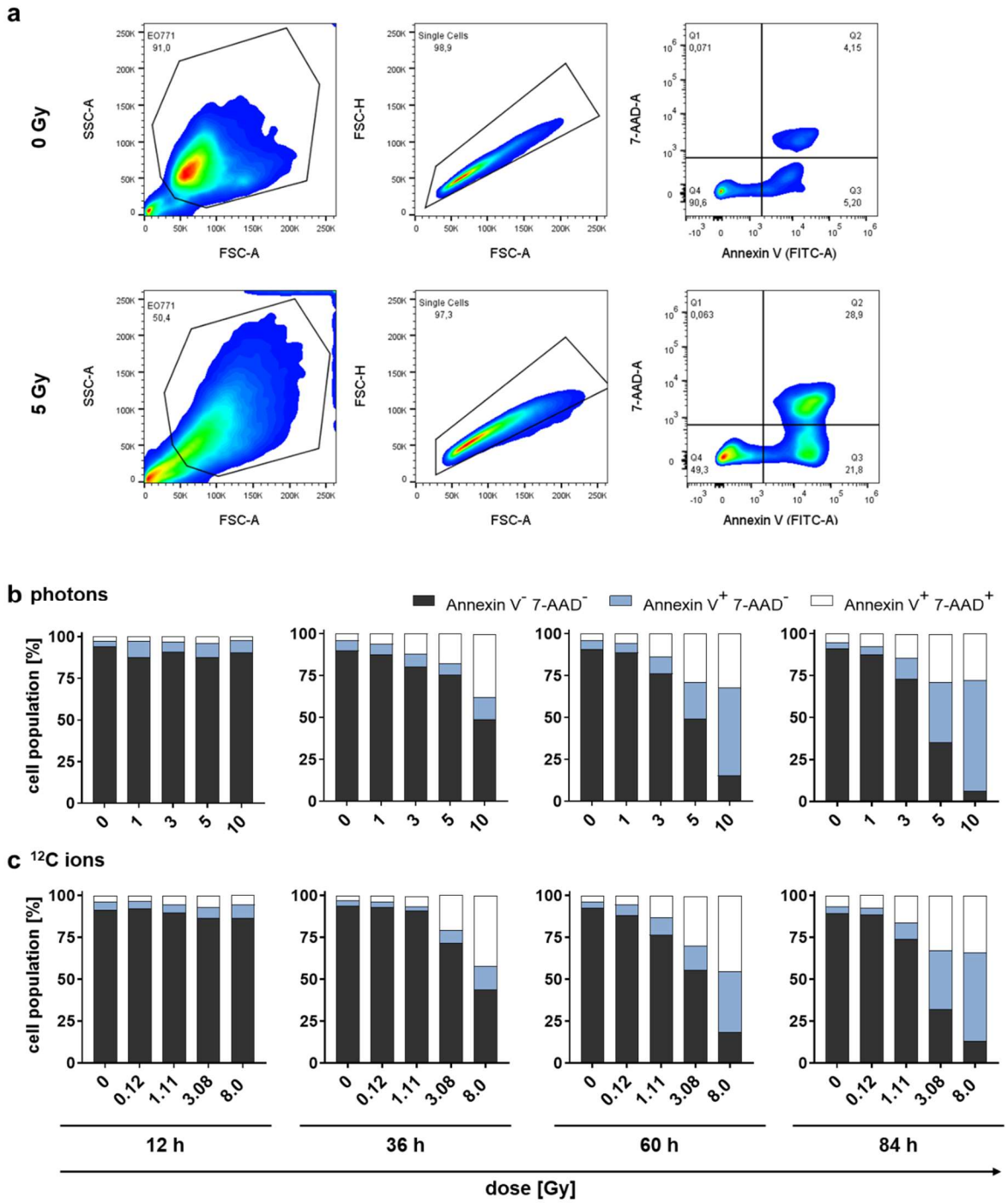


**Figure 3.2: Radiation-induced early and late apoptosis/necrosis in EO771 cells**. EO771 cells were irradiated with photons and biologically equivalent doses of carbon ions. 12, 36, 60 and 84 h after irradiation, cells were stained with Annexin V-FITC and 7-AAD. **(a)** Gating strategy as exemplified for 0 Gy and 5 Gy photons 60 h after irradiation: cells (FSC-A vs. SSC-A) → single cells (FSC-A vs. FSC-H) → 7-AAD-A vs. Annexin V (FITC-A). **(b)** and **(c)** Quantification of viable cells (Annexin $V^-$ $7\text{-}AAD^-$), early apoptotic cells (Annexin $V^+$ $7\text{-}AAD^-$), and late apoptotic/necrotic cells (Annexin $V^+$ $7\text{-}AAD^+$). Representative results of one out of two independent experiments are shown.

### 3.1.3 Remodeling of cell cycle stages after irradiation

In a next step, the effect of photon and carbon ion irradiation on the distribution of cell cycle stages was examined. The DNA content of irradiated EO771 cells was used to classify the cells into four different cell cycle phases. Exemplary histograms of cells irradiated with 0, 3, and 10 Gy photons (12 h after irradiation) are shown in Figure 3.3a. Cells within the first peak contained a single set of chromosomes and represented cells in the G0/G1 phase, while the second peak, with a doubled DNA content, consisted of cells in the G2/M phase. In between, cells were classified into S phase, in which the DNA is replicated. Cells with DNA content below the G0/G1 peak had entered the subG1 phase, which mostly comprises apoptotic cells. Individual histograms showing cell cycle analyses are depicted Supplementary Figure 5.2.

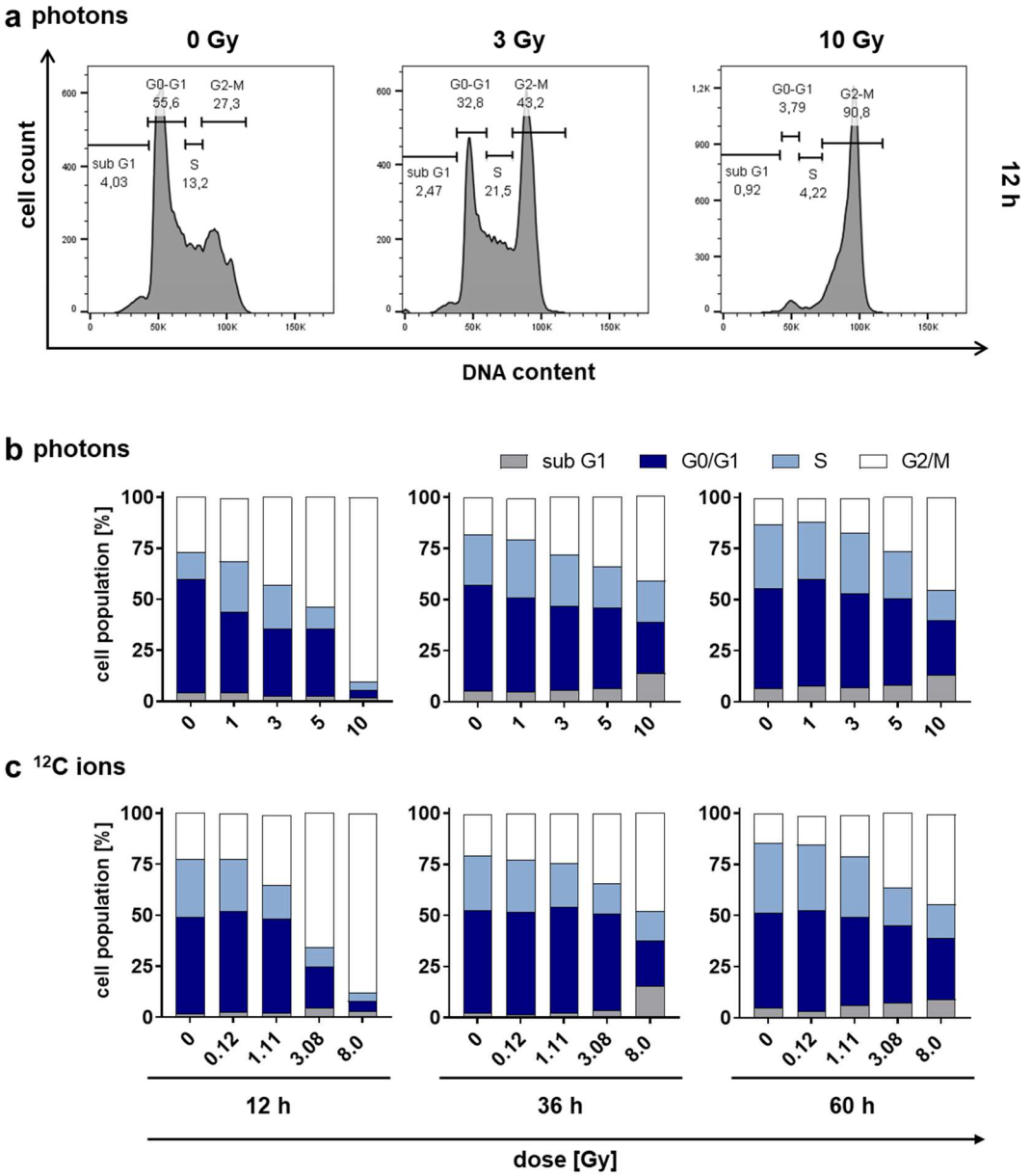


**Figure 3.3: Cell cycle analysis of irradiated EO771 cells.** 12, 36, and 60 h after irradiation of EO771 cells with graded doses of photons or biologically equivalent doses of carbon ions, cell cycle stages were analyzed. **(a)** Classification into subG1, G0/G1, S, or G2/M phase based on the DNA content, as measured by PI staining and subsequent flow cytometric analysis. Gating strategy: cells (FSC-A vs. SSC-A) → single cells (FSC-A vs. FSC-H) → single cells (PI-A vs. PI-W) → cell cycle stage (PI-A vs. count). Exemplarily histograms for cells irradiated with 0, 3, and 10 Gy photons (12 h after irradiation) are depicted. **(b)** and **(c)** Quantification of cell cycle stages. Representative results of one out of two independent experiments are shown.

For both photon and carbon ion radiation, major remodeling of the distribution of cell cycle stages was observed 12 h after irradiation (Figure 3.3b and c). With increasing doses, cells accumulated in the G2/M phase. The effect was most pronounced after irradiation with 10 Gy photons and 8 Gy carbon ions, where 90% and 87% of cells accumulated in the G2/M phase, respectively, compared to approximately 25% in unirradiated cells. A slight difference was detected for 5 Gy photons vs. 3.08 Gy carbon ions, where 54% compared to 66% were found in G2/M phase, but the overall pattern was similar. Regarding later time points, there was a normalization of the cell cycle distribution towards untreated cells, although there was still the tendency that more cells were found in the G2/M phase after irradiation with the highest doses. As seen in section 3.1.2, there was an increase of apoptotic cells (subG1) when using higher doses for irradiation 36 and 60 h after irradiation. Since in cell cycle analysis only adherent cells were analyzed, the proportion of subG1 cells were lower compared to the apoptosis assay described before.

## 3.2 Immunomodulatory effects of photon and carbon ion irradiation

### 3.2.1 Enhanced expression of immunomodulatory molecules after irradiation

After having analyzed irradiation-induced cytotoxic effects, the immunomodulatory impact of photon and carbon ion irradiation was assessed. To this end, both gene and cell surface expression of the immune checkpoint molecules PD-L1 and CD73 and the MHC class I molecules H2-$D^b$ and H2-$K^b$ were investigated in irradiated EO771 cells.

Regarding gene expression first, applying BEDs of photons and carbon ions induced a dose-dependent increase in mRNA expression of all analyzed genes within 24 h (Figure 3.4). Analyses 12 h after irradiation showed only minor changes in gene expression compared to unirradiated cells and no clear dose dependency was detected irrespective of the radiation type. Interestingly, while changes in gene expression for PD-L1 were highest 36 h after irradiation, changes in gene expression of CD73 peaked 24 h after irradiation and the effect was gone after 36 h. The gene expression of both MHC I isotypes H2-$D^b$ and H2-$K^b$ was gradually upregulated to a similar extent 24 and 36 h after irradiation. Irradiation-induced fold changes in gene expression of H2-$K^b$ were most consistent between three independent experiments with the result that several conditions were significant different compared to unirradiated cells. When comparing irradiation with photons and carbon ions, no major differences were observed.

Besides gene expression also the protein expression of PD-L1, CD73, H2-$D^b$ and H2-$K^b$ on the surface of irradiated EO771 cell was analyzed by flow cytometry (Figure 3.5). Again, an overall dose-dependent increase in surface expression was observed. However, in contrast to irradiation-induced gene expression, the gradual effect was visible already 12 h after irradiation. After 36 h, the surface expression was even enhanced, primarily for EO771 cells irradiated with doses greater than 5 Gy photons and 3.08 Gy carbon ions, respectively. Especially for PD-L1, there was an increase of expression after 36 h, which is in line with the qPCR data showing greatest changes in PD-L1 mRNA expression 36 h after irradiation. In contrast, while there was no increased gene expression of CD73 detected 36 h after irradiation, a dose-dependent increase in surface expression was still observed on the protein level. As mRNAs are characterized by comparably short half-lives, an effect might still be visible on the protein, but not on the mRNA level.

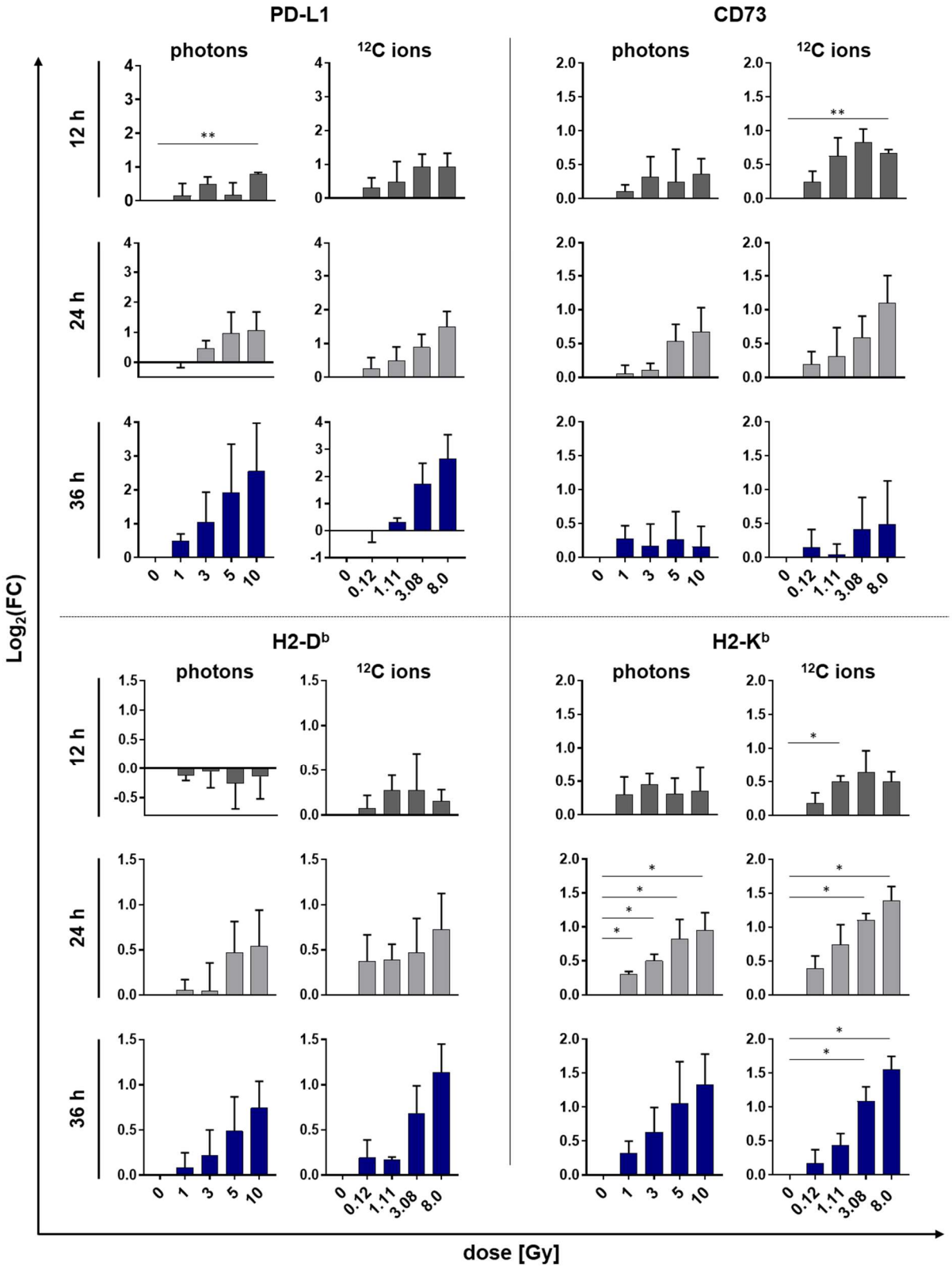


**Figure 3.4: Gene expression profiles of immunomodulatory surface molecules in irradiated EO771 cells.** Quantitative PCR analysis of PD-L1, CD73 and MHC class I molecule (H2-$D^b$ and H2-$K^b$) expression 12, 24, and 36 h after irradiation with photons or biologically equivalent doses of carbon ions. Target gene expression was normalized to the housekeeping gene Ppia and fold changes (FC) of target gene expression over control (0 Gy) were $log_2$-transformed. Mean values ± SD of three independent experiments each performed in technical triplicates are shown. The median $Log_2$(FC) of target gene expression for each treatment was tested against the hypothetical value of 0 using a two-tailed t test and correction of p values for multiple testing was done by Holm-Bonferroni method. Multiplicity adjusted p values are shown.

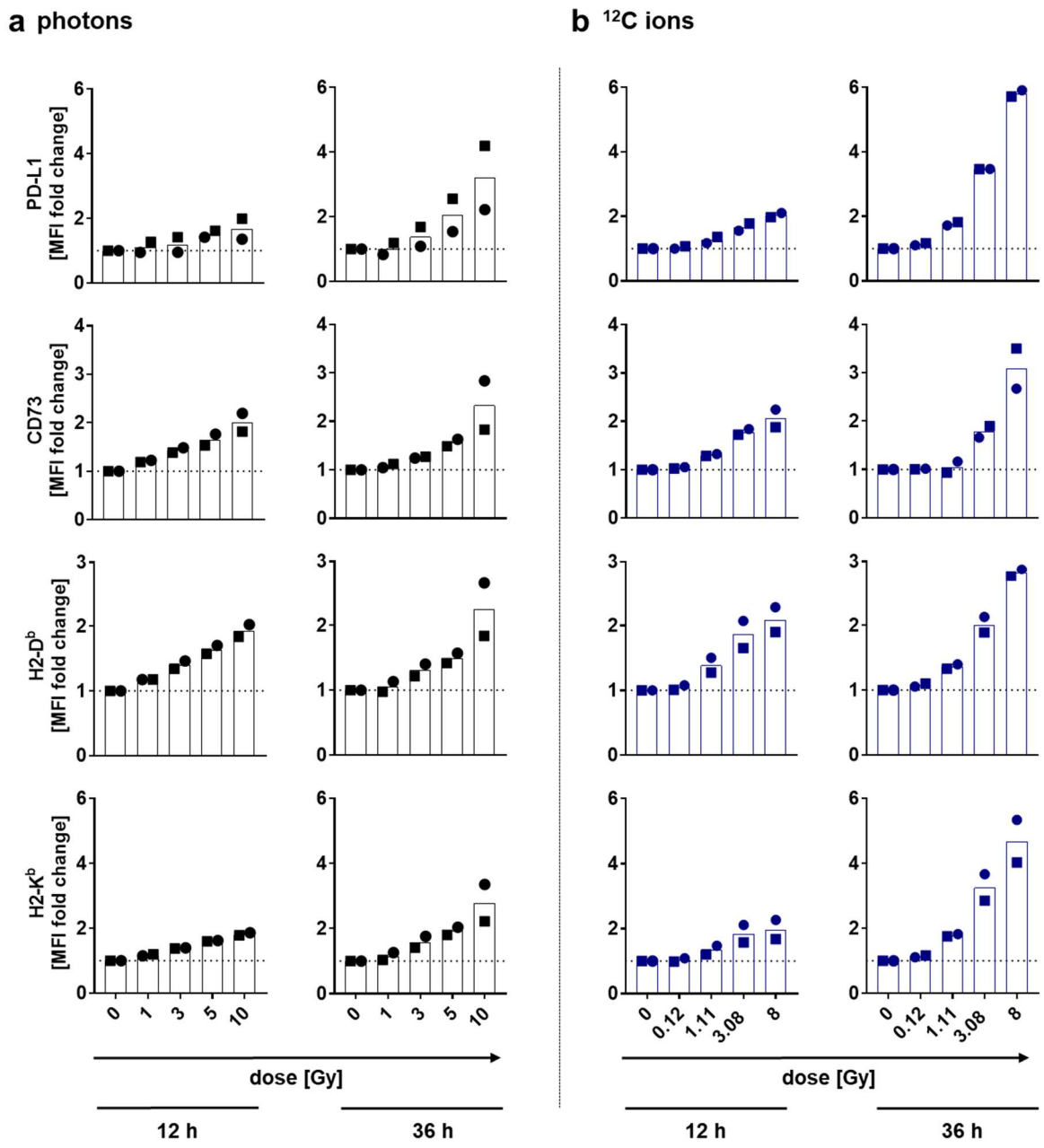


**Figure 3.5: Cell surface expression of immunomodulatory molecules on irradiated EO771.** Flow cytometric analysis of PD-L1, CD73 and MHC class I (H2-D$^b$ and H2-K$^b$) cell surface expression on EO771 cells 12 and 36 h after irradiation with increasing doses of photons **(a)** or biologically equivalent doses of carbon ions **(b)**. Depicted are fold changes of mean fluorescence intensity (MFI) normalized to MFI of unirradiated cells. Results of two experiments performed are shown (squares: experiment 1; dots: experiment 2). Cells were pre-gated on: cells (FSC-A vs. SSC-A) → single cells (FSC-A vs. FSC-H) → live cells (FSC-A vs. live/dead cell marker).

When comparing suface expression of target molecules on cells irradiated with equivalent doses of photons vs. carbon ions 12 h after irradiation, mean fold changes over untreated EO771 cells, were comparable. Interestingly, 36 h after irradiation, the magnitude of increase in PD-L1 and H2-K$^b$ expression was higher upon carbon ion irradiation when using doses greater than 3.08 Gy compared to treatment with BEDs of photons. Thus, irradiation with 10 Gy photons induced a 3.2 times higher expression of PD-L1 compared to unirradiated cells, while the fold change of cells irradiated with the equivalent dose of 8 Gy carbon ions was even 5.8 times higher. This difference was not reflected by the qPCR data showing enhanced mRNA expression levels with both irradiation types to similar extent. Regarding surface expression of

CD73 and H2-D$^b$, a slight, but less pronounced increase after irradiation of cells with 8 Gy carbon ions compared to 10 Gy photons was observed.
Histograms showing the flow cytometric analyses of PD-L1, CD73, H2-K$^b$ and H2-D$^b$ surface expression 12 and 36 h after irradiation are depicted in Supplementary Figure 5.3.

### 3.2.2 Enhanced expression of the danger signal molecule HMGB1 after irradiation

Next, the impact of photon and carbon ion radiation on the secretion of HMGB1, a well-known DAMP, was investigated 36, 60, and 64 h after irradiation. Secreted HMGB1 was measured in cell culture supernatants and normalized to cell counts to compensate for the strong viability effects induced by irradiation, which are described in section 3.1.
After photon irradiation, only EO771 cells irradiated with doses greater than 5 Gy secreted higher amounts of HMGB1 compared to untreated cells (Figure 3.6a). While the secreted concentration of HMGB1 remained almost constant over time with approximately 20 ng/ml per 1 x $10^6$ cells when cells were irradiated with 5 Gy photons, the concentration increased from 35 ng/ml to 220 ng/ml HMGB1 per 1 x $10^6$ cells from 36 to 84 h after irradiation with 10 Gy photons. Regarding HMGB1 secretion after carbon ion irradiation, the overall pattern was similar to photon irradiation (Figure 3.6b). Thus, when applying doses lower or equal to 1.11 Gy carbon ions, HMGB1 concentrations were comparable to untreated cells for all time points. With the highest dose of 8 Gy carbon ions, HMGB1 concentration increased overtime to a similar extent as observed for cells irradiated with the biologically equivalent dose of 10 Gy photons. A slight difference was measured for 3.08 Gy carbon ions compared to 5 Gy photons, where HMGB1 concentrations increased from 36 to 84 h after irradiation.

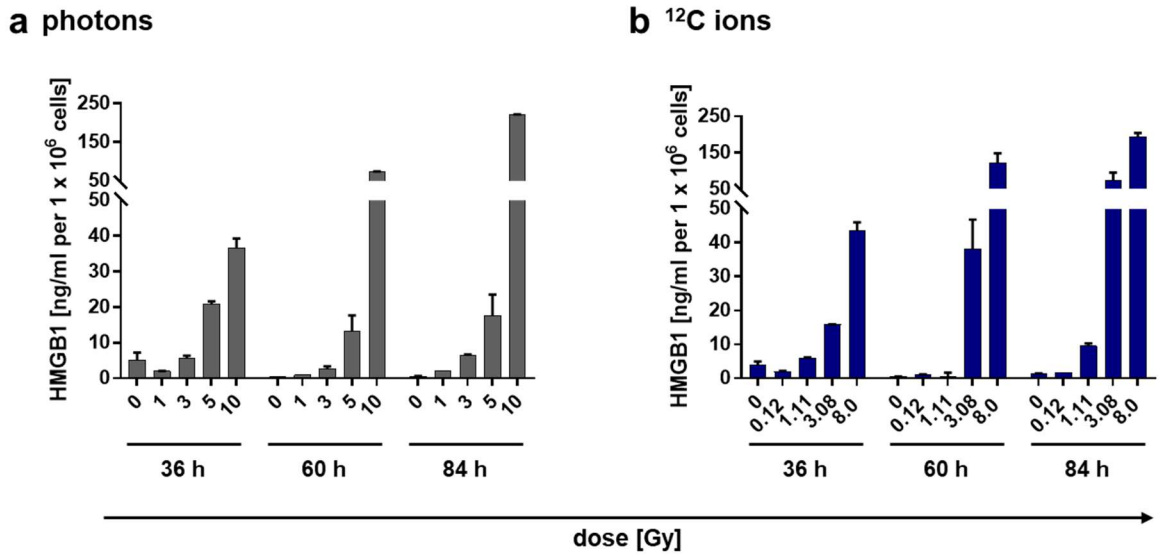


**Figure 3.6: Radiation-induced secretion of high mobility group box 1 (HMGB1).** EO771 cells were irradiated with graded doses of photons **(a)** or biologically equivalent doses of carbon ions **(b)**. 36, 60, and 84 h after irradiation, HMGB1 secretion into cell culture supernatant was determined by ELISA. HMGB1 concentration was normalized to 1 x $10^6$ EO771 cells. Representative results of one out of two independent experiments are shown.

## 3.3 CTL-mediated cytolysis of EO771 cells after irradiation

After having observed that both photon and carbon ion irradiation induced the upregulation of immune checkpoint and MHC class I molecules as well as the secretion of HMGB1, the functional relevance of these changes was further investigated. For this purpose, a luciferase-based cytotoxicity assay was established, in which EO771/Luci/OVA cells, stably expressing luciferase (Luci) and ovalbumin (OVA), were co-cultured with an OVA-specific CTL line to investigate CTL-mediated lysis of irradiated tumor cells. First, an appropriate tumor cell number was determined for the assay (Supplementary Figure 5.4, left). While all tested cell numbers would have been suitable, as no saturation of the relative luminesce units (RLUs) within the time span of the assay were measured, 5000 EO771/Luci/OVA cells per well were selected for further experiments. In a next step, OVA-specific CTLs (effector cells) were titrated on EO771/Luci/OVA cells (target cells), and effector to target cell (E:T) ratios of 1:5 and 1:10 were further used (Supplementary Figure 5.4, right). Finally, also the IFN-γ secretion by OVA-specific CTLs upon stimulation with irradiated EO771/Luci/OVA cells was to be investigated and suitable CTL numbers in IFN-γ ELISpot assays were identified by applying graded CTL numbers. Based on this assay, 400 and 800 CTLs per 50 000 targets were selected (Supplementary Figure 5.4b).

In a next step, 12 h after irradiation of EO771/Luci/OVA cells with graded doses of photons and BEDs of carbon ions, cells were co-cultured with OVA-specific CTLs. Following photon irradiation, enhanced cytolysis of target cells was observed when increasing doses were applied, although the extent varied between different independent biological repetitions (Figure 3.7a). Notably, when using an E:T ratio of 1:5 in the 2$^{nd}$ repetition, cytolysis of unirradiated cells already accounted for 60% indicating that too many CTLs were applied in this experiment so that irradiation could only slightly increase CTL-mediated killing. When cells were irradiated with carbon ions, susceptibly to CTL-mediated killing was even more enhanced compared to photon irradiation and results of independent biological experiments were more consistent (Figure 3.7b). Thus, when comparing maximal equivalent doses in co-cultures with an E:T ratio of 1:10, irradiation with 10 Gy photons increased cytolysis 1.3-1.7-fold compared to untreated cells, while tumor cell killing was increased 3.0–3.4-fold upon treatment with 8 Gy carbon ions. When culturing irradiated EO771/Luci/OVA cells without CTLs for the time span of the cytotoxicity assay, cell viability was similar for all doses and even slightly enhanced with increasing doses, as exemplarily shown for carbon ion-irradiated cells indicating that irradiation-induced cytotoxicity *per se* was only marginal during the luciferase-based cytotoxicity assay (Figure 3.7c). Slight differences were most likely due to small variations in cell counting. These were corrected by normalization to RLU values of EO771/Luci/OVA cells cultured without CTLs for the calculation of cytolysis. Interestingly, neither after photon irradiation nor after carbon ion irradiation, the IFN-γ secretion by OVA-specific CTLs was affected (Figure 3.7d).

Overall, these results suggest that the enhanced cytolysis upon irradiation was due to increased susceptibility of the target cell line to CTL-mediated killing and not due to enhanced effector function of the CTL line, when targeting irradiated cells.

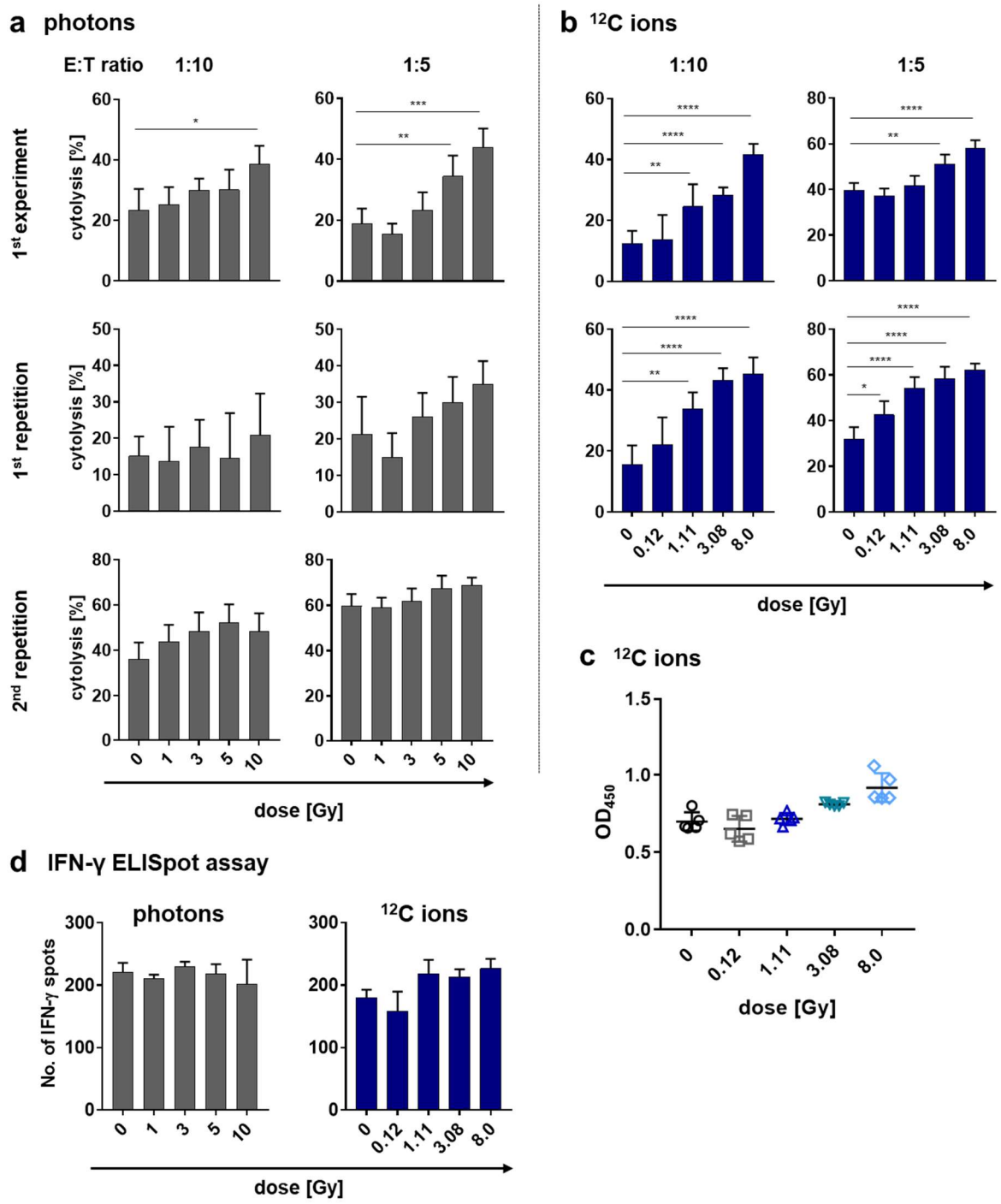


**Figure 3.7: Irradiation enhanced susceptibility to CTL-mediated cytolysis**. EO771/Luci/OVA cells were irradiated with increasing doses of photons **(a)** or biologically equivalent doses of carbon ions **(b)**. Cytolysis of target cells by OVA-specific CTLs was measured by luciferase-based cytotoxicity assay with effector to target cell (E:T) ratios of 1:10 and 1:5 in three (photons) or two (carbon ions) independent experiments. Assays were performed in quadruplicates and results presented as mean ± SD were analyzed by a two-tailed t test with correction for multiple comparison by Holm-Bonferroni method. Multiplicity adjusted p values are shown. **(c)** To control for irradiation-induced cell death of target cells during luciferase-based cytotoxicity assays, cell viability of irradiated EO771/Luci/OVA, cultured without CTLs, was measured. (d) In parallel to the cytotoxicity assays, IFN-γ secretion by OVA-specific CTLs was measured in INF-γ ELISpot assays.

## 3.4 Gene expression analysis upon RNA and miRNA sequencing after irradiation

### 3.4.1 Differential gene expression after photon vs. carbon ion irradiation

Next, EO771 cells were irradiated with 5 Gy photons and 3.08 Gy carbon ions, the doses selected for further *in vivo* RT, and 24 h after irradiation subjected to RNA and small RNA sequencing to gain a broader overview of gene expression affected by irradiation besides the immunomodulatory genes investigated in section 3.2.1.

**a**

| | groups | No. of upregulated DEGs/miRNAs | No. of downregulated DEGs/ miRNAs |
|---|---|---|---|
| **RNA** | untreated vs 5 Gy photons | 222 | 55 |
| | untreated vs 3.08 Gy $^{12}$C ions | 270 | 25 |
| | 5 Gy photons vs 3.08 Gy $^{12}$C ions | 0 | 0 |
| **miRNA** | untreated vs 5 Gy photons | 16 | 39 |
| | untreated vs 3.08 Gy $^{12}$C ions | 26 | 29 |
| | 5 Gy photons vs 3.08 Gy $^{12}$C ions | 6 | 4 |

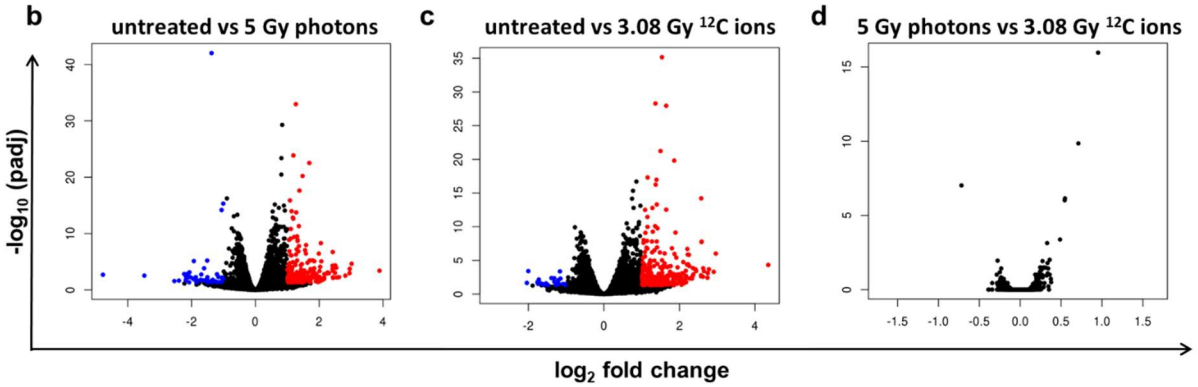


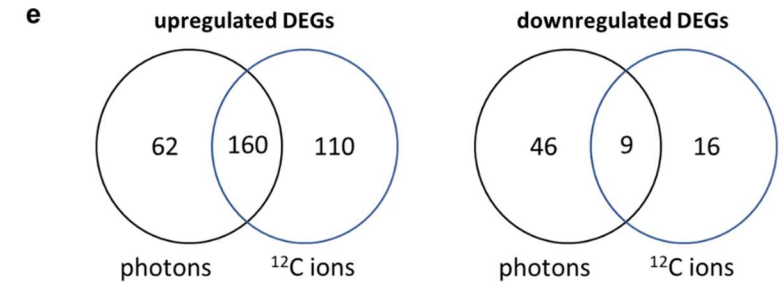


**Figure 3.8: Differential gene and miRNA expression after photon and carbon ion irradiation in EO771 cells.** **(a)** Number of differently expressed genes (DEGs) and miRNAs, upregulated or downregulated after irradiation of EO771 with 5 Gy photons and 3.08 Gy carbon ions, respectively. **(b) – (d)** Volcano plots comparing DEGs in untreated vs. 5 Gy photons, untreated vs. 3.08 Gy carbon ions, and 5 Gy photons vs. 3.08 Gy carbon ions. DEGs were defined as genes showing a $\log_2$ fold change greater than 1.0 as well as an adjusted p value lower than 0.05. Upregulated DEGs are presented in red, downregulated DEGs in blue. Volcano plots were provided by GENEWIZ. **(e)** Venn diagrams showing shared upregulated and downregulated DEGs between photon- and carbon ion-irradiated cells.

Overall, irradiation affected RNA expression to a greater extent than miRNA expression when regarding the total number of differently expresses genes (DEGs) and miRNAs (Figure 3.8a). Compared to untreated cells, irradiation with both photons and carbon ions predominantly led to an upregulation of gene expression rather than a downregulation of gene expression

(Figure 3.8a-c). Indeed, there were slight differences between the number of DEGs upregulated (222 vs. 270) and downregulated (55 vs. 25) when comparing 5 Gy photon and 3.08 Gy carbon ion irradiation to untreated cells, respectively. However, when directly comparing gene expression between cells irradiated with 5 Gy photons and 3.08 Gy carbon ions, no DEGs were identified (Figure 3.8d). Overall, this corroborates the results described after *in vitro* irradiation so far (section 3.1 to 3.3). Thus, even after analyzing a magnitude of genes by RNA sequencing, photon and carbon ion irradiation induce similar biological effects *in vitro*. Still, when comparing the DEGs identified for photons and carbon ions compared to untreated cells, respectively, not all genes were overlapping. Regarding the upregulated DEGs, 160 genes among 222 and 270 DEGs were shared, whereas within the downregulated DEGs 9 out of 16 and 46 were overlapping (Figure 3.8e).
Interestingly, the total number of miRNAs that was differentially expressed after irradiation was comparably low (Figure 3.8a). However here, six miRNAs were more frequently expressed in carbon ion-irradiated compared to photon-irradiated cells and four miRNAs were downregulated.

### 3.4.2 *In silico* pathway analysis using differentially expressed genes

Next, the 222 (photons) and 270 (carbon ions) upregulated DEGs identified by RNA sequencing (Figure 3.8a) were used for *in silico* pathway analysis to identify potential biological pathways activated upon photon and carbon ion irradiation. Analysis was performed with the Functional Annotation Bioinformatics Microarray Analysis tool DAVID. Here, the analysis was focused on pathway prediction using the KEGG pathway and BioCarta tools.
When performing DAVID functional annotation clustering for photon- and carbon ion-irradiated samples, four different clusters were identified (Table 3-1).

**Table 3-1: DAVID functional annotation clustering.** Genes differentially upregulated after photon and carbon ion irradiation compared to untreated EO771 cells were subjected to pathway analysis. Identified clusters, enrichment scores (ES), and annotation terms are shown. Terms were either predicted after carbon ion irradiation or both photon and carbon ion irradiation. The counts indicate the number of genes associated with the annotation term for either photon- or carbon ion-irradiated cells.

| Cluster (ES: photons/$^{12}$C ions) | biological term | predicted for | counts photons/$^{12}$C ions |
|---|---|---|---|
| **cluster 1 (ES: 2.72/1.54)** | focal adhesion | both | 10/9 |
| | ECM-receptor interaction | both | 7/6 |
| | PI3K-Akt signaling pathway | both | 8/7 |
| | protein digestion and absorption | $^{12}$C ions | -/4 |
| | amoebiasis | $^{12}$C ions | -/4 |
| **cluster 2 (ES: 0.92/1.04)** | chemokine signaling | both | 6/8 |
| | glutamatergic synapse | both | 4/3 |
| | morphine addiction | both | 3/3 |
| **cluster 3 (0.80/0.86)** | circadian entrainment | both | 4/4 |
| | cholinergic synapse | both | 4/4 |
| | dopaminergic synapse | both | 3/4 |
| **cluster 4 (0.65/0.5)** | gastric acid secretion | both | 3/3 |
| | adrenergic signaling in cardiomyocytes | both | 4/3 |
| | insulin secretion | both | 3/3 |
| | cAMP signaling pathway | both | 4/4 |

Having observed that no DEGs were found when comparing 5 Gy photon to 3.08 Gy carbon ion irradiation, all four clusters were shared between photon- and carbon ion–irradiated samples with only two annotation terms being exclusively found in cluster 1 after carbon ion irradiation. Based on the enrichment score the overall importance of a cluster can be evaluated and clusters with an enrichment score ≥ 1.3 are considered most meaningful [280]. In this analysis, this threshold only applied for cluster 1, which covers genes associated with focal adhesion, ECM-receptor interaction, and PI3K-Akt signaling pathway after both photon and carbon ion irradiation. Based on the enrichment score, the other three predicted clusters appeared less relevant. Moreover, also single biological terms were identified by DAVID functional annotation chart. Beside the terms annotated for the clustered analysis, several further biological terms were predicted (Supplementary Table 5-1). Among these, biological terms were associated with NK cell-mediated cytotoxicity, chemokine signaling pathways, and infectious diseases (staphylococcus aureus infection, tuberculosis, legionellosis). Moreover, after carbon ion irradiation, genes associated with TNF and Toll-like receptor signaling pathways were annotated. Pathway analysis for downregulated DEGs did not yield any meaningful results, probably due to the low number of evaluable genes (Figure 3.8a).

## 3.5 Establishment of a bilateral tumor model

### 3.5.1 EO771/OVA cells are not suitable for bilateral tumor growth *in vivo*

Having characterized radiogenic and immunomodulatory effects of photon and carbon ion irradiation on EO771 *in vitro,* the further aim was to treat tumor-bearing C57BL/6 mice with RT plus immune checkpoint blockade *in vivo*. Here, not only antitumor effects on the irradiated tumor site, but also effects on a distant, non-irradiated tumor site were to be investigated. Therefore, a bilateral syngeneic mouse model was established, in which mice were challenged with two s.c. tumor cell injections, one at the right hind leg (tumor #1) and the other one at the left flank (tumor #2). Injections were given with different cell numbers or at shifted time points to prevent outgrowth of the second tumor before RT could show a therapeutic effect. For this purpose, different application schedules using EO771/OVA cells stably expressing OVA, which would allow to investigate antigen-specific T cell responses *in vivo*, were tested.

Before starting with bilateral tumor cell injections, unilateral tumor growth using four different cell numbers of EO771/OVA cells were tested to determine tumorigenic cell doses (Supplementary Figure 5.5). Tumor growth was dose-dependent with tumors growing more rapidly when higher tumor cell numbers were injected. Based on unilateral tumor growth curves, $2 \times 10^6$ (tumor #1) and $2.5 \times 10^5$ (tumor #2) EO771/OVA cells were used for bilateral tumor cell injections at the same day. As a control, both cell numbers were used for unilateral tumor cell injections (Figure 3.9a). As before, unilateral tumors grew out exponentially in a dose-dependent manner. By contrast, when using $2.5 \times 10^5$ EO771/OVA cells in the bilateral model, tumor growth was impaired. Thus, two out of nine tumors did not grow at all and the outgrowth of the remaining seven tumors was clearly delayed. Moreover, also one tumor injected with $2 \times 10^6$ cells was rejected after initial growth in the bilateral model.

In the bilateral tumor model, one has to consider that mice need to be sacrificed as soon as tumor #1 reaches the termination criterion of one diameter being greater than 15 mm. Consequently, also the growth of tumor #2 cannot be further monitored. Still, when comparing the tumor volume on day 13 and day 17 after tumor cell injection, the tumor volume of tumors injected with $2.5 \times 10^5$ cells in the bilateral model were significantly smaller compared to tumors grown unilateraly (Figure 3.9b). In addition, the outgrowth of tumor #1 injected with $2 \times 10^6$ EO771/OVA cells was slightly delayed, even though there was no significant difference.

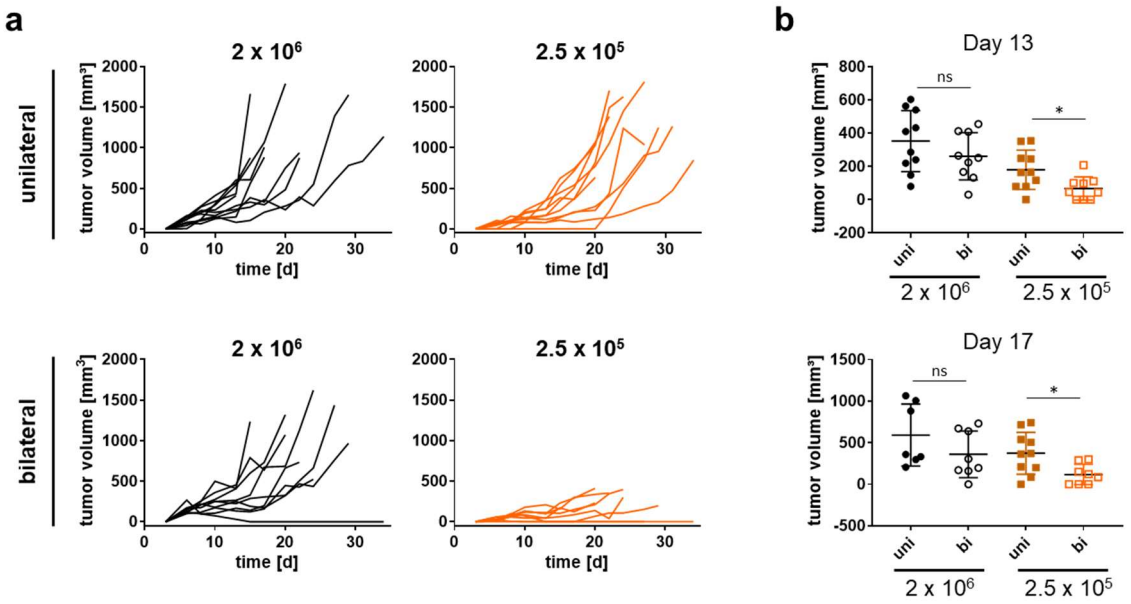


**Figure 3.9**: **Bilateral tumor implantations affect growth of EO771/OVA tumors *in vivo*. (a)** C57BL/6 mice were injected (s.c) with 2 x $10^6$ and/or 2.5 x $10^5$ EO771/OVA cells unilaterally (top) or bilaterally (bottom). Individual tumor growth curves are depicted (n = 9-10). **(b)** Comparison of tumor volume on day 13 and 17 after tumor cell injection, respectively. Dots represent individual mice and mean values ± SD are shown. Volumes of tumors injected with equal amounts of EO771/OVA cells were compared using a two-tailed t test. uni: unilateral, bi: bilateral.

Next, a different schedule was tested, injecting equal tumor cell numbers two or four days apart. When injecting 1 x $10^6$ EO771/OVA cells on day 0 and day 2, tumor #1 grew comparable to unilateral tumors (Supplementary Figure 5.5), while growth of tumor #2 was impaired (Figure 3.10a). Thus, one out of twelve tumors #2 did not grow at all, three tumors were rejected after initial outgrowth, and the remaining tumors showed delayed outgrowth. When tumors were injected with 1 x $10^6$ EO771/OVA cells four days apart, eight out of ten tumors #2 did not grow at all (Figure 3.10b). Here, also the growth of tumor #1 was affected, as tumors grew more inhomogenously with two tumors #1 being rejected completely.

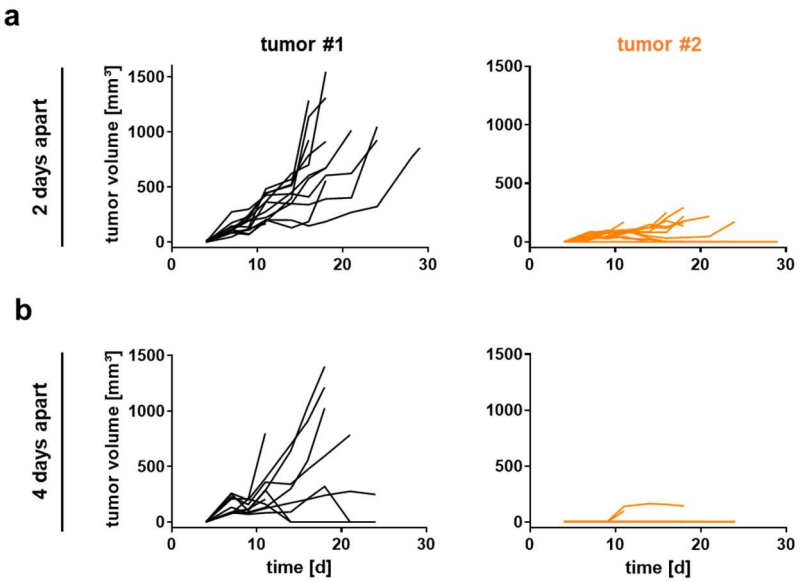


**Figure 3.10. Tumor #2 shows impaired tumor growth upon bilateral injection of EO771/OVA cells.** C57BL/6 mice were bilaterally implanted (s.c). with 1 x $10^6$ EO771/OVA cells on day 0 for tumor #1 and day 2 **(a)** or day 4 **(b)** for tumor #2. Individual growth curves of tumor #1 and tumor #2 are depicted (n=10-12).

Taken together, EO771/OVA cells are not suitable for bilateral tumor growth, as particularly the outgrowth of tumor #2 is impaired. Consequently, the bilateral EO771/OVA model would be to be too unstable to investigate *bone fide* therapeutic effects. The fact that tumors injected four days after initial tumor challenge did not grow at all suggests that an immune response was primed by tumor #1 leading to the rejection of tumor #2. The relevant antigen was most likely OVA, which originates from chicken.

### 3.5.2 Bilateral tumor model with parental EO771 cells

Assuming that OVA expression was too immunogenic for bilateral tumor growth with EO771/OVA cells, the parental EO771 cell line was further used. Mice were challenged with equal tumor cell numbers two days apart. Based on previous experiments performed in our lab, 2 x $10^5$, 4 x $10^5$, or 8 x $10^5$ EO771 cells were injected to identify appropriate cell numbers for the bilateral EO771 model.

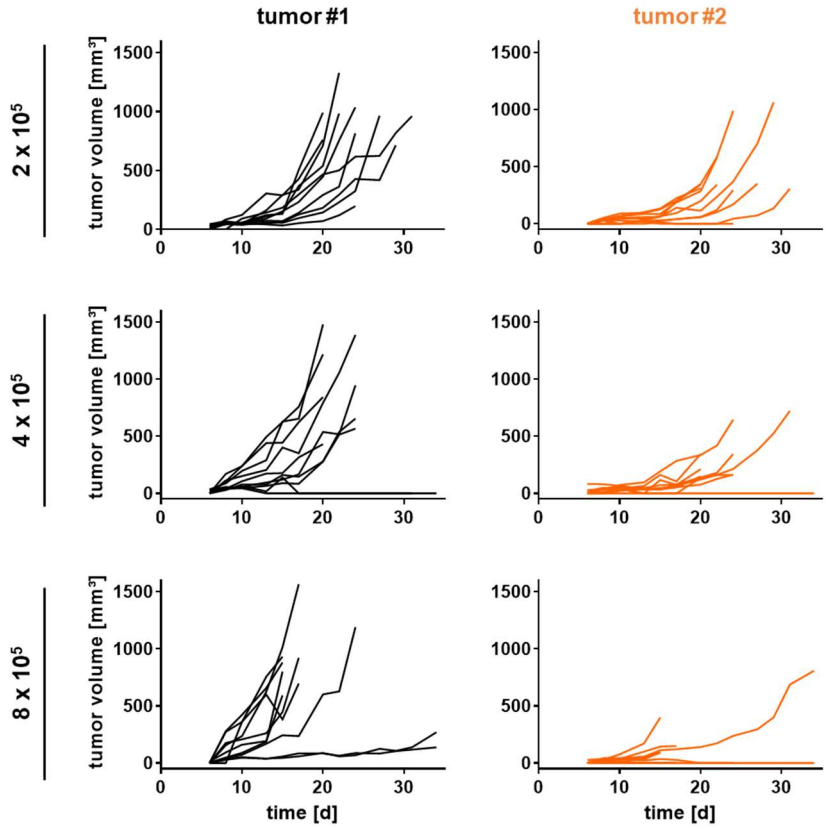


**Figure 3.11: Bilateral tumor growth using parental EO771 cells.** C57BL/6 mice were bilaterally injected (s.c.) with 2 x $10^5$, 4 x $10^5$, or 8 x $10^5$ EO771 cells on day 0 for tumor #1 and day 2 for tumor #2. Individual growth curves of tumor #1 and tumor #2 are depicted (n=10).

In contrast to tumor growth with the EO771/OVA cell line, tumor #2 was clearly growing out when using parental EO771 cells (Figure 3.11). With the lowest cell number used for injections (2 x $10^5$ cells), the highest volumes of tumor #2 were reached. This was mainly due to tumor #1, since it was growing slower with fewer cells injected thereby allowing extended monitoring of tumor #2. Regarding injections with 4 x $10^5$ cells, tumor #2 generally did not grow very large before mice needed to be sacrificed, but most tumors seemed to trend towards an exponential growth. Finally, with the highest cell number of 8 x $10^5$ EO771 cells, growth of tumor #1 was

most inhomogeneous. While most tumors grew out rapidly, outgrowth of three tumors was clearly delayed. Moreover, in some cases tumor #2 did not grow out at all, also in the mice surviving more than 20 days.
In the end, 4 x $10^5$ EO771 cells were selected for the bilateral tumor model. Based on the trend towards an exponential tumor growth of tumor #2, it can be assumed that tumor #2 would have continued to grow out exponentially if outgrowth of tumor #1 was controlled by RT. Moreover, in contrast to injections with 2 x $10^5$ cells, the time window to observe therapeutic effects on the non-irradiated tumor site (tumor #2) appeared extended.

## 3.6 Therapeutic effects induced by radioimmunotherapy

### 3.6.1 Monotherapy with immune checkpoint-blocking antibodies

Before testing combination therapy approaches, the therapeutic effects of monotherapy with checkpoint-blocking antibodies against PD-L1 and CTLA-4 were investigated. A treatment schedule published by Twyman-Saint Victor *et al.* [261] was used as reference and mice received three i.p. injections with anti-PD-L1 (aPD-L1) antibodies, anti-CTLA-4 (aCTLA-4) antibodies, or IgG controls on day 9, 12, and 15 after tumor cell implantation (Figure 3.12a).

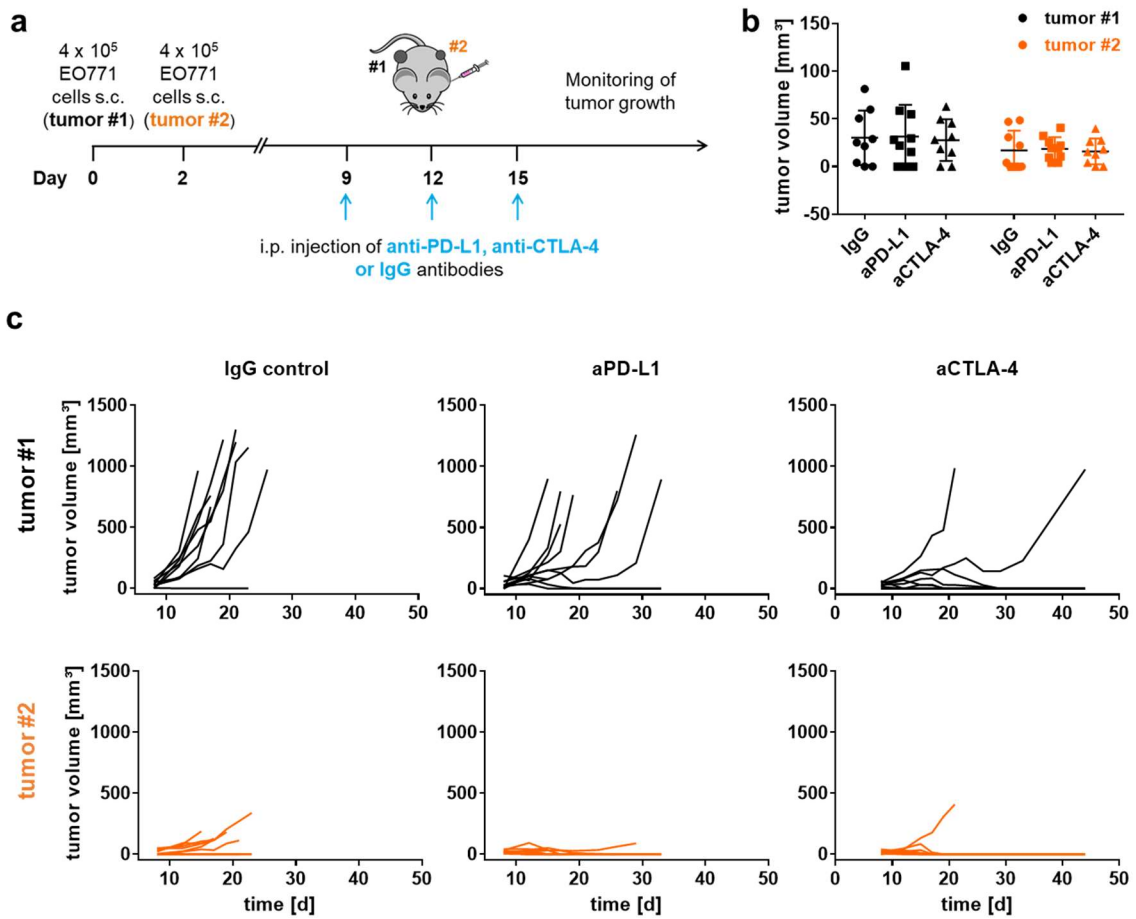


**Figure 3.12: Monotherapy with immune checkpoint-blocking antibodies against PD-L1 and CTLA-4.** **(a)** Treatment schedule: C57BL/6 mice were bilaterally challenged with time-shifted tumor cell injections (s.c.) using 4 x $10^5$ EO771 cells. On day 9, 12 and 15, mice received i.p. injections of checkpoint-blocking antibodies against PD-L1, CTLA-4, or IgG controls. **(b)** Randomization of mice into three groups (n= 9-10) based on the tumor volume of tumor #1 and tumor #2 on day 8. **(c)** Individual growth curves of tumor #1 and tumor #2 are shown.

On day 8, mice were randomized into three groups based on the volume of both tumors. However, in this pilot experiment, the mean volume of tumor #1 and tumor #2 was around 30 $mm^3$ and 15 $mm^3$, respectively, and some mice did not have a palpable tumor on one of the sides when starting the treatment (Figure 3.12b). Consequently, even in the IgG control group, in one mouse tumor #1 and in three mice tumor #2 did not grow out at all (Figure 3.12c). Anti-PD-L1 treatment induced tumor regression and tumor growth delay in about half of the tumors #1, while tumor #2 barely grew out. Furthermore, anti-CTLA-4 monotherapy resulted in complete tumor regression in around 80% of the mice. As checkpoint blockade was to be combined with RT in further experiments, the treatment start was postponed by 3 days so that tumors were established with mean volumes of tumor #1 between 120-200 $mm^3$.

### 3.6.2 Construction of a shielding device for local photon RT of tumor #1

For *in vivo* experiments with photon irradiation, an x-ray irradiation system, called Faxitron Mulitrad225, was used. As the machine contains a closed chamber, in which x-rays travel canonically and cannot be focused, a shielding device that allows precise and reproducible irradiation of tumor #1 and shielding of tumor #2 was constructed in collaboration with Armin Runz (DKFZ, Heidelberg). To avoid scattered irradiation, tumors had to be vertically centered beneath the irradiation source. To this end, a Plexiglas plate was built, which allowed precise insertion into the irradiator and to which the positioning plate and the lead shield were fixed in a key-lock system (Figure 3.13a). The anesthetized mouse was placed on the positioning plate (Figure 3.13b), on which the blue square indicates the shielded area and the circle the beamline with a diameter of 13 mm. Tumor #1, located at the right hind leg, had to be positioned in the beamline, which was ensured using a frame with the dimensions of the lead shield (Figure 3.13c).

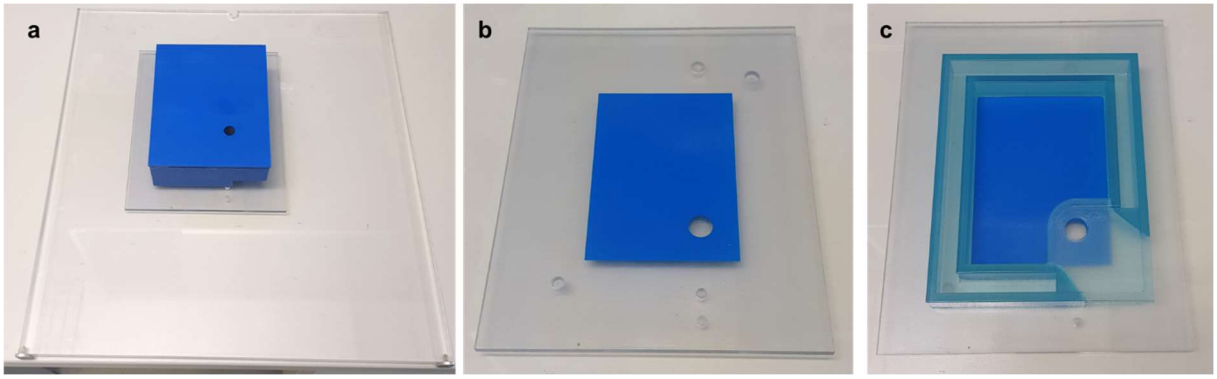


**Figure 3.13: Shielding device for local photon irradiation of tumor #1. (a)** The shielding device was composed of a Plexiglas plate, which was inserted to the MultiRad225 irradiator. In a key-lock manner, the positioning plate and the lead shield were fixed ensuring that tumor #1 was vertically centered beneath the irradiation source. **(b)** Positioning plate, on which the anesthetized mouse was placed. The circle indicates the beamline and thus the position of tumor #1. **(c)** The frame allows to control for the correct positioning of tumor #1 in the beamline. The shielding device was designed and constructed by Armin Runz. Dosimetry was performed by Dr. Peter Häring and Clemens Lang.

### 3.6.3 Monotherapy with photon RT

Next, the response of EO771 tumors to monotherapy with photons was investigated. Based on the *in vitro* experiments, a dose of 5 Gy photons for *in vivo* RT was defined which was locally delivered to tumor #1 on three consecutive days. The treatment schedule is depicted in Figure 3.14a. Thus, mice were bilaterally challenged with time-shifted tumor cell injections and after 12 days mice were randomized into two groups according to the volumes of tumor #1 and

tumor #2 (Figure 3.14b). As expected, tumor #1 had a bigger volume compared to tumor #2, with mean values of approximately 200 $mm^3$ and 50 $mm^3$, respectively. Overall, outgrowth of tumor #1 was quite inhomogeneous, but tumors sizes were evenly distributed into both groups. Then, tumor #1 was irradiated with three fractions of 5 Gy photons and growth of both tumors was monitored. Results from tumor take experiments were validated in untreated mice (section 3.5.2). Accordingly, tumor #1 grew out quickly so that mice had to be sacrificed before tumor #2 was proceeding into the exponential growth phase (Figure 3.14c). In the irradiated group, approximately half of tumors #1 clearly responded to the therapy as shown by a delayed outgrowth of these tumors. One tumor #1 even regressed completely. In the other half of the animal collective, growth of tumor #1 showed a kinetic comparable to untreated mice. In this subgroup, tumors were most likely too big at the start of the treatment and thus monotherapy with irradiation could not control tumor growth. Importantly, irradiation did not have a therapeutic effect on tumor #2 and mice finally had to be sacrificed due to the outgrowth of the non-irradiated tumor site. Consequently, when regarding the survival of both groups, there were no major differences observed (Figure 3.14d). Towards the end of the survival curves, there is a tendency of better survival in irradiated mice, which was not significant due to the outgrowth of tumor #2 in responding mice.

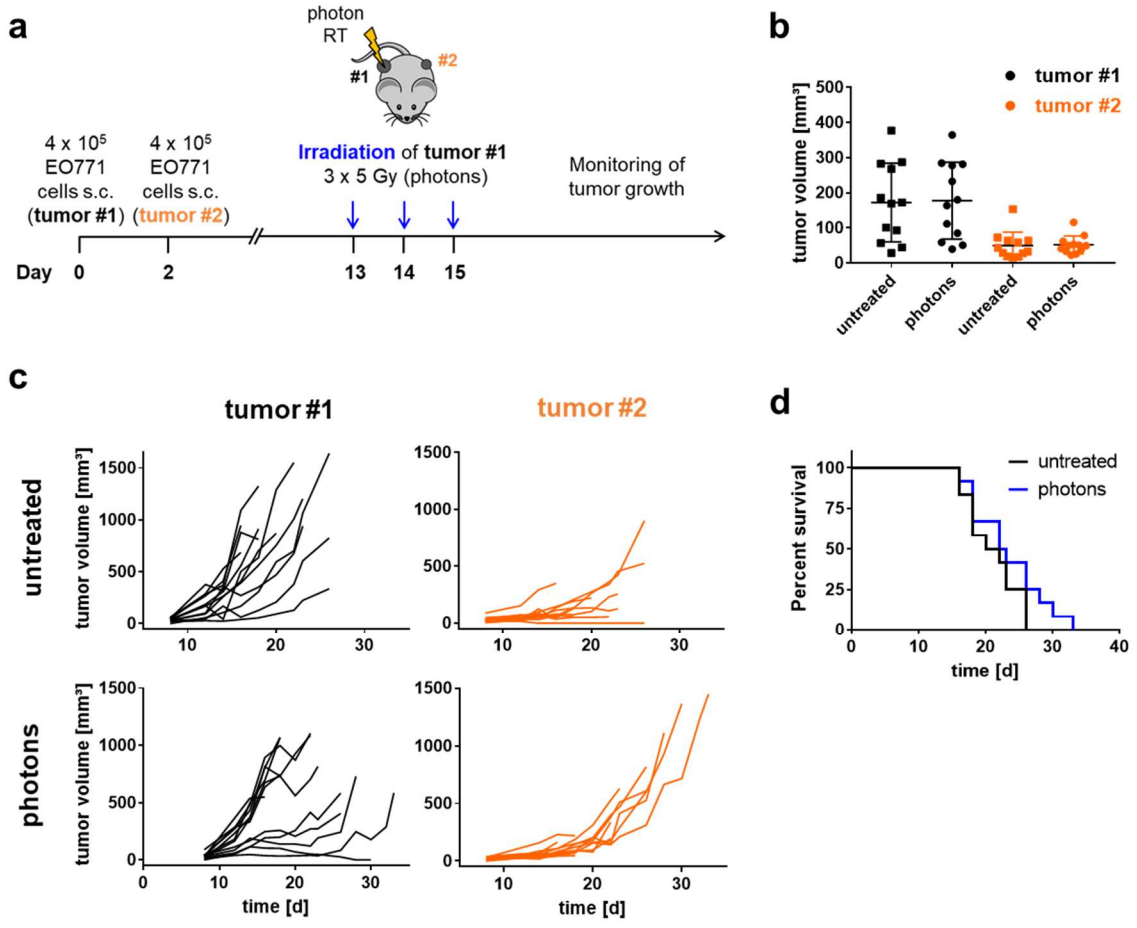


**Figure 3.14: Treatment of EO771 tumors with fractionated photon RT as monotherapy. (a)** Treatment schedule: C57BL/6 mice were bilaterally challenged (s.c.) with time-shifted tumor cell injections using 4 x $10^5$ EO771 cells. When tumors were established, tumor #1 was irradiated with 5 Gy on three consecutive days and tumor growth was monitored. **(b)** On day 12, mice were randomized into two groups based on the volume of tumor #1 and tumor #2 (n=12). **(c)** Individual growth curves of tumor #1 and tumor #2 of untreated mice and mice treated with photon RT. **(d)** Kaplan-Meier survival analysis. Significance was determined using a log-rank (Mantel-Cox) test.

Driven by the observation that the outgrowth of tumor #2 was rather slow compared to tumor #1, monotherapy with 3 x 5 Gy photon irradiation was repeated, but the cell numbers used for tumor cell injections were changed from 4 x $10^5$ to 2 x $10^5$ based on tumor take experiments described in section 3.5.2. In this experiment, photon radiotherapy again lead to tumor growth delay and regression of tumor #1 in a fraction of mice, which resulted in a significantly better survival of mice treated with RT compared to untreated mice (Supplementary Figure 5.6). However, the outgrowth of tumor # 2 was rather inhomogeneous also in untreated mice.

### 3.6.4 Combining photon RT with checkpoint blockade against PD-L1

Having tested different schedules for tumor cell injections as well as photon RT and immune checkpoint blockade as monotherapy, an optimized treatment schedule for combination therapy was set up, which was used in all further experiments (Figure 3.15a). Accordingly, mice were bilaterally injected with 4 x $10^5$ EO771 cells one day apart. When tumors were established, tumor #1 was irradiated with a fraction of 5 Gy photons on three consecutive days. Starting with the first day of irradiation, immune checkpoint-specific antibodies or respective IgG controls were concurrently administered three times with three days apart.
In a first step, photon irradiation was combined with aPD-L1 checkpoint blockade. Tumors were randomized into three groups one day before treatment start (Figure 3.15b). Here, the mean volume of tumor #1 and tumor #2 accounted for 150-200 $mm^3$ and 40-50 $mm^3$, respectively. Anti-PD-L1 treatment alone had no impact on growth of tumor #1 showing that immune checkpoint blockade against PD-L1 alone is ineffective in the bilateral EO771 tumor model when tumors are established (Figure 3.15c). Notably, outgrowth of tumor #2 could only be monitored until tumor #1 in the same mouse reached a termination criterion. However, at least in part of the tumors #2, the start of an exponential outgrowth was detected. Moreover, the observation that aPD-L1 therapy was ineffective was confirmed when the experiment was repeated (Supplementary Figure 5.7). Here, also an exponential outgrowth of tumor #2 was visible. Photon RT alone lead to tumor growth delay or regression of tumor #1 without affecting growth of tumor #2 (Figure 3.15c) confirming the results described in the previous section. Combination of photon RT and aPD-L1 antibodies even enhanced tumor control of tumor #1, especially for bigger tumors, compared to photon RT alone. Thus, tumor volumes were directly compared on day 18, one day before the first mice had to be sacrificed after reaching the maximal tumor diameter. Indeed, the tumor volume was significantly lower when mice were treated with photon RT + IgG control and photon RT + aPD-L1, respectively, compared to aPD-L1 therapy (Figure 3.15d). On day 18, there was a tendency towards a decreased tumor volume in the photon RT + aPD-L1 group compared to the photon RT + IgG control group, which proved to be significant on day 22. Finally, in two mice also tumor #2 was completely rejected after combination therapy leading to complete responses in 25% of mice and thus, significantly better survival of mice in this group (Figure 3.15e).
These findings were reproduced when the experiment was repeated (Supplementary Figure 5.7). Briefly, a significantly better survival was observed in mice treated with photon RT + aPD-L1 compared to monotherapy with RT or aPD-L1, respectively. Again, there was a strong therapeutic effect on tumor #1, while 25% of mice responded with tumor growth delay or regression of tumor #2.

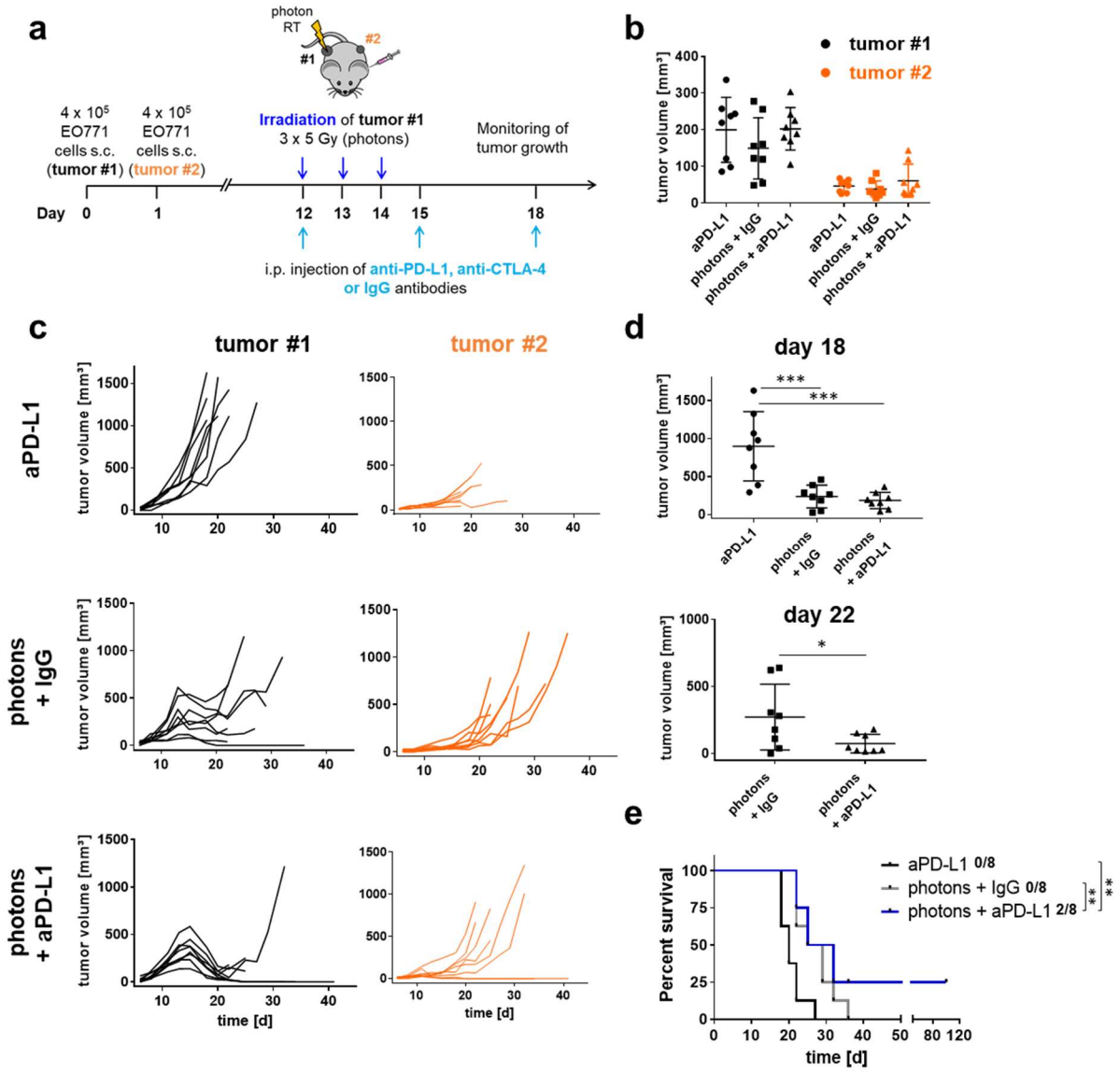


**Figure 3.15: Combining photon RT with immune checkpoint blockade against PD-L1. (a)** Treatment schedule: C57BL/6 mice were bilaterally challenged with time-shifted tumor cell injections (s.c.) using 4 x $10^5$ EO771 cells. When tumors were established, tumor #1 was irradiated with 5 Gy photons on three consecutive days. On day 12, 15, and 18, mice received i.p. injections of anti-PD-L1 antibodies or IgG control. **(b)** One day before treatment start, mice were randomized into three groups based on the volume of tumor #1 and tumor #2 (n=8). **(c)** Individual growth curves of tumor #1 and tumor #2 of mice treated with anti-PD-L1 antibodies, photon RT plus IgG control or photon RT plus anti-PD-L1 antibodies. **(d)** Comparison of tumor volumes for tumor #1 on day 18 and 22 after tumor cell injection, respectively. In the groups shown in the respective plots, day 18 and 22 represent the last days before the first mice had to be sacrificed within after reaching the maximal tumor diameter. Dots represent individual mice and mean values ± SD are shown. Significance was determined by one-way ANOVA with post-hoc Turkey's test (day 18) or using a two-tailed t test (day 22). **(e)** Kaplan-Meier survival analysis. In addition, complete response rates for each group are shown. Significance was determined using a log-rank (Mantel-Cox) test with Holm-Bonferroni correction.

### 3.6.5 Anti-PD-L1 vs. anti-CTLA-4 therapy in combination with photon RT

Next, photon RT was combined with immune checkpoint blockade against CTLA-4 and the effects were compared to combination therapy with aPD-L1 antibodies. Using the same treatment schedule as described before (Figure 3.15a), photon therapy plus aCTLA-4 therapy showed superior therapeutic effects compared to the combination with aPD-L1 antibodies and monotherapy with photon irradiation (Figure 3.16a). Accordingly, complete regression of

tumor #1 was observed in all mice and of tumor #2 in the majority of mice in the photon RT + aCTLA-4 group. Regarding the photon RT + IgG control and photon RT + aPD-L1 group results of the previous experiments were confirmed. Notably, tumor volume at the beginning of the therapy was slightly lower compared to the previous experiment accounting for mean volumes of approximately 115 $mm^3$ and 40 $mm^3$ for tumor #1 and tumor #2, respectively (Figure 3.16b). Consequently, photon RT alone induced a similar therapeutic effect on tumor #1 as photon RT plus aPD-L1 therapy. It appears that only for bigger tumor volumes aPD-L1 antibodies provide a synergistic effect to photon RT compared to RT alone.
Overall, there were long-lasting complete responses in 80% of mice after photon RT plus aCTLA-4 checkpoint blockade, which resulted in a significantly better survival of mice in this group compared to all other groups (Figure 3.16c and d). Moreover, there was a significantly better survival observed in mice treated with photon RT or photon RT + aPD-L1 antibodies compared to untreated mice. Also in this experiment, two long-lasting complete responses were observed after combined RT plus aPD-L1 therapy, but still there was no significant survival benefit compared to the photon RT alone.

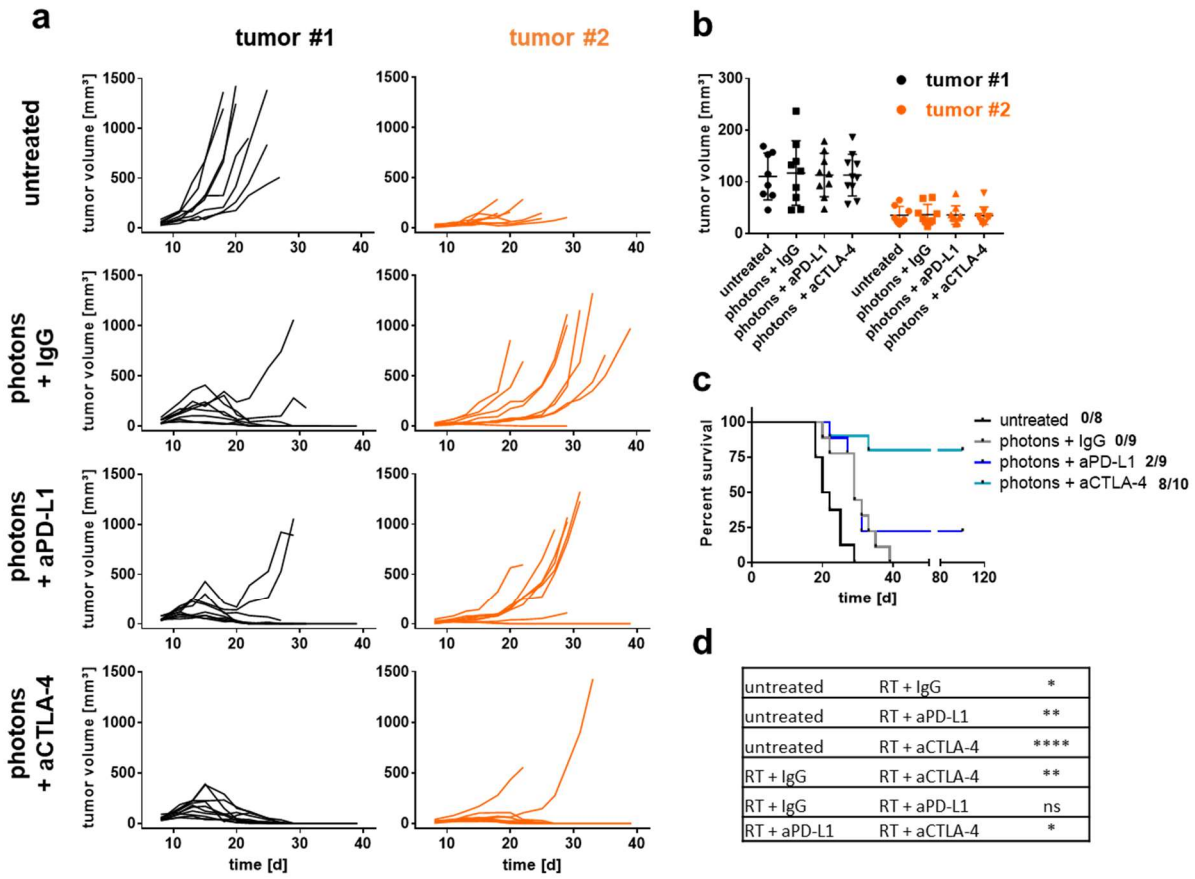


**Figure 3.16: Anti-PD-L1 vs. anti-CTLA-4 therapy in combination with photon RT. (a)** Individual growth curves of tumor #1 and tumor #2 of untreated mice or mice treated with photon RT + IgG control, photon RT plus anti-PD-L1 antibodies or photon RT plus anti-CTLA-4 antibodies. **(b)** One day before treatment start, mice were randomized into four groups based on the volume of tumor #1 and tumor #2 (n=8-9). **(c)** Kaplan-Meier survival analysis. In addition, complete response rates for each group are shown. **(d)** Comparison of groups depicted in the Kaplan-Meier survival analysis. Significance was determined using a log-rank (Mantel-Cox) test with Holm-Bonferroni correction.

### 3.6.6 Combining photon RT with dual immune checkpoint blockade

Finally, the combination of photon RT plus dual immune checkpoint blockade against PD-L1 and CTLA-4 was tested, as this was shown to be most efficient in controlling outgrowth of tumor #1 and tumor #2 in the B16F10 model [261]. In the previous experiment, photon RT plus aCTLA-4 therapy was already very efficient in inducing tumor regression when the mean volumes of tumor #1 and tumor #2 during randomization were approximately 115 $mm^3$ and 40 $mm^3$, respectively (Figure 3.16). Accordingly, photon RT plus dual immune checkpoint blockade was only started when tumor #1 and tumor #2 had reached a greater mean volume of 220-230 $mm^3$ and 70-80 $mm^3$, respectively (Figure 3.17b).

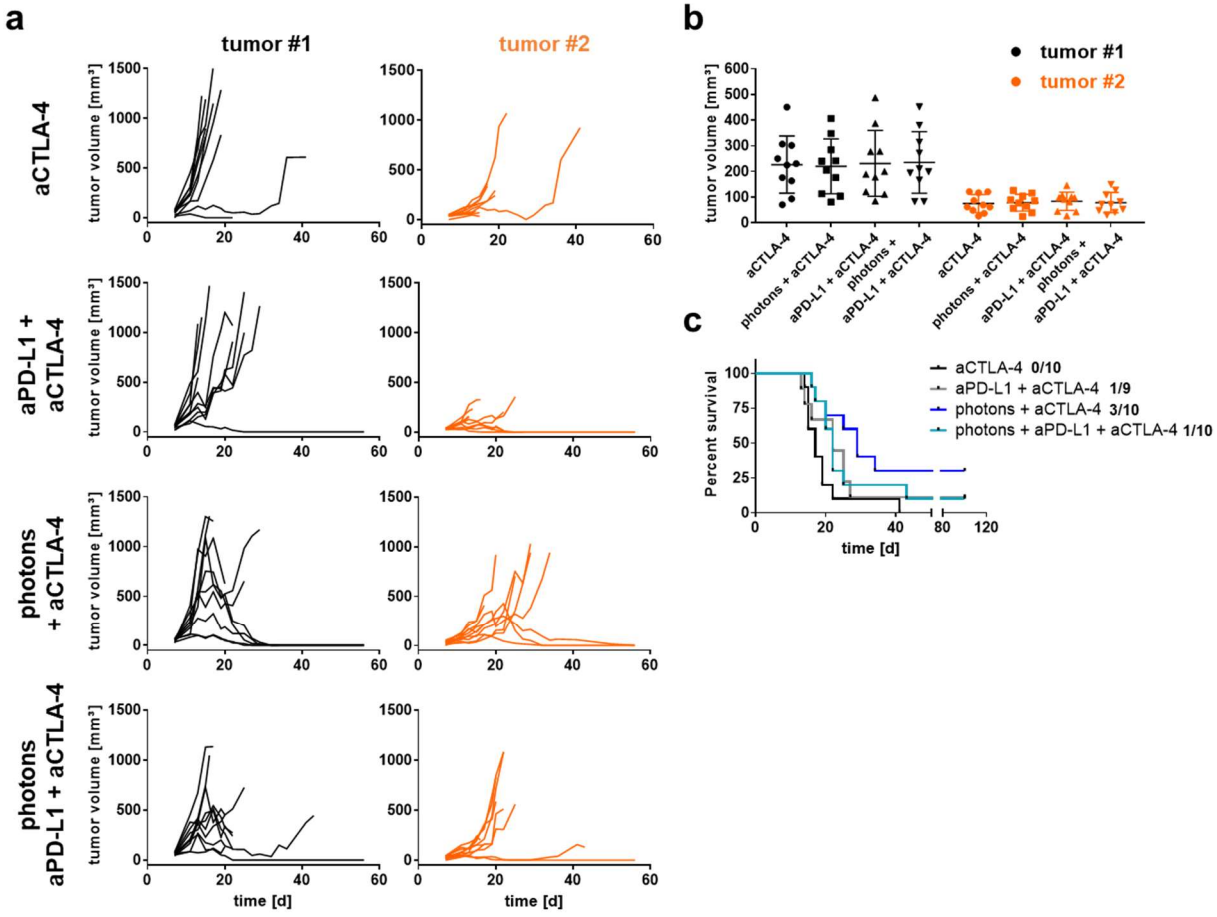


**Figure 3.17: Combining photon RT with dual immune checkpoint blockade. (a)** Individual growth curves of tumor #1 and tumor #2 of mice treated with anti-CTLA-4 antibodies, dual checkpoint blockade (anti-PD-L1 plus anti-CLTA-4 antibodies), photon RT plus anti-CTLA-4 antibodies, or photon RT plus dual checkpoint blockade. **(b)** One day before treatment start, mice were randomized into four groups based on the volume of tumor #1 and tumor #2 (n=10). **(c)** Kaplan-Meier survival analysis. In addition, complete response rates for each group are shown. Significance was determined using a log-rank (Mantel-Cox) test with Holm-Bonferroni correction.

Treatment of mice with aCTLA-4 antibodies did not affect outgrowth of tumor #1 in the majority of cases (Figure 3.17a), while the outgrowth of tumor #2 could only be monitored until mice had to be sacrificed due to the rapid outgrowth of tumor #1. Still, in the aCTLA-4 group, the start of an exponential growth of tumor #2 became apparent. In the group treated with dual immune checkpoint blockade, all but one tumors #1 grew out quickly, although part of the tumors showed slightly delayed outgrowth. Moreover, in three out of ten mice tumor #2 regressed completely after dual immune checkpoint blockade alone. Interestingly, the survival

of mice could not be further improved, when photon RT was combined with dual immune checkpoint blockade (Figure 3.17c). Indeed, the outgrowth of tumor #1 could be controlled to some extent by photon RT plus dual immune checkpoint blockade, but tumor #2 grew out exponentially in 80% of mice. Finally, photon RT plus aCTLA-4 therapy led to complete responses in 30% of mice. Notably, one tumor #1 regressed completely after it had reached a volume of over 1000 $mm^3$ highlighting the enormous therapeutic potential of combination of photon RT plus aCTLA-4 antibodies.
Overall, when starting treatment with comparably large tumor volumes, photon RT plus aCTLA-4 therapy was most efficient in inducing tumor regression of both tumor #1 and #2. Still, the percentage of surviving animals did not differ significantly from any of the other groups. These results suggest that addition of aPD-L1 checkpoint blockade to photon RT plus aCTLA-4 therapy does not further increase the therapeutic efficacy. Moreover, dual immune checkpoint alone might induce strong tumor regression in smaller tumors. Consequently, dual immune checkpoint blockade was not further investigated.

### 3.6.7 Local carbon ion RT of tumor #1

In a next step, the aim was to test combined RT plus immune checkpoint blockade using carbon ion RT, which was performed at the HIT. In contrast to photon RT, the body of the mouse and thus tumor #2 did not have to be shielded by lead, as carbon ion radiation can be precisely directed towards tumor #1, while sparing surrounding tissue. A holder allowing local irradiation of tumor #1 was previously designed by Dr. Mahmoud Moustafa (HIT, Heidelberg) (Figure 3.18a).

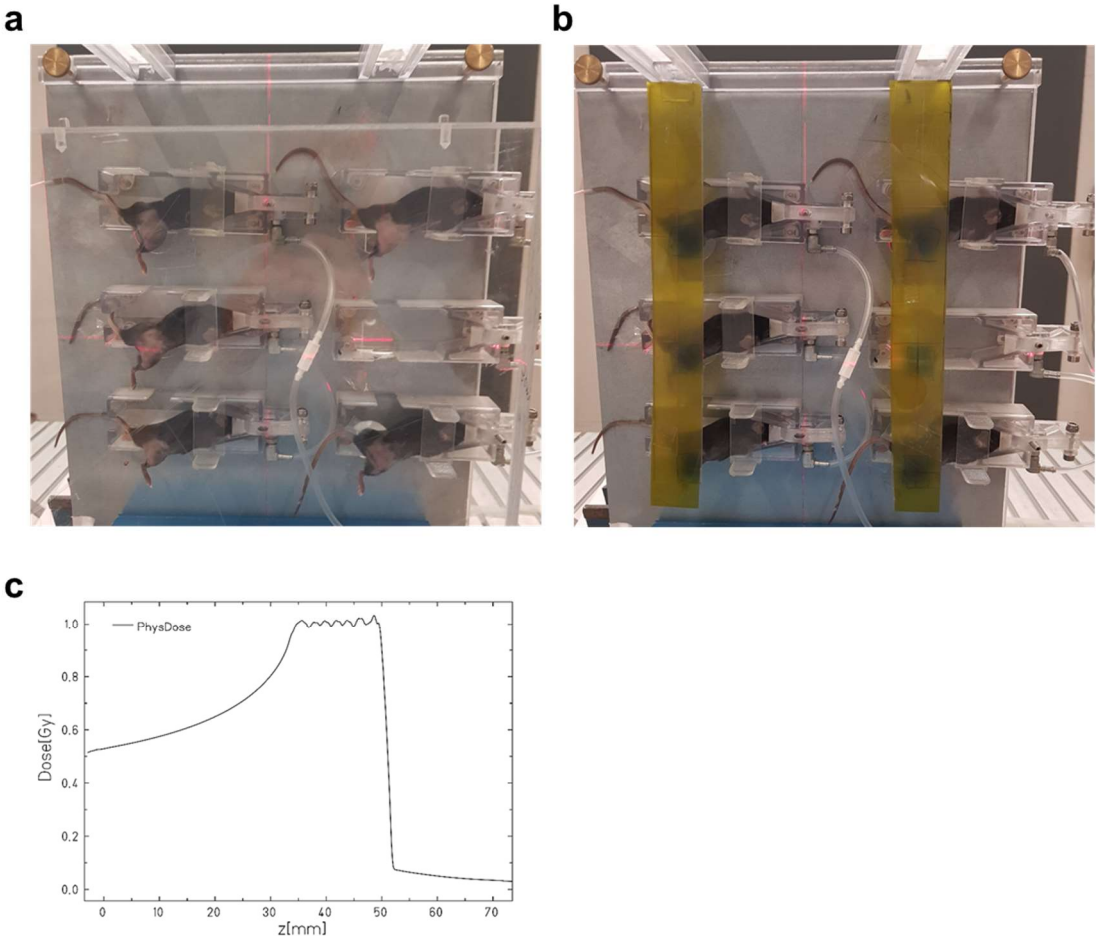

**Figure 3.18: Device for local carbon ion RT of tumor #1. (a)** Mice were positioned in a holder, to which isoflurane was directed to keep mice in anesthesia. Based on lasers, the holder was positioned in the irradiation field. A 30 mm Plexiglas absorber was used to adjust the extended Bragg peak. **(b)** Before starting irradiation of tumor #1, the irradiation field (blue) was tested on filters. These filters were used before each irradiation to ensure correct positioning of tumor #1 in the irradiation field. **(c)** Depth-dose profile of carbon ion irradiation showing the 20 mm extended break peak. Notably, this graph was made during calibration using 1 Gy. The holder was designed by Dr. Mahmoud Moustafa. The graph was provided by Dr. Stephan Brons.

Six mice were placed in a holder and kept in anesthesia by isoflurane. The holder was positioned into the correct plane by two lasers. Before starting carbon ion RT of murine tumors, the irradiation scheme was once tested on filters (yellow) visualizing the irradiation field (blue) (Figure 3.18b). These filters were then used to precisely position tumor #1 in the irradiation field before every irradiation. The irradiation field itself had a comparable diameter (13 mm) as the one used for photon RT (Figure 3.13). Moreover, also the angle of irradiation was the same, as tumors were hit vertically by the beamline. When regarding the dose-depth profile of the irradiation plan, an extended Bragg Peak was used allowing irradiation with a depth of 20 mm so that the whole tumor was irradiated (Figure 3.18c). The irradiation plan and dose-depth profile were provided by Dr. Stephan Brons (HIT, Heidelberg).

### 3.6.8 Carbon ion RT plus checkpoint blockade against PD-L1 or CTLA-4

Carbon ion RT of murine EO771 tumors was performed with the same treatment schedule used for photon RT. Thus, mice were challenged with bilateral tumor cell injections, tumor #1 was irradiated on three consecutive days, and mice received three i.p. injections of aPD-L1 or aCTLA-4 antibodies (Figure 3.15a). Due to the different physical properties of carbon ion radiation compared to photon radiation, a physical dose of 3.08 Gy was used for irradiation, which had been defined as biologically equivalent to 5 Gy photons in a clonogenic survival assay *in vitro* (Figure 3.1a).

As with photon RT, the combination of carbon ion RT with aCTLA-4 checkpoint blockade yielded superior therapeutic effects on both tumor sites (Figure 3.19a). Thus, complete tumor regression of tumor #1 was observed in 100% of mice, and in five out of nine mice also tumor #2 regressed completely leading to a significantly better survival compared to all other treatment groups (Figure 3.19c). Moreover, in two mice a growth delay of tumor #2 was observed and only two tumors #2 appeared unaffected by the treatment. The combination therapy of carbon ion RT and aPD-L1 antibody efficiently controlled the outgrowth of tumor #1, although two tumors grew out again after initial regression, but the progress could not be monitored further due to the outgrowth of tumor #2. Furthermore, growth control of tumor #1 was slightly superior compared to carbon ion RT alone. However, for both carbon ion RT + aPD-L1 and carbon ion RT + IgG groups, tumor #2 grew out exponentially so that no difference in survival was observed between both groups.

In this experiment, mean volume of tumor #1 and tumor #2 at treatment start accounted for 130 $mm^3$ and 50 $mm^3$, respectively (Figure 3.19b). Driven by the observation that the therapeutic effect of photon RT appeared to correlate with the tumor volume at the beginning of the treatment, the experiment was repeated with bigger starting volumes of tumor #1 and tumor #2 (180 $mm^3$ and 75 $mm^3$, respectively) (Supplementary Figure 5.8). Also with carbon ion RT, tumor control was reduced when the starting volume of tumors was higher. Thus, in the repetition experiment, carbon ion RT only marginally affected outgrowth of tumor #1 and additional administration of aPD-L1 antibody could only slightly increase the therapeutic effect. As expected, tumor #2 did not respond to these therapies. Remarkably, combination therapy with carbon ion RT plus aCTLA-4 checkpoint blockade was again very efficient with superior control of these large tumors #1. Moreover, even though the mean volume of tumor #2 was

already 75 mm³ at treatment start, half of the tumors #2 regressed completely or showed a tumor growth delay, which lead to a significantly better survival of the carbon ion RT + aCTLA-4 group compared to the three other groups.

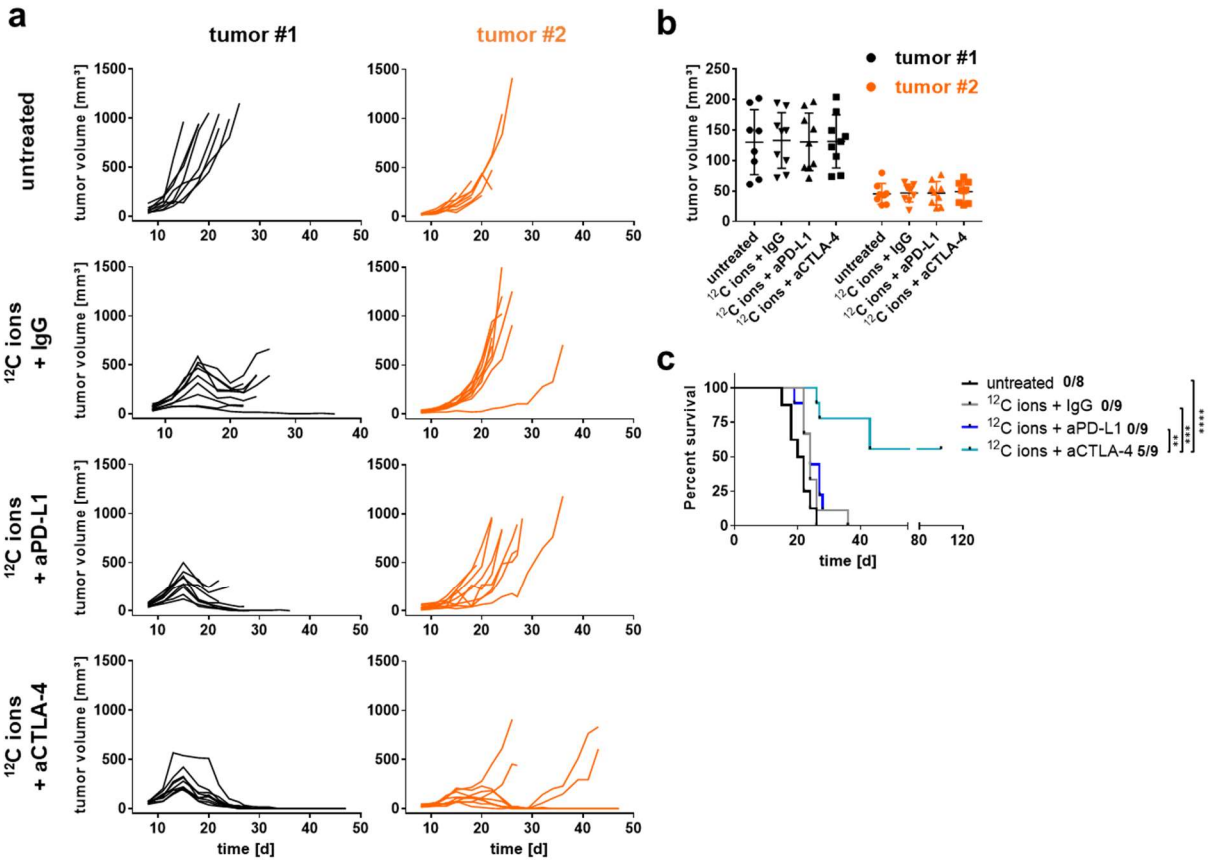


**Figure 3.19: Carbon ion RT plus immune checkpoint blockade against PD-L1 or CTLA-4**. **(a)** Individual growth curves of tumor #1 and tumor #2 of untreated mice or mice treated with carbon ion RT, carbon ion RT plus anti-PD-L1 antibodies, or carbon ion RT plus anti-CTLA-4 antibodies. **(b)** One day before treatment start, mice were randomized into four groups based on the volume of tumor #1 and tumor #2 (n=8-9). **(c)** Kaplan-Meier survival analysis. In addition, complete response rates for each group are shown. Significance was determined using a log-rank (Mantel-Cox) test with Holm-Bonferroni correction.

### 3.6.9 Carbon ion vs. photon RT in combination with anti-CTLA-4 therapy

Finally, as there are always slight inter-experimental variations of tumor growth, a side-by-side comparison of RT with 5 Gy photons and 3.08 Gy carbon ions with or without aCTLA-4 blockade was performed. In this experiment, the mean volume of tumor #1 and tumor #2 accounted for approximately 175 mm³ and 45 mm³, respectively (Figure 3.20b). Notably, the variance in tumor size among the untreated group was very high in this experiment, as consistent randomization was prioritized for the treatment groups. Nevertheless, even small tumors progressed quickly in the untreated group (Figure 3.20a).

Regarding RT alone, photon RT appeared slightly more effective in tumor growth control of tumor #1 compared to carbon ion RT. Thus, the response of tumors #1 to photon irradiation was quicker and more persistent compared to carbon ion-irradiated tumors, for which big tumors continued to grow out rapidly and only showed transient tumor regression. Yet, no potential differences in survival could be monitored as mice had to be sacrificed due to the outgrowth of tumor #2 (Figure 3.20c and d). Remarkably, when additionally applying aCTLA-4

antibodies to photon and carbon ion RT, respectively, there was no difference observed for the outgrowth of tumor #1. As before, in both groups, tumor growth was controlled efficiently leading to complete regression of the majority of tumors #1, while 45% and 67% of tumors #2 regressed after combination therapy with photon and carbon ion RT, respectively. Regarding the Kaplan-Meier survival analysis, previous results were reproduced. Thus, monotherapy with photon or carbon ion RT significantly prolonged the survival of mice compared to untreated mice. Durable responses lasting over 80 days after treatment start were observed for both groups with combination therapies resulting in a significant survival benefit compared to untreated mice and mice treated with RT alone. Indeed, percentage of surviving animals was slightly better after immune checkpoint blockade with carbon ion RT compared to photon RT (67% vs. 45%, respectively), but overall, there was no significant difference in survival between these two groups.

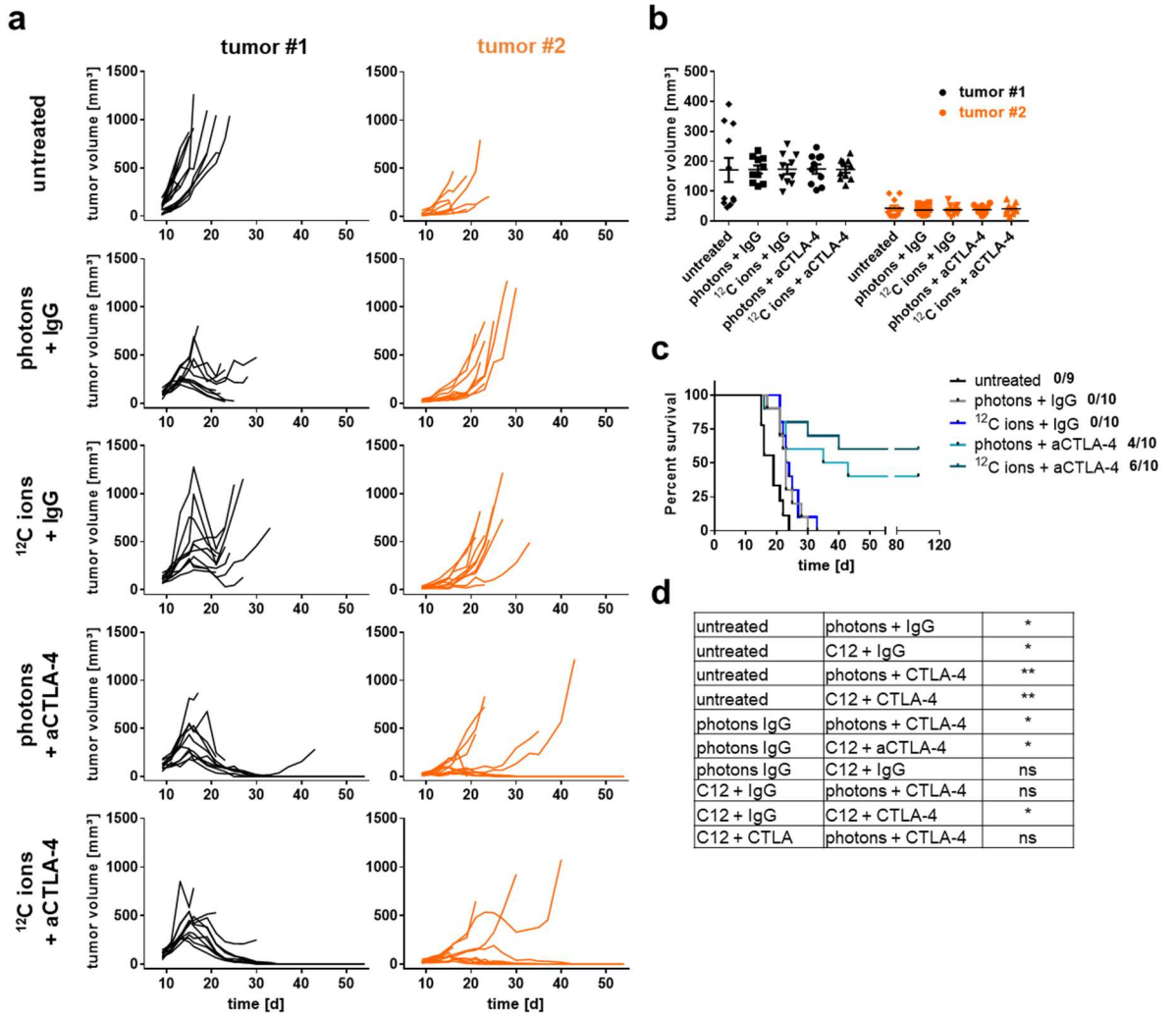


| | | |
|---|---|---|
| untreated | photons + IgG | * |
| untreated | C12 + IgG | * |
| untreated | photons + CTLA-4 | ** |
| untreated | C12 + CTLA-4 | ** |
| photons IgG | photons + CTLA-4 | * |
| photons IgG | C12 + aCTLA-4 | * |
| photons IgG | C12 + IgG | ns |
| C12 + IgG | photons + CTLA-4 | ns |
| C12 + IgG | C12 + CTLA-4 | * |
| C12 + CTLA | photons + CTLA-4 | ns |

**Figure 3.20: Carbon ion vs. photon RT in combination with immune checkpoint blockade against CTLA-4.** **(a)** Individual growth curves of tumor #1 and tumor #2 of untreated mice or mice treated with photon RT, carbon ion RT, photon RT plus anti-CTLA-4 antibodies, or carbon ion RT plus anti-CTLA-4 antibodies. **(b)** One day before treatment start, mice were randomized into five groups based on the volume of tumor #1 and tumor #2 (n=8-9). **(c)** Kaplan-Meier survival analysis. In addition, complete response rates for each group are shown. **(d)** Comparison of groups depicted in the Kaplan-Meier survival analysis. Significance was determined using a log-rank (Mantel-Cox) test with Holm-Bonferroni correction.

## 3.7 Immune cell infiltration in tumors treated with photon vs. carbon ion RT plus anti-CTLA-4 checkpoint blockade

### 3.7.1 Immune cell infiltration in untreated EO771 tumors

After having investigated the effects of combined RT plus immune checkpoint blockade on tumor growth and survival of mice, tumor-infiltrating immune cell populations possibly involved in tumor regression were to be characterized. For this purpose, three antibody panels for flow cytometry were designed: (1) A T cell panel identifying $CD4^+$ and $CD8^+$ T cells, as well as $CD4^+CD25^+CD127^-Foxp3^+$ Tregs. Moreover, the phenotype regarding effector/memory function was assessed by CD44 and CD62L staining. (2) A panel analyzing inhibitory immune checkpoint molecules and co-stimulatory molecules expressed on $CD4^+$ and $CD8^+$ T cells including the immune checkpoint molecules PD-1, CTLA-4, CD73, LAG-3 as well as the co-stimulatory molecules 4-1BB, CD69, and OX-40. (3) A myeloid immune cell panel characterizing M1-like and M2-like macrophages and MDSCs.
Before applying these panels on murine tumors treated with radioimmunotherapy, the flow cytometry staining was tested on untreated tumors to gain insights into the baseline immune cell infiltration. Moreover, as in later experiments the amount of tumor samples was too large to be acquired directly after harvesting of the tumors, fixation of samples was necessary. To assure that fixation does not change the staining, unfixed and fixed samples were compared in this experiment. Thus, cells from the same sample were split in two parts and either acquired directly after staining (unfixed) or fixed and permeabilized, and acquired the next day.
When digested tumor samples were stained with the T cell panel, fixation did not change the percentage of any of the surface markers (Figure 3.21a). Within the whole tumor mass, around 15% of cells were $CD45^+$ leukocytes from which approximately 40% were viable cells. Consequently, the whole tumor was infiltrated by around 6% viable $CD45^+$ leukocytes. Among these, both $CD4^+$ and $CD8^+$ T cells accounted for approximately 8-10%, so that total frequencies of T cells represented 15-20% among $CD45^+$ leukocytes in EO771 tumors. Moreover, all T cells were $CD44^+CD62L^-$ pointing towards a T effector and/or T effector memory phenotype. To identify Tregs an intracellular staining of Foxp3 was performed, for which two different protocols were tested. Thus, after surface staining cells were either kept in fixation solution overnight or fixed for 30 min and kept in permeabilization washing buffer (perm wash) overnight. In either case, the intracellular Foxp3 staining was done on the next day before acquisition. Here, the group in which the fixation solution was incubated overnight showed reduced percentages of $Foxp3^+$ cells and a higher variance of the tumor samples in the group. Consequently, the protocol in which cells were kept in perm wash was used for further experiments.
Stainings for immune checkpoint and co-stimulatory molecules resulted in no major differences between unfixed and fixed samples (Figure 3.21b). At baseline, high percentages of $CD8^+$ and moderate proportions of $CD4^+$ T cells expressing the immune checkpoint molecules PD-1 and LAG-3 infiltrated the tumor. CD73 expression was predominantly found in the $CD4^+$ T cell compartment. Surprisingly, CTLA-4-expressing cells were neither detected in $CD4^+$ nor in $CD8^+$ T cells, although CTLA-4 expression would be expected on Tregs [281]. As CTLA-4 is not only expressed on the surface, but also in intracellular vesicles a combined extra- and intracellular staining was performed in the next experiments, in which CTLA-4 positive cells could be detected (e.g. section 3.7.3 and 3.7.4). More than half of the $CD4^+$ and $CD8^+$ T cells expressed the co-stimulatory molecule 4-1BB, while CD69 and OX-40 were only expressed in moderate to low proportions.

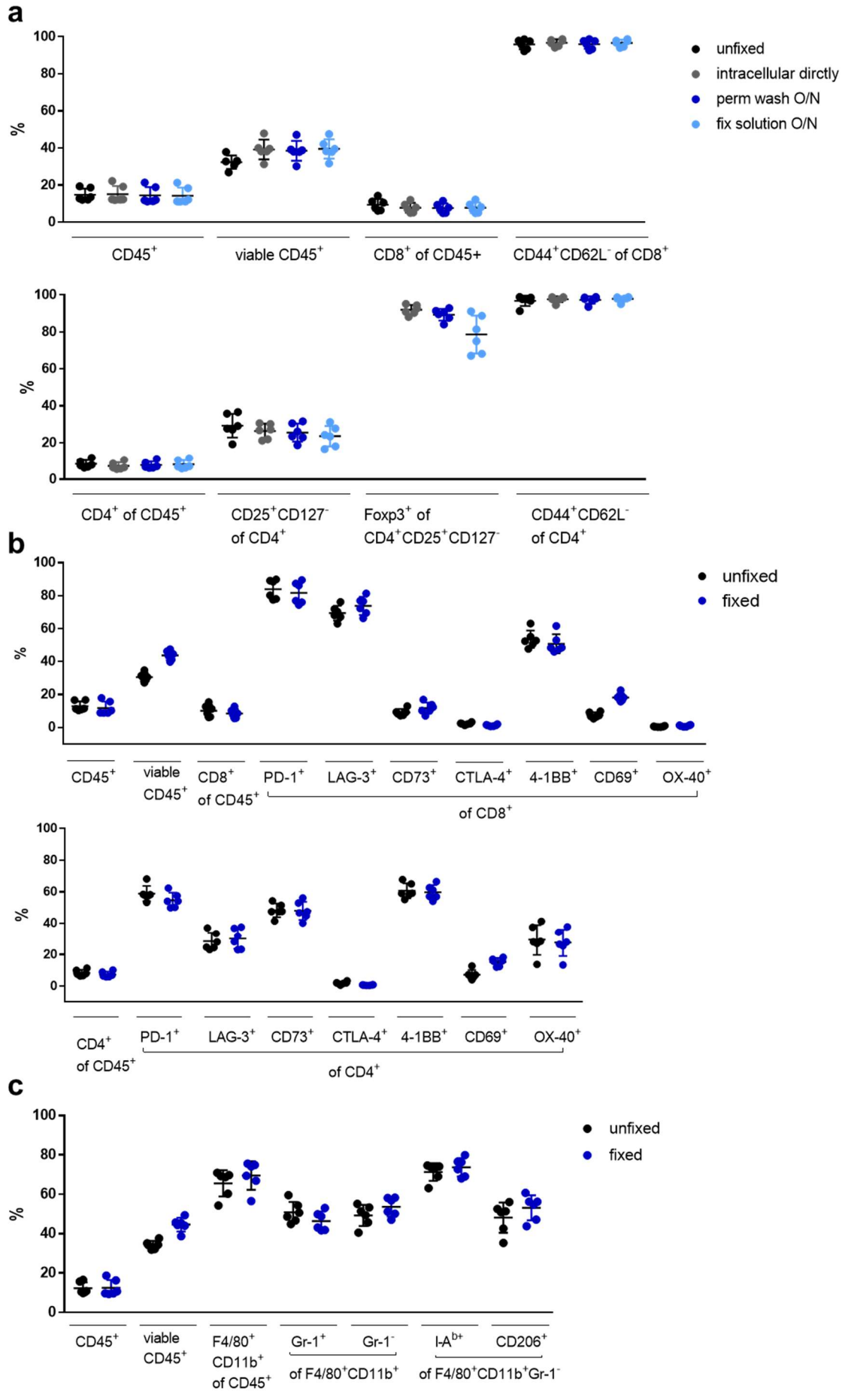
a
%
unfixed
intracellular dirctly
perm wash O/N
fix solution O/N
CD45+
viable CD45+
CD8+ of CD45+
CD44+CD62L- of CD8+
CD4+ of CD45+
CD25+CD127- of CD4+
Foxp3+ of CD4+CD25+CD127-
CD44+CD62L- of CD4+
b
unfixed
fixed
CD45+
viable CD45+
CD8+ of CD45+
PD-1+
LAG-3+
CD73+
CTLA-4+
4-1BB+
CD69+
OX-40+
of CD8+
CD4+ of CD45+
of CD4+
c
F4/80+ CD11b+ of CD45+
Gr-1+
Gr-1-
of F4/80+CD11b+
I-Ab+
CD206+
of F4/80+CD11b+Gr-1-

**Figure 3.21: Effects of fixation on flow cytometry staining in untreated murine tumors.** Flow cytometry stainings directly acquired (unfixed) were compared to fixed/permeabilized stainings of the same sample for three panels characterizing: **(a)** T cells, **(b)** inhibitory immune checkpoint and co-stimulatory molecules expressed on T cells, and **(c)** myeloid cells. For the intracellular staining of Foxp3 in the T cell panel, two staining protocols were further compared, keeping the cells in perm wash buffer or fixation solution overnight (O/N).

Finally, fixation did not affect the staining of the macrophage panel, which showed similar percentages of viable $CD45^+$ leukocytes as the two other panels (Figure 3.21c). EO771 tumors were infiltrated by a high percentage of $CD11b^+F4/80^+$ myeloid cells with around 70%. From these, around half of the cells were MDSCs ($CD11b^+F4/80^+Gr\text{-}1^+$), while the other half represented macrophages ($CD11b^+F4/80^+Gr\text{-}1^-$). Regarding the polarization of macrophages, 75% of cells expressed the M1-like marker MHC class II ($I\text{-}A^b$) and 50% expressed the M2-like marker CD206. For further experiments, antibodies for staining NK1.1 and CD11c were added to the macrophage panel in order to identify NK cells and DCs, respectively.

### 3.7.2 T cell infiltration in tumor #1

Next, immune cell infiltration was investigated after treatment of tumors with photon or carbon ion RT plus aCTLA-4 checkpoint blockade, as aCTLA-4 therapy showed superior therapeutic effects compared to aPD-L1 checkpoint blockade. Murine tumors were treated in the same manner as for survival experiments, either receiving three fractions of 5 Gy photons or 3.08 Gy carbon ions (Figure 3.15a). However, mice only received two injections of aCTLA-4 antibodies as tumors were harvested for analysis on day 5 or day 6 after treatment start for photon and carbon ion RT, respectively. In total, four different groups were compared: (1) untreated mice, (2) mice treated with aCTLA-4 monotherapy, (3) mice treated with RT plus IgG control, and (4) mice treated with combined RT plus aCTLA-4 antibody. At first, immune cell infiltration in the irradiated tumor site (tumor #1) will be described starting with the investigation of T cell infiltration and subtypes. Dot plots of flow cytometry stainings and the gating strategy are exemplified in Supplementary Figure 5.9.

Both photon and carbon ion RT with or without aCTLA-4 antibodies significantly enhanced $CD45^+$ leukocyte frequencies in tumor #1 (Figure 3.22a and b). While photon RT increased the proportions from approximately 60% in untreated to 80% in irradiated tumors, carbon ion RT induced an increase from 40% to 80% (untreated vs. irradiated). In addition, in the carbon ion experiment, $CD45^+$ leukocyte frequencies were significantly higher in the aCTLA-4 group over the untreated group. However, the baseline infiltration of $CD45^+$ leukocytes in untreated tumors was lower in the carbon ion experiment compared to the photon experiment.

Among $CD45^+$ leukocytes, monotherapy with photon RT significantly increased the proportions of $CD4^+$ T cells compared to both groups treated with anti-CTLA-4 antibodies. This result came along with a significantly increased infiltration by $CD25^+CD127^-Foxp3^+$ Tregs after photon RT, both among $CD4^+$ T cells and $CD45^+$ leukocytes. Simultaneously, the administration of aCTLA-4 antibodies as mono- or combination therapy significantly decreased the proportions of Tregs within $CD4^+$ T cells. Thus, while after photon RT around 40% of $CD4^+$ T cells were Tregs, only 15-20% were Tregs after aCTLA-4 antibody administration.

After carbon ion RT, results were comparable with some minor differences. Thus, proportions of $CD4^+$ T cells among $CD45^+$ leukocytes were highest in untreated tumors and significantly decreased when tumors were treated by carbon ion RT. Considering the proportions of Tregs among $CD4^+$ T cells, numbers were significantly increased after carbon ion RT + IgG control. However, when regarding the percentage of Tregs within $CD45^+$ leukocytes, numbers were comparable between the untreated and carbon ion RT + IgG group. The differences between proportions in Tregs among $CD4^+$ T cells and $CD45^+$ leukocytes were *vice versa* compared to

the photon experiments. Still, one has to consider that the proportions of Tregs in untreated mice varied between both experiments. With certainty, aCTLA-4 treatment also decreased the numbers of Tregs after carbon ion RT. When considering the frequencies of Tregs among $CD45^+$ leukocytes, it seemed that the proportions of Tregs were less elevated after carbon ion compared to photon irradiation. Finally, almost 100% of $CD4^+$ T cells expressed CD44 but not CD62L in any of the treatment groups pointing towards a T effector and/or T effector memory phenotype.

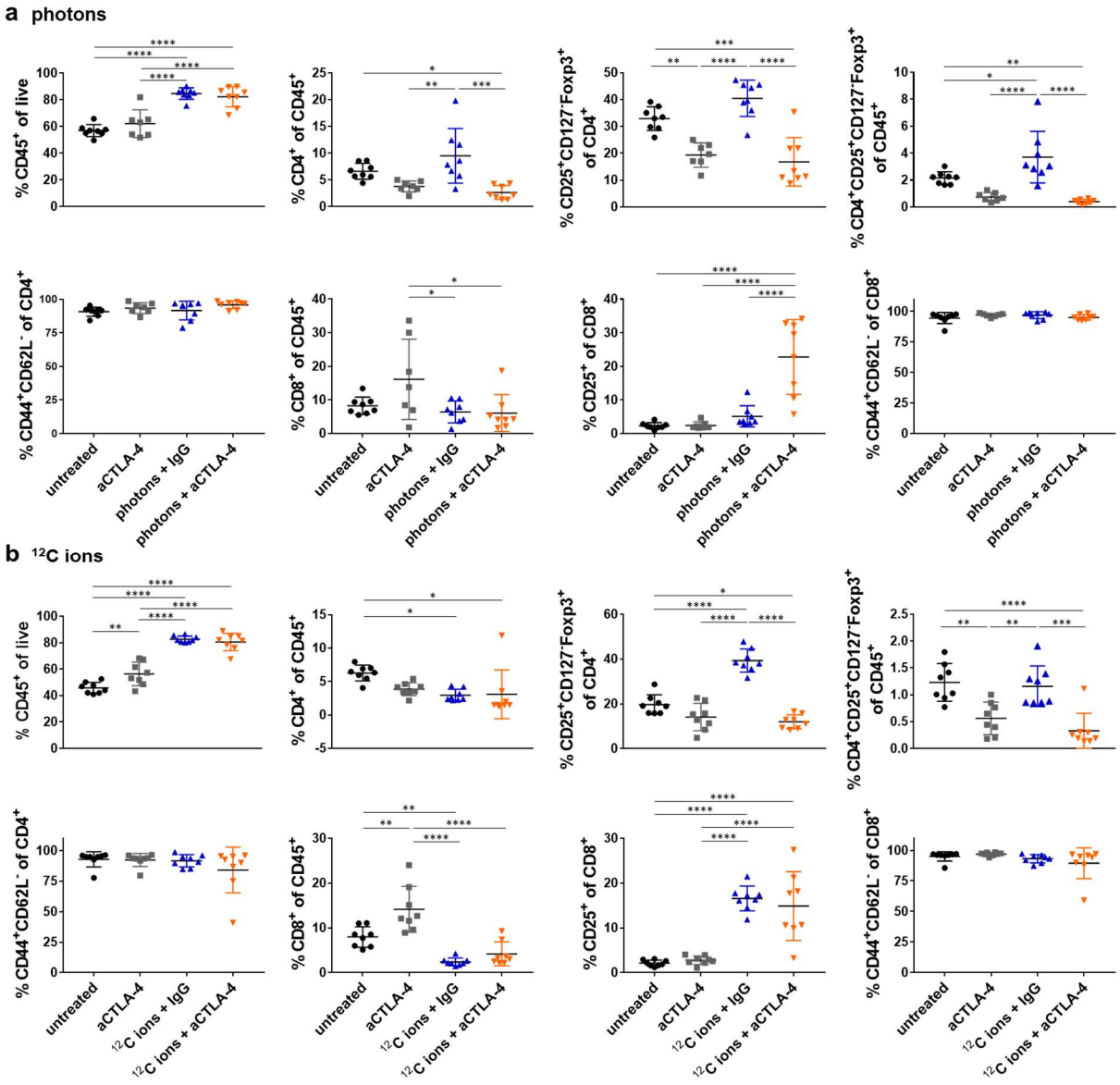


**Figure 3.22: T cell infiltration in tumor #1 after treatment of EO771 tumors with RT plus anti-CTLA-4 antibodies.** Mice were left untreated or were treated with anti-CTLA-4 antibodies, RT plus IgG control, or RT plus anti-CTLA-4 antibodies. RT was either performed with photons **(a)** or carbon ions **(b)**. Five days (photons) or six days (carbon ions) after treatment start, T cell infiltration was investigated by flow cytometry. Thus, infiltration of tumors by leukocytes was determined by $CD45^+$ staining. From these, $CD4^+$ T cells and their proportions of Tregs ($CD25^+CD127^-Foxp3^+$) were identified. The effector phenotype was determined by CD44/CD62L staining. Moreover, the proportion of $CD8^+$ T cells, their activation status ($CD25^+$) and their effector phenotype (CD44/CD62L) were assessed. Significance was determined by one-way ANOVA with post-hoc Turkey's test.

Beside $CD4^+$ T cells, $CD8^+$ T cells were analyzed. Overall, RT with both photons and carbon ions significantly decreased the amount of $CD8^+$ T cells within $CD45^+$ leukocytes. This effect was more pronounced after carbon ion irradiation. Moreover, aCTLA-4 monotherapy significantly increased the proportions of $CD8^+$ T cells in the carbon ion experiment and also in the photon experiment this tendency was observed. Interestingly, administration of aCTLA-4 antibodies together with RT did still not recover the depletion of $CD8^+$ T cells by irradiation. Both after combination therapy with photon and carbon ion RT plus aCTLA-4 antibodies, proportions of activated $CD8^+$ T cells were increased as highlighted by their CD25 expression. Furthermore, after carbon ion RT alone, there was a significant increase of $CD8^+$ T cell numbers expressing $CD25^+$ compared to the untreated and the aCTLA-4 group. As for $CD4^+$ T cells, regardless of the therapy and radiation type, almost all $CD8^+$ T cells were $CD44^+CD62L^-$ pointing towards an effector/effector memory phenotype.
Regarding photon RT, the experiment was repeated once yielding very comparable results (Supplementary Figure 5.10). Notably, this experiment did not include an untreated group and like after carbon ion RT, analysis was performed on day six after treatment start.

### 3.7.3 Functional phenotype of $CD4^+$ T cells within tumor #1

Not only the amount of immune cells within the tumor matters, but also the functional phenotype is of importance to identify potential antitumor functions. Consequently, T cells were stained for a number of inhibitory immune checkpoint molecules (PD-1, LAG-3, CTLA-4, and CD73) as well as activating co-stimulatory molecules (4-1BB, OX-40 and CD69) [51, 282]. However, as no OX-40 expression on T cells was detected in any of the groups, OX-40 will not be presented in the following. Both the percentage of T cells expressing these markers and the level of expression as identified by the median fluorescence intensity (MFI) of the positive population were analyzed. The gating strategy is exemplified in Supplementary Figure 5.11. In the following paragraph, the functional phenotype of $CD4^+$ T cells within tumor #1 will be described.
Overall, the expression profiles of immune checkpoint molecules were comparable after photon and carbon ion RT (Figure 3.23a and b). Thus, the percentage of $CD4^+$ T cells expressing PD-1 was elevated after aCTLA-4 monotherapy, but was significantly decreased when combining aCTLA-4 therapy with RT. Simultaneously, among $CD4^+PD\text{-}1^+$ T cells the level of expression was highest after aCTLA-4 monotherapy, in particular in the photon experiment. In addition, the amount of $CD4^+LAG\text{-}3^+$ T cells was significantly decreased after combination therapy. Interestingly, the level of LAG-3 expression varied between the two experiments. While in the photon experiment, LAG-3 expression was significantly higher in untreated tumors compared to treated tumors, in the carbon ion experiment expression levels were highest in the carbon ion RT + aCTLA-4 group. Yet, in the latter, there was only a significant difference to the aCTLA-4 group observed, whereas differences to the untreated and the carbon ion RT + IgG group were only marginal.
Considering CTLA-4 expression, in both experiments, the administration of aCTLA-4 antibodies with or without RT significantly reduced the amount of $CD4^+$ T cells expressing CTLA-4. At the same time, there was a significant increase in the amount of $CD4^+CTLA\text{-}4^+$ T cells after RT alone, which came along with significantly increased levels of expression. Overall, the pattern of CTLA-4 expression resembled the infiltration pattern by Tregs (Figure 3.22) being in accordance with the fact that CTLA-4 is constitutively expressed on Tregs [281]. Finally, the percentage of $CD73^+$ cells among $CD4^+$ T cells was significantly reduced in the aCTLA-4 group for both experiments. By contrast, when combining aCTLA-4 therapy with RT, proportions were similar (carbon ion RT) or even significantly higher (photon

RT) compared to untreated tumors. However, among CD4⁺CD73⁺ T cells the expression levels of CD73 were significantly lower in any of the treatment groups compared to untreated tumors. Notably, in the second experiment performed with photon irradiation, the proportions and expression level of CD4⁺ T cells expressing CD73 were significantly decreased in the photon RT + aCTLA-4 group being at a similar level as in the aCTLA-4 group (Supplementary Figure 5.12).

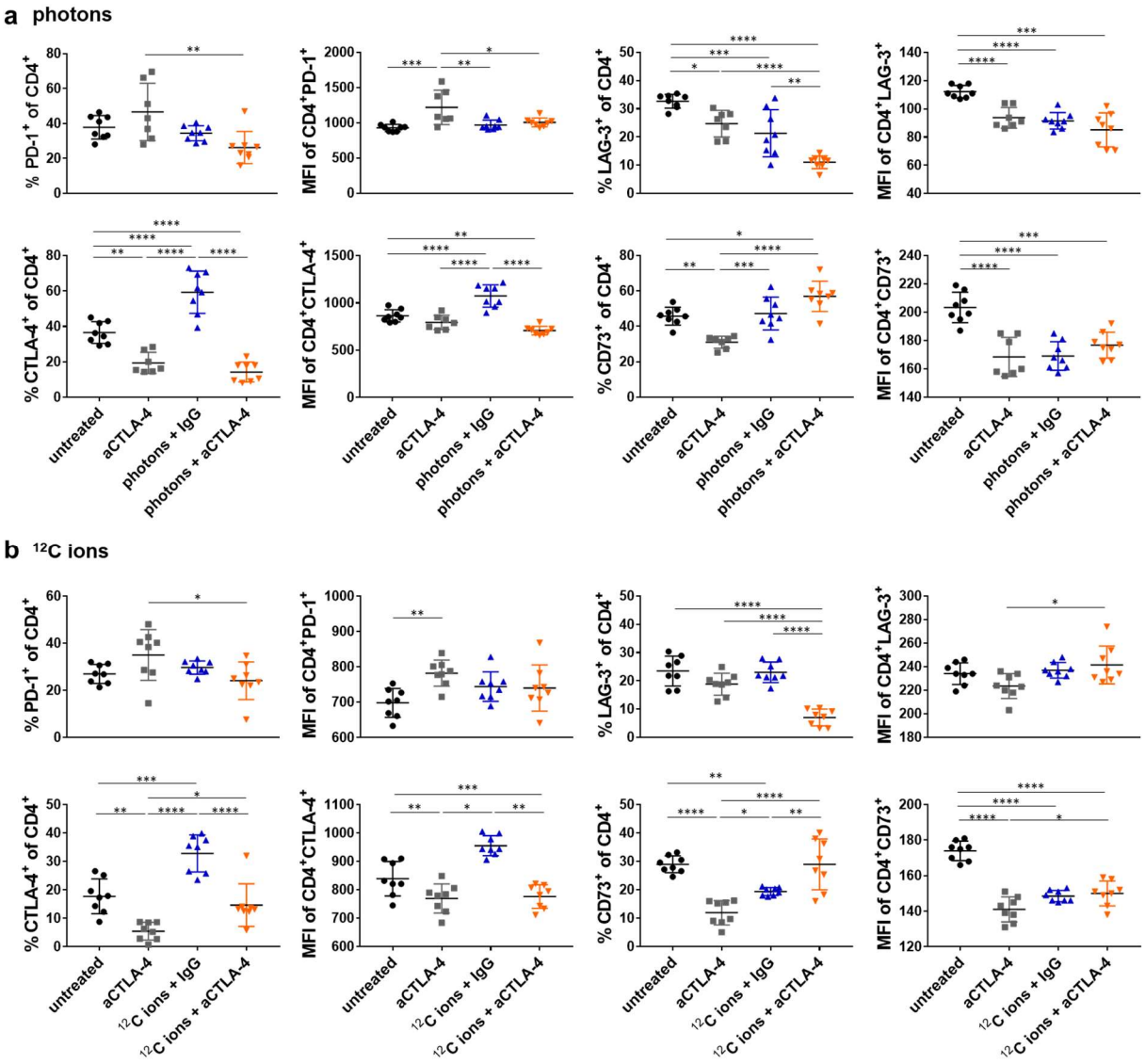


**Figure 3.23: Immune checkpoint molecules expressed on CD4⁺ T cells in tumor #1 after treatment of EO771 tumors with RT plus anti-CTLA-4 antibodies.** Mice were left untreated or treated with anti-CTLA-4 antibodies, RT plus IgG control, or RT plus anti-CTLA-4 antibodies. RT was either performed with photons **(a)** or carbon ions **(b)**. Five days (photons) or six days (carbon ions) after treatment start, expression of the immune checkpoint molecules PD-1, LAG-3, CTLA-4, and CD73 on CD4⁺ T cells was investigated by flow cytometry. Both the proportion (%) and the level of surface expression defined by the median fluorescence intensity (MFI) were assessed. Significance was determined by one-way ANOVA with post-hoc Turkey's test.

Next, expression of 4-1BB and CD69 was analyzed as an indicator for T cell activation. In both the photon and carbon ion experiment, the proportion of CD4⁺ T cells expressing 4-1BB was significantly decreased upon administration of aCTLA-4 antibodies with or without RT (Figure 3.24a and b). Interestingly, while expression levels were significantly reduced after

photon RT + IgG and photon RT + aCTLA-4 compared to untreated tumors, 4-1BB expression was significantly upregulated after carbon ion RT. Finally, the number of CD4$^+$ T cells expressing CD69 was generally low, ranging from 1% to 10%, but still differences between groups could be observed. In the photon experiment, the proportion of CD69$^+$ expressing cells was increased when aCTLA-4 antibodies were administered, whereas in the carbon ion experiment, irradiation induced slightly upregulated amounts of CD4$^+$ T cells expressing CD69. Considering the level of CD69 expression, no differences were observed. In the repetition experiment performed with photon irradiation, results were comparable (Supplementary Figure 5.13).

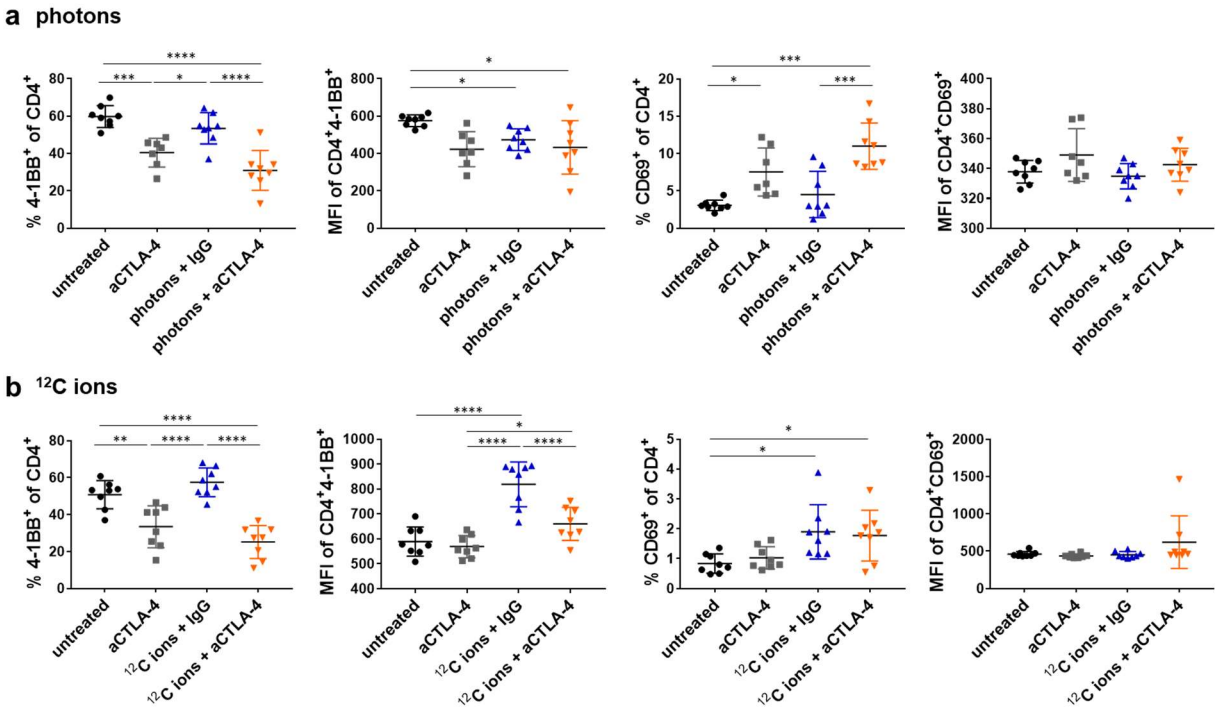


**Figure 3.24: Co-stimulatory molecules expressed on CD4$^+$ T cells in tumor #1 after treatment of EO771 tumors with RT plus anti-CTLA-4 antibodies**. Mice were left untreated or were treated with anti-CTLA-4 antibodies, RT plus IgG control, or RT plus anti-CTLA-4 antibodies. RT was either performed with photons **(a)** or carbon ions **(b).** Five days (photons) or six days (carbon ions) after treatment start, expression of the co-stimulatory molecules 4-1BB and CD69 on CD4$^+$ T cells were investigated by flow cytometry. Both the proportion (%) and the level of expression defined by the median fluorescence intensity (MFI) were assessed. Significance was determined by one-way ANOVA with post-hoc Turkey's test.

### 3.7.4 Functional phenotype of CD8$^+$ T cells within tumor #1

In addition, immune checkpoint and co-stimulatory molecules were analyzed on CD8$^+$ T cells. In both experiments, aCTLA-4 monotherapy did not affect the amount of CD8$^+$ PD-1$^+$ T cells, whereas RT plus IgG control and RT plus aCTLA-4 treatment significantly decreased the percentage of PD-1$^+$ cells among CD8$^+$ T cells from around 80% in untreated to roughly 40-50% in irradiated tumors (Figure 3.25a and b). These results differ from the observation made in CD4$^+$ T cells, where only the combination therapy, but not RT alone reduced the amount of PD-1$^+$ cells. While the level of expression was in addition lowest in the photon RT + aCTLA-4 group, PD-1 expression in the carbon ion RT + aCTLA-4 group was comparable to untreated tumors and only slightly reduced in the aCTLA-4 group. Similar to PD-1 expression, the proportion of CD8$^+$LAG-3$^+$ T cells was significantly reduced by RT with or

without aCTLA-4 therapy. This effect was observed after both photon and carbon ion RT, but the magnitude of reduction varied. In the photon experiment, around 35% of $CD8^+$ T cells in untreated tumors expressed LAG-3, which was reduced to 5-10% following RT. Moreover, proportion of $CD8^+LAG\text{-}3^+$ cells were significantly decreased in the aCTLA-4 group compared to the untreated group. In contrast, in the carbon ion experiment, percentages of $LAG\text{-}3^+$ cells among $CD8^+$ T cells were similar in the aCTLA-4 and untreated group with 27-30% and RT decreased the numbers to approximately 20%. As for $CD4^+$ T cells, the level of expression differed between the photon and the carbon ion experiment. While there was a slight but insignificant reduction of LAG-3 expression after photon RT, carbon ion RT significantly increased the surface levels of LAG-3 compared to the unirradiated groups.

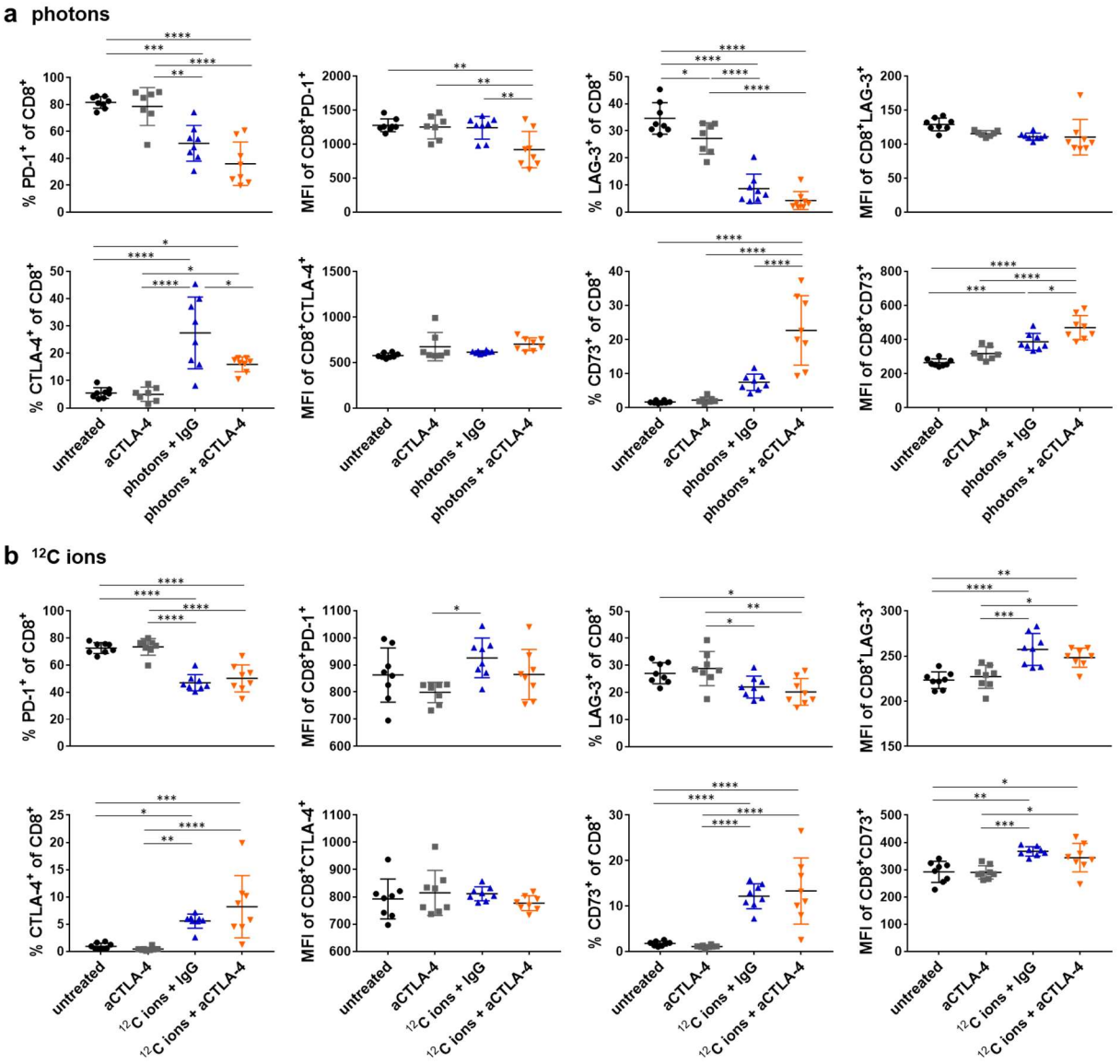


**Figure 3.25: Immune checkpoint molecules expressed on $CD8^+$ T cells in tumor #1 after treatment of EO771 tumors with RT plus anti-CTLA-4 antibodies.** Mice were left untreated or treated with anti-CTLA-4 antibodies, RT plus IgG control, or RT plus anti-CTLA-4 antibodies. RT was either performed with photons **(a)** or carbon ions **(b)**. Five days (photons) or six days (carbon ions) after treatment start, expression of the immune checkpoint molecules PD-1, LAG-3, CTLA-4, and CD73 on $CD8^+$ T cells was investigated by flow cytometry. Both the proportion (%) and the level of expression defined by the median fluorescence intensity (MFI) were assessed. Significance was determined by one-way ANOVA with post-hoc Turkey's test.

In both the untreated and aCTLA-4 group, CTLA-4 and CD73 were hardly expressed in $CD8^+$ T cells. After RT with photons or carbon ions plus/minus aCTLA-4 therapy, the number of $CD8^+$ T cells expressing CTLA-4 and CD73 significantly increased. However, after monotherapy with photons, the increased proportion of $CD8^+CD73^+$ T cells was only a tendency. When the experiment was repeated, proportions of $CD8^+CD73^+$ after photon RT alone were significantly increased compared to aCTLA-4 monotherapy, while still significantly lower compared to the photon RT + aCTLA-4 group (Supplementary Figure 5.12). CTLA-4 expression levels did not differ in any of the groups. Regarding CD73, increased proportions of CD73-expressing cells came along with an increased expression of CD73 after carbon ion irradiation. After photon RT, CD73 expression levels were highest in the photon RT + aCTLA-4 group followed by the photon RT + IgG and aCTLA-4 group.

Finally, after having observed that $CD8^+$ T cells expressed the activation marker CD25 after combination therapy, $CD8^+$ T cells were analyzed for the expression of 4-1BB and CD69. Interestingly, both radiation types decreased the amount of $CD8^+$ T cells expressing 4-1BB regardless of CTLA-4 therapy, which also did not induce an effect on 4-1BB as monotherapy (Figure 3.26a and b). This is in contrast to $CD4^+$ T cells, where aCTLA-4 therapy, but not RT alone decreased the proportions of 4-1BB-expressing cells (Figure 3.24). However as observed after carbon ion RT in $CD4^+$ T cells, the expression levels of 4-1BB were significantly increased after photon and carbon ion RT plus aCTLA-4 checkpoint blockade as wells as after carbon ion monotherapy in the $CD8^+$ T cell compartment. Similarly, increasing proportions of $CD8^+$ T cells expressed CD69 after combination therapy and carbon ion monotherapy, but not photon monotherapy. Furthermore, CD69 expression levels were upregulated after photon RT, which was not observed after carbon ion RT.

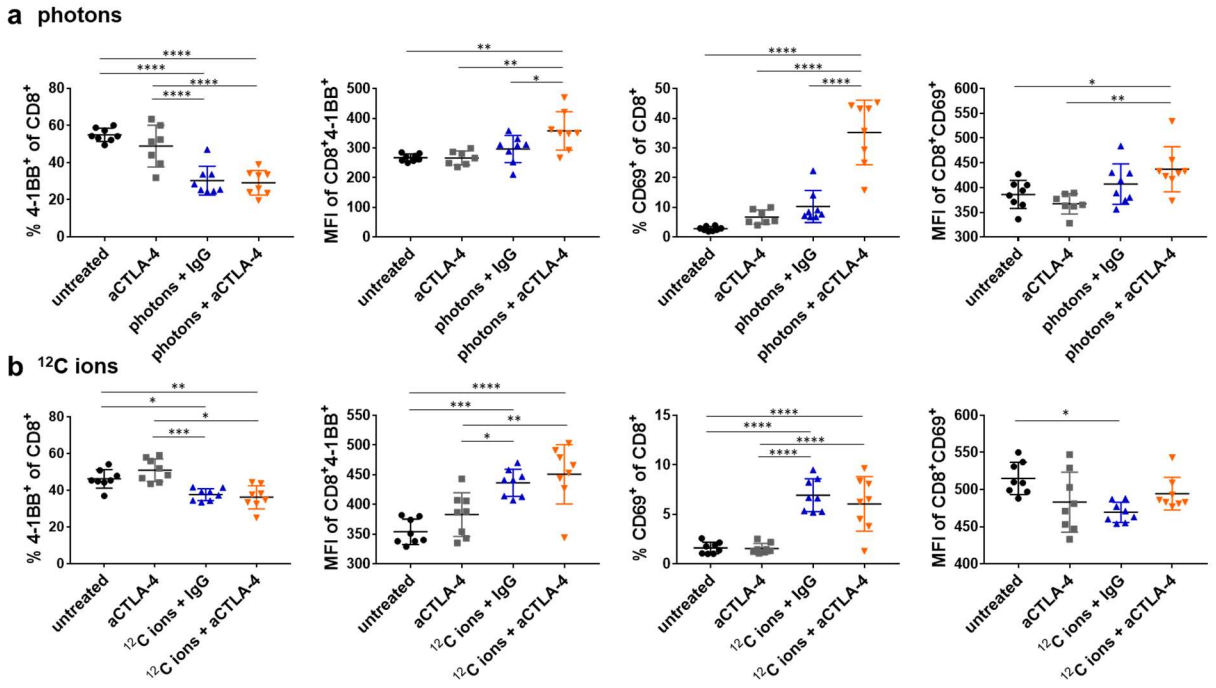


**Figure 3.26: Co-stimulatory molecules expressed on $CD8^+$ T cells in tumor #1 after treatment of EO771 tumors with RT plus anti-CTLA-4 antibodies**. Mice were left untreated or treated with anti-CTLA-4 antibodies, RT plus IgG control, or RT plus anti-CTLA-4 antibodies. RT was either performed with photons **(a)** or carbon ions **(b)**. Five days (photons) or six days (carbon ions) after treatment start, expression of the co-stimulatory molecules 4-1BB and CD69 on $CD8^+$ T cells were investigated by flow cytometry. Both the proportion (%) and the level of expression defined by the median fluorescence intensity (MFI) were assessed. Significance was determined by one-way ANOVA with post-hoc Turkey's test.

Notably, in the repetition experiment with photon irradiation, there was no difference observed in the proportion of $CD8^+4\text{-}1BB^+$ T cells between the aCTLA-4, photon RT + IgG, and photon RT + aCTLA-4 group (Supplementary Figure 5.13).

### 3.7.5 Infiltration of NK cells and DCs in tumor #1

Beside T cells, infiltration of NK cells and DCs in tumor #1 was analyzed after RT. The gating strategy is depicted in Supplementary Figure 5.14. After photon RT, the percentages of $NK1.1^+$ NK cells were elevated among $CD45^+$ leukocytes and also with additional aCTLA-4 therapy, there was a trend towards increasing proportions of NK cells (Figure 3.27a). Likewise, carbon ion RT induced a significant increase of NK cell numbers when applied as monotherapy or combination therapy (Figure 3.27b). Moreover, RT decreased the amounts of DCs among $CD45^+$ leukocytes, which was more significant after photon RT compared to carbon ion RT.

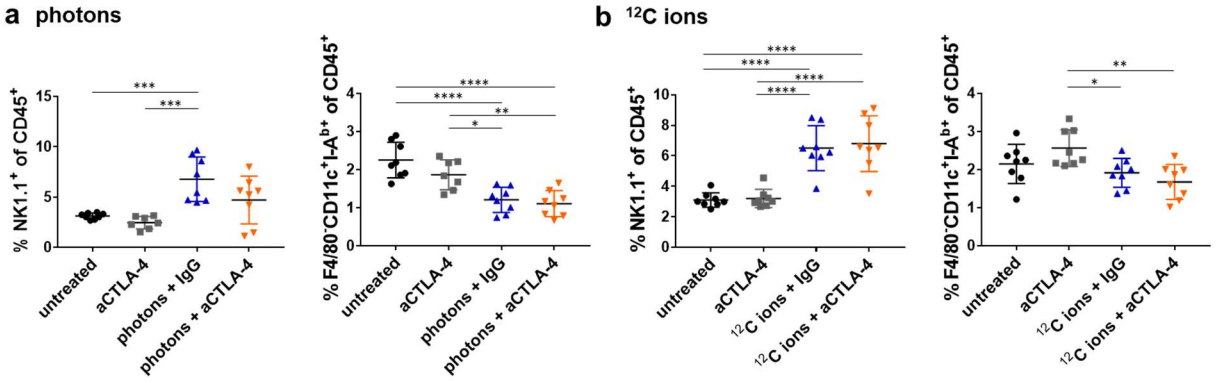


**Figure 3.27: Infiltration by NK cells and DCs in tumor #1 after treatment of EO771 tumors with RT plus anti-CTLA-4 antibodies.** Mice were left untreated or treated with anti-CTLA-4 antibodies, RT plus IgG control, or RT plus anti-CTLA-4 therapies. RT was either performed with photons **(a)** or carbon ions **(b)**. Five days (photons) or six days (carbon ions) after treatment start, immune cell infiltration was investigated by flow cytometry. From $CD45^+$ leukocytes, infiltration by NK cells ($NK1.1^+$) and DCs ($F4/80^-CD11c^+I\text{-}A^{b+}$) was assessed. Significance was determined by one-way ANOVA with post-hoc Turkey's test.

### 3.7.6 Myeloid cell infiltration in tumor #1

Finally, the infiltration of tumor #1 by myeloid cells after treatment with RT plus aCTLA-4 antibodies was analyzed. The gating strategy to distinguish MDSCs and macrophages as well as the polarization of the latter is exemplified in Supplementary Figure 5.14.

In contrast to T cells, NK cells, and DCs, EO771 tumors showed a high infiltration of myeloid cells. Photon RT plus aCTLA-4 blockade induced a significant decrease of $F4/80^+CD11b^+Gr\text{-}1^-$ macrophages as well as an increase in $F4/80^+/CD11b^+Gr\text{-}1^+$ MDSC proportions among $CD45^+$ leukocytes (Figure 3.28a). Interestingly, in the repetition experiment performed with photons the opposite effect was observed (Supplementary Figure 5.15). After carbon ion RT, no significant differences in the infiltration by macrophages and MDSCs between the four groups were found (Figure 3.28b). Concerning the polarization status of macrophages, the baseline of macrophages expressing the M1-like marker $I\text{-}A^b$ in untreated tumor was already quite high with around 60-80% and treatment only slightly varied the proportions. Photon RT plus IgG control significantly increased the proportions of $I\text{-}A^b$-expressing macrophages, while adding carbon ion RT to aCTLA-4 therapy significantly decreased the amount of $I\text{-}A^{b+}$ cells among macrophages. Remarkably, the level of I-Ab expression showed high variations within any of the treatment groups in the photon experiment and consequently no differences were observed. In contrast, after carbon ion RT, with or without aCTLA-4 treatment, $I\text{-}A^b$ expression

was significantly decreased. When regarding the percentage of M1-like macrophages among CD45$^+$ leukocytes, photon RT alone significantly increased their proportions compared to any of the other groups, while no differences were found after carbon ion RT. Effects on the M2-like marker CD206 were more distinct. Thus, both after photon and carbon ion irradiation, CD206 expression among macrophages, among CD45$^+$ leukocytes and the expression level of CD206 were significantly increased compared to unirradiated tumors. aCTLA-4 monotherapy did not have any impact on any of the macrophage populations.

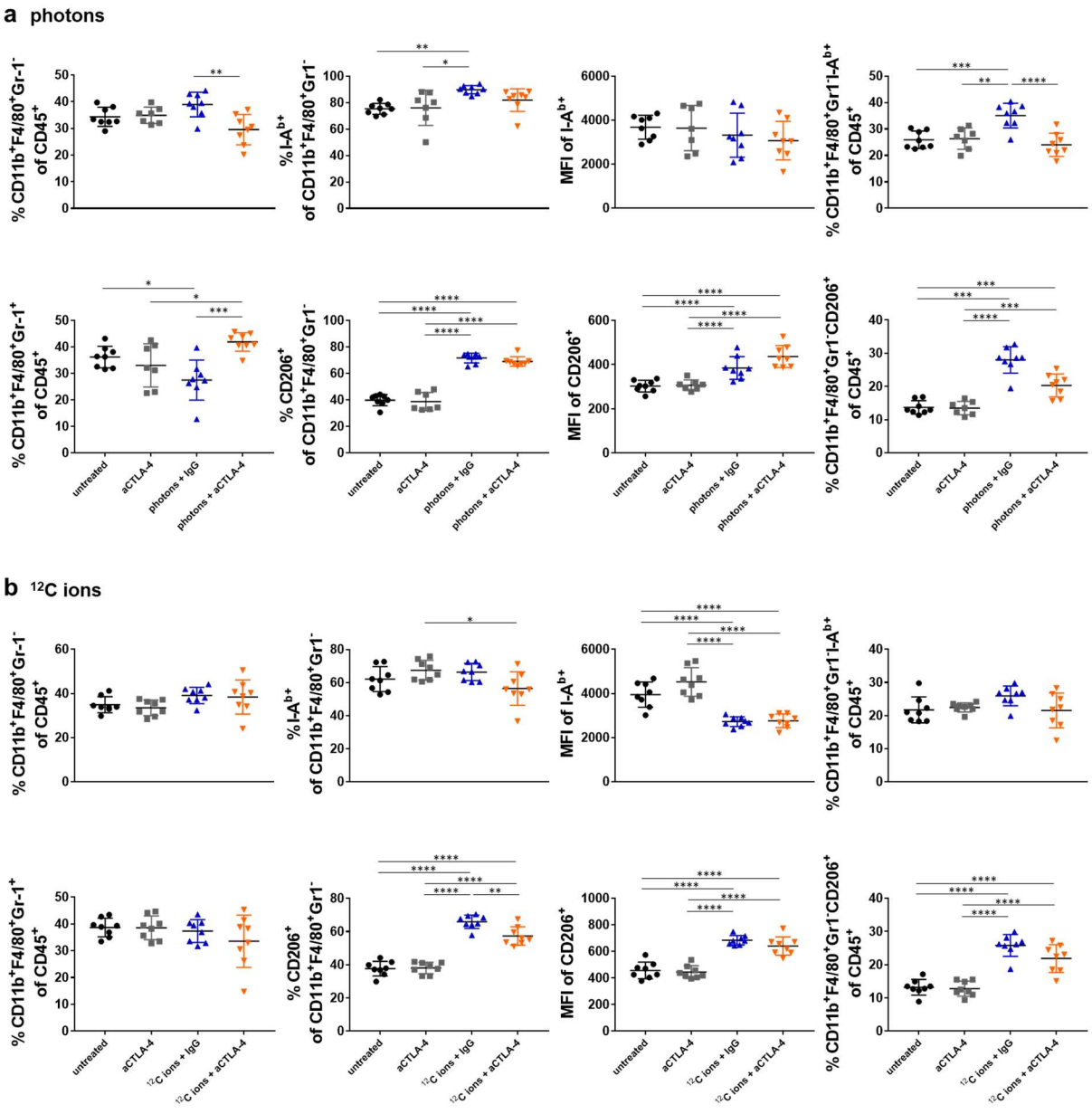


**Figure 3.28: Myeloid cell infiltration in tumor #1 after treatment of EO771 tumors with RT plus anti-CTLA-4 antibodies.** Mice were left untreated or treated with anti-CTLA-4 antibodies, RT plus IgG control, or RT plus anti-CTLA-4 antibodies. RT was either performed with photons **(a)** or carbon ions **(b)**. Five days (photons) or six days (carbon ions) after treatment start, myeloid cell infiltration was investigated by flow cytometry. Proportions of macrophages (F4/80$^+$CD11b$^+$Gr-1$^-$) and MDSCs (F4/80$^+$CD11b$^+$Gr-1$^+$) among CD45$^+$ leukocytes were identified. The polarization status of macrophages was further determined by staining of the M1-like marker I-A$^b$ and the M2-like marker CD206. For both makers the percentages among macrophages, the level of expression defined by the median fluorescence intensity (MFI), and the proportion among total CD45$^+$ leukocytes were assessed. Significance was determined by one-way ANOVA with post-hoc Turkey's test.

### 3.7.7 T cell infiltration in tumor #2

Besides tumor #1, immune cell infiltration in tumor #2, which was located outside the irradiation field, was characterized. When applying the three panels for characterization of (1) T cell subtypes, (2) immune checkpoint and co-stimulatory molecules expressed on T cells, and (3) myeloid cells, fewer differences between the four treatment groups were observed, which came along with high variations of data points within a group. Thus, in the following only cell types and markers that were significantly different between groups will be mainly discussed.
There were no significant differences in the $CD45^+$ leukocyte infiltration between any of the groups observed in the photon experiment (Figure 3.29a). In contrast, in the carbon ion experiment, aCTLA-4 monotherapy significantly increased $CD45^+$ proportions, and also in the carbon ion RT + aCTLA-4 group a tendency towards higher $CD45^+$ frequencies was observed (Figure 3.29b). When comparing the photon and carbon ion experiment, one has to consider that the baseline frequency of $CD45^+$ leukocytes in untreated tumors was higher in the photon compared to the carbon ion experiment (60% vs. 70%).

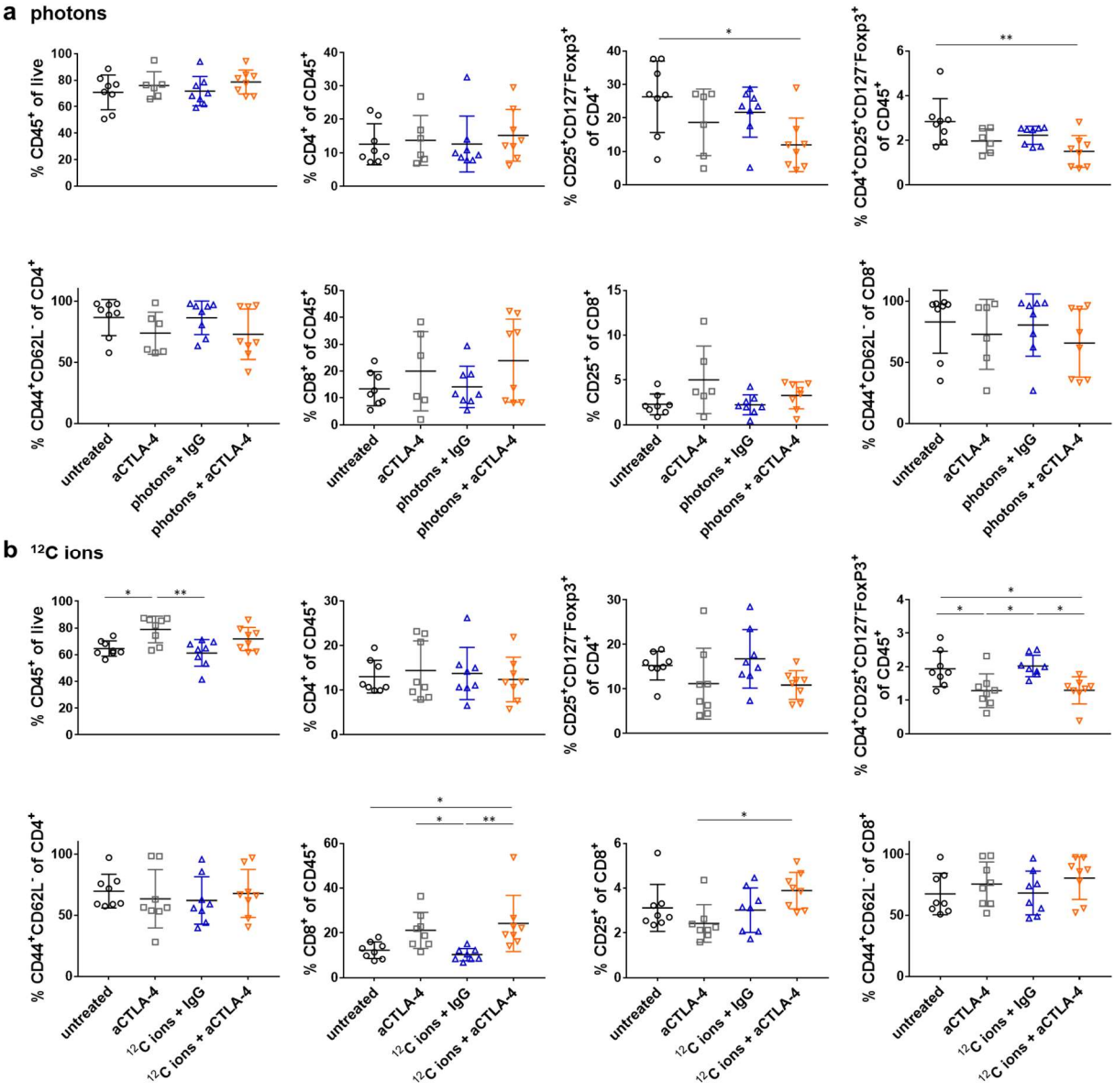

**Figure 3.29: T cell infiltration in tumor #2 after treatment of EO771 tumors with RT plus anti-CTLA-4 antibodies.** Mice left untreated or treated with anti-CTLA-4 antibodies, RT plus IgG control, or RT plus anti-CTLA-4 antibodies. Tumor #1 was irradiated, while tumor #2 was outside the irradiation field. RT was either performed with photons **(a)** or carbon ions **(b)**. Five days (photons) or six days (carbon ions) after treatment start, immune cell infiltration was investigated by flow cytometry. Thus, infiltration of tumors by leukocytes was determined by $CD45^+$ staining. Among these, $CD4^+$ T cells and their proportions of Tregs ($CD25^+CD127^-Foxp3^+$) were identified. The effector phenotype was determined by CD44/CD62L staining. Moreover, the proportion of $CD8^+$ T cells, their activation status ($CD25^+$) and their effector phenotype (CD44/CD62L) were assessed. Significance was determined by one-way ANOVA with post-hoc Turkey's test.

Both after photon and carbon ion RT, there were no differences in $CD4^+$ T cell frequencies observed. However, when regarding the proportion of $CD25^+CD127^-Foxp3^+$ Tregs, the amount of Tregs among $CD4^+$T cells and $CD45^+$ leukocytes was significantly decreased in the photon RT + aCTLA-4 group compared to untreated tumors. Similar to the observations made in tumor #1 (Figure 3.22b), the proportions of Tregs among $CD45^+$ leukocytes in tumor #2 were significantly decreased when mice received aCTLA-4 therapy, regardless of RT, in the carbon ion experiment (Figure 3.29b). Interestingly, while in tumor #1 the majority of T cells displayed and effector T cell phenotype as marked by $CD44^+CD62L^-$ expression (Figure 3.22) in several tumors #2 the proportion of $CD44^+CD62L^-$ cells were far below 100%. Cells that were not $CD44^+CD62L^-$ exhibited a double negative ($CD44^-CD62L^-$) phenotype (not shown).
Considering $CD8^+$ T cells, aCTLA-4 therapy with or without RT significantly increased the frequencies of $CD8^+$ T cells in the carbon ion experiment, whereas the proportion of $CD8^+$ T cells expressing CD25 was significantly increased when mice received combination therapy compared to aCTLA-4 monotherapy. In the photon experiment, no significant differences between the groups were observed for $CD8^+$ T cell infiltration. Still, also here a tendency towards higher frequencies in the two groups treated with aCTLA-4 antibodies was detected, which was probably not significant due to the great variance within the groups. The proportions of $CD8^+$ T cells expressing CD25 did not significantly differ between the groups and only a tendency towards increased numbers in the aCTLA-4 group was observed, which is opposite to the observations made in the carbon ion experiment. Expression patterns of CD44 and CD62L in the $CD8^+$ T cell compartment were comparable to the ones observed for $CD4^+$ T cells, with some tumors being predominantly infiltrated by $CD44^+CD62L^-$ effector cells and some tumors showing increased frequencies of double negative populations ($CD44^-CD62L^-$, not shown).

### 3.7.8 Functional markers expressed on T cells in tumor #2

In a next step, immune checkpoint and co-stimulatory molecules expressed on $CD4^+$ and $CD8^+$ T cells were investigated. In the $CD4^+$ T cell compartment, the expression of CTLA-4 and CD73 conformed to the observations made for Treg infiltration (Figure 3.29). Thus, in the photon experiment, decreased frequencies $CD4^+$ T cells expressing CTLA-4 and decreased CTLA-4 expression levels were found when mice were treated with the combination therapy of photon RT plus aCTLA-4 therapy (Figure 3.30a). Furthermore, in the carbon ion experiment, CTLA-4 expression levels of $CD4^+$CTLA-$4^+$ T cells were significantly decreased in both groups receiving aCTLA-4 antibodies (Figure 3.30b). Regarding CD73 expression, in the photon experiment, decreased proportions of $CD4^+$ T cells expressing CD73 after combination therapy and decreased MFI values of CD73 in the aCTLA-4 and the photon RT + aCTLA-4 groups were found. Likewise, these trends were observed in the carbon ion experiment, however differences were not significant. Staining for the immune checkpoint molecules PD-1 and LAG-3 on $CD4^+$ T cells did not show differences between any of the groups and was characterized by a high variability within the samples of each group (Supplementary Figure

5.16). With the exception of PD-1 expression levels, which were significantly increased after photon and carbon ion RT plus anti-CTLA-4 therapy. Furthermore, the variability observed for the co-stimulatory molecules 4-1BB and CD69 on $CD4^+$ T cells was quite large. However, similar to tumor #1 (Figure 3.24), there was a trend towards decreased proportions of $CD4^+4\text{-}1BB^+$ T cells after aCTLA-4 treatment (Supplementary Figure 5.16). Moreover, in the carbon ion experiment, 4-1BB expression levels were significantly decreased in the two groups treated with aCTLA-4 antibodies.

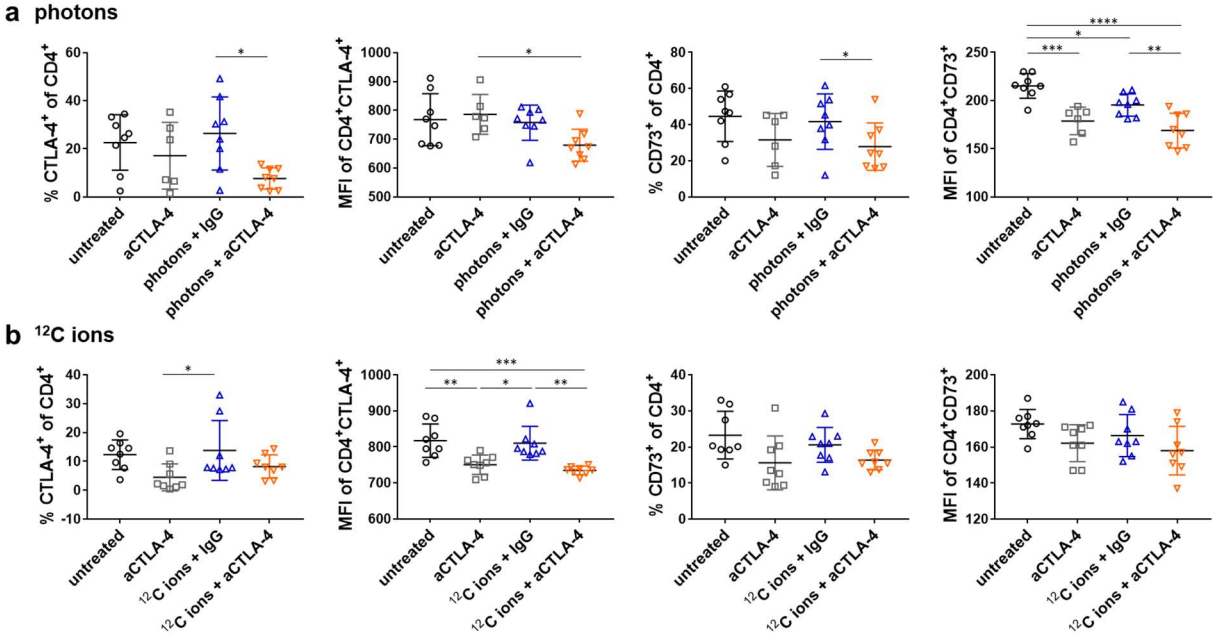


**Figure 3.30: Immune checkpoint molecules expressed on $CD4^+$ T cells in tumor #2 after treatment of EO771 tumors with RT plus anti-CTLA-4 antibodies.** Mice were left untreated or treated with anti-CTLA-4 antibodies, RT plus IgG control, or RT plus anti-CTLA-4 antibodies. Tumor #1 was irradiated, while tumor #2 was outside the irradiation field. RT was either performed with photons **(a)** or carbon ions **(b)**. Five days (photons) or six days (carbon ions) after treatment start, expression of the immune checkpoint molecules CTLA-4 and CD73 on $CD4^+$ T cells were investigated by flow cytometry. Both the proportion (%) and the level of expression defined by the median fluorescence intensity (MFI) were assessed. Significance was determined by one-way ANOVA with post-hoc Turkey's test.

Expression of the immune checkpoint and co-stimulatory molecules in tumor #2 was also analyzed on $CD8^+$ T cells. However, the variability in the data was quite big and despite some single significant differences, overall no clear immunological pattern could be read out of the data (Supplementary Figure 5.17).

### 3.7.9 Myeloid cell infiltration in tumor #2

Finally, the myeloid compartment in tumor #2 was investigated. In the photon experiment, no considerable differences between the four treatment groups were observed regarding the infiltration of MDSCs, macrophages, and the polarization of macrophages. Again, there was a high variability between the single tumors within a group (Supplementary Figure 5.18).
In the carbon ion experiment, the range of macrophage frequencies were comparable in all groups, whereas the proportion of MDSCs was reduced after aCTLA-4 monotherapy and upon combination therapy the amount of MDSCs tended to be decreased (Figure 3.31). Regarding the functional polarization status of macrophages, aCTLA-4 monotherapy increased the

expression levels of I-A$^b$. Moreover, the frequencies of macrophages expressing the M2-like marker CD206 were increased in the carbon ion RT + aCTLA-4 group, together with increased expression levels in the two irradiated groups. However, when regarding the frequencies of M1-like and M2-like macrophages among total CD45$^+$ leukocytes, there were no differences observed.

Besides T cells and myeloid cells, also NK cells and DCs were analyzed in tumor #2, but no differences between groups were found (Supplementary Figure 5.19).

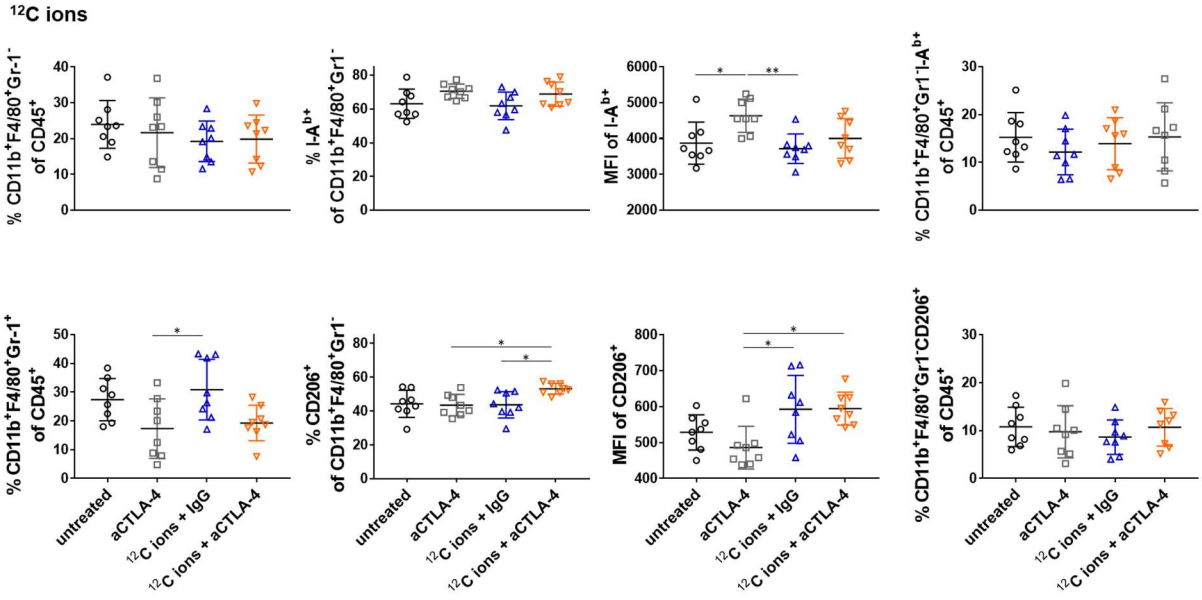


**Figure 3.31: Myeloid cell infiltration in tumor #2 after treatment of EO771 tumors with RT plus anti-CTLA-4 antibodies.** Mice were left untreated or treated with anti-CTLA-4 antibodies, RT plus IgG control, or RT plus anti-CTLA-4 antibodies. Tumor #1 was irradiated, while tumor #2 was outside the irradiation field. Irradiation was performed with carbon ions. Six days after treatment start, myeloid cell infiltration was investigated by flow cytometry. Proportions of macrophages (F4/80$^+$CD11b$^+$Gr-1$^-$) and MDSCs (F4/80$^+$CD11b$^+$Gr-1$^+$) among CD45$^+$ leukocytes were identified. The polarization status of macrophages was further determined by staining of the M1-like marker I-A$^b$ and the M2-like marker CD206. For both makers the percentages among macrophages, the level of expression defined by the median fluorescence intensity (MFI), and the proportion among total CD45$^+$ leukocytes were assessed. Significance was determined by one-way ANOVA with post-hoc Turkey's test.

### 3.7.10 Protein expression analysis in tumor #2 after photon RT with or without anti-CTLA-4 checkpoint blockade

Finally, in a small pilot experiment, lysates of tumor #2 from mice treated with photon RT plus IgG control and photon RT plus aCTLA-4 therapy were subjected to a protein profiling assay (ScioCD microarrays from Sciomics). Notably, samples were analyzed 9 days after treatment start. When analyzing the differently expressed proteins in tumor #2 of mice treated with photon RT plus IgG control compared to photon RT plus aCTLA-4 antibodies, the three replicates of each group formed distinct clusters (Figure 3.32a). Overall, 70 proteins were differently expressed between both groups, with 50 proteins being more abundant and 20 proteins being less abundant in the RT + aCTLA-4 group compared to the RT + IgG group (Figure 3.32b). Regarding differentially expressed proteins, various proteins associated with immune-cell functions were detected. (Figure 3.32c, Supplementary Table 5-2). On the one hand, several pro-inflammatory proteins were more abundant in the photon RT + aCTLA-4 group including the activating NK-cell receptor KI2L2, interleukins IL17 and IL18, and MHC class I molecules (HLA-I). On the other hand, also immunosuppressive proteins were present at increased levels including TGFB1/2, the TGF-β family members BMP4 and BMP6, and the immune checkpoint

molecule LAG-3. Notably, a number of abundant proteins were associated with TNF signaling like TNFB (LTA), TNFA, TNF13, TNFL8, TNFL6 (FASLG), and TNF14. Moreover, increased protein levels of the tumor suppressor p53 were found. Furthermore, a number of chemokines were differently expressed as well: while CCL23, CCL26, CXCL11, PF4 were more abundant in the photon RT + aCTLA-4 group, CCL15, CCL25, CCL28, CCL7, CCL8, CXCL9 were less abundantly expressed. Remarkably, important pro-inflammatory factors like CD80 and INF-γ were found to be less abundantly expressed within the RT + aCTLA-4 group.

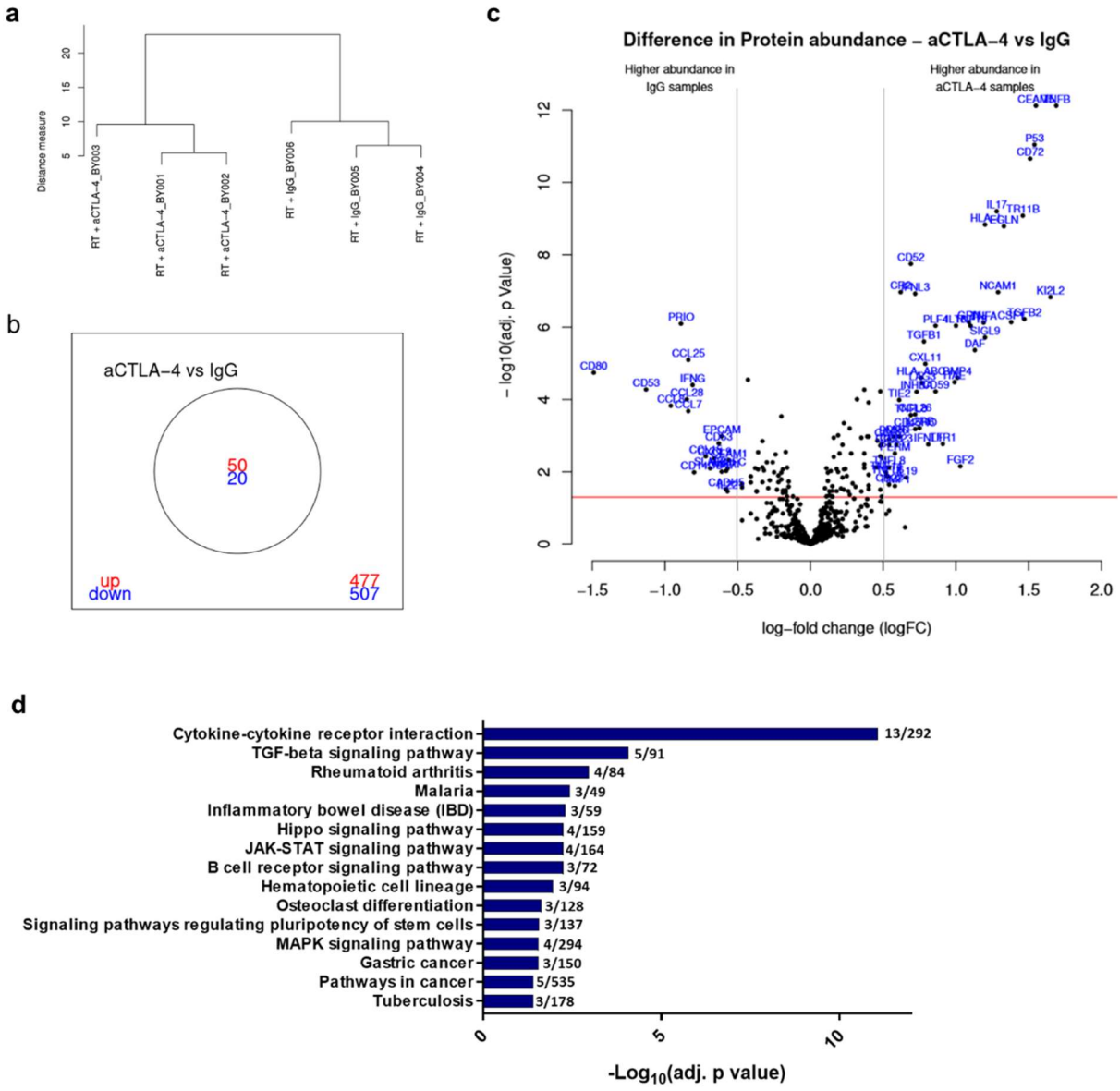


**Figure 3.32: Difference in protein abundance in tumor #2 treated with RT plus IgG compared to RT plus anti-CTLA-4 therapy**. **(a)** Hierarchigal clustering of protein extracts based on differently expressed proteins. **(b)** Venn diagram showing number of differentially expressed proteins. Red numbers indicate more abundant proteins and blue numbers less abundant proteins in the photon RT plus anti-CTLA-4 group compared to the photon RT plus IgG group. **(c)** Volcano plot showing proteins that were of higher abundance in the RT + aCTLA-4 group (right) or of higher abundance in the RT plus IgG group (left). The volcano plot visualises log-fold changes (logFC) and corresponding p values adjusted for multiple testing. The cutoff for logFC (vertical lines) and the adjusted p value (horizontal red line) were set to 0.5 and 0.05, respectively. **(d)** KEGG pathway analysis with differentially expressed genes within the photon RT + aCTLA-4 group. Graph shows the top 15 predicted pathways and the respective adjusted p value depicted as –Log10. The numbers indicate the overlap of genes with the respective pathway. Plots from (a)-(c) were provided by Sciomics.

Finally, using the proteins more abundantly expressed in the RT + aCTLA-4 group, a KEGG pathway analysis was performed with the Enrichr tool [277, 278]. Pathways associated with cytokine-cytokine receptor interaction were most distinct with an overlap of 13 genes and the highest -$Log_{10}$ p value, followed by the TGF-β signaling pathway (Figure 3.32d). The other pathways showed fewer overlapping genes and were less significant. These included pathways associated with diseases like rheumatoid arthritis, malaria, inflammatory bowel disease or cancer as well as signaling pathways such as the hippo signaling, JAK-STAT and MAPK signaling pathways. Overall, the individual proteins and predicted pathways point towards an induction of both pro- and anti-inflammatory immune responses in tumor #2 after combination therapy.

## 3.8 Tumor re-challenge of mice with complete responses after photon RT plus immune checkpoint blockade

Mice that had shown durable complete responses after therapy with photon RT plus checkpoint-inhibiting antibodies against PD-L1 or CTLA-4 were re-challenged with EO771 tumor cell implantation 3-6 month after initial therapy. All naïve mice developed a tumor, whereas in the group of mice previously treated with photon RT plus aPD-L1 antibodies only one out of four, and among mice treated with photon RT plus aCTLA-4 antibodies none of the ten mice developed a tumor (Figure 3.33a). To identify, if pre-treated mice had generated an EO771-specific memory T cell response, splenocytes of these mice were co-cultured with irradiated EO771 target cells in different E:T ratios and the INF-γ response was determined. As expected, no INF-γ response was observed in naïve mice (Figure 3.33b). In the photon RT + aCTLA-4 group, there was a significant increase of INF-γ spots for both E:T ratios of 20:1 and 10:1 indicating the establishment of a memory T cell response against EO771 cells, which is in accordance with the rejection of the second tumor cell engraftment. Interestingly, 75% of mice pre-treated with photon RT plus aPD-L1 antibodies rejected the second tumor cell engraftment, but no INF-γ responses were detected.

Moreover, the specificity of the T cell response for EO771 in comparison to other tumor cell lines and one potential epitope was investigated. This epitope originates from the envelope protein gp-70 of the murine leukemia virus (MuLV), representing a shared immunogenic antigen expressed in a variety of murine tumor cell lines [274, 279]. First, the gene expression of the envelope protein was determined for EO771, B16F10 and RMA cells, which all originate from C57BL/6 mice. The lowest expression of gp-70 was found in RMA cells, while expression was around 350-fold and 1000-fold higher in EO771 and B16F10 cells, respectively (Figure 3.33c). Further, specificity was determined by co-culturing splenocytes not only with EO771 cells, but also with B16F10 cells in different E:T ratios, the KSPWFTTL peptide of gp-70 with different effector cell numbers, RMA cells (E:T = 20:1), medium as a negative control, and anti-CD3/CD28 beads as a positive control. When comparing mean numbers of IFN-γ spots, the number of IFN-γ spots was significantly higher after co-culture with EO771 cells compared to B16F10 cells, KPWFTTL peptide, RMA cells and medium indicating the specificity of the response (Figure 3.33d). Indeed, the response to peptide tended to be slightly increased compared to B16F10 and RMA cells, however there was no significant difference observed.

Supplementary Figure 5.20 depicts the number of INF-γ spots for all tested conditions in each individual mouse. The responsiveness to CD3/CD28 beads shows the functionality of splenocytes (with exception of one mouse). In the photon RT + aCTLA-4 group, the recognition of EO771 cells was clearly visible, and in the majority of mice graded numbers of effector cells resulted in decreased numbers of INF-γ spots. However, the variance in the technical triplicates was quite large in some samples. This is most likely not due to the biological

response, but rather a technical problem as some of the wells of the ELISpot plate did not work properly as exemplified for one plate in Supplementary Figure 5.21. Still, despite the high variance in technical triplicates, mean numbers of IFN-γ spots were significantly higher in the photon RT + aCTLA-4 group, compared to the photon RT + aPD-L1 and naïve group (Figure 3.33b).

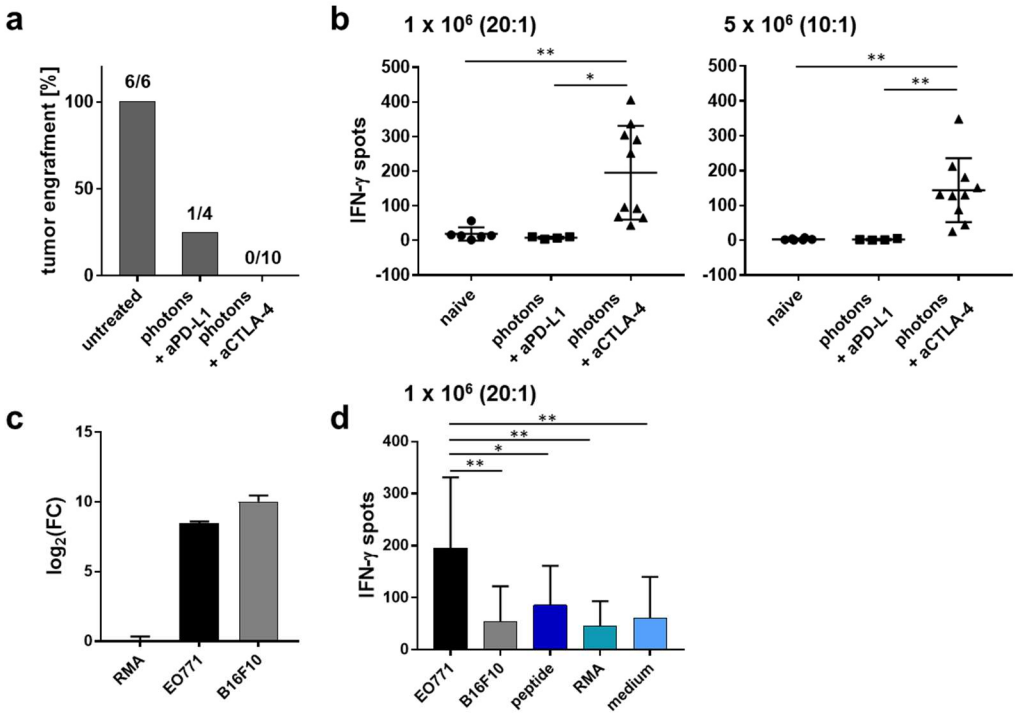


**Figure 3.33: Re-challenge of mice with complete responses after photon RT plus immune checkpoint inhibition. (a)** Percentage of tumor engraftment in naïve mice or mice with complete responses after treatment with photon radiotherapy plus anti-PD-L1 and anti-CTLA-4 antibodies, respectively. **(b)** Co-culture of splenocytes with EO771 target cells with effector cell numbers of 1 x $10^6$ and 5 x $10^5$ splenocytes representing effector to target cell ratios of 20:1 and 10:1, respectively. INF-γ release was determined by INF-γ ELISpot assay. **(c)** Quantitative PCR analysis of gp-70 expression, the envelope protein of the murine leukemia virus, in RMA, EO771, and B16F10 cells. Target gene expression was normalized to the housekeeping gene Ppia and fold changes (FC) of target gene expression over RMA cells were $log_2$-transformed. Mean values ± SD of triplicates are shown. **(d)** Specificity of the T cell response was assessed by co-culture of splenocytes from mice treated with photon RT + aCTLA-4 antibodies with EO771 cells, B16F10 cells, KSPWFTTL peptide (epitope for gp-70), RMA cells or medium with 1 x $10^6$ (20:1) target cells. IFN- γ release was determined by IFN-γ ELISpot assays.

# 4 Discussion

## 4.1 Definition of biologically equivalent radiation doses of photons and carbon ions

RT has been a cornerstone of cancer management for several decades. While the main mode of action is particularly attributed to the cytotoxic effects ionizing radiation exerts on cancer cells, more recently also the immunogenic potential of RT has been widely investigated. Within this thesis, the overall aim was to characterize the cytotoxic and immunomodulatory effects of radiation on the murine breast cancer cell line EO771, both *in vitro* and *in vivo*. Importantly, the goal was to compare radiogenic effects of both the classical photon radiation and carbon ion radiation. To this end, biologically equivalent doses of both radiation types ranging from high to low dose were applied to receive a broad overview of radiogenic effects *in* vitro before applying RT in the *in vivo* model.

Biological equivalent doses and the RBE for photon compared carbon ion radiation are cell line-specific and dose-dependent parameters, which depend on various factors like the radiosensitivity and cell cycle phase of the cells, the biological endpoint measured, the cellular oxygen concentration, as well as the dose-rate and beam quality [283-285]. Here, equivalent doses and RBEs for EO771 cells were determined by a clonogenic survival assay, an assay commonly used to determine the cytotoxic effects of radiation. After irradiation with graded doses, the capability of cells to form colonies of more than 50 cells and thus unlimited cell division was analyzed [286]. Survival curves for photon and carbon ion irradiation showed different shapes (Figure 3.1a). The survival curve of photon-irradiated cells exhibited a distinct shoulder in the lower dose range at the beginning of the curve, while it transitioned into an almost exponential curve in the higher dose range. This shape is characteristic for survival curves after photon irradiation [287, 288]. Thus, in the lower dose range SSBs predominate, which only partially affect clonality as SSBs are sub-lethal damage that can be quite efficiently repaired. After irradiation with higher photon doses, multiple hit events from different radiation tracks, such as multiple SSBs, can more efficiently induce cell death as represented by the exponential decline in the survival curve [198]. In contrast, after carbon ion irradiation a steeper dose-response relationship was observed. Here, the survival curve was exponential also in the lower dose range indicating that single hit events cause lethal DNA damage, such as DSBs, even at lower doses. Importantly, while photon irradiation may also induce dispersed DSBs, carbon ion irradiation forms DSBs in close proximity, called clustered DSBs, which are more difficult to be repaired compared to dispersed DSBs [289].

This differential impact of photon and carbon ion irradiation on DNA damage largely depends on the physical differences between both radiation types. Thus, carbon ion radiation exhibits a high LET characterized by high energy loss along the pathway of the beam. This results in a higher number of ionizations per unit distance inducing increased lethal DNA damage and chromosomal abrogation compared to photons exhibiting a low LET [177]. Moreover, carbon ion irradiation and photon irradiation are characterized by different depth-dose profiles with carbon ions being characterized by the Bragg Peak and photon irradiation by a build-up effect close to the irradiation source and constant loss of irradiation dose along the beam pathway traveled (Figure 1.4) [189]. However, in this *in vitro* setting, where both photon and carbon ion irradiation can be precisely targeted to the cell monolayer, this physical advantage of carbon ion irradiation only plays a minor role and is rather important in *in vivo* irradiations, where surrounding tissues and organs at risk can be affected by irradiation. Similarly, the independence of carbon ion irradiation on oxygen levels is rather irrelevant in the clonogenic survival assay as cells were kept under normoxic conditions [290].

To gain a broad overview, radiogenic effects using four doses ranging from low to high dose were further investigated for *in vitro* studies. For photon ion irradiation, 1, 3, 5, and 10 Gy were selected and based on the clonogenic survival assays equivalent doses of 0.12, 1.11, 3.08 and 8 Gy carbon ions were determined for EO771 cells. Given that survival curves for photon and carbon ion irradiation revealed distinct shapes of the survival curves, the RBE between photon and carbon ion irradiation was dose-dependent being inversely proportional to the radiation dose. Thus, the RBE for the lowest dose accounted for 8.3, while it decreased to 1.25 for the highest dose, where both survival curves are characterized by an exponential regression (Figure 3.1b). To characterize radiogenic and immunomodulatory effects that are independent of cytotoxic effects, dose-dependent RBEs were applied to calculate the photon-equivalent carbon ion doses.

Overall, the breast cancer cell line EO771 showed a comparably high sensitivity to irradiation-induced cytotoxicity. In our group, similar experiments were performed with the murine pancreatic cancer cell lines PDA30364/OVA, which was considerably less radiosensitive to photons as indicated by the different surviving fractions at 2 Gy photon radiation (SF2) of 0.49 and 0.87, for EO771 and PDA30364/OVA cells, respectively [291, 292]. In a study characterizing the radiosensitivity of 27 canine cancer cell lines, the five cell lines showing the highest radiosensitivity showed SF2 values between 0.19 to 0.44, while the value of the five most radioresistant cancer cell lines were above 0.86. Interestingly, radiosensitivity was not primarily dependent on the cancer entity, as one bladder cancer cell line classified into the top five radiosensitive group, and the other one into the top five radioresistant group [293]. In accordance with studies in human cell lines, radiosensitive cells showed higher occurrence and persistence of DSBs as indicated by histone H2AX phosphorylation, which is probably independent of the cancer entity, but rather associated with DNA repair mechanisms. Results on whether increased radioresistance is indeed accompanied by increased expression of DNA damage signaling genes vary between different studies [293-296]. Still, targeting of DSB repair mechanisms might be a promising option to overcome radioresistance [297]. Interestingly, in our hands, the pancreatic cancer cell line showed an increased sensitivity to carbon ion irradiation compared to EO771 cells as indicated by higher RBEs in the pancreatic cell line. Thus, a physical dose of approximately 3.1 carbon ions was equivalent to 5 Gy and 10 Gy photons for EO771 and PDA30364/OVA, respectively. [292]. In a study investigating the radiosensitivity of peripheral blood lymphocytes (PBLs) to irradiation it was shown that radiosensitivity was varying between different donors and was not correlating with photon and carbon ion-irradiated PBLs of the same donor [298]. Thus, cells being sensitive to photon irradiation do not necessarily have to be sensitive to carbon ion irradiation. However, to investigate underlying mechanisms for EO771 cells, further investigations of DNA damage and DNA repair pathways would be necessary.

## 4.2 Radiogenic effects on proliferation, cell cycle arrest and apoptosis

Having determined photon-equivalent doses for carbon ions, irradiated EO771 were further characterized in terms of proliferation, cell cycle arrest and apoptosis, which are interconnected and associated with irradiation-induced cytotoxicity. As expected from clonogenic survival assays, proliferation was inversely correlated to the irradiation dose (Figure 3.1c). While low dose irradiation with 1 Gy photons and 0.12 Gy carbon ions hardly affected proliferation, high dose irradiation with 10 Gy photons and 8 Gy carbon ions almost completely abrogated proliferation. Remarkably, matched doses of photons and carbon ions resulted in comparable proliferation patterns corroborating the results of the clonogenic

survival assay and the determination of BEDs. Interestingly, EO771 cells irradiated with 5 Gy photons still proliferated to some extent, while irradiation with 5 Gy photons did not give rise to any colonies in survival assays. This highlights the difference between both assays, as cells in bulk might still be mitotically active and or even proliferate, while they are not able to form colonies from single cells. In facht, irradiated cells may enter a senescent state [210]. Moreover, in the proliferation assay, cells were monitored daily over 84 h after irradiation, whereas clonogenic survival was assessed 12 days after irradiation.

The decreased proliferation was accompanied by a dose-dependent cell cycle arrest in the G2/M phase being most pronounced after irradiation with 10 Gy photons and 8 Gy carbon ions (Figure 3.3). This can be explained by the fact that the cell cycle arrest is closely related to DNA damage. Thus, upon sensing DNA damage in the nucleus, checkpoint and cyclin-dependent kinases are activated inducing cell cycle arrest to provide sufficient time for the orchestration of complex DNA repair mechanisms [211]. Accordingly, higher doses most likely initiated increased and more severe DNA damage resulting in increased numbers of cells arresting at the G2 checkpoint. However, the cell cycle arrest was only transient as the cell's fate can go into two directions afterwards. Thus, cells may either continue to proliferate after successful DNA repair or severe DNA damage may cause cell death [299]. Likewise, a dose-dependent increase in early and late apoptotic cells peaking 84 h after irradiation was observed. Radiation can induce different forms of cell death. First, severe DNA damage can initiate premature mitosis leading to mitotic catastrophe. Before succumbing to mitotic death, which is a regulated process associated with the intrinsic apoptotic pathway, cells may undergo several cell divisions, which may explain why the majority of dead cells were only seen 84 h after irradiation. Furthermore, mitotic catastrophe has an impact on the shape of the cells as improper cytokinesis results in the formation of tetraploid cells and thus, swelling of irradiated cells [202, 203]. This swelling effect was clearly visible under the microscope (not shown) and in flow cytometric analyses after irradiation of EO771 cells (Supplementary Figure 5.1). Moreover, irradiation induces the intrinsic and extrinsic pathway, as well as senescence [211]. To clarify, which pathway of cell death was predominant after irradiation of EO771 cells further experiments would be necessary. Here, only cells with diploid DNA content were analyzed in the cell cycle experiments. However, one could also consider cells with higher DNA content indicating aneuploidy. For instance, for doses higher than 3.08 Gy, 7-13% of cells were aneuploid (not shown). However, to make profound statements on the karyotype and thus the mode of cell death, one should further include a DAPI staining of cell nuclei as done by Kobayashi *et al.* Thus, apoptotic cells were identified by apoptotic bodies, nuclear condensation and fragmentation, mitotic catastrophe by nuclei showing several lobes, and senescent cells by heterochromatic foci [300].

Overall, the effects of both irradiation types on proliferation, cell cycle arrest, and apoptosis were comparable. Indeed, there are studies reporting a more pronounced cell cycle arrest in cervical cancer and glioblastoma cell lines as well as fibroblasts after carbon ion irradiation compared to photon irradiation [301-303]. However, one has to consider that most reports compared physical doses and not BEDs.

## 4.3 Immunomodulatory effects of irradiation

Beside cytotoxicity, a second mode of action of radiation has become more and more apparent. RT is believed to induce ICD and thus, to initiate antitumor immune responses. Indeed, historically apoptosis is considered a non-immunogenic form of cell death [304-306], however treatment with doxorubicin has been shown to induce caspase-dependent apoptosis eliciting an antitumor immune response [307]. Likewise, RT has been shown to induce *bona fide* ICD as vaccination with irradiated tumor cells protected mice from subsequent tumor inoculation [257, 308, 309].

Different danger molecules released upon irradiation-induced ICD have been described. Among these is the danger signal HMGB1, which plays a pivotal role in the activation of various types of immune cells [217, 310, 311]. Here, extracellular HMGB1 was upregulated to similar levels after irradiation of EO771 cells with both photons and carbon ions in a dose-dependent manner (Figure 3.6). These findings are in accordance with Yoshimoto *et al.*, who showed comparable extracellular HMGB1 release after irradiation with biologically equivalent doses of photon and carbon ion irradiation in five different cell lines [312]. Of note, while extracellular HMGB1 is frequently associated with a pro-inflammatory response, sustained HMGB1 expression might even promote cancer growth and migration [313, 314]. Besides HMGB1, extracellular ATP is associated with irradiation-induced ICD, which is also released in a caspase-dependent manner [315, 316]. In a small pilot experiment, extracellular ATP release after irradiation of EO771 cells was investigated, but no increase in extracellular ATP levels upon irradiation were found (not shown). However, extracellular ATP has a very short half-life [317] and assay conditions might need further improvements. For instance, real-time ATP assays exhibiting the kinetics of ATP might be suitable to detect irradiation-induced ATP release. Finally, surface expression of calreticulin, heat shock proteins HSP70 and HSP90, and cytosolic dsDNA could be further investigated danger signals to characterize irradiation-induced ICD in EO771 cells [257, 318-320].

Next, the effect of radiation on various immunomodulatory receptors was investigated. This study shows that the expression of both MHC class I isotypes (H2-$D^b$ and H2-$K^b$) is upregulated on the mRNA and protein level in a dose-dependent manner after photon and carbon ion irradiation to a similar extent (Figure 3.4, Figure 3.5). Mechanistically, MHC class I upregulation might be induced by the increased expression of type I IFNs upon irradiation [321]. Type I IFNs in turn may be produced in response to cytosolic dsDNA fragments released after irradiation, which activate the cGAS-STING pathway [219]. *In vivo*, MHC class I upregulation might be of importance increasing the extent of presented epitopes and counteracting potential escape mechanisms of tumor cells downregulating MHC class I expression [322]. Furthermore, irradiation can enhance the generation of neoantigens and thus, increased MHC class I presentation could be beneficial for presentation of neoepitopes [323]. In a recent, study Lhuiller *et al.* reported that RT increased the frequencies of immunogenic mutations in a poorly immunogenic mouse model. Interestingly, one MHC I-restricted neoepitope was presented in six fold higher amount on irradiated compared to unirradiated cells [324].

However, irradiation did not only induce the upregulation of MHC class I molecules in EO771 cells, but also the expression of the immune checkpoint molecules PD-L1 and CD73 in a dose-dependent manner (Figure 3.4, Figure 3.5). Again, effects were very comparable for photon and carbon ion-irradiated cells. Likewise, increased PD-L1 expression after photon irradiation was shown in melanoma and glioblastoma cell lines, which was accompanied by increased levels of intracellular INF-γ [325]. Enhanced intracellular expression of IFN-γ upon irradiation might be a possible explanation for the upregulation of PD-L1, as IFN-γ activates the JAK1/2-STAT1/2/3-IRF1 axis thereby regulating PD-L1 expression [326-328]. Moreover, a direct link

between DNA damage and PD-L1 expression has been proposed recently. Thus, Sato *et al*. showed that DSBs induce the upregulation of PD-L1 expression in an ATM/ATR/CHK1-dependent manner ultimately leading to the activation of STAT1/3 and phosphorylation of interferon regulatory factor (IRF1), a key transcription factor regulating PD-L1 expression [329]. In fact, the observation that RT increases PD-L1 expression provides a rational for combining RT with immune checkpoint blockade against PD-1/PD-L1, which will be discussed in detail in section 4.6. While the upregulation of PD-L1 upon irradiation is well studied, less is known about the immune checkpoint molecule CD73. In the present study, it was shown that similar to PD-L1, CD73 expression is upregulated with increasing doses of photon and carbon ion irradiation. *In vivo*, radiation-induced expression of CD73 together with enhanced release of ATP might promote immunosuppression, as CD73 converts AMP to adenosine, which is a known immunosuppressor [61]. Accordingly, in a rectal cancer model, RT increased both the expression of CD73 and adenosine in subcutaneous tumors. However, when combining RT with a CD73-blocking antibody an improved control of both a local tumor and distant metastases was achieved [330].

Having observed immunomodulatory changes after irradiation, the effect of radiation on CTL-mediated killing was investigated. When co-culturing irradiated EO771/Luci/OVA cells with an OVA-specific CTL line, tumor cell killing increased with higher irradiation doses applied (Figure 3.7a and b). Overall, photon and carbon ion irradiation provoked similar effects, although CTL-mediated killing of irradiated cells was slightly more persistent after carbon ion irradiation. Importantly, cell proliferation of irradiated cells during the time course of the assay was monitored to exclude that tumor cells are dying due to the irradiation *per se* and thus, independently of OVA-specific CTLs (Figure 3.7d). Similar proliferation of tumor cells between all the conditions showed that increased killing was actually evoked by the CTL line. Indeed, slight differences in in proliferation were observed, which were most likely due to slight variations in counting of the cells. However, the formula for calculating cytolysis includes tumor cells cultured without OVA-specific CTLs correcting for variations in cell counting.

Interestingly, INF-γ release by the effector CTL line was not affected by irradiation (Figure 3.7c). Consequently, increased target cell killing was due to an enhanced susceptibility of irradiated target cells rather than caused by increased effector functions of the CTL line. Possibly, cells are under enhanced stress with increasing doses and CTL-mediated cytotoxicity can synergize with irradiation-induced cytotoxicity. In fact, it has been shown that CTLs require higher levels of T cell receptor (TCR) occupancy for IFN-γ secretion than for cytolysis [331]. Thus, increased H2-$D^b$ and H2-$K^b$ expression levels induced by irradiation might have enhanced the target cell lysis without affecting IFN-γ secretion levels. Moreover, the OVA-specific cell line that was used highly expresses PD-1 [291], so that IFN-γ secretion might be negatively influenced by the increased expression of PD-L1 on EO771 cells after irradiation. Finally, the OVA-specific CTL line is weekly re-stimulated with OVA antigens and was thus maximally activated at the time point of the experiment. The effects of ICD and immunomodulatory receptors might be more relevant *in vivo* with a complex TME compared to a pre-activated T cell line *in vitro*. Overall, results presented in this study are in line with other studies showing an increased susceptibility of irradiated target cells to antigen-specific killing [230, 332, 333].

## 4.4 Photon vs. carbon ion irradiation *in vitro* and definition of an irradiation dose for *in vivo* experiments

Considering all results of the *in vitro* experiments, the impact of irradiation with photons and RBE-matched doses of carbon ions on cytotoxicity, immunomodulation and CTL-mediated

cytolysis was altogether comparable. Many of the observed effects are directly linked to cellular stress and DNA damage responses, such as the release of danger signals, the expression of type I IFNs, as well as the upregulation of MHC class I and PD-L1 surface expression [219, 329, 334]. Indeed, previous studies report differences between photon and carbon ion irradiation in terms of cell cycle arrest, damage responses, or ROS production. However, in these studies, physical irradiation doses were used meaning that e.g. irradiation with 1 Gy photons was compared to 1 Gy carbon ions [335, 336]. In the present study, BEDs of photon versus carbon ion irradiation were compared. Under these conditions, irradiation-induced cytotoxicity should be comparable and induced similar immunomodulatory effects on the molecules studied in this thesis. Thus, it seems that radiation-induced cytotoxicity primarily drives radiogenic effects independently of the exact pattern of DNA damage (dispersed vs. clustered DSBs for photon and carbon ion irradiation, respectively [178, 179]). Accordingly, when analyzing the transcriptome of EO771 cells irradiated with 5 Gy photons vs. 3.08 Gy carbon ions by RNA sequencing, not a single gene was differently expressed between both groups (Figure 3.8). Furthermore, considering upregulated DEGs of photon-irradiated vs. untreated cells and carbon ion-irradiated vs. untreated cells, respectively, similar pathways were predicted *in silico* (Table 3-1). The only annotated cluster yielding a meaningful enrichment score was associated with focal adhesion, ECM-receptor interactions and PI3K-Akt signaling pathways. Indeed, photon radiation has been shown to increase focal adhesion and extracellular matrix proteins, which might favor metastatic spread. Again, the DNA-damage sensing kinases ATM and ATR are associated with ECM remodeling [337, 338]. However, increased adhesion can not only be associated with metastatic spread, but also promote adherence and transmigration of leukocytes via I-CAM-1 [222, 339], whose expression was upregulated in irradiated EO771 cells independent from the type of radiation. To verify the pathway prediction, further analyses on cell adhesion would be necessary. Interestingly, although *in vitro* irradiation of EO771 cells induced cytotoxicity, cell cycle arrest, apoptosis and immunomodulation, no clusters associated with these radiogenic effects were predicted.

Based on the results of *in vitro* irradiation of EO771 cells, a suitable photon and biologically equivalent carbon ion dose for further *in vivo* experiments was defined. Generally, the maximum doses of 10 Gy photons and 8 Gy carbon ions resulted in the highest changes of proliferation, G2/M cell cycle arrest, and apoptosis compared to unirradiated cell. Moreover, the mRNA and surface expression of MHC class I molecules was markedly increased, HMGB1 secretion enhanced, and susceptibility to CTL-mediated cytolysis peaked when applying the highest doses. On the other hand, also the immune checkpoint molecules PD-L1 and CD73 were distinctly upregulated after high-dose irradiation, which did not seem to have a major effect in the luciferase-based cytotoxicity assay, but might be much more relevant in a complex TME *in vivo*. Moreover, higher doses might have multiple further immunosuppressive effects that were not analyzed in this study and inhibit abscopal effects [250, 258]. Regarding low doses, irradiation with 1 Gy photons and 0.12 Gy carbon ions did not have major effects on cytotoxicity and immunomodulation, while irradiation with 3 Gy photons and 1.11 Gy carbon ions affected immunomodulation to some extent, but cytotoxicity only marginally.

Eventually irradiation with 5 Gy photons and 3.08 Gy carbon ions were selected for further *in vivo* experiments, as these doses efficiently inhibited proliferation and induced apoptosis and cell death, which is very important for tumor control. Moreover, CTL-mediated cytolysis was still efficient, HMGB1 was secreted to a moderate extent, and the expression of the checkpoint molecules PD-L1 and CD73 as well as the MHC class I isotypes H2-D$^b$ and H2-K$^b$ was intermediate, which might be beneficial *in vivo*.

## 4.5 Establishing a bilateral EO771 tumor model and treatment schedules for radioimmunotherapy

In the EO771 tumor model, not only the effects of RT on a local tumor was to be investigated, but also on distant, non-irradiated tumors. To this end, a tumor model was established, in which mice were challenged with contralateral s.c. tumor cell injections. In the first experiments, the OVA-expressing cell line EO771/OVA was used, as OVA expression would allow monitoring of tumor-specific T cells *in vivo* and provide the possibility for combining RT with an adoptive transfer of OVA-specific CTLs. Performing tumor take experiments with unilateral tumor cell injections with graded cell numbers first, all tested cell concentration gave rise to tumors (Supplementary Figure 5.5). However, only cell numbers greater than 1 x $10^6$ cells induced rapidly growing tumors, while the parental cell line resulted in comparable tumor growth with only 2 x $10^5$ to 4 x $10^5$ cells indicating that OVA-expression bears immunogenicity to some extent. In fact, bilateral tumor cell injections with different cell numbers or time-shifted injections of equal cell numbers resulted in a delayed or absent growth of tumor #2. While, for example OVA-expressing B16-OVA and EG.7 cells were shown to be suitable for bilateral tumor growth [340, 341], EO771/OVA appeared to be too immunogenic. Hence, the first implantation of EO771/OVA cells for tumor #1 possibly primed an immune response against OVA preventing the outgrowth of tumor #2. Accordingly, due to its strong immunogenicity as xenogenic antigen originating from chicken, the OVA-specific CTL epitope $OVA_{257–264}$ is frequently used as a model antigen in vaccination studies [342-345]. Consequently, the parental EO771 cell line was further used for the bilateral tumor model. Based on literature [261, 264, 346], equal numbers of EO771 cells were injected two days apart. However, as tumor #2 was still growing slower compared to tumor #1, both tumor cell lines were finally injected one day apart.

Therapeutic effects on distant tumor sites (abscopal effects), which would be effects on tumor #2 in the bilateral EO771 model, have been described to occur predominantly upon combined radioimmunotherapy [261, 347-350]. As immunotherapy, immune checkpoint blocking antibodies against PD-L1 and CTLA-4 were used, as they are clinically most relevant leading to superior tumor control and durable responses in several tumor entities [136-138]. Before starting the combination therapy of RT plus immune checkpoint blockade, the therapeutic effects on EO771 with the respective monotherapies was tested and a suitable treatment schedule for a combination therapy in the bilateral tumor model was defined. Based on a publication by Twyman-Saint Victor *et al.* [261], treatment with immune checkpoint-blocking antibodies against PD-L1 and CTLA-4 was applied on day 9, 12, and 15 after tumor cell injection. However, in this pilot experiment, EO771 tumors were quite small at the beginning of the treatment (mean tumor volume below 30 mm³) resulting in tumor regression of tumor #1 in some of the mice, and tumor #2 in the majority of mice (Figure 3.12). Overall, when starting the treatment early, anti-CTLA-4 therapy was more effective compared to anti-PD-L1 therapy. When comparing results to the publication of Twyman-Saint Victor *et al.*, one needs to consider that the authors used the B16F10 tumor model and Matrigel for tumor implantation and thus tumor growth kinetics and therapeutic efficacies cannot be directly compared. In general, B16F10 is considered a poorly immunogenic model, rather insensitive to immune checkpoint blockade, and associated with an aggressive and rapid tumor growth *in vivo* [351-354]. Finally, the administration of immune checkpoint-inhibiting antibodies was postponed by three days, when tumor volumes ranged between 120-200 mm³. This is in line with another study using the EO771 model showing that checkpoint blockade against PD-1 or CTLA-4 was ineffective when tumor volumes were greater than 100 mm³ at the beginning of the treatment [355]. Overall, therapy with immune checkpoint antagonists in the EO771 tumor model is only sparsely described in literature. Moreover, most studies use anti-PD-1

checkpoint blockade [356-358], rather than anti-CTLA-4 and anti-PD-L1 therapy, which were used in this study.
For treatment with radiotherapy, a fractionated irradiation schedule was applied. On the one hand, fractionated schedules more closely mimic clinical RT schedules, which aim to spare adjacent normal tissue [170]. On the other hand, preclinical models have shown that fractionated RT is superior to single dose RT in inducing abscopal effects. Thus, when murine tumors were treated with checkpoint blockade plus fractionated RT (3 x 8 Gy and 5 x 6 Gy) and single dose RT with 20 Gy, respectively, abscopal effects were only observed using fractionated schedules [264]. Here, when applying fractionated photon RT with 3 x 5 Gy as monotherapy to EO771 tumors, irradiated tumor #1 could be controlled to some extent depending on the volume of the tumor when starting the therapy (Figure 3.14, Supplementary Figure 5.6). As expected from literature, outgrowth of tumor #2 was not affected by irradiation of tumor #1 [261, 347-350].
Finally, a treatment schedule for combination therapy of RT plus checkpoint blockade was defined. Previously, concurrent treatment has been shown to be superior compared to sequential administration of checkpoint blocking antibodies one week after the last fraction [265]. Thus, mice were contralaterally injected with EO771 tumors one day apart. When tumors were established around day 11-12, treatment was started with fractionated RT on three consecutive days and three injections of checkpoint-blocking antibodies starting on the first day of RT.

## 4.6 Combination therapy of RT plus checkpoint blockade

First, combination therapy with photon RT plus checkpoint blockade against anti-PD-L1 was tested. Again, tumors #1 responded to RT alone, which could be enhanced when adding checkpoint-blocking antibodies against PD-L1 (Figure 3.15, Supplementary Figure 5.7). However, therapeutic effects on tumor #2 were sparsely observed and only in tumors showing a comparably small volume at the beginning of the therapy. Notably, when combining RT with anti-CTLA-4 antibodies, the therapeutic effect on both tumor #1 and tumor #2 was enhanced resulting in up to 80% of complete responses with durable regression of both tumors (Figure 3.16). These findings were reproduced when using carbon ion irradiation inducing similar antitumor effects on local and distant tumors (Figure 3.19, Supplementary Figure 5.8). Of note, therapies were tested on different tumor volumes and it appeared that therapeutic efficacy correlated with the tumor volume at treatment start. Thus, the smaller tumor #1 at the beginning of the therapy, the more efficient was the control of tumor growth. Consequently, to truly compare photon versus carbon ion RT, a side-by-side comparison of RT plus anti-CTLA-4 therapy was performed (Figure 3.20). Interestingly, when considering monotherapy with RT, photon RT appeared slightly superior to carbon ion RT in controlling tumor growth of tumor #1. However, due to the outgrowth of tumor #2, which was again not affected by RT alone, no differences in survival could be observed between both groups. This highlights one limitation of the bilateral tumor model, as long-term monitoring of tumor #1 cannot be performed, if tumor #2 grows out unaffected. Having observed different antitumor efficacy of monotherapy with photon and carbon ion RT *in vivo*, biologically equivalent doses that were determined by clonogenic survival assays in *vitro*, might not be fully transferable to the *in vivo* situation, where tumors are surrounded by the tumor stroma, vasculature and the TME. It would be worthwhile to investigate, if these discrepancies between *in vitro* and *in vivo* RBEs also occur in other tumor models. Yet, to our knowledge, there is no study published that compares therapeutic efficacies using RBE-matched doses of photon and carbon ion irradiation *in vivo*. Possibly, one

could determine BEDs and RBEs *in vivo,* however this would be much more elaborative and the clonogenic survival assays seems to provide a suitable approximation. Indeed, in the clinical situation, RBE values are frequently approximated to values between 2 and 3 based on empirical data and experience from photon RT schemes [359]. Importantly, when combining RT with anti-CTLA-4 therapy, there was no difference at both tumor sites between photon versus carbon ion RT. Since RT is frequently applied as combination therapy nowadays [360-362], exact definitions of RBEs might be less relevant.

Remarkably, anti-CTLA-4 therapy was more efficient in the EO771 model compared to anti-PD-L1 therapy. Although both therapies are considered as immune checkpoint inhibitors leading to the (re-)activation of T cell responses, they have distinct mechanisms of actions, which might explain the difference in therapeutic efficacy observed in this study. Anti-CTLA-4 antibodies target an early phase of the immune response enabling efficient T cell priming, activation, and proliferation in the lymph nodes. Moreover, blocking of CTLA-4 on Tregs can counteract their suppressive functions [363]. Accordingly, several preclinical studies reported that effective anti-CTLA-4 therapy depends on ADCC -mediated Treg depletion [364, 365]. In humans, it is under debate whether clinically approved anti-CTLA-4 antibodies deplete Tregs. Recently, Sharma *et al.* showed that treatment of melanoma, prostate cancer, and bladder cancer patients with ipilimumab induced increased T cell infiltration, but no significant differences in the abundance of Tregs [366]. These findings highlight the limitations of preclinical mouse models, which cannot be directly transferred to the human situation. Modification of the Fc receptor might be a potential strategy to achieve ADCC-mediated Treg depletion also in clinical applications [367]. In contrast to anti-CTLA-4 antibodies, checkpoint blockade of PD-1/PD-L1 predominantly intervenes with the effector phase of an immune response restoring T cell functions within the peripheral tissue. Furthermore, the expression patterns differ, with PD-1 being expressed on activated T cells, B cells, and macrophages and PD-L1 being expressed on tumor cells and leukocytes, whereas CTLA-4 expression is restricted to T cells [363]. In fact, a preclinical study did not only show the restoration of T cell responses after anti-PD-L1 therapy, but also improved DC and myeloid cell maturation in a chronic lymphocytic leukemia model [368]. Yoshida *et al.* recently reported that PD-1-specific antibodies also might have Treg-depleting mechanisms [369]. However, if these preclinical findings translate to mechanisms of action in humans still needs to be elucidated.

While combined RT and immunotherapy had not been investigated in the EO771 tumor model so far, other preclinical models corroborate the rationale for combining RT plus immunotherapy. In the B16F10 model, photon RT plus dual immune checkpoint blockade against CTLA-4 and PD-L1 led to superior tumor control eliciting abscopal effects [261]. As the EO771 tumor model was already quite responsive to RT plus anti-CTLA-4 therapy, RT plus dual immune checkpoint blockade was tested on mice that had developed large tumors. However, in this setting, dual immune checkpoint blockade did not result in any survival benefit or increased abscopal effects compared to anti-CTLA-4 therapy when combined with photon RT (Figure 3.17). A study by Rodriguez-Ruiz *et al.* showed that local and distant tumor control cannot only be achieved by combining RT with immune checkpoint-blocking antibodies, but also anti-4-1BB agonists synergized with photon RT [348]. Moreover, local and distant tumor control have been reported when combining RT with TRL9 agonists, anti-VISTA therapy, anti-OX-40 agonists, and intra-tumoral DC injections [370-373]. The suitable combination of RT plus immunotherapy might also depend on the fractionation scheme. Thus, treatment with anti-PD-L1 and anti-TIGIT antibodies were most efficient when combined with 3 x 8 Gy compared to 18 x 2 Gy. In contrast, when only anti-PD-L1 therapy was combined with RT, 18 x 2 Gy performed better than 3 x 8 Gy in the same study [374]. This highlights a major

challenge of RT, as optimal fractionation schedules still need to be elucidated. Interestingly, in a prostate cancer model, PD-L1 expression was shown to be upregulated by RT with 3 x 5 Gy, but anti-PD-L1 blockade did not yield in any survival benefit indicating that RT does not generally synergize with immunotherapy [375]. While the combination therapies described so far were performed with the classical photon irradiation, also first reports describing a synergism between carbon ion RT and immunotherapy have been published. Thus, in an osteosarcoma model, carbon ion therapy plus dual immune checkpoint blockade induced local and distant antitumor effects [376]. Moreover, there is one study by Helm *et al.* directly comparing carbon ion RT to photon RT when combined with dual immune checkpoint blockade in an osteosarcoma model. Indeed, the authors show superior tumor control by carbon ion RT, however they use physical doses of 10 Gy for both photon and carbon ion radiation neglecting the physical differences between photon and carbon ion RT [377].

## 4.7 Immune cell infiltration in the irradiated tumor site (tumor #1)

Having observed clear differences in therapeutic efficacies between the treatment groups, the immune cell infiltration in tumor #1 and tumor #2 was characterized to define, which immune cell populations might be associated with antitumor responses. To this end, the focus was set on combination therapy with checkpoint blockade against CTLA-4 due to its superior efficacy in the EO771 tumor model. In tumor #1 clear immune profiles were observed that were largely overlapping between photon and carbon ion RT. First, RT increased leukocyte infiltration into tumor #1 (Figure 3.22). Different mechanisms of irradiation-induced immune cell infiltration have been described. (1) RT potentially modulates the tumor vasculature. Different dose regimes were shown to enhance pericyte coverage and perfusion in a prostate and lung cancer model, which might facilitate immune cell infiltration [378]. By contrast, other studies report vessel destruction, increased hypoxia, and reduced perfusion after high-dose irradiation with single doses exceeding 10 Gy [379-381]. Overall, the relationship between tumor vasculature and RT does not seem to be fully elucidated yet. (2) Expression of cellular adhesion molecules like ICAM-1 and VCAM-1 is upregulated by RT possibly facilitating adherence and transmigration of leukocytes [222]. (3) Increased levels of irradiation-induced chemokines, including CXCL10 and CXCL16, might attract leukocytes to the TME [223, 224]. Generally, leukocytes might either be tumor-resident before RT or newly infiltrating after RT. Regarding T cell infiltration, the draining lymph nodes seem to be crucial. Thus, Zhang *et al.* showed that blockade of the draining lymph nodes largely reduced the infiltration of total and antigen-specific $CD8^+$ CTLs after RT both in local and distant tumors [349]. Likewise, Marciscano *et al.* showed that irradiation of the draining lymph nodes reduces T cell trafficking and infiltration into tumors [382]. Importantly, both tumor-resident and newly infiltrated immune cells were crucial for therapeutic efficacy of combined RT plus anti-PD-1 blockade in the CT26 model [383].

Considering $CD4^+$ T cell infiltration, two major observations were made in the present study. First, RT alone increased the proportions of Tregs among $CD4^+$ T cells. Mechanistically, Tregs are comparably radioresistant, while *de novo* synthesis might be initiated by irradiation-induced TGF-β activation [384-386]. Second, anti-CTLA-4 therapy significantly reduced frequencies of Tregs both after monotherapy and combination therapy highlighting the Treg-depleting functions of CTLA-4 antagonists in preclinical models [364, 365]. At the same time, $CD8^+$ T cell infiltration was increased by anti-CTLA-4 monotherapy, but decreased by both radiation types. When only considering frequencies of infiltrated cells, one could assume that anti-CTLA-4 therapy was most beneficial as Treg numbers were reduced and $CD8^+$ T cell infiltration increased. However, tumor growth curves showed that anti-CTLA-4 monotherapy hardly

affected tumor growth. On the one hand, one needs to consider that irradiation-induced cytotoxicity exerts strong antitumor effects, also independent of immune cells. Thus, depending on the tumor stage, RT alone might be effective despite increased Treg frequencies and reduced $CD8^+$ CTL numbers. On the other hand, it is not only the frequencies that matter, but also the functional status of immune cells. In fact, in the Panc02 model, preexisting tumor-infiltrating lymphocytes showed reduced proliferative potential after irradiation with 20 Gy, however still retained their motility and enhanced tumor-specific effector functions [387].
Expression of immune checkpoint molecules and co-stimulatory markers appeared most beneficial after combination therapy compared to the other treatment groups being in line with superior tumor growth control. Thus, both $CD4^+$ and $CD8^+$ T cells showed decreased frequencies of cells expressing the immune checkpoint molecules PD-1 and LAG-3 compared to untreated tumors (Figure 3.23, Figure 3.25). This points towards antitumor effector functions, as co-expression of both markers is associated with an exhausted T cell phenotype [388]. Moreover, expression of CTLA-4, which is constitutively expressed in Tregs [281], was significantly decreased in $CD4^+$ T cells, which is in consistence with the decreased frequencies of Tregs. In addition, CD73 is a marker expressed by Tregs [389]. Surprisingly, while the number of CD73-expressing $CD4^+$ T cells was reduced after anti-CTLA-4 monotherapy, frequencies were increased after combination therapy. However, CD73 expression is not only confined to Tregs, but also inflammatory Th17 are positive for CD73 [390]. In fact, Th17 cells are associated with both pro- and anti-inflammatory function [39], however in the present study the antitumor functions seemed to predominate. Regarding expression of CTLA-4 and CD73 in $CD8^+$ T cells, both markers were significantly upregulated after treatment with RT plus anti-CTLA-4 antibodies. Interestingly, in contrast to its reputation as a suppressive marker, CD73 expression on circulating $CD8^+$ CTLs has been associated with better survival and superior functions in AML patients. Indeed, $CD73^-CD8^+$ CTLs showed higher levels of PD-1 and LAG-3 expression [391, 392], which was also observed in the present study. CTLA-4 expression is generally lower in $CD8^+$ T cells compared to $CD4^+$ T cells [393] and functional relevance of $CD8^+CTLA\text{-}4^+$ CTLs remains to be elucidated. Interestingly, expression of the co-stimulatory molecule 4-1BB was the lowest in combination therapy group, both in $CD4^+$ and $CD8^+$ T cells (Figure 3.24, Figure 3.26). Moreover, while CD69-expressing T cells were most abundant in the combination group, the overall percentages were rather low and thus might be less relevant. However, this does not necessarily mean that T cells were less activated, but might rather be affected by the time point of analysis. Thus, both markers are transiently upregulated in the early phase after T cell stimulation [394]. Downregulation of these co-stimulatory molecules might reflect the tight control of the inflammatory response. Overall, the analysis of immune checkpoint and co-stimulatory molecules point towards activated and non-exhausted T cells that synergize with the cytotoxic effects of RT to control tumor growth.
Indeed, RT alone was associated with higher frequencies of Tregs and $CD4^+CTLA\text{-}4^+$ T cells highlighting the suppressive effects of ionizing radiation. However, particularly in the $CD8^+$ compartment an immune signature associated with pro-inflammatory immune responses was detected. Pointing towards the immunostimulatory capacities of RT, irradiated tumors showed comparably low frequencies of PD-1 and LAG-3-expressing $CD8^+$ T cells, together with increased proportions of CTLA-4- and CD73-expressing $CD8^+$ T cells, which closely resembles the marker expression profiles of $CD8^+$ T cells after combination therapy. Overall, it appeared that monotherapy with RT induced rather pro-inflammatory responses in the $CD8^+$ compartment and anti-inflammatory responses in the $CD4^+$ compartment. In fact, a study in renal cell carcinoma patients analyzed tumors resected after SBRT showing that RT reshapes the T cell repertoire initiating increased T cell clonality, transient expansion of tumor-

enriched clonotypes in the periphery, and transcriptional signatures associated with immunogenicity [395].
Apart from T cells, the infiltration of tumor #1 by NK cells, DCs, and myeloid cells was analyzed. Overall, frequencies of NK cells were rather low, but could be increased by RT with or without immune checkpoint blockade against CTLA-4 (Figure 3.27), which most likely enhances antitumor cytotoxicity. Indeed, NK cells are relevant in antitumor responses in the EO771 model, as NK cell depletion promotes tumor growth [396]. In contrast to NK cells, frequencies of DCs were decreased after RT. Although DCs are essential for T cell priming and cross-presentation, they are rather associated with a dysfunctional phenotype and anergizing functions within the TME [75, 76] and thus, low frequencies might be beneficial. Surprisingly, the combination therapy increased the frequencies of MDSCs and M2-like macrophages (Figure 3.28), which would contradict the superior therapeutic efficacy. In fact, these results are in line with previous reports showing that irradiation-induced CSF-1 expression promotes polarization of M2-like TAMs, which are in addition comparably radioresistant [245-247]. However, although around 70% of all leukocytes in EO771 tumors are myeloid cells, they might be functionally less involved in antitumor immune responses compared to T cells. Likewise, decreased numbers of TAMs after splenectomy did not affect the growth of primary EO771 tumors [397]. Depletion experiments of immune cell populations could clarify, which immune cells are essential for antitumor immune responses induced by combination therapy.
Finally, when comparing photon versus carbon ion RT, the overall infiltrating immune cell profiles were comparable. In the combination therapy group, no major differences in immune cell infiltration of tumor #1 were observed, which is in line with comparable efficacy in tumor growth control (Figure 3.20). Interestingly, expression of immune checkpoint molecules and co-stimulatory molecules on $CD8^+$ T cells after carbon ion RT alone closely resembled the carbon ion RT plus anti-CTLA-4 group with some markers being expressed to a similar extent. In contrast, after photon RT, frequencies of PD-1 and LAG-3 expressing T cells were indeed decreased compared to untreated tumors, however to a smaller extent compared to tumors treated with photon RT plus anti-CTLA-4 antibody. These data might indicate that $CD8^+$ T cells might have superior effector functions after monotherapy with carbon ion RT compared to photon RT. However, this is contradictory to the observation made in tumor growth experiments, where photon RT appeared more effective than carbon ion RT. Certainly, further experiments are necessary to clarify this discrepancy. First, experiments should be repeated in side-by-side studies to validate these findings. Second, IFN-γ and granzyme B secretion by $CD8^+$ CTLs could be analyzed to prove functional activation in addition to phenotypic characterization. For instance, in an osteosarcoma model, single dose RT with 5.3 Gy carbon ions did not result in increased frequencies of $CD8^+$ T cells expressing granzyme B compared to untreated tumors [376]. Lastly, one should more closely investigate the cytotoxic affect *in vivo* that might be enhanced after photon RT and thus leading to improved tumor control. Still, to our knowledge, this study is the first one providing such comprehensive immune cell profiling after carbon ion RT plus checkpoint blockade.

## 4.8 Antitumor effects in distant tumor sites (tumor #2)

In the present study, it was reproducibly shown that combined therapy of photon and carbon ion RT plus anti-CTLA-4 checkpoint blockade induced growth regression not only of irradiated tumors, but also at distant tumors sites (tumor #2). The observation that local irradiation can initiate abscopal effects on tumor metastases was already observed in the 1950s and increasing evidence suggests that RT provides an *in situ* vaccine promoting antitumor immune

responses [252, 398]. Consequently, immune cell infiltration in tumor #2 was analyzed, but immune cell profiles were less informative compared to tumor #1, mainly due to the huge variations in individual samples within all treatment groups.

Still, a few differences were observed, which were shared by the anti-CTLA-4 and the combination therapy group and can primarily be accredited to the effects of an anti-CTLA-4 therapy. On the one hand, frequencies of Tregs were decreased, which was accompanied by decreased expression of CTLA-4 and CD73 by $CD4^+$ T cells (Figure 3.29, Figure 3.30). On the other hand, the proportions of $CD8^+$ T cells were increased, however with high variation in the expression of immune checkpoint molecules and co-stimulatory molecules. Overall, one cannot distinguish, if immune cell infiltration in tumor #2 was mainly driven by anti-CTLA-4 therapy or also by an *in situ* vaccination effects from RT. Thus, in the bilateral EO771 tumor model, it could not be clearly determined, whether tumor regression in tumor #2 after combination therapy was due to real abscopal effects initiated by ICD induced upon RT. Possibly, due to the control of tumor #1 by RT, anti-CTLA-4 therapy can take its time to operate on tumor #2 after combination therapy. Unfortunately, as tumor #1 grows out exponentially after anti-CTLA-4 therapy, one cannot monitor the effects of monotherapy on tumor #2. One solution to further track tumor #2 after anti-CTLA-4 therapy would be surgical removal of tumor #1. Still, even though there were no differences observed between the anti-CTLA-4 and RT plus anti-CTLA-4 group in tumor cell infiltration, this does not necessarily mean that no abscopal effects occurred. Thus, one needs to consider that immune cells were only analyzed at one time point and irradiation-induced immune effects on distant tumors might only occur later. In fact, in a bilateral B16-CD133 tumor model treated with RT plus anti-PD-L1 antibodies, increased numbers $CD8^+INF\text{-}\gamma^+$ CTLs in distant tumors were only found on day 15, but not on day 8 after starting the treatment. By contrast, enhanced frequencies of $CD8^+INF\text{-}\gamma^+$ CTLs were infiltrating the local irradiated tumor at both time points [349]. In the present study, tumors could not be analyzed at later time points due to the outgrowth of tumor #1 in the control groups (untreated and aCTLA-4 group). To clarify, if true abscopal effects have occurred, analysis of the TCR repertoire might give some indication. Dovedi *et al*. showed that the TCR diversity in a distant tumor site was increased after combination therapy, but not monotherapies, with RT plus anti-PD-L1 antibody, indicating that combination therapy induced an immune response beyond both monotherapies alone [383]. Moreover, Ruhland *et al.* developed a method for antigen tracking [399], which could be used to demonstrate the occurrence of true abscopal effects. Thus, if tumor #1 was transduced to express ZsGreen, DCs and other phagocytic cells would take up the dye. If true abscopal effects occur, one would not only expect the dye in the draining lymph nodes of tumor #1, but also in the lymph nodes of tumor #2.

In a small pilot experiment, cell surface marker and cytokine expression profiling by ScioCD in tumor #2 was performed to get further insights beside the flow cytometry analysis, why tumors #2 regressed after photon RT plus anti-CTLA-therapy, but not upon monotherapy with photon RT (Figure 3.32). As changes in immune cell activation might only occur later in tumor #2 [349], tumors were analyzed 9 days after starting the treatment, which was feasible as outgrowth of tumor #1 had been controlled by RT in both groups. Overall, 50 proteins were more abundantly expressed in the photon RT + CTLA-4 group compared to the photon RT + IgG group. Some of these proteins were associated with pro-inflammatory responses. Thus, one of the most abundantly differently expressed proteins was the activating NK-cell receptor KI2L2 pointing towards contribution of NK cells in antitumor responses, which is in line with a previous study showing the relevance of NK cells for controlling EO771 tumors [396]. Moreover, increased expression levels of MHC class I molecules, and IL-17, which is in particular produced by Th17 cells, are indicative for a pro-inflammatory T cell responses.

Indeed, activated T cells might be attracted to the tumor by CXCL11 [400], which also showed higher abundancy in the RT + aCTLA-4 group. Remarkably, eight out of the 50 enriched proteins were members of the TNF superfamily, which exert pleiotropic functions. Among them was TNF-α, which may induce apoptosis of tumor cells, block Tregs, and promote M1 polarization of macrophages [401]. However, also immunosuppressive proteins were enhanced including members of the TGF-β family and LAG-3, which might be an escape mechanism of tumors. Additional blocking of TGF-β or LAG-3 might be promising to further enhance antitumor efficacy [402, 403]. Interestingly, p53 was among the most abundant genes, which might be a stress response of tumor cells. However, p53 is mutated in EO771 cells and is probably not functional [271]. In fact, it has been shown that mutant p53 accumulates in tumor cells upon stress, as degradation pathways are impaired [404]. Surprisingly, CD80, the ligand for CTLA-4, and INF-γ were less abundantly expressed after photon RT plus anti-CTLA-4 blockade compared to RT alone. Classically, CD80 expression is confined to APCs [52], however the CD80 expression detected in this experiment might rather have originated from EO771 cells, as IFN-γ was shown to induce CD80 expression on tumor cell lines, which might be an escape mechanism of tumors presenting a ligand for anti-CTLA-4 [405, 406]. After anti-CTLA-4 therapy, this interaction would be blocked.

While abscopal effects have been reported with increasing frequencies in preclinical models after radioimmunotherapy [261, 349, 370-373, 407] (see also section 4.6), abscopal affects in humans are only rarely observed [253-256]. First of all, one needs to consider that mouse models have several limitations and can never completely mimic the situation in humans. Thus, most of the bilateral studies use heterotopic tumor cell implantations, in which a large number of tumor cells are injected s.c. into the flank or hind leg of a mouse, which largely differs from long-lasting tumorigenesis in humans [408]. Still, these models are frequently used, as heterotopic models are quite easy to handle and RT can be quite easily applied. Moreover, the distant tumor, which should mimic metastases formation, is implanted with the same tumor cell line, whereas in humans metastases might have evolved being molecularly different from the primary tumor [409]. Studies with orthotropic and autochthonous mouse models would more closely mimic human tumors and it would be of great interest, if abscopal affects also occur in these models. Indeed, with the development of preclinical irradiators that perform precise RT of inlying murine tumors guided by CT imaging would allow such studies [410]. Moreover, using tumor models that spontaneously develop metastases, like the 4T1 model [411], could show if radioimmunotherapy also affects true metastases located in different organs of the body. Still, mouse models provide some valuable mechanistic insights, how abscopal effects occur. Thus, it has been shown that irradiation-induced cytosolic dsDNA stimulates the cGAS-STING pathway and subsequent release of type I IFNs, which seems to be essential for the induction of abscopal effects. In fact, clearance of dsDNA by autophagy was shown to reduce the occurrence of abscopal effects and upregulation of Trex1 upon high single doses greater than 12-18 Gy, but not fractionated schedules with 3 x 8 Gy, degraded ds DNA and impaired abscopal effects. [257, 258]. This highlights one major challenge of radioimmunotherapy, as optimal timing and dosing for the induction of abscopal effects are still under debate. However, a magnitude of phase I/II clinical trials have been initiated recently (e.g. NCT02406183, NCT02562625, NCT02538471), which might finally increase the understanding of abscopal effects in patients.

## 4.9 Induction of tumor-specific memory T cell responses upon radioimmunotherapy

To investigate, if cured mice had developed EO771-specific memory T cell responses after radioimmunotherapy, mice were re-challenged with EO771 tumor cell injections >3 month after initial tumor cell implantation. In mice treated with photon RT plus anti-CTLA-4 antibody, two observations pointed towards a tumor-specific memory formation. (1) All ten mice rejected a secondary tumor cell engraftment, whereas all naïve mice developed tumors (Figure 3.33). (2) When splenocytes of regressor mice were co-cultured with EO771 cells, a distinct IFN-γ response was observed indicating that splenic memory T cells became activated upon antigen exposure. The lack of IFN-γ response upon stimulation with B16F10 and RMA cells (both of C57BL/6 origin), confirmed that memory responses were EO771-specific. Moreover, one potential epitope was analyzed, which might be recognized by memory T cells. The epitope was derived from gp-70, which is the envelope protein of MuLV and a shared antigen expressed in a variety of murine tumor cell lines [274, 279], including EO771 as shown by qPCR analysis in the present study. However, when adding the gp-70-specific CTL epitope to splenocytes of regressor mice, no signficanlty increased numbers of IFN-γ spots were observed compared to medium control. Consequently, the epitope of gp-70 is most likely not the major antigen that is recognized on EO771 cells. Furhtermore, if memory responses were directed against gp-70, one would expect recognition of B16F10 cells, as these express gp-70 to a higher level compared to EO771 (at least at the mRNA level). Thus, EO771-specific neoantigens most likely drive antitumor immune responses.
Intrestingly, while three out of four mice pre-treated with photon RT plus anti-PD-L1 antibodies rejected tumor cell engraftment, no robust IFN-γ reponse against EO771 cells was observed. Similar results were reported by Veinalde *et al.*, who showed that re-challenge of mice cured with an oncolytic measles virus armed with an anti-PD-L1 antibody rejected secondary tumor cell engraftment to 100%. However, IFN-γ secretion was not affected when splenocytes were stimulated with target cells [155]. In accordance with the enhanced antitumor efficacy, photon RT plus anti-CTLA-4 seemed to evoke stronger and more persistant memory responses. Thus, memory cells might have prevented secondary tumor cell engraftment, but might not be detectable in the spleen 2 weeks after re-challenge. Moreover, only IFN-γ respsones at one time point occuring in the spleen were studied. However, different memory T cell subsets show distinct migration patterns and it might be conceivable that memory responses might be only detectable in the periphery or at other time points [412].

## 4.10 Summary and outlook

The current work shows that RBE-matched doses of classical photon radiation and radiation with carbon ions induce similar cytotoxic and immunomodulatory effects in the EO771 breast cancer model *in vitro* and *in vivo*. Previous studies demonstrated that carbon ion radiation has biological and physical advantages over photon radiation, however little had been known about immunomodulatory effects caused by carbon ion irradiation.
Throughout this study, biologically equivalent doses of photons and carbon ions as determined by clonogenic survival assays were used in comparative side-by-side experiments. Applying BED of photons and carbon ions to EO771 cells, it was found that both irradiation types reduced cell proliferation, initiated a transient G2/M cell cycle arrest, and induced apoptosis and cell death in a dose-dependent manner. Moreover, the expression of MHC class I molecules, immune checkpoint molecules (PD-L1 and CD73), and the danger signal HMGB1 were shown to be dose-dependently increased. Of note, irradiation also enhanced the

susceptibility of EO771 cells towards CTL-mediated lysis in a dose-dependent way. Interestingly, immunomodulation induced by photon and carbon ion irradiation was comparable, when similar cytotoxicity was induced with RBE-matched doses. Moreover, the magnitude of cytotoxic effects was associated with the extent of immunomodulation. These results may indicate that immunomodulation is directly linked to cytotoxicity and DNA damage. To prove this hypothesis, DNA damage and repair mechanisms and their effect on immunomodulation should be investigated.

*In vivo*, combined radioimmunotherapy with immune checkpoint blockade against CTLA-4 proved most efficient in controlling outgrowth of both local and distant (non-irradiated) tumors. Remarkably, up to 80% of mice showed complete responses and even very large tumors (volume reaching > 1000 $mm^3$) were completely rejected highlighting the huge therapeutic potential of radioimmunotherapy. Based on flow cytometric analyses, tumors #1 treated with RT plus anti-CTLA-4 checkpoint blockade were infiltrated by higher amounts of T cells with activated phenotype and by reduced frequencies of Tregs compared to untreated tumors. Interestingly, these tumors showed stronger accumulation of M2-like macrophages, which however, did not appear to impair regression of tumors #1. Depletion experiments targeting T cells, NK cells and macrophages might enable identification of the immune cell population(s) actually driving the anti-tumor immune response.

In fact, distant tumors were reproducibly rejected after combination therapy, but analysis of immune cell infiltration could not clarify which immune cell populations were responsible for tumor regression. Here, future experiments should focus on the identification of mechanisms responsible for distant tumor cell rejection and elucidate if these were true abscopal effects. For instance, analysis of the TCR repertoire in both tumors could help to clarify these questions. Remarkably, a tumor-specific memory response was formed in 100% of mice that had shown complete responses after photon RT plus anti-CTLA-4 therapy. It is therefore planned to characterize the tumor–specific memory responses established in mice upon carbon ion RT plus immune checkpoint blockade.

When comparing monotherapy with photons and carbon ions in the EO771 tumor model, photon RT appeared slightly superior compared to carbon ion RT. To investigate the underlying mechanisms, further analysis of the cytotoxic effects and studies on the tumor vasculature and on stromal cells could give some insights. Although the RBE-matched photon and carbon ion doses induced comparable cytotoxicity *in vitro*, the situation might be different *in vivo*, where tumors are embedded within a complex TME. To study radiogenic effects on the irradiated tumor site, experiments with unilateral tumor cell injections are more suitable, as mice do not need be sacrificed at premature time points due to the outgrowth of the distant tumor.

Taken together, this preclinical study provides a broad overview of immunomodulatory effects induced by photon and carbon ion irradiation *in vitro* and *in vivo.* It furthermore shows that radioimmunotherapy with photon or carbon ion irradiation holds great therapeutic potential for the treatment of local and distant tumors. Here, radioimmunotherapy using carbon ions appears as preferable treatment regimen, due its favorable physical characteristics allowing focused energy release at the targeted tumor site even in deeper tissues, while sparing surrounding tissue from harmful irradiation.

To our knowledge, this is the first study showing a comprehensive side-by-side investigation of the radio-immunogenic effects caused *in vivo* by carbon ion and photon RT, respectively, using RBE-matched doses.

# 5 Supplementary Material

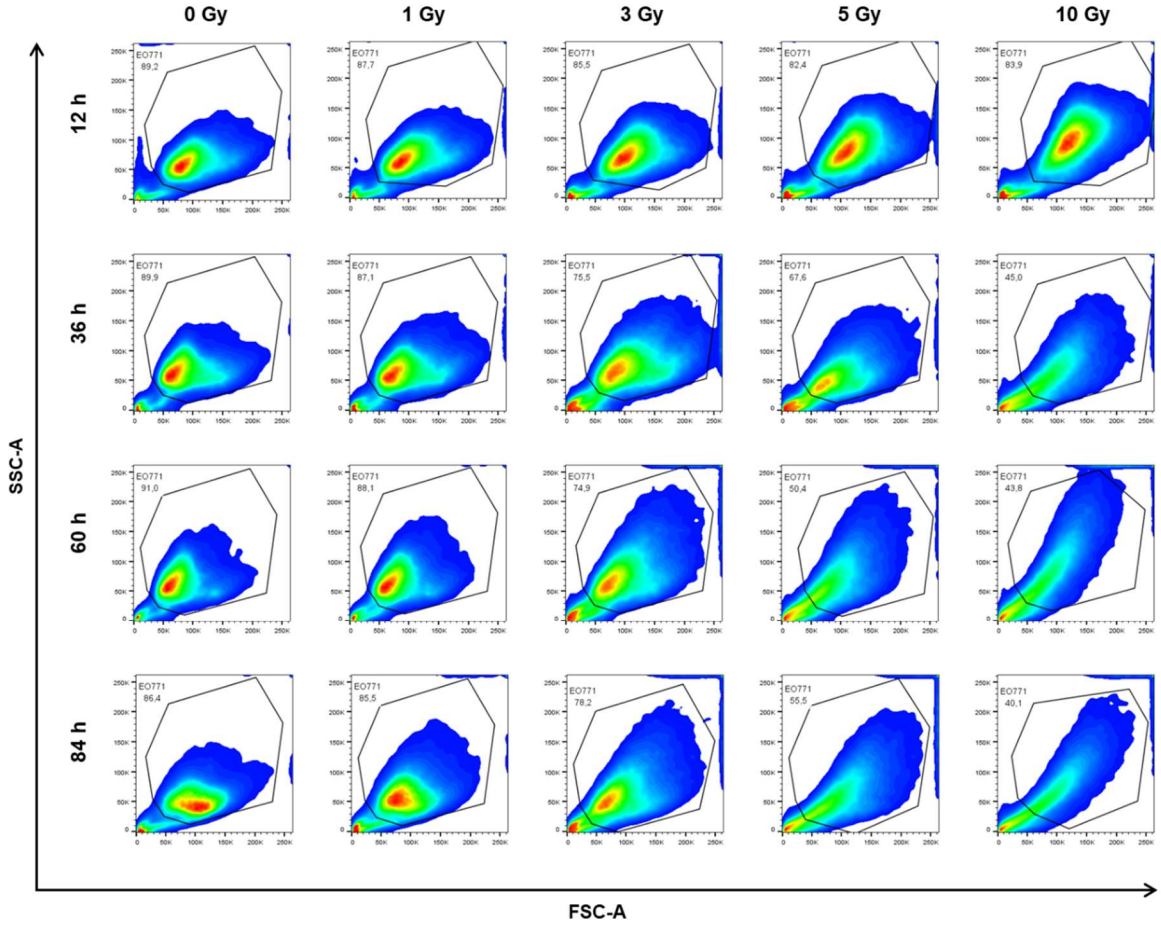


**Supplementary Figure 5.1. Morphological changes of EO771 cells after irradiation.** Having irradiated EO771 cells with graded doses of photons, cells were analyzed by flow cytometry for size (FSC-A) and granularity (SSC-A) after 12, 36, 60 and 84 h.

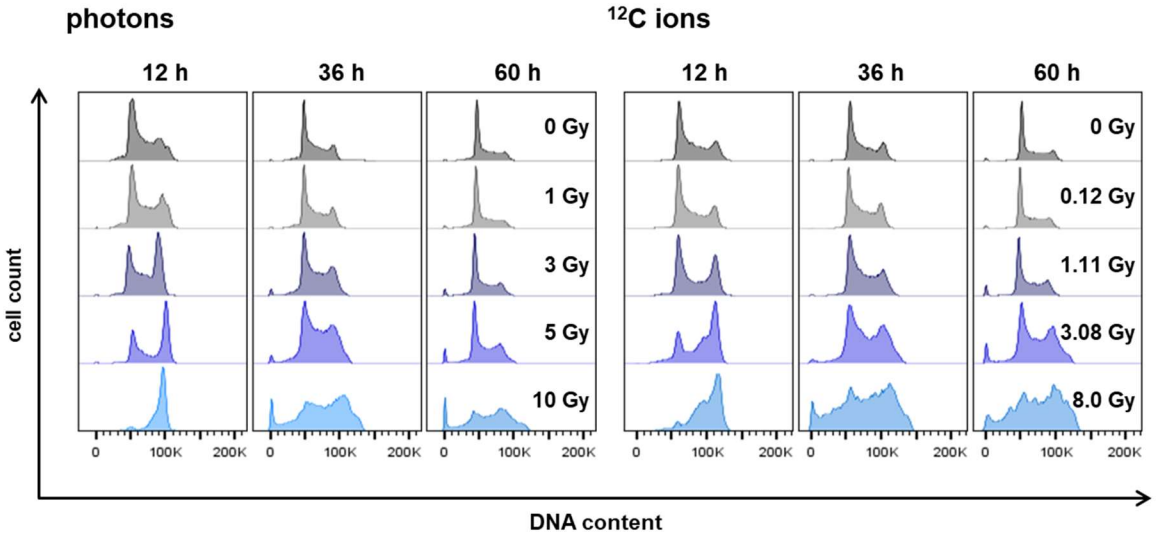


**Supplementary Figure 5.2: Cell cycle analysis of irradiated EO771 cells**. 12, 36, and 60 h after irradiation of EO771 cells with graded doses of photons or biologically equivalent doses of carbon ions, cell cycle stages were analyzed by staining of DNA with PI and subsequent flow cytometric analysis. Histograms of cell cycle analysis for cells irradiated with photons (left) and carbon ions (right), respectively. Representative results of one out of two independent experiments are shown. Gating strategy: cells (FSC-A vs. SSC-A) → single cells (FSC-A vs. FSC-H) → single cells (PI-A vs. PI-W) → PI-A vs. count.

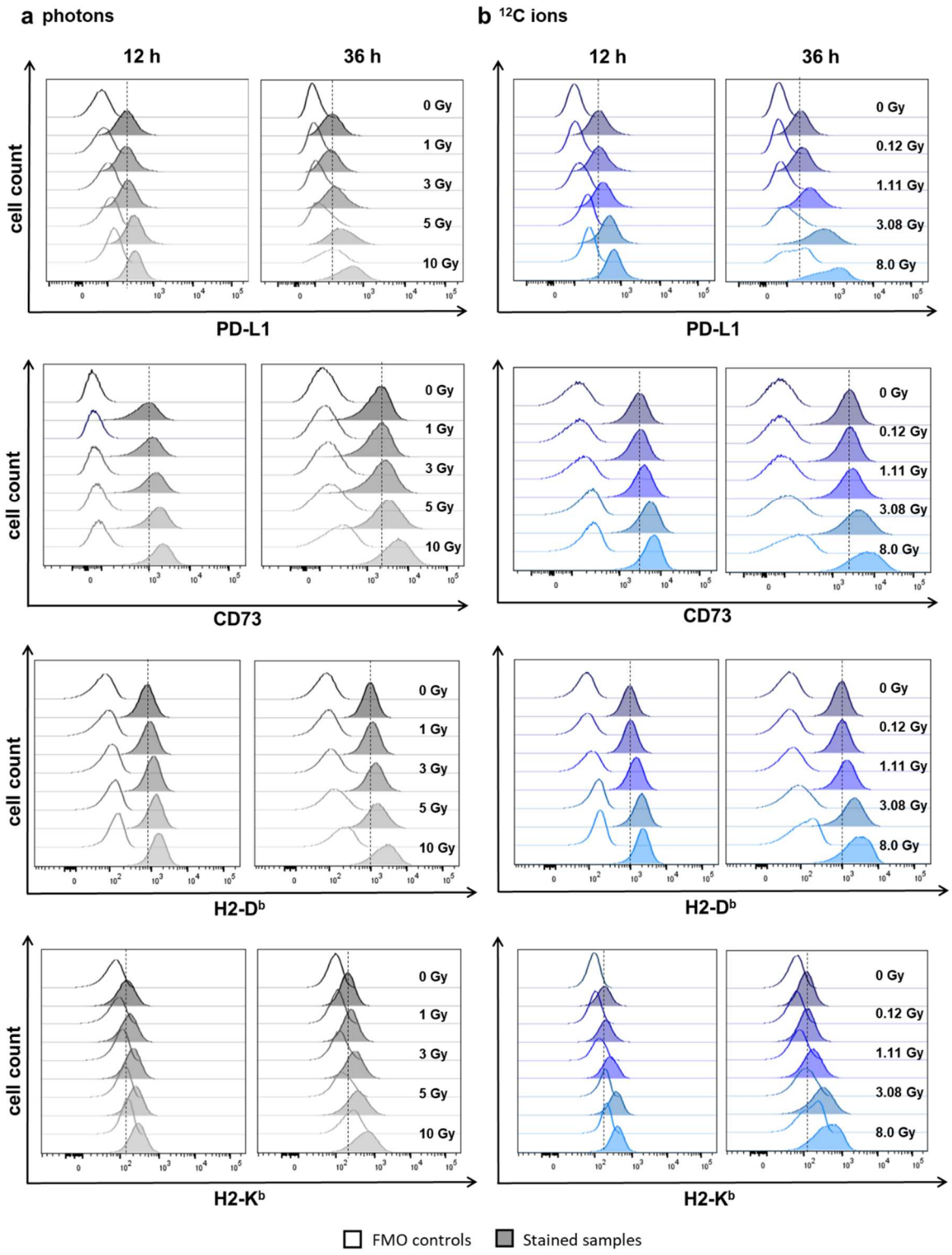


**Supplementary Figure 5.3: Cell surface expression of immunomodulatory molecules on irradiated EO771.** **(a)** and **(b)** Hisotgrams of flowcytometric analysis of PD-L1, CD73 and MHC-I (H2-D$^b$ and H2-K$^b$) cell surface expression on EO771 cells 12 and 36 h after irradiation with graded doses of photons or biologically equivalent doses of carbon ions. Clear histograms show fluorescence minus one (FMO) controls, filled histograms stained samples. Representative results of one out of two independent experiments are shown.

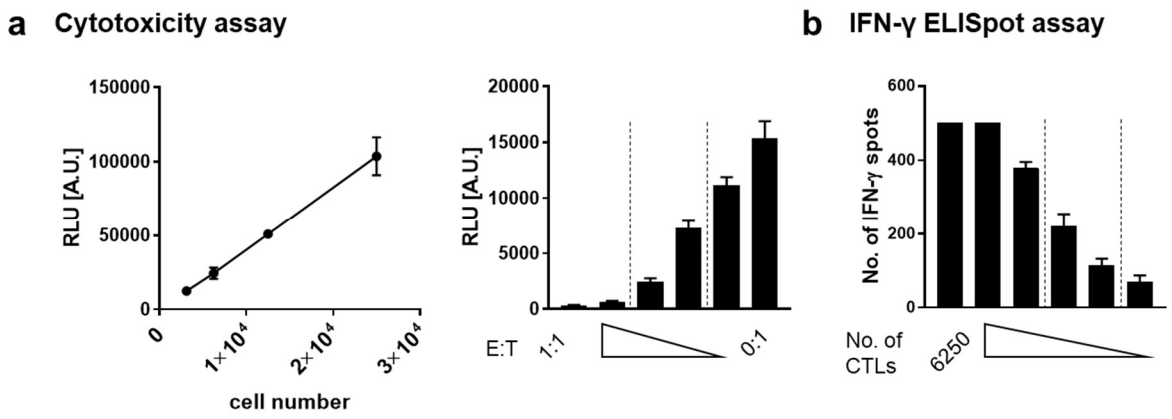


**Supplementary Figure 5.4: Establishment of co-cultures of EO771/Luci/OVA cells and OVA-specific CTLs**. **(a)** Setup of a luciferase-based cytotoxicity assay. Titration of EO771/Luci/OVA cell numbers. Relative luminescence units (RLU) were determined 18 h after seeding (left). Titration of OVA-specific CTLs on 5000 EO771/Luci/OVA cells, starting with an effector to target cell (E:T) ratio of 1:1 followed by serial 1:2 dilutions (right). 18 h after starting the co-culture, the assay was developed. **(b)** Setup of IFN-γ ELISpot assay. Titration of OVA-specific CTLs on 50 000 EO771/Luci/OVA cells, starting with 6250 CTLs followed by serial 1:2 dilutions. The assay was developed 18 h after starting the co-culture. Dashed lines indicate E:T ratios selected for further experiments.

**Supplementary Table 5-1: DAVID functional annotation chart.** Genes differentially upregulated after photon or carbon ion irradiation compared to untreated EO771 cells were subjected to pathway analysis. Most relevant biological terms are shown. Default p-values (<0.1) were used. Terms were either predicted after photon irradiation, carbon ion irradiation or both after photon and carbon ion irradiation. The counts indicate the number of genes associated with the annotation term for either photon or carbon ion-irradiated cells.

| biological term | predicted for | counts photons/$^{12}$C ions |
|---|---|---|
| Focal adhesion | both | 10/9 |
| ECM-receptor interaction | both | 7/6 |
| Staphylococcus aureus infection | both | 5/6 |
| Natural killer cell mediated cytotoxicity | both | 6/6 |
| Tuberculosis | both | 7/7 |
| B Lymphocyte Cell Surface Molecules | both | 3/3 |
| Leukocyte transendothelial migration | both | 5/6 |
| Renin secretion | both | 4/4 |
| Chemokine signaling pathway | both | 6/8 |
| PI3K-Akt signaling pathway | photons | 8/- |
| Legionellosis | photons | 4/- |
| Circadian entrainment | photons | 4/- |
| Estrogen signaling pathway | photons | 4/- |
| Pancreatic secretion | photons | 4/- |
| TNF signaling pathway | $^{12}$C ions | -/6 |
| Toll-like receptor signaling pathway | $^{12}$C ions | -/5 |
| Salivary secretion | $^{12}$C ions | -/4 |
| Rheumatoid arthritis | $^{12}$C ions | -/4 |
| Protein digestion and absorption | $^{12}$C ions | -/4 |

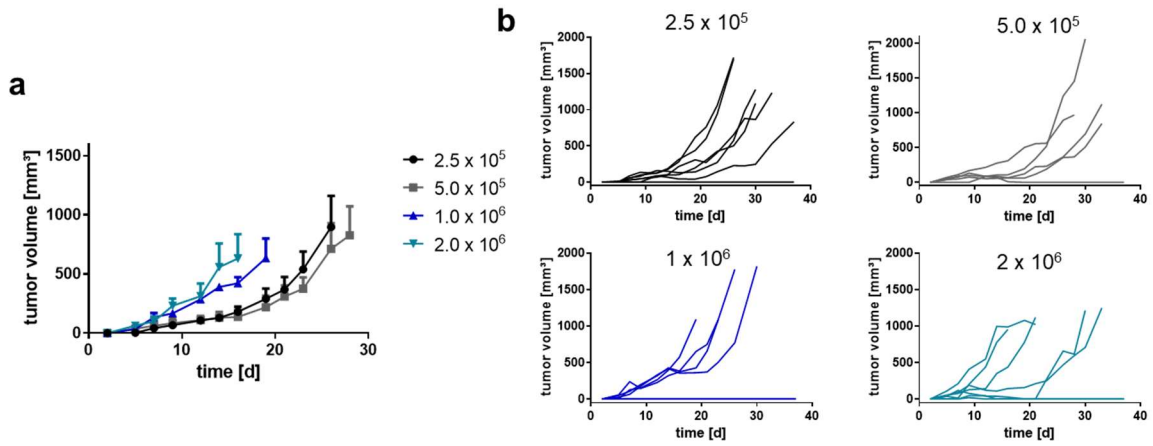


**Supplementary Figure 5.5: Unilateral growth of EO771/OVA tumors.** C57BL/6 mice were injected s.c. with 2.5 x $10^5$, 5 x $10^5$, 1 x $10^6$, and 2 x $10^6$ EO771/OVA cells, respectively. **(a)** Tumor growth curves. Mean values + SEM are shown; mice without tumor growth were not considered. **(b)** Individual tumor growth curves.

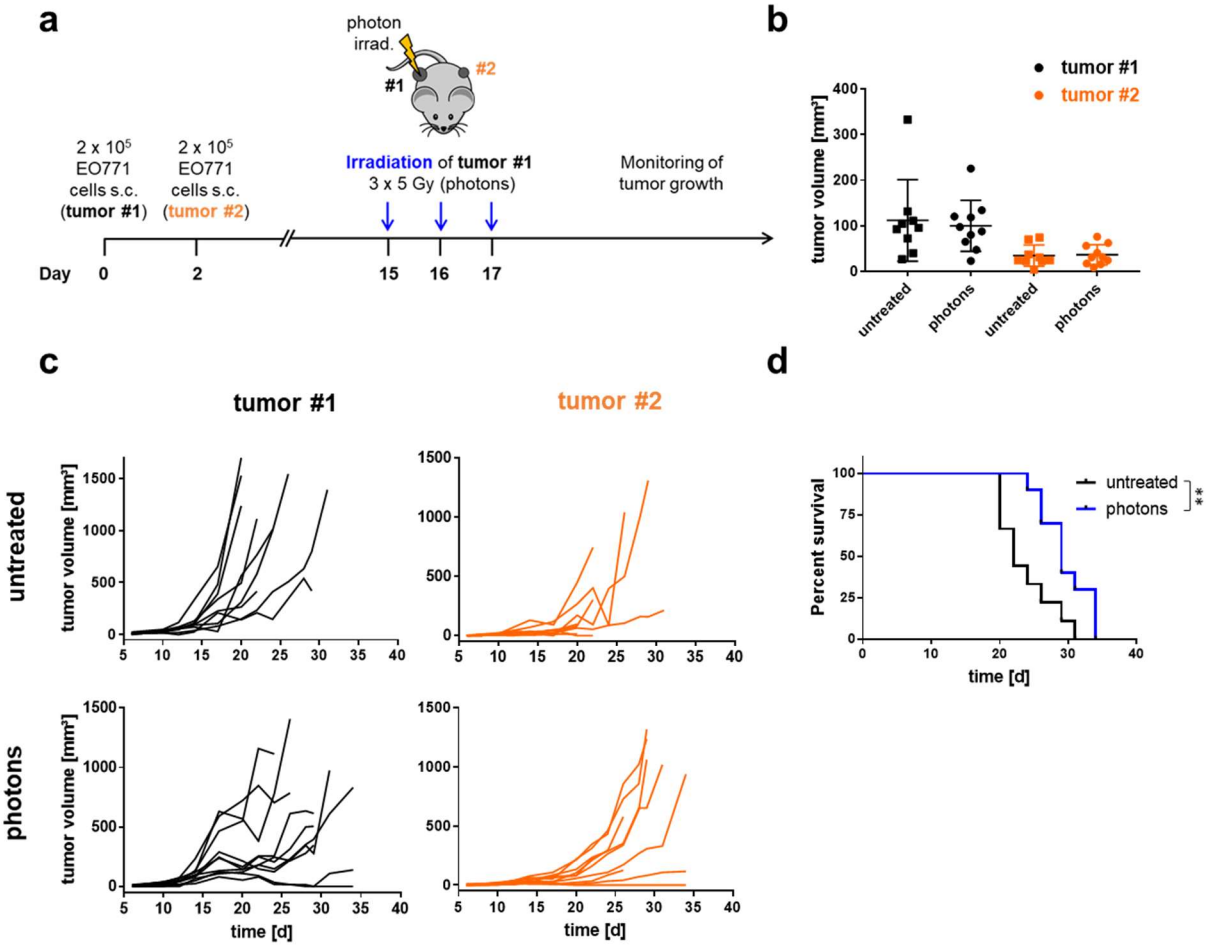


**Supplementary Figure 5.6: Treatment of EO771 tumors with photon RT as monotherapy**. **(a)** Treatment schedule: C57BL/6 mice were bilaterally challenged with time-shifted tumor cell injections (s.c.) using 2 x $10^5$ EO771 cells. When tumors were established, tumor #1 was irradiated with 5 Gy photons on three consecutive days and tumor growth was monitored. **(b)** On day 14, mice were randomized into two groups based on the volume of tumor #1 and tumor #2. **(c)** Individual growth curves of tumor #1 and tumor #2 of untreated mice and mice treated with photon RT. (d) Kaplan-Meier survival analysis. Significance was determined using a log-rank (Mantel-Cox) test.

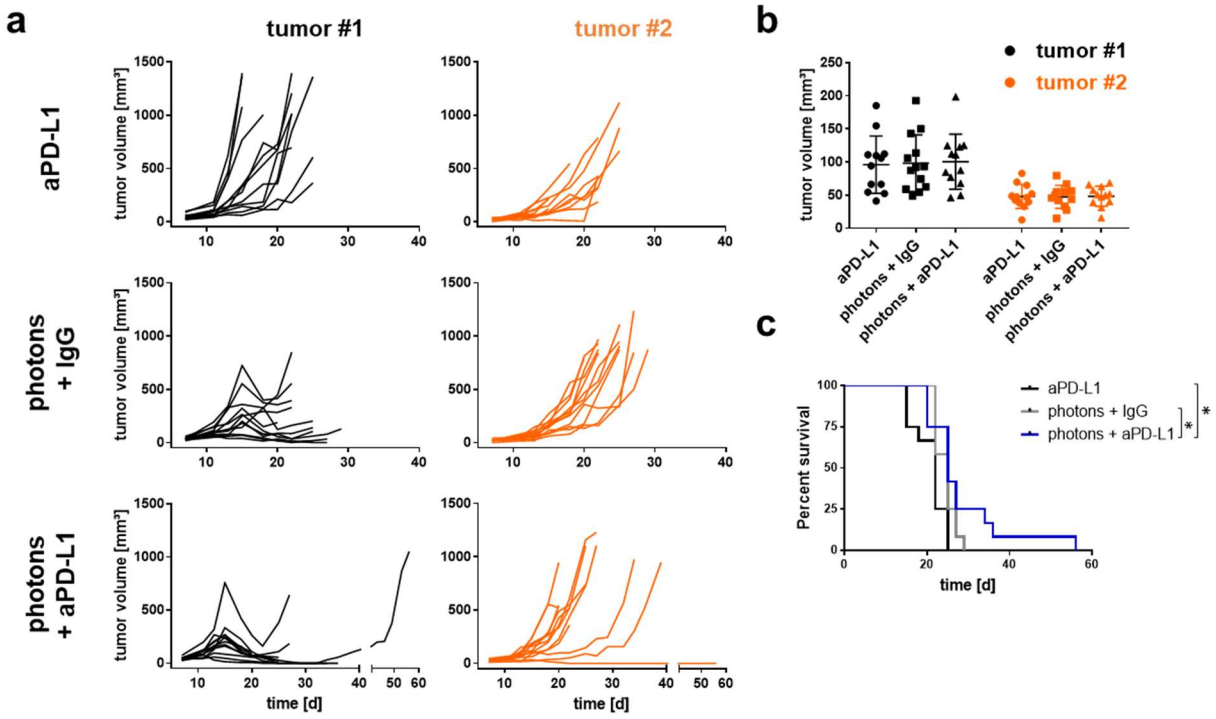


**Supplementary Figure 5.7: Combining photon RT with checkpoint blockade against PD-L1. (a)** Individual growth curves of tumor #1 and tumor #2 of mice treated with anti-PD-L1 antibodies, photon RT plus IgG control, or combined photon RT plus anti-PD-L1 antibodies. **(b)** One day before treatment start, mice were randomized into three groups based on the volume of tumor #1 and tumor #2 (n=12). **(c)** Kaplan-Meier survival analysis. Significance was determined using a log-rank (Mantel-Cox) test with Holm-Bonferroni correction.

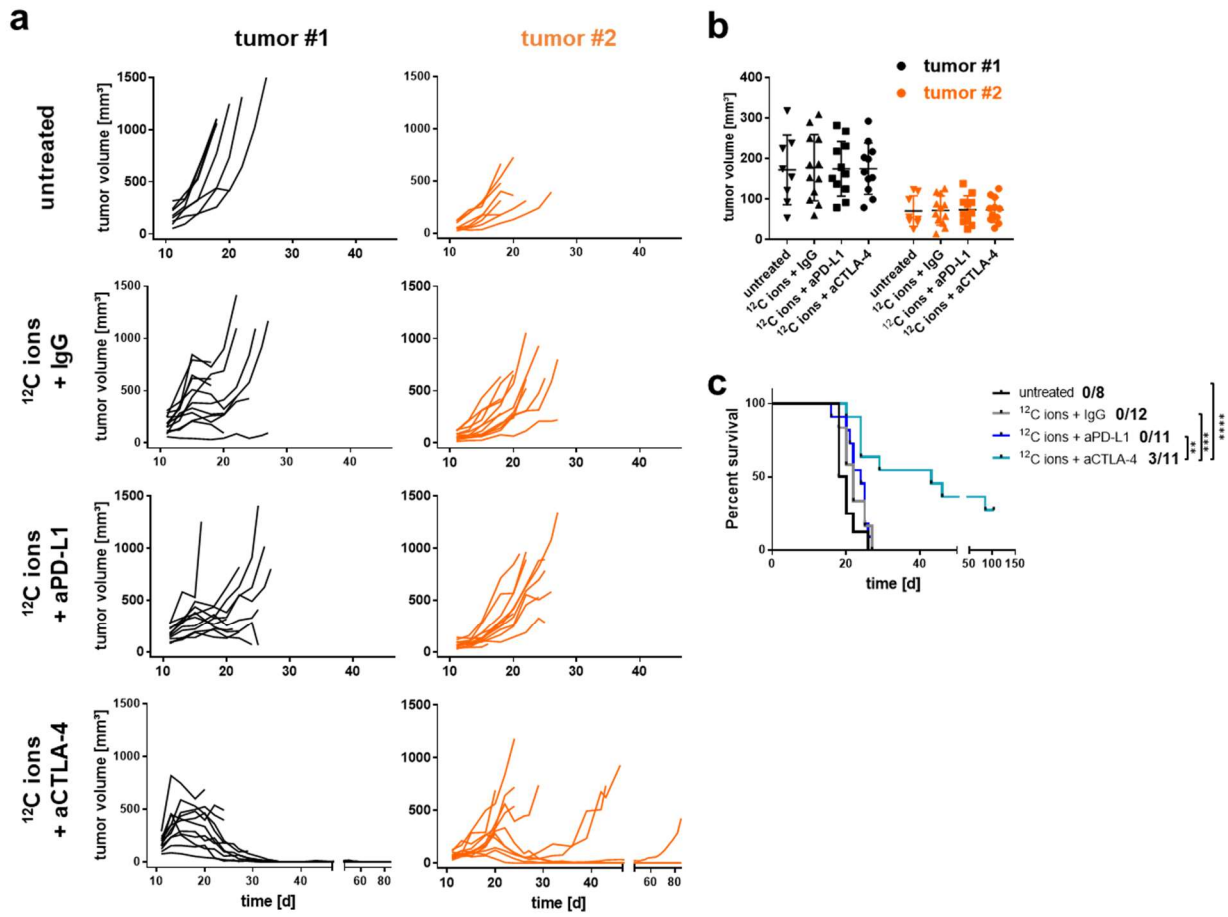


**Supplementary Figure 5.8: Carbon ion RT plus checkpoint blockade against PD-L1 or CTLA-4. (a)** Individual growth curves of tumor #1 and tumor #2 of untreated mice or mice treated with carbon ion RT, carbon ion RT plus anti-PD-L1 antibodies, and carbon ion RT plus anti-CTLA-4 antibodies, respectively. **(b)** One day before treatment start, mice were randomized into four groups based on the volume of tumor #1 and tumor #2 (n=8-12). **(c)** Kaplan-Meier survival analysis. In addition, complete response rates for each group are shown. Significance was determined using a log-rank (Mantel-Cox) test with Holm-Bonferroni correction.

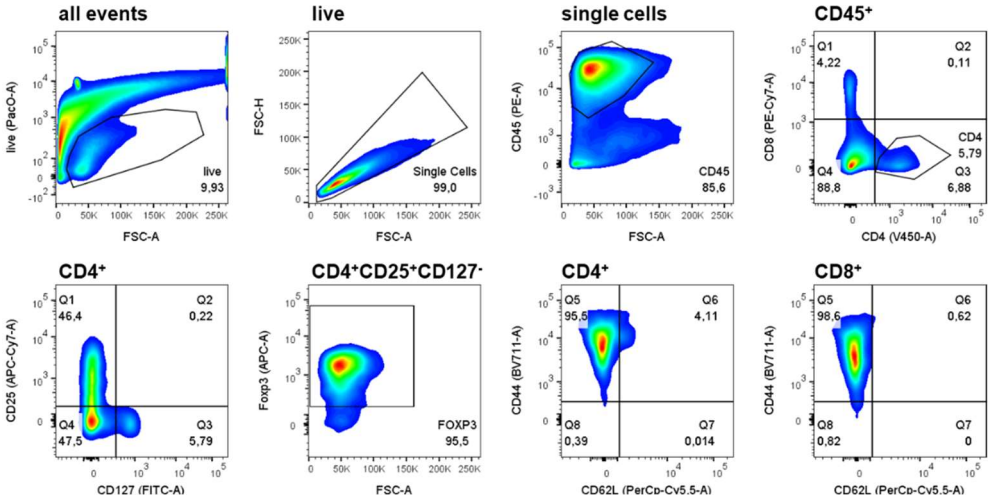


**Supplementary Figure 5.9: Gating strategy of the T cell panel**. Events were first gated on live cells, single cells and CD45$^+$ leukocytes. CD45$^+$ leukocytes were further divided into CD4$^+$ and CD8$^+$ T cells. CD4$^+$ cells were then gated on CD25$^+$CD127$^-$Foxp3$^+$ to identify regulatory T cells. For both CD4$^+$ and CD8$^+$ T cells, the effector phenotype was determined by gating on CD44 and CD62L.

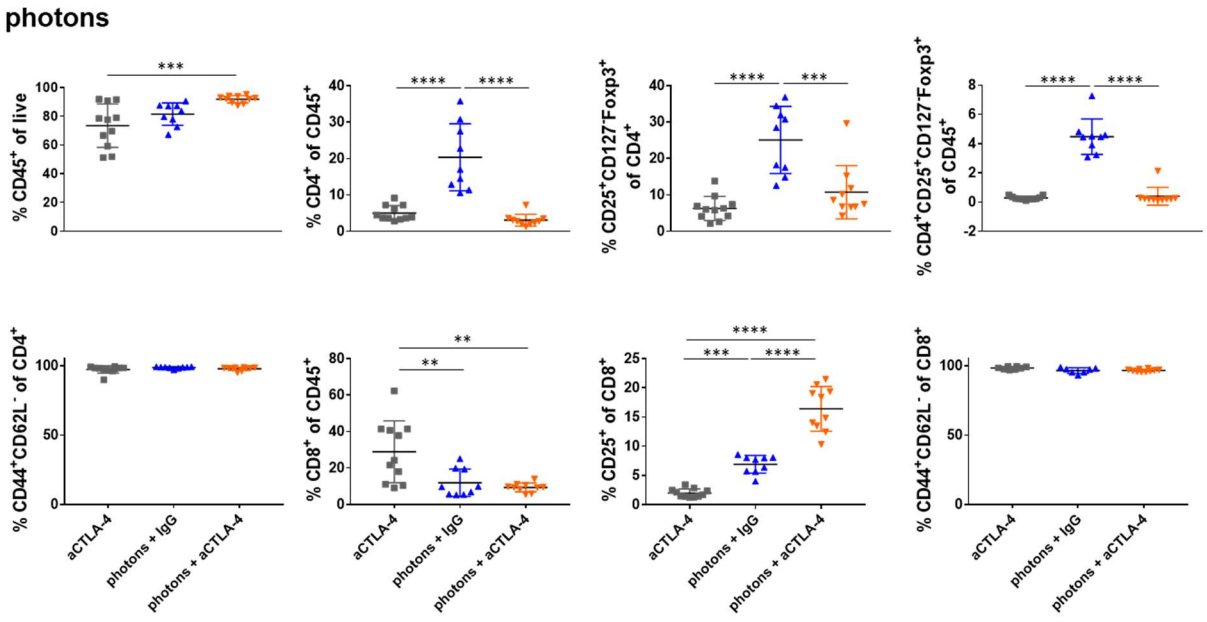


**Supplementary Figure 5.10: T cell infiltration in tumor #1 after treatment of EO771 tumors with RT plus anti-CTLA-4 antibodies.** Mice were treated with anti-CTLA-4 antibodies, photon RT plus IgG, or photon RT plus anti-CTLA-4 antibodies. Six days after treatment start, immune cell infiltration was analyzed by flow cytometry. Infiltration of tumors by leukocytes was determined by CD45$^+$ staining. CD4$^+$ T cells and their proportions of Tregs (CD25$^+$CD127$^-$Foxp3$^+$) were identified among CD45$^+$ leukocytes. The effector phenotype was determined by CD44/CD62L staining. Moreover, the proportion of CD8$^+$ T cells, their activation status (CD25$^+$) and their effector phenotype (CD44/CD62L) were assessed. Significance was determined by one-way ANOVA with post-hoc Turkey's test.

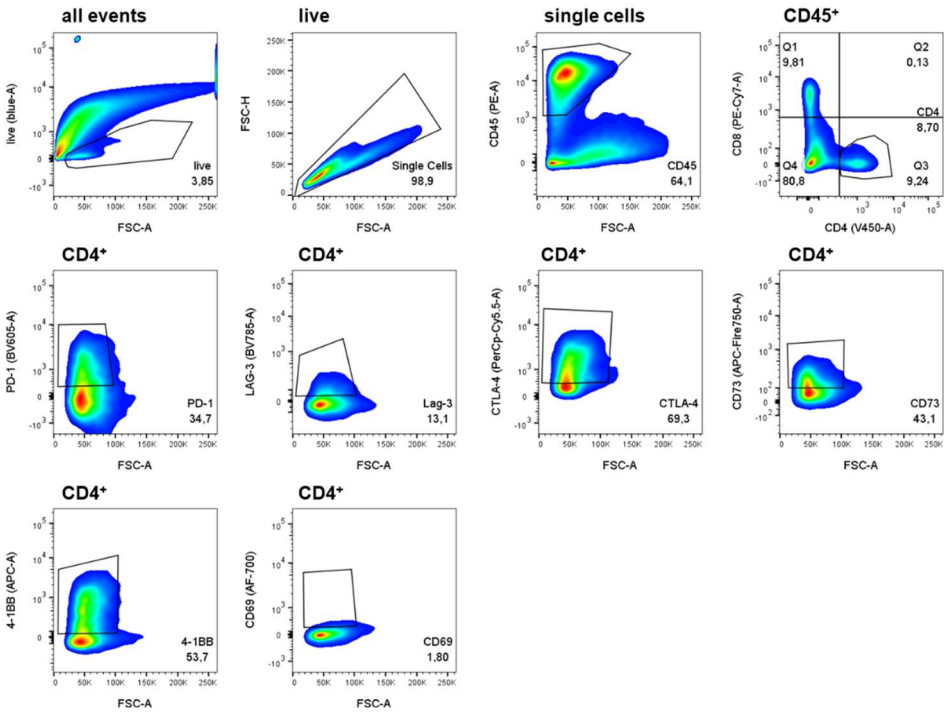


**Supplementary Figure 5.11: Gating strategy of inhibitory immune checkpoint molecules and co-stimulatory molecules on T cells**. Events were first gated on live cells, single cells and CD45$^+$ leukocytes. CD45$^+$ leukocytes were further divided into CD4$^+$ and CD8$^+$ T cells. Both CD4$^+$ and CD8$^+$ (not shown) were then analyzed for the surface expression of the immune checkpoint molecules PD-1, LAG-3, CTLA-4, and CD73 as well as the co-stimulatory molecules 4-1BB and CD69.

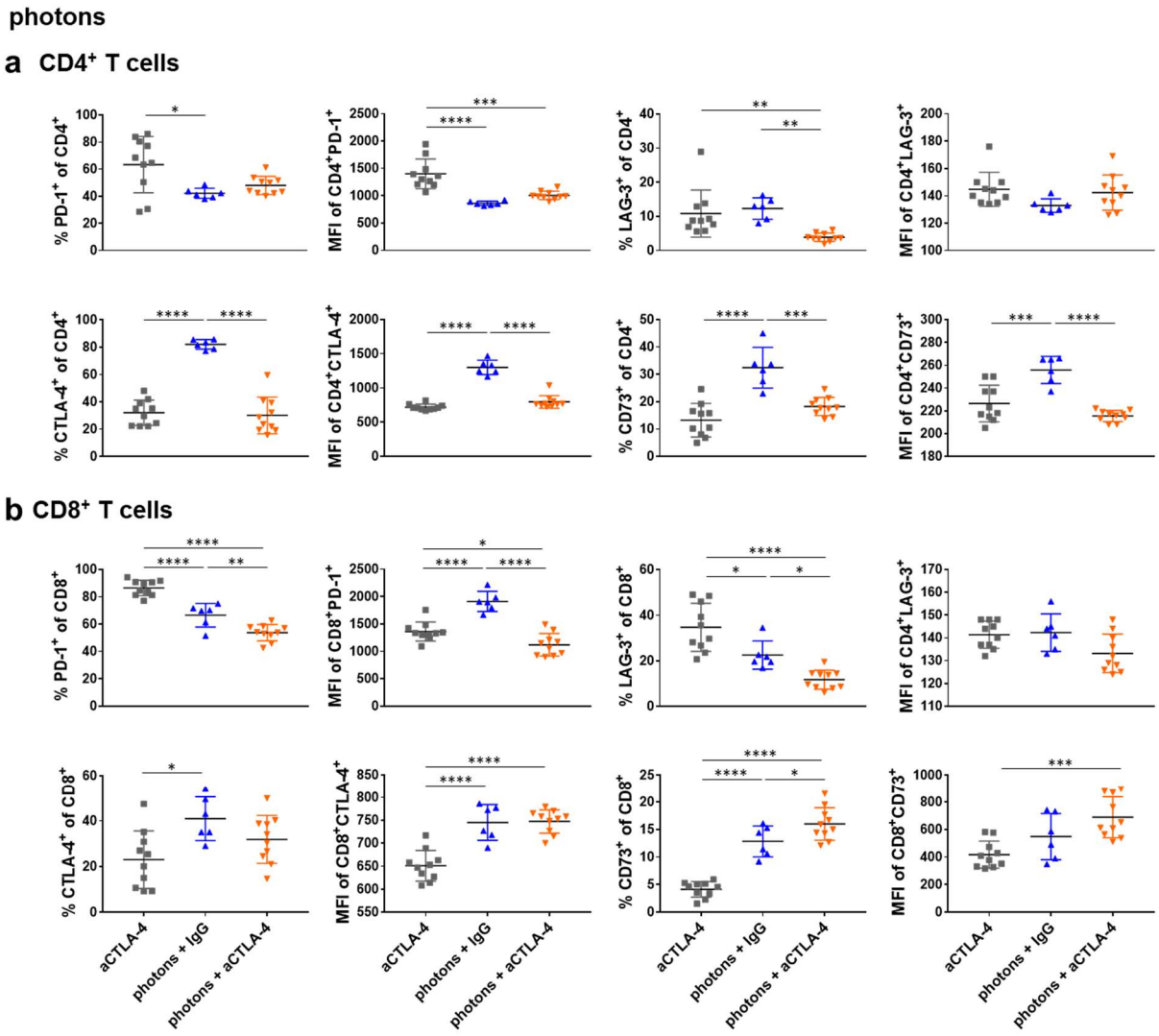


**Supplementary Figure 5.12**: **Immune checkpoint molecules expressed on T cells in tumor #1 after treatment of EO771 tumors with RT plus anti-CTLA-4 antibodies.** Mice were treated with anti-CTLA-4 antibodies, photon RT plus IgG control, or photon RT plus anti-CTLA-4 antibodies. Six days after treatment start, immune checkpoint molecules expressed on $CD4^+$ T cells **(a)** and $CD8^+$ T cells **(b)** were investigated by flow cytometry. Both the proportion (%) and the level of surface expression defined by the median fluorescence intensity (MFI) were determined for the immune checkpoint molecules PD-1, LAG-3, CTLA-4, and CD73. Significance was determined by one-way ANOVA with post-hoc Turkey's test.

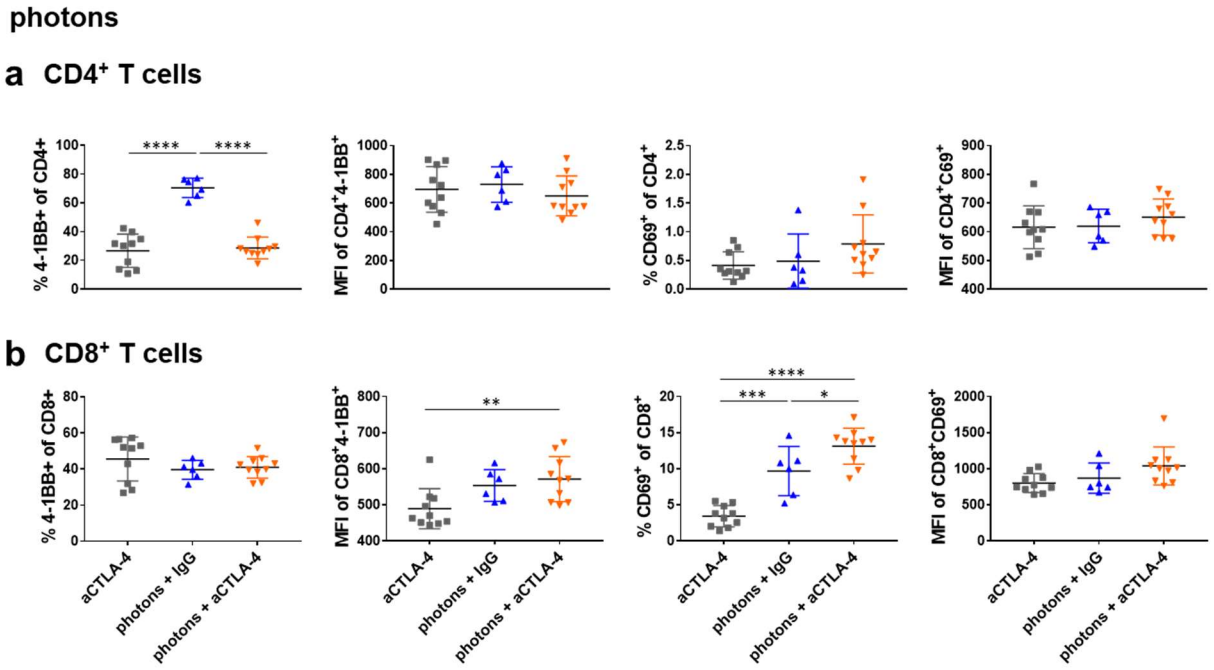


**Supplementary Figure 5.13**: **Co-stimulatory molecules expressed on T cells in tumor #1 after treatment of EO771 tumors with RT plus anti-CTLA-4 antibodies**. Mice were treated with anti-CTLA-4 antibodies, photon RT plus IgG control, or photon RT plus anti-CTLA-4 antibodies. Six days after treatment start, co-stimulatory molecules expressed on $CD4^+$ T cells **(a)** and $CD8^+$ T cells **(b)** were investigated by flow cytometry. Both the proportion (%) and the level of surface expression defined by the median fluorescence intensity (MFI) were determined for the co-stimulatory molecules 4-1BB and CD69. Significance was determined by one-way ANOVA with post-hoc Turkey's test.

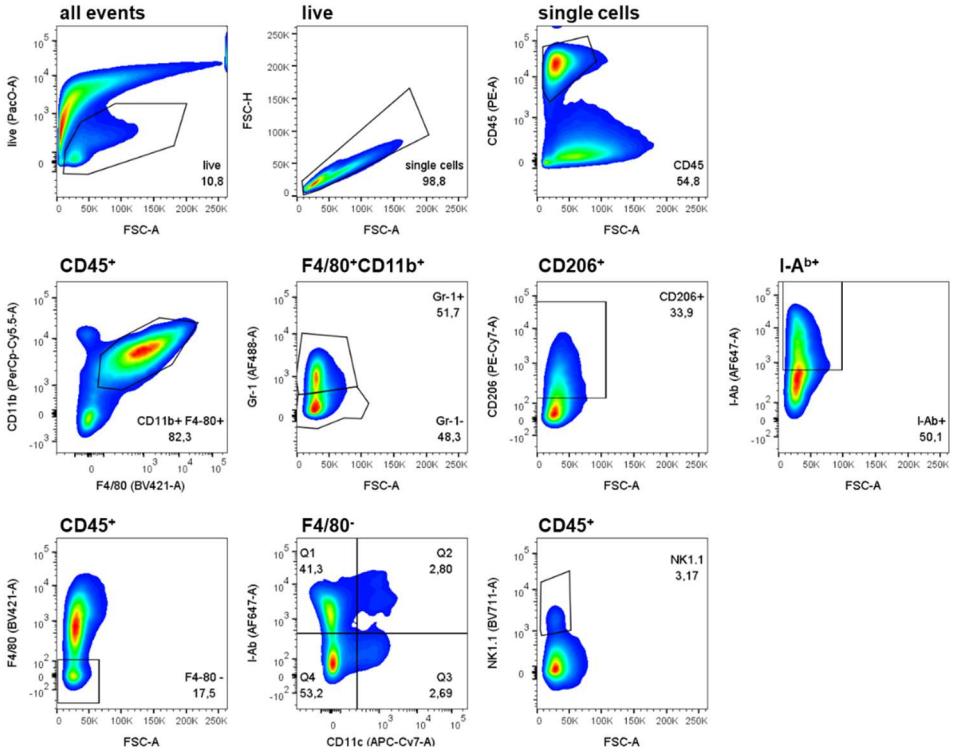


**Supplementary Figure 5.14: Gating strategy of the macrophage cell panel**. Events were first gated on live cells, single cells and CD45$^+$ leukocytes. CD45$^+$ leukocytes were further gated on F4/80$^+$CD11b$^+$ myeloid cells. Among these, macrophages and MDSCs were distinguished based on Gr-1$^-$ and Gr-1$^+$ expression, respectively. To identify DCs, CD45$^+$ leukocytes were gated on F4/80$^-$CD11c$^+$I-A$^{b+}$ cells. NK cells were identified from CD45$^+$ cells by NK1.1.

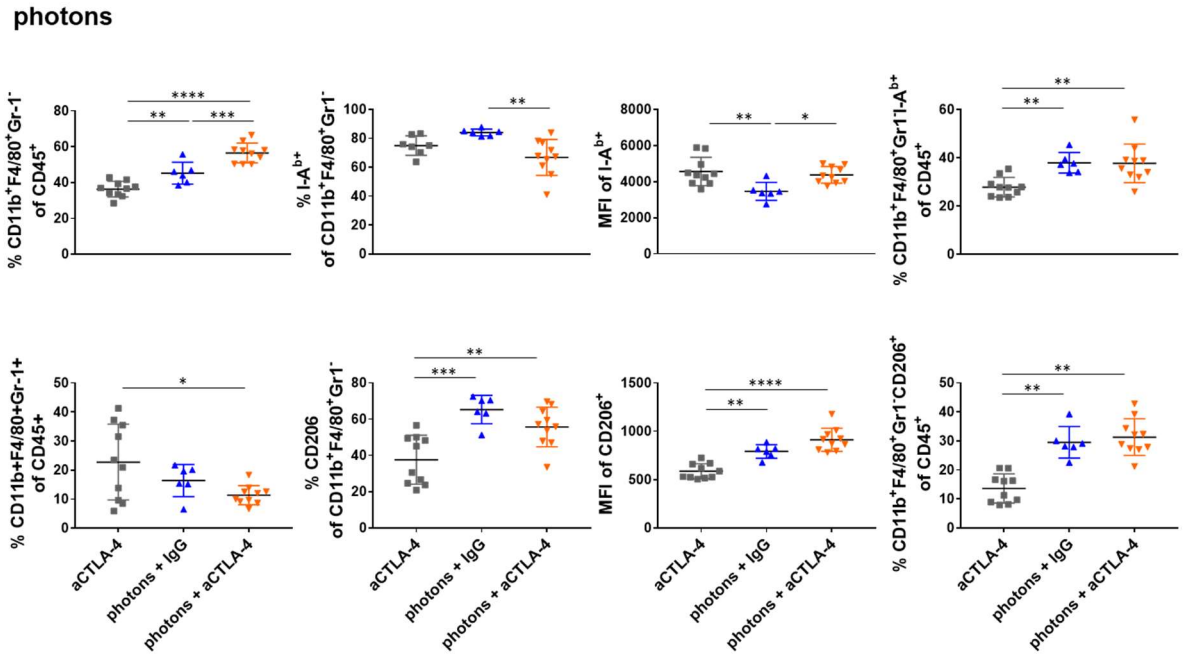


**Supplementary Figure 5.15: Myeloid cell infiltration in tumor #1 after treatment of EO771 tumors with RT plus anti-CTLA-4 antibodies.** Mice were treated with anti-CTLA-4 antibodies, photon RT + IgG control, or photon RT plus anti-CTLA-4 antibodies. Six days after treatment start, myeloid cell infiltration was investigated by flow cytometry. Proportions of macrophages (F4/80$^+$CD11b$^+$Gr-1$^-$) and MDSCs (F4/80$^+$CD11b$^+$Gr-1$^+$) were identified among CD45$^+$ leukocytes. The functional polarization status of macrophages was further determined by staining of the M1-like marker I-A$^b$ and the M2-like marker CD206. For both makers the percentages among macrophages (%), the level of expression defined by the median fluorescence intensity (MFI), and the proportion among total CD45$^+$ leukocytes were assessed. Significance was determined by one-way ANOVA with post-hoc Turkey's test.

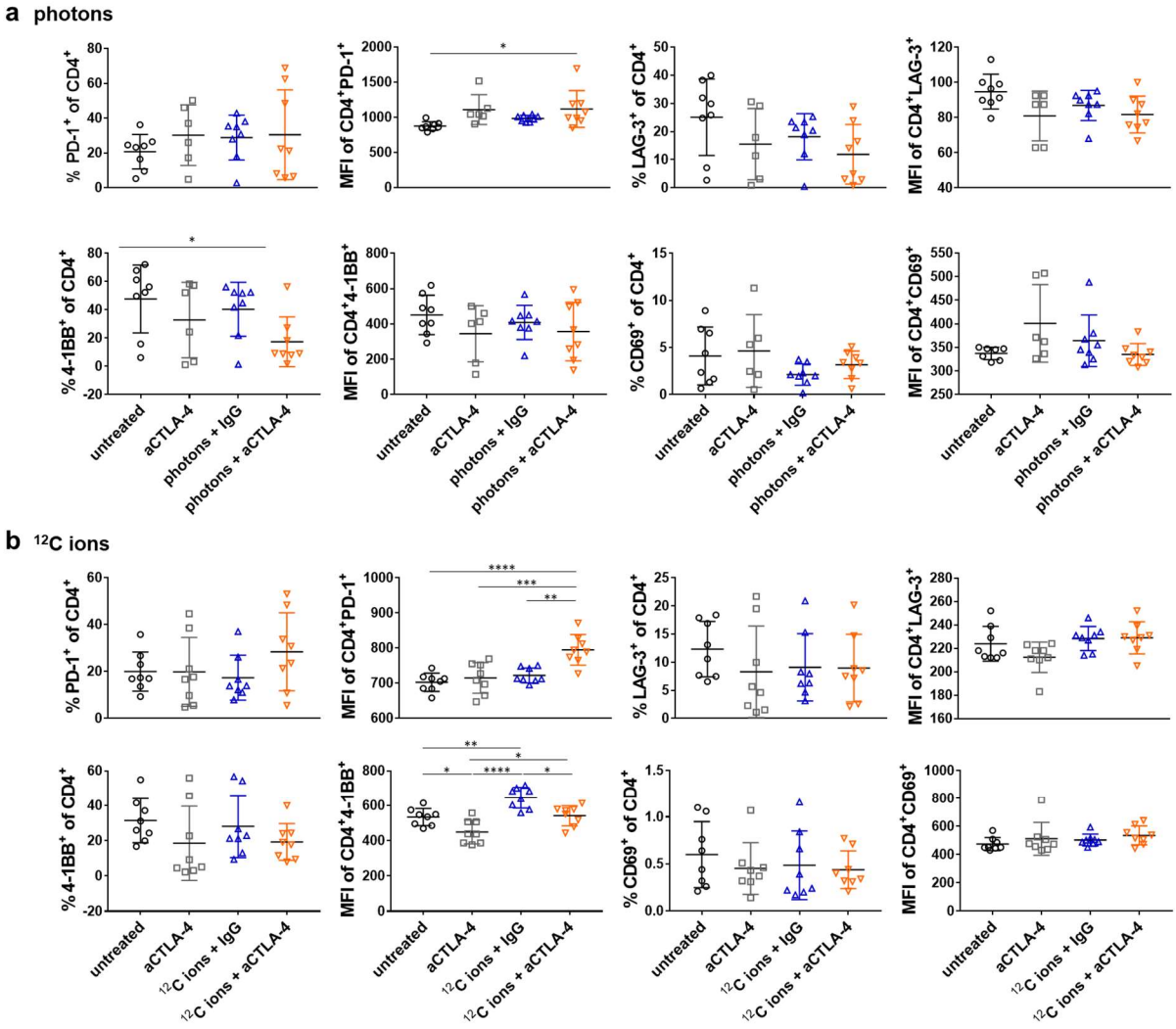


**Supplementary Figure 5.16: Immunomodulatory markers expressed on CD4⁺ T cells in tumor #2 after treatment of EO771 tumors with RT plus anti-CTLA-4 antibodies.** Mice were left untreated or treated with anti-CTLA-4 antibodies, RT plus IgG control, or RT plus anti-CTLA-4 antibodies. Tumor #1 was irradiated, while tumor #2 was outside the irradiation field. RT was either performed with photons **(a)** or carbon ions **(b)**. Five days (photons) or six days (carbon ions) after treatment start, surface expression of the immune checkpoint molecules PD-1 and LAG-3 as well as the co-stimulatory molecules 4-1BB and CD69 on CD4⁺ T cells was investigated by flow cytometry. Both the proportion (%) and the level of expression defined by the median fluorescence intensity (MFI) were assessed. Significance was determined by one-way ANOVA with post-hoc Turkey's test.

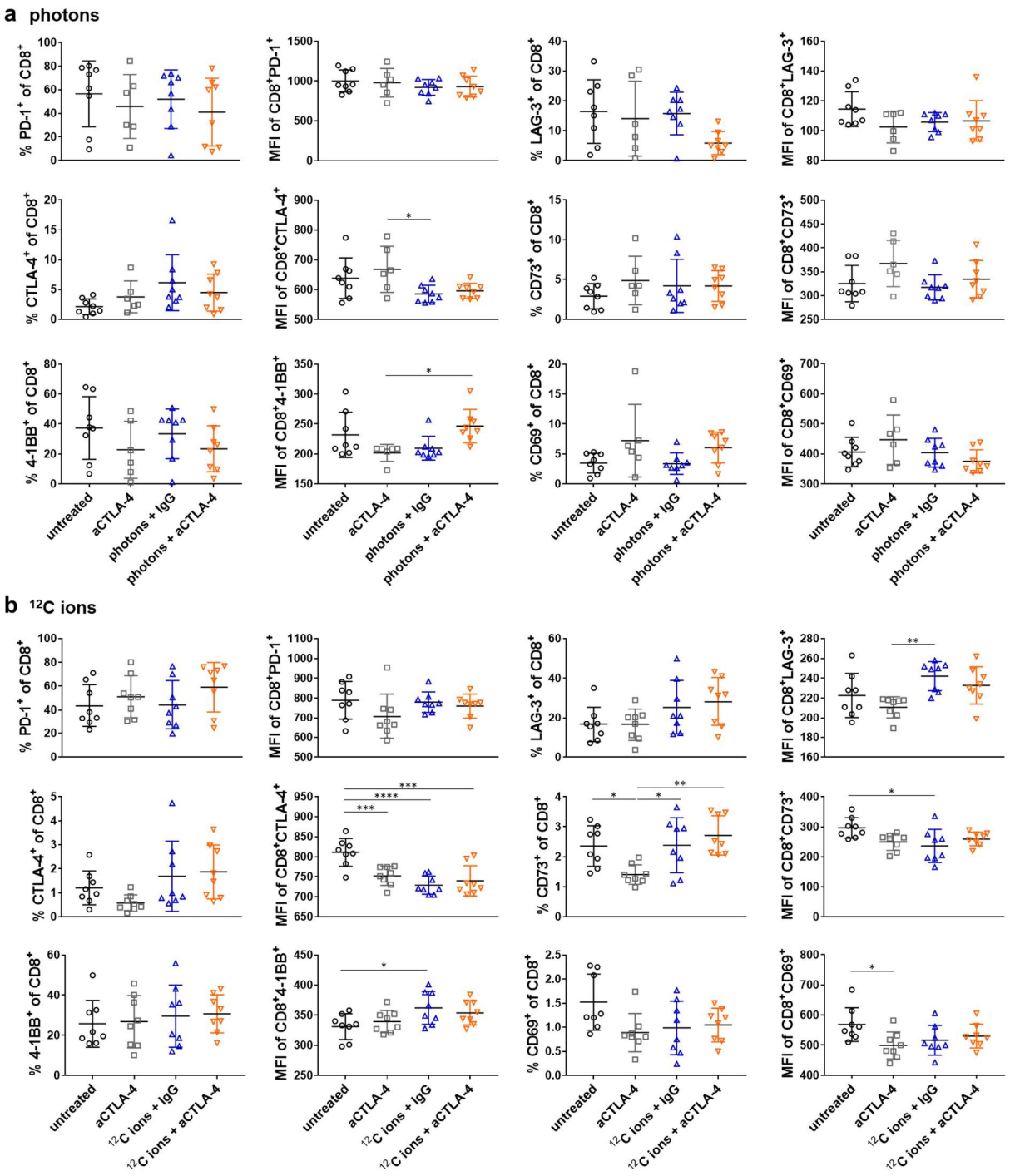


**Supplementary Figure 5.17: Immunomodulatory markers expressed on CD8⁺ T cells in tumor #2 after treatment of EO771 tumors with RT plus anti-CTLA-4 antibodies.** Mice were left untreated or treated with anti-CTLA-4 antibodies, RT plus IgG control, or RT plus anti-CTLA-4 antibodies. Tumor #1 was irradiated, while tumor #2 was outside the irradiation field. RT was either performed with photons **(a)** or carbon ions **(b)**. Five days (photons) or six days (carbon ions) after treatment start, surface expression of the immune checkpoint molecules PD-1, LAG-3, CTLA-3 and CD73 as well as the co-stimulatory molecules 4-1BB and CD69 on CD8⁺ T cells were investigated by flow cytometry. Both the proportion (%) and the level of expression defined by the median fluorescence intensity (MFI) were assessed. Significance was determined by one-way ANOVA with post-hoc Turkey's test.

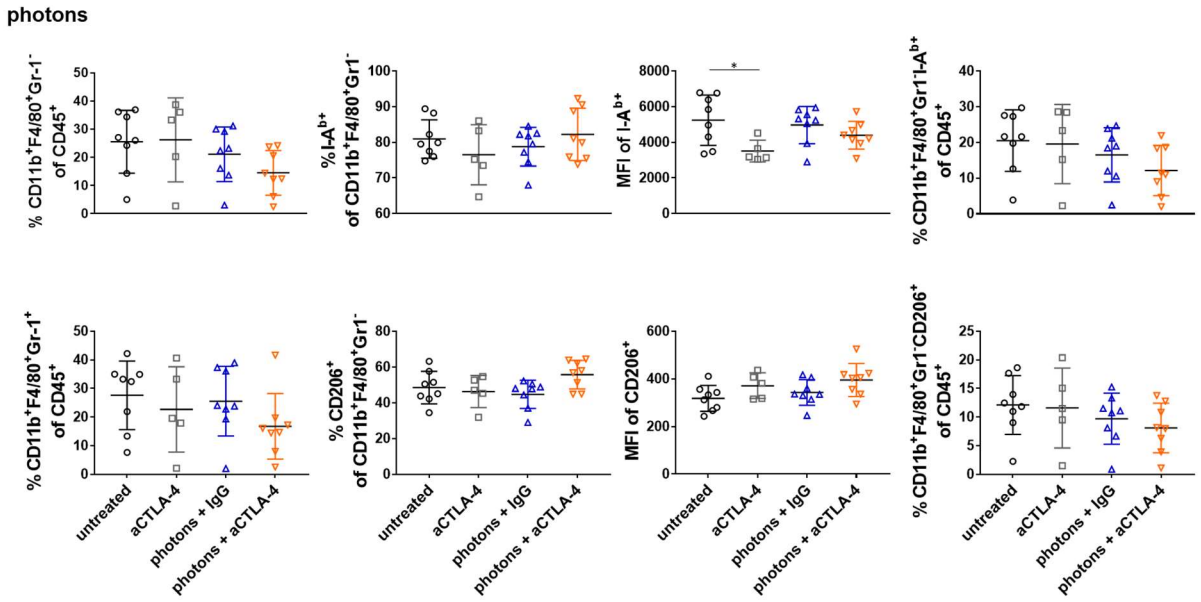


**Supplementary Figure 5.18: Myeloid cell infiltration in tumor #2 after treatment of EO771 tumors with RT plus anti-CTLA-4 antibodies.** Mice were left untreated or treated with anti-CTLA-4 antibodies, photon RT plus IgG control, or photon RT plus anti-CTLA-4 antibodies. Tumor #1 was irradiated, while tumor #2 was outside the irradiation field. Five days after treatment start, myeloid cell infiltration was investigated by flow cytometry. Proportions of macrophages ($F4/80^+CD11b^+Gr\text{-}1^-$) and MDSCs ($F4/80^+CD11b^+Gr\text{-}1^+$) were identified among $CD45^+$ leukocytes. The functional polarization status of macrophages was further determined by staining of the M1-like marker $I\text{-}A^b$ and the M2-like marker CD206. For both makers the percentages among macrophages, the level of expression defined by the median fluorescence intensity (MFI), and the proportion among total $CD45^+$ leukocytes were assessed. Significance was determined by one-way ANOVA with post-hoc Turkey's test.

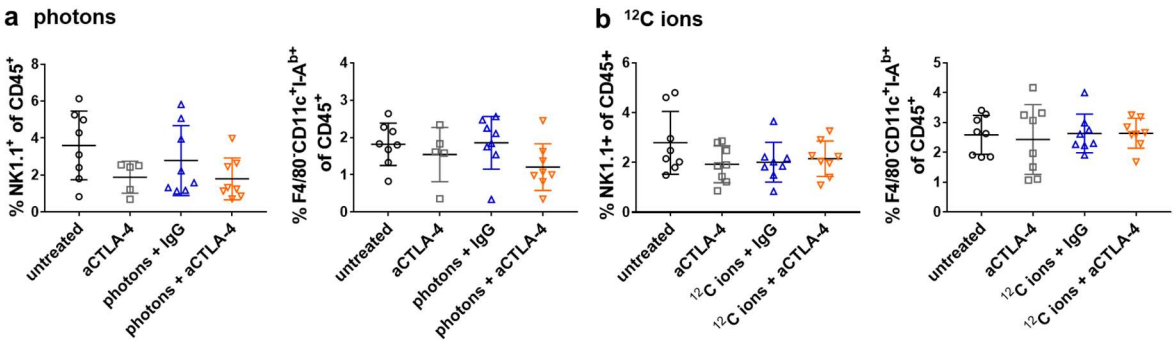


**Supplementary Figure 5.19: Infiltration of NK cells and DCs in tumor #2 after treatment of EO771 tumors with RT plus anti-CTLA-4 antibodies.** Mice were left untreated or treated with anti-CTLA-4 antibodies, RT plus IgG control, or RT plus anti-CTLA-4 antibodies. Tumor #1 was irradiated, while tumor #2 was outside the irradiation field. RT was either performed with photons **(a)** or carbon ions **(b)**. Five days (photons) or six days (carbon ions) after treatment start, immune cell infiltration was investigated by flow cytometry. From $CD45^+$ leukocytes, infiltration by NK cells ($NK1.1^+$) and DCs ($F4/80^-CD11c^+I\text{-}A^{b+}$) was assessed. Significance was determined by one-way ANOVA with post-hoc Turkey's test.

**Supplementary Table 5-2: Proteins with differential abundance in tumor #2.** Proteins with a positive log fold change (logFC) had a higher abundance in the photon RT + aCTLA-4 group, proteins with negative logFC in the photon RT + IgG group. P values adjusted for multiple testing are shown.

| Higher abundance in RT + aCTLA-4 group | | | Higher abundance in RT + IgG group | | |
|---|---|---|---|---|---|
| **Protein** | **logFC** | **adj.P.Val** | **Protein** | **logFC** | **adj.P.Val** |
| TNFB | 1.69 | 7.54E-13 | CEAM1 | -0.56 | 0.00472221 |
| KI2L2 | 1.65 | 1.48E-07 | VEGFC | -0.57 | 0.00808968 |
| CEAM5 | 1.55 | 7.54E-13 | IL22 | -0.57 | 0.03463432 |
| P53 | 1.54 | 9.05E-12 | MPRI | -0.58 | 0.0093979 |
| CD72 | 1.51 | 2.19E-11 | CADH5 | -0.58 | 0.03002578 |
| TGFB2 | 1.47 | 5.97E-07 | EPCAM | -0.61 | 0.00102823 |
| TR11B | 1.46 | 8.31E-10 | CD47 | -0.61 | 0.00986119 |
| CSF1 | 1.38 | 7.28E-07 | CD53 | -0.63 | 0.00163895 |
| EGLN | 1.33 | 1.62E-09 | CXCL9 | -0.66 | 0.00423544 |
| NCAM1 | 1.29 | 1.08E-07 | SLAF8 | -0.69 | 0.00796545 |
| IL17 | 1.28 | 6.25E-10 | CCL15 | -0.72 | 0.00370416 |
| HLA-I | 1.2 | 1.46E-09 | CD14 | -0.8 | 0.01029776 |
| SIGL9 | 1.2 | 1.92E-06 | IFNG | -0.81 | 3.96E-05 |
| TNFA | 1.19 | 7.49E-07 | CCL25 | -0.84 | 8.00E-06 |
| DAF | 1.13 | 4.31E-06 | CCL7 | -0.84 | 0.00020785 |
| TNF13 | 1.1 | 9.12E-07 | CCL28 | -0.85 | 9.83E-05 |
| GRN | 1.09 | 7.28E-07 | PRIO | -0.89 | 8.00E-07 |
| FGF2 | 1.03 | 0.00700246 | CCL8 | -0.96 | 0.00014855 |
| BMP4 | 1.01 | 2.52E-05 | CD53 | -1.13 | 5.27E-05 |
| IL18 | 1 | 9.12E-07 | CD80 | -1.49 | 1.81E-05 |
| ITAE | 0.99 | 3.30E-05 | | | |
| TFR1 | 0.91 | 0.00169387 | | | |
| PLF4 | 0.86 | 9.12E-07 | | | |
| CD59 | 0.86 | 5.94E-05 | | | |
| IFNL1 | 0.81 | 0.00173623 | | | |
| CXL11 | 0.79 | 1.04E-05 | | | |
| TGFB1 | 0.78 | 2.49E-06 | | | |
| LAG3 | 0.77 | 3.48E-05 | | | |
| HLA-ABC | 0.76 | 2.52E-05 | | | |
| IL2RB | 0.75 | 0.0006125 | | | |
| INHBA | 0.73 | 6.08E-05 | | | |
| IFNL3 | 0.72 | 1.18E-07 | | | |
| CCL26 | 0.72 | 0.0002582 | | | |
| CD45RO | 0.72 | 0.00065474 | | | |
| CD52 | 0.69 | 1.78E-08 | | | |
| TNFL8 | 0.69 | 0.00026876 | | | |
| IL19 | 0.66 | 0.01434837 | | | |
| CR2 | 0.62 | 1.07E-07 | | | |
| TIE2 | 0.61 | 0.0001028 | | | |
| CNTF | 0.61 | 0.00102823 | | | |
| CCL23 | 0.59 | 0.00180916 | | | |
| PERM | 0.58 | 0.00308231 | | | |
| TIMP1 | 0.58 | 0.024622 | | | |
| BMP6 | 0.57 | 0.00106748 | | | |
| CCR7 | 0.54 | 0.00126124 | | | |
| CD59 | 0.54 | 0.00180916 | | | |
| TNFL8 | 0.54 | 0.00744666 | | | |
| CD22 | 0.54 | 0.02233624 | | | |
| TNFL6 | 0.53 | 0.01331796 | | | |
| TNF14 | 0.52 | 0.01045173 | | | |

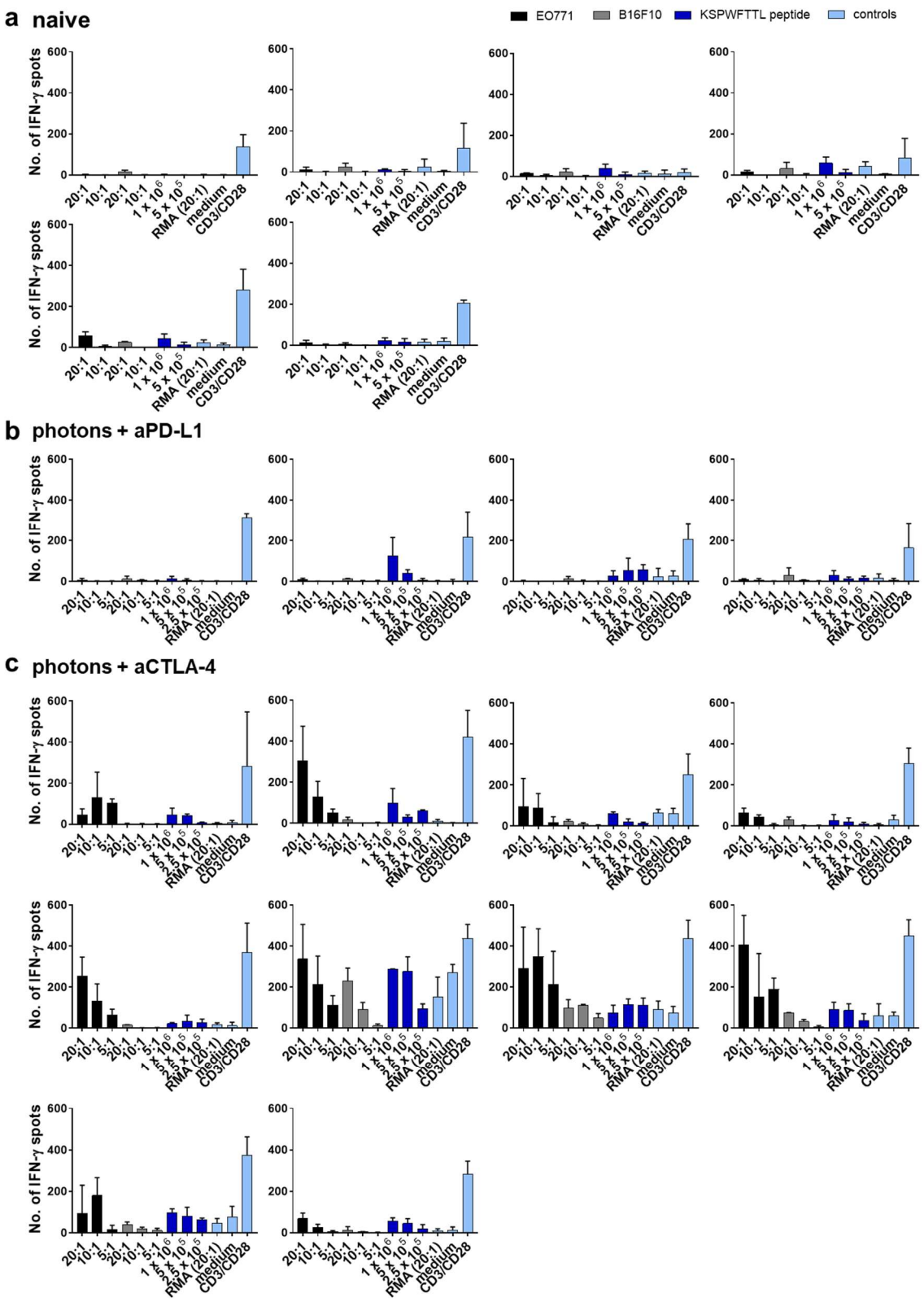


**Supplementary Figure 5.20: Memory T cell responses in individual mice that had shown complete responses after photon RT plus immune checkpoint blockade.** Mice were re-challenged with EO771 tumor cell injections. After 14 days, splenocytes of naïve mice **(a)** or regressor mice after photon RT plus anti-PD-L1 **(b)** or anti-CTLA-4 **(c)** antibodies were co-cultured with EO771 cells, B16F10 cells, KSPWFTTL peptide, RMA cells, medium (negative control) or CD3/CD28 beads (positive control). Different effector cell numbers (1 x $10^6$, 5 x $10^5$, 2.5 x $10^5$), yielding effector to target cell ratios of 20:1, 10:1, 5:1, were used. The number of IFN-γ spots was determined in IFN-γ ELISpot assays.

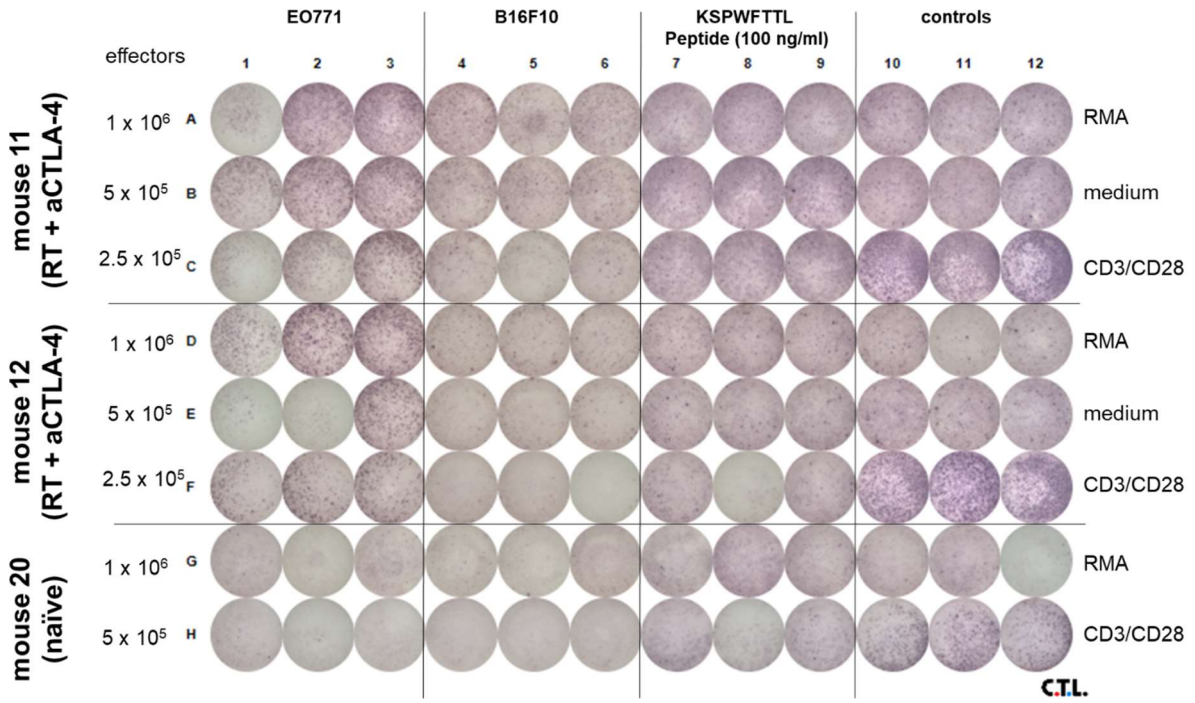


**Supplementary Figure 5.21: Representative INF-γ ELISpot plate for analyzing memory T cell responses in mice that had shown complete responses after photon RT plus immune checkpoint blockade.** Splenocytes of naïve mice or regressor mice after photon RT plus anti-CTLA-4 checkpoint blockade were co-cultured with EO771 cells, B16F10 cells, the KSPWFTTL peptide, RMA cells, medium (negative control) and CD3/CD28 beads (positive control). Different effector cell numbers (1 x $10^6$, 5 x $10^5$, 2.5 x $10^5$) were used. Memory T cell responses were determined by IFN-γ spots in IFN-γ ELISpot assays performed in technical triplicates.

# 6 References


1. Weinberg, R.A., *The Biology of Cancer - Second Edition*. 2014: Garland Science.
2. Bray, F., et al., *Global cancer statistics 2018: GLOBOCAN estimates of incidence and mortality worldwide for 36 cancers in 185 countries.* CA Cancer J Clin, 2018. **68**(6): p. 394-424.
3. Colditz, G.A., T.A. Sellers, and E. Trapido, *Epidemiology - identifying the causes and preventability of cancer?* Nat Rev Cancer, 2006. **6**(1): p. 75-83.
4. Hanahan, D. and R.A. Weinberg, *Hallmarks of cancer: the next generation.* Cell, 2011. **144**(5): p. 646-74.
5. Chaplin, D.D., *Overview of the immune response.* J Allergy Clin Immunol, 2010. **125**(2 Suppl 2): p. S3-23.
6. Medzhitov, R., *Toll-like receptors and innate immunity.* Nat Rev Immunol, 2001. **1**(2): p. 135-45.
7. Abel, A.M., et al., *Natural Killer Cells: Development, Maturation, and Clinical Utilization.* Front Immunol, 2018. **9**: p. 1869.
8. Dunkelberger, J.R. and W.C. Song, *Complement and its role in innate and adaptive immune responses.* Cell Res, 2010. **20**(1): p. 34-50.
9. Bonilla, F.A. and H.C. Oettgen, *Adaptive immunity.* J Allergy Clin Immunol, 2010. **125**(2 Suppl 2): p. S33-40.
10. Burnet, M., *Cancer: a biological approach. III. Viruses associated with neoplastic conditions. IV. Practical applications.* Br Med J, 1957. **1**(5023): p. 841-7.
11. Old, L.J. and E.A. Boyse, *Antigenic Properties of Experimental Leukemias. I. Serological Studies in Vitro with Spontaneous and Radiation-Induced Leukemias.* J Natl Cancer Inst, 1963. **31**: p. 977-95.
12. Shankaran, V., et al., *IFNgamma and lymphocytes prevent primary tumour development and shape tumour immunogenicity.* Nature, 2001. **410**(6832): p. 1107-11.
13. Wilkins, K., et al., *Cutaneous malignancy and human immunodeficiency virus disease.* J Am Acad Dermatol, 2006. **54**(2): p. 189-206; quiz 207-10.
14. Adami, J., et al., *Cancer risk following organ transplantation: a nationwide cohort study in Sweden.* Br J Cancer, 2003. **89**(7): p. 1221-7.
15. Galon, J., et al., *Type, density, and location of immune cells within human colorectal tumors predict clinical outcome.* Science, 2006. **313**(5795): p. 1960-4.
16. Wolf, D., et al., *The expression of the regulatory T cell-specific forkhead box transcription factor FoxP3 is associated with poor prognosis in ovarian cancer.* Clin Cancer Res, 2005. **11**(23): p. 8326-31.
17. Vinay, D.S., et al., *Immune evasion in cancer: Mechanistic basis and therapeutic strategies.* Semin Cancer Biol, 2015. **35 Suppl**: p. S185-S198.
18. Schreiber, R.D., L.J. Old, and M.J. Smyth, *Cancer immunoediting: integrating immunity's roles in cancer suppression and promotion.* Science, 2011. **331**(6024): p. 1565-70.
19. Kim, R., M. Emi, and K. Tanabe, *Cancer immunoediting from immune surveillance to immune escape.* Immunology, 2007. **121**(1): p. 1-14.
20. Vesely, M.D., et al., *Natural innate and adaptive immunity to cancer.* Annu Rev Immunol, 2011. **29**: p. 235-71.
21. Hornyak, L., et al., *The Role of Indoleamine-2,3-Dioxygenase in Cancer Development, Diagnostics, and Therapy.* Front Immunol, 2018. **9**: p. 151.
22. Vigneron, N., *Human Tumor Antigens and Cancer Immunotherapy.* Biomed Res Int, 2015. **2015**: p. 948501.
23. Wurz, G.T., C.J. Kao, and M.W. DeGregorio, *Novel cancer antigens for personalized immunotherapies: latest evidence and clinical potential.* Ther Adv Med Oncol, 2016. **8**(1): p. 4-31.
24. Schumacher, T.N., W. Scheper, and P. Kvistborg, *Cancer Neoantigens.* Annu Rev Immunol, 2019. **37**: p. 173-200.

25. Markov, O.V., et al., *Molecular and Cellular Mechanisms of Antitumor Immune Response Activation by Dendritic Cells.* Acta Naturae, 2016. **8**(3): p. 17-30.
26. Chen, D.S. and I. Mellman, *Oncology meets immunology: the cancer-immunity cycle.* Immunity, 2013. **39**(1): p. 1-10.
27. Durgeau, A., et al., *Recent Advances in Targeting CD8 T-Cell Immunity for More Effective Cancer Immunotherapy.* Front Immunol, 2018. **9**: p. 14.
28. Vihervuori, H., et al., *Tumor-infiltrating lymphocytes and CD8(+) T cells predict survival of triple-negative breast cancer.* J Cancer Res Clin Oncol, 2019. **145**(12): p. 3105-3114.
29. An, N., et al., *The prognostic role of circulating CD8(+) T cell proliferation in patients with untreated extensive stage small cell lung cancer.* J Transl Med, 2019. **17**(1): p. 402.
30. Tian, C., et al., *Prognostic significance of tumor-infiltrating CD8(+) or CD3(+) T lymphocytes and interleukin-2 expression in radically resected non-small cell lung cancer.* Chin Med J (Engl), 2015. **128**(1): p. 105-10.
31. Kennedy, R. and E. Celis, *Multiple roles for CD4+ T cells in anti-tumor immune responses.* Immunol Rev, 2008. **222**: p. 129-44.
32. Quezada, S.A., et al., *Tumor-reactive CD4(+) T cells develop cytotoxic activity and eradicate large established melanoma after transfer into lymphopenic hosts.* J Exp Med, 2010. **207**(3): p. 637-50.
33. Xie, Y., et al., *Naive tumor-specific CD4(+) T cells differentiated in vivo eradicate established melanoma.* J Exp Med, 2010. **207**(3): p. 651-67.
34. Linnemann, C., et al., *High-throughput epitope discovery reveals frequent recognition of neo-antigens by CD4+ T cells in human melanoma.* Nat Med, 2015. **21**(1): p. 81-5.
35. Kreiter, S., et al., *Mutant MHC class II epitopes drive therapeutic immune responses to cancer.* Nature, 2015. **520**(7549): p. 692-6.
36. Ott, P.A., et al., *An immunogenic personal neoantigen vaccine for patients with melanoma.* Nature, 2017. **547**(7662): p. 217-221.
37. Sahin, U., et al., *Personalized RNA mutanome vaccines mobilize poly-specific therapeutic immunity against cancer.* Nature, 2017. **547**(7662): p. 222-226.
38. Disis, M.L., *Immune regulation of cancer.* J Clin Oncol, 2010. **28**(29): p. 4531-8.
39. Asadzadeh, Z., et al., *The paradox of Th17 cell functions in tumor immunity.* Cell Immunol, 2017. **322**: p. 15-25.
40. Ellyard, J.I., L. Simson, and C.R. Parish, *Th2-mediated anti-tumour immunity: friend or foe?* Tissue Antigens, 2007. **70**(1): p. 1-11.
41. Workman, C.J., et al., *The development and function of regulatory T cells.* Cell Mol Life Sci, 2009. **66**(16): p. 2603-22.
42. Sanmamed, M.F., et al., *Agonists of Co-stimulation in Cancer Immunotherapy Directed Against CD137, OX40, GITR, CD27, CD28, and ICOS.* Semin Oncol, 2015. **42**(4): p. 640-55.
43. Moran, A.E., M. Kovacsovics-Bankowski, and A.D. Weinberg, *The TNFRs OX40, 4-1BB, and CD40 as targets for cancer immunotherapy.* Curr Opin Immunol, 2013. **25**(2): p. 230-7.
44. Hernandez-Chacon, J.A., et al., *Costimulation through the CD137/4-1BB pathway protects human melanoma tumor-infiltrating lymphocytes from activation-induced cell death and enhances antitumor effector function.* J Immunother, 2011. **34**(3): p. 236-50.
45. Ye, Q., et al., *CD137 accurately identifies and enriches for naturally occurring tumor-reactive T cells in tumor.* Clin Cancer Res, 2014. **20**(1): p. 44-55.
46. Elpek, K.G., et al., *Ex vivo expansion of CD4+CD25+FoxP3+ T regulatory cells based on synergy between IL-2 and 4-1BB signaling.* J Immunol, 2007. **179**(11): p. 7295-304.
47. Barsoumian, H.B., E.S. Yolcu, and H. Shirwan, *4-1BB Signaling in Conventional T Cells Drives IL-2 Production That Overcomes CD4+CD25+FoxP3+ T Regulatory Cell Suppression.* PLoS One, 2016. **11**(4): p. e0153088.
48. Deng, J., et al., *OX40 (CD134) and OX40 ligand, important immune checkpoints in cancer.* Onco Targets Ther, 2019. **12**: p. 7347-7353.
49. Piconese, S., et al., *A non-redundant role for OX40 in the competitive fitness of Treg in response to IL-2.* Eur J Immunol, 2010. **40**(10): p. 2902-13.

50. Placke, T., H.G. Kopp, and H.R. Salih, *Glucocorticoid-induced TNFR-related (GITR) protein and its ligand in antitumor immunity: functional role and therapeutic modulation.* Clin Dev Immunol, 2010. **2010**: p. 239083.
51. Massa, C. and B. Seliger, *The tumor microenvironment: Thousand obstacles for effector T cells.* Cell Immunol, 2019. **343**: p. 103730.
52. Seidel, J.A., A. Otsuka, and K. Kabashima, *Anti-PD-1 and Anti-CTLA-4 Therapies in Cancer: Mechanisms of Action, Efficacy, and Limitations.* Front Oncol, 2018. **8**: p. 86.
53. Gros, A., et al., *PD-1 identifies the patient-specific CD8(+) tumor-reactive repertoire infiltrating human tumors.* J Clin Invest, 2014. **124**(5): p. 2246-59.
54. Ishikawa, M., et al., *High PD-1 expression level is associated with an unfavorable prognosis in patients with cervical adenocarcinoma.* Arch Gynecol Obstet, 2020. **302**(1): p. 209-218.
55. Zhang, Y., et al., *Prognostic significance of programmed cell death 1 (PD-1) or PD-1 ligand 1 (PD-L1) Expression in epithelial-originated cancer: a meta-analysis.* Medicine (Baltimore), 2015. **94**(6): p. e515.
56. Li, Y., et al., *Prognostic impact of programed cell death-1 (PD-1) and PD-ligand 1 (PD-L1) expression in cancer cells and tumor infiltrating lymphocytes in colorectal cancer.* Mol Cancer, 2016. **15**(1): p. 55.
57. Schneider, S., et al., *PD-1 and PD-L1 expression in HNSCC primary cancer and related lymph node metastasis - impact on clinical outcome.* Histopathology, 2018. **73**(4): p. 573-584.
58. Buisson, S. and F. Triebel, *LAG-3 (CD223) reduces macrophage and dendritic cell differentiation from monocyte precursors.* Immunology, 2005. **114**(3): p. 369-74.
59. Huang, C.T., et al., *Role of LAG-3 in regulatory T cells.* Immunity, 2004. **21**(4): p. 503-13.
60. Bono, M.R., et al., *CD73 and CD39 ectonucleotidases in T cell differentiation: Beyond immunosuppression.* FEBS Lett, 2015. **589**(22): p. 3454-60.
61. Roh, M., et al., *Targeting CD73 to augment cancer immunotherapy.* Curr Opin Pharmacol, 2020. **53**: p. 66-76.
62. Monney, L., et al., *Th1-specific cell surface protein Tim-3 regulates macrophage activation and severity of an autoimmune disease.* Nature, 2002. **415**(6871): p. 536-41.
63. Gao, X., et al., *TIM-3 expression characterizes regulatory T cells in tumor tissues and is associated with lung cancer progression.* PLoS One, 2012. **7**(2): p. e30676.
64. Zhu, C., et al., *The Tim-3 ligand galectin-9 negatively regulates T helper type 1 immunity.* Nat Immunol, 2005. **6**(12): p. 1245-52.
65. Dolina, J.S., T.J. Braciale, and Y.S. Hahn, *Liver-primed CD8+ T cells suppress antiviral adaptive immunity through galectin-9-independent T-cell immunoglobulin and mucin 3 engagement of high-mobility group box 1 in mice.* Hepatology, 2014. **59**(4): p. 1351-65.
66. Nakano, M., et al., *PD-1+ TIM-3+ T cells in malignant ascites predict prognosis of gastrointestinal cancer.* Cancer Sci, 2018. **109**(9): p. 2986-2992.
67. Kuai, W., et al., *Prognostic Impact of PD-1 and Tim-3 Expression in Tumor Tissue in Stage I-III Colorectal Cancer.* Biomed Res Int, 2020. **2020**: p. 5294043.
68. Devilard, E., et al., *Nectin-3 (CD113) interacts with Nectin-2 (CD112) to promote lymphocyte transendothelial migration.* PLoS One, 2013. **8**(10): p. e77424.
69. Manieri, N.A., E.Y. Chiang, and J.L. Grogan, *TIGIT: A Key Inhibitor of the Cancer Immunity Cycle.* Trends Immunol, 2017. **38**(1): p. 20-28.
70. Kiessling, R., E. Klein, and H. Wigzell, *"Natural" killer cells in the mouse. I. Cytotoxic cells with specificity for mouse Moloney leukemia cells. Specificity and distribution according to genotype.* Eur J Immunol, 1975. **5**(2): p. 112-7.
71. Wu, S.Y., et al., *Natural killer cells in cancer biology and therapy.* Mol Cancer, 2020. **19**(1): p. 120.
72. Meza Guzman, L.G., N. Keating, and S.E. Nicholson, *Natural Killer Cells: Tumor Surveillance and Signaling.* Cancers (Basel), 2020. **12**(4).

73. Zhang, S., et al., *Prognostic Significance of Tumor-Infiltrating Natural Killer Cells in Solid Tumors: A Systematic Review and Meta-Analysis.* Front Immunol, 2020. **11**: p. 1242.
74. Terren, I., et al., *NK Cell Metabolism and Tumor Microenvironment.* Front Immunol, 2019. **10**: p. 2278.
75. Fu, C. and A. Jiang, *Dendritic Cells and CD8 T Cell Immunity in Tumor Microenvironment.* Front Immunol, 2018. **9**: p. 3059.
76. Veglia, F. and D.I. Gabrilovich, *Dendritic cells in cancer: the role revisited.* Curr Opin Immunol, 2017. **45**: p. 43-51.
77. Hinshaw, D.C. and L.A. Shevde, *The Tumor Microenvironment Innately Modulates Cancer Progression.* Cancer Res, 2019. **79**(18): p. 4557-4566.
78. Pollard, J.W., *Macrophages define the invasive microenvironment in breast cancer.* J Leukoc Biol, 2008. **84**(3): p. 623-30.
79. Zhou, J., et al., *Tumor-Associated Macrophages: Recent Insights and Therapies.* Front Oncol, 2020. **10**: p. 188.
80. Chen, Y., et al., *Tumor-associated macrophages: an accomplice in solid tumor progression.* J Biomed Sci, 2019. **26**(1): p. 78.
81. Denning, T.L., et al., *Lamina propria macrophages and dendritic cells differentially induce regulatory and interleukin 17-producing T cell responses.* Nat Immunol, 2007. **8**(10): p. 1086-94.
82. Munn, D.H., et al., *Inhibition of T cell proliferation by macrophage tryptophan catabolism.* J Exp Med, 1999. **189**(9): p. 1363-72.
83. Rodriguez, P.C., et al., *Arginase I production in the tumor microenvironment by mature myeloid cells inhibits T-cell receptor expression and antigen-specific T-cell responses.* Cancer Res, 2004. **64**(16): p. 5839-49.
84. Cassetta, L., et al., *Deciphering myeloid-derived suppressor cells: isolation and markers in humans, mice and non-human primates.* Cancer Immunol Immunother, 2019. **68**(4): p. 687-697.
85. Schlecker, E., et al., *Tumor-infiltrating monocytic myeloid-derived suppressor cells mediate CCR5-dependent recruitment of regulatory T cells favoring tumor growth.* J Immunol, 2012. **189**(12): p. 5602-11.
86. Groth, C., et al., *Immunosuppression mediated by myeloid-derived suppressor cells (MDSCs) during tumour progression.* Br J Cancer, 2019. **120**(1): p. 16-25.
87. Kumar, V., et al., *The Nature of Myeloid-Derived Suppressor Cells in the Tumor Microenvironment.* Trends Immunol, 2016. **37**(3): p. 208-220.
88. Noman, M.Z., et al., *PD-L1 is a novel direct target of HIF-1alpha, and its blockade under hypoxia enhanced MDSC-mediated T cell activation.* J Exp Med, 2014. **211**(5): p. 781-90.
89. Movahedi, K., et al., *Identification of discrete tumor-induced myeloid-derived suppressor cell subpopulations with distinct T cell-suppressive activity.* Blood, 2008. **111**(8): p. 4233-44.
90. Ai, L., et al., *Prognostic role of myeloid-derived suppressor cells in cancers: a systematic review and meta-analysis.* BMC Cancer, 2018. **18**(1): p. 1220.
91. Mei, J., et al., *Cxcr2 and Cxcl5 regulate the IL-17/G-CSF axis and neutrophil homeostasis in mice.* J Clin Invest, 2012. **122**(3): p. 974-86.
92. Akbay, E.A., et al., *Interleukin-17A Promotes Lung Tumor Progression through Neutrophil Attraction to Tumor Sites and Mediating Resistance to PD-1 Blockade.* J Thorac Oncol, 2017. **12**(8): p. 1268-1279.
93. Fridlender, Z.G., et al., *Polarization of tumor-associated neutrophil phenotype by TGF-beta: "N1" versus "N2" TAN.* Cancer Cell, 2009. **16**(3): p. 183-94.
94. Wu, L., et al., *Tumor-Associated Neutrophils in Cancer: Going Pro.* Cancers (Basel), 2019. **11**(4).
95. Cao, J., et al., *Neutrophil-to-Lymphocyte Ratio Predicts PSA Response and Prognosis in Prostate Cancer: A Systematic Review and Meta-Analysis.* PLoS One, 2016. **11**(7): p. e0158770.

96. Chen, J., et al., *Meta-analysis of associations between neutrophil-to-lymphocyte ratio and prognosis of gastric cancer.* World J Surg Oncol, 2015. **13**: p. 122.
97. Cheng, H., et al., *Prognostic role of the neutrophil-to-lymphocyte ratio in pancreatic cancer: a meta-analysis.* Sci Rep, 2015. **5**: p. 11026.
98. Sahai, E., et al., *A framework for advancing our understanding of cancer-associated fibroblasts.* Nat Rev Cancer, 2020. **20**(3): p. 174-186.
99. Vacchelli, E., et al., *Trial watch: Tumor-targeting monoclonal antibodies for oncological indications.* Oncoimmunology, 2015. **4**(1): p. e985940.
100. Nejadmoghaddam, M.R., et al., *Antibody-Drug Conjugates: Possibilities and Challenges.* Avicenna J Med Biotechnol, 2019. **11**(1): p. 3-23.
101. Ellerman, D., *Bispecific T-cell engagers: Towards understanding variables influencing the in vitro potency and tumor selectivity and their modulation to enhance their efficacy and safety.* Methods, 2019. **154**: p. 102-117.
102. Buque, A., et al., *Trial Watch: Immunomodulatory monoclonal antibodies for oncological indications.* Oncoimmunology, 2015. **4**(4): p. e1008814.
103. Eskiocak, U., et al., *Differentiated agonistic antibody targeting CD137 eradicates large tumors without hepatotoxicity.* JCI Insight, 2020. **5**(5).
104. Etxeberria, I., et al., *New emerging targets in cancer immunotherapy: CD137/4-1BB costimulatory axis.* ESMO Open, 2020. **4**(Suppl 3).
105. Oberst, M.D., et al., *Potent Immune Modulation by MEDI6383, an Engineered Human OX40 Ligand IgG4P Fc Fusion Protein.* Mol Cancer Ther, 2018. **17**(5): p. 1024-1038.
106. Alves Costa Silva, C., et al., *New pathways in immune stimulation: targeting OX40.* ESMO Open, 2020. **5**(1).
107. Vonderheide, R.H., *CD40 Agonist Antibodies in Cancer Immunotherapy.* Annu Rev Med, 2020. **71**: p. 47-58.
108. Cohen, A.D., et al., *Agonist anti-GITR monoclonal antibody induces melanoma tumor immunity in mice by altering regulatory T cell stability and intra-tumor accumulation.* PLoS One, 2010. **5**(5): p. e10436.
109. Heinhuis, K.M., et al., *Safety, Tolerability, and Potential Clinical Activity of a Glucocorticoid-Induced TNF Receptor-Related Protein Agonist Alone or in Combination With Nivolumab for Patients With Advanced Solid Tumors: A Phase 1/2a Dose-Escalation and Cohort-Expansion Clinical Trial.* JAMA Oncol, 2019: p. 1-8.
110. Ungefroren, H., *Blockade of TGF-beta signaling: a potential target for cancer immunotherapy?* Expert Opin Ther Targets, 2019. **23**(8): p. 679-693.
111. Wolchok, J.D., et al., *Nivolumab plus ipilimumab in advanced melanoma.* N Engl J Med, 2013. **369**(2): p. 122-33.
112. Hamid, O., et al., *Safety and tumor responses with lambrolizumab (anti-PD-1) in melanoma.* N Engl J Med, 2013. **369**(2): p. 134-44.
113. Hodi, F.S., et al., *Improved survival with ipilimumab in patients with metastatic melanoma.* N Engl J Med, 2010. **363**(8): p. 711-23.
114. Schadendorf, D., et al., *Pooled Analysis of Long-Term Survival Data From Phase II and Phase III Trials of Ipilimumab in Unresectable or Metastatic Melanoma.* J Clin Oncol, 2015. **33**(17): p. 1889-94.
115. Robert, C., et al., *Pembrolizumab versus Ipilimumab in Advanced Melanoma.* N Engl J Med, 2015. **372**(26): p. 2521-32.
116. Larkin, J., et al., *Combined Nivolumab and Ipilimumab or Monotherapy in Untreated Melanoma.* N Engl J Med, 2015. **373**(1): p. 23-34.
117. Zappasodi, R., J.D. Wolchok, and T. Merghoub, *Strategies for Predicting Response to Checkpoint Inhibitors.* Curr Hematol Malig Rep, 2018. **13**(5): p. 383-395.
118. Ayoub, N.M., K.M. Al-Shami, and R.J. Yaghan, *Immunotherapy for HER2-positive breast cancer: recent advances and combination therapeutic approaches.* Breast Cancer (Dove Med Press), 2019. **11**: p. 53-69.
119. Brignone, C., et al., *First-line chemoimmunotherapy in metastatic breast carcinoma: combination of paclitaxel and IMP321 (LAG-3Ig) enhances immune responses and antitumor activity.* J Transl Med, 2010. **8**: p. 71.

120. Wang-Gillam, A., et al., *A phase I study of IMP321 and gemcitabine as the front-line therapy in patients with advanced pancreatic adenocarcinoma.* Invest New Drugs, 2013. **31**(3): p. 707-13.
121. Legat, A., et al., *Vaccination with LAG-3Ig (IMP321) and Peptides Induces Specific CD4 and CD8 T-Cell Responses in Metastatic Melanoma Patients--Report of a Phase I/IIa Clinical Trial.* Clin Cancer Res, 2016. **22**(6): p. 1330-40.
122. Allard, B., et al., *Targeting CD73 enhances the antitumor activity of anti-PD-1 and anti-CTLA-4 mAbs.* Clin Cancer Res, 2013. **19**(20): p. 5626-35.
123. Perrot, I., et al., *Blocking Antibodies Targeting the CD39/CD73 Immunosuppressive Pathway Unleash Immune Responses in Combination Cancer Therapies.* Cell Rep, 2019. **27**(8): p. 2411-2425 e9.
124. Hay, C.M., et al., *Targeting CD73 in the tumor microenvironment with MEDI9447.* Oncoimmunology, 2016. **5**(8): p. e1208875.
125. Sakuishi, K., et al., *Targeting Tim-3 and PD-1 pathways to reverse T cell exhaustion and restore anti-tumor immunity.* J Exp Med, 2010. **207**(10): p. 2187-94.
126. Zhang, Q., et al., *Blockade of the checkpoint receptor TIGIT prevents NK cell exhaustion and elicits potent anti-tumor immunity.* Nat Immunol, 2018. **19**(7): p. 723-732.
127. Rosenberg, S.A., et al., *Adoptive cell transfer: a clinical path to effective cancer immunotherapy.* Nat Rev Cancer, 2008. **8**(4): p. 299-308.
128. Rosenberg, S.A., et al., *Use of tumor-infiltrating lymphocytes and interleukin-2 in the immunotherapy of patients with metastatic melanoma. A preliminary report.* N Engl J Med, 1988. **319**(25): p. 1676-80.
129. Dudley, M.E., et al., *Adoptive cell therapy for patients with metastatic melanoma: evaluation of intensive myeloablative chemoradiation preparative regimens.* J Clin Oncol, 2008. **26**(32): p. 5233-9.
130. Schwartzentruber, D.J., et al., *In vitro predictors of therapeutic response in melanoma patients receiving tumor-infiltrating lymphocytes and interleukin-2.* J Clin Oncol, 1994. **12**(7): p. 1475-83.
131. Goff, S.L., et al., *Tumor infiltrating lymphocyte therapy for metastatic melanoma: analysis of tumors resected for TIL.* J Immunother, 2010. **33**(8): p. 840-7.
132. Wolfl, M., et al., *Activation-induced expression of CD137 permits detection, isolation, and expansion of the full repertoire of CD8+ T cells responding to antigen without requiring knowledge of epitope specificities.* Blood, 2007. **110**(1): p. 201-10.
133. Chacon, J.A., et al., *Co-stimulation through 4-1BB/CD137 improves the expansion and function of CD8(+) melanoma tumor-infiltrating lymphocytes for adoptive T-cell therapy.* PLoS One, 2013. **8**(4): p. e60031.
134. Friese, C., et al., *CTLA-4 blockade boosts the expansion of tumor-reactive CD8(+) tumor-infiltrating lymphocytes in ovarian cancer.* Sci Rep, 2020. **10**(1): p. 3914.
135. Platten, M. and R. Offringa, *Cancer immunotherapy: exploiting neoepitopes.* Cell Res, 2015. **25**(8): p. 887-8.
136. Robbins, P.F., et al., *Mining exomic sequencing data to identify mutated antigens recognized by adoptively transferred tumor-reactive T cells.* Nat Med, 2013. **19**(6): p. 747-52.
137. Cohen, C.J., et al., *Isolation of neoantigen-specific T cells from tumor and peripheral lymphocytes.* J Clin Invest, 2015. **125**(10): p. 3981-91.
138. Martin, S.D., et al., *A library-based screening method identifies neoantigen-reactive T cells in peripheral blood prior to relapse of ovarian cancer.* Oncoimmunology, 2017. **7**(1): p. e1371895.
139. Chrusciel, E., et al., *Adoptive Cell Therapy-Harnessing Antigen-Specific T Cells to Target Solid Tumours.* Cancers (Basel), 2020. **12**(3).
140. Zhao, L. and Y.J. Cao, *Engineered T Cell Therapy for Cancer in the Clinic.* Front Immunol, 2019. **10**: p. 2250.
141. zur Hausen, H., *Papillomaviruses--to vaccination and beyond.* Biochemistry (Mosc), 2008. **73**(5): p. 498-503.

142. Castle, P.E. and M. Maza, *Prophylactic HPV vaccination: past, present, and future.* Epidemiol Infect, 2016. **144**(3): p. 449-68.
143. Spinner, C., et al., *Human Papillomavirus Vaccine Effectiveness and Herd Protection in Young Women.* Pediatrics, 2019. **143**(2).
144. Chang, M.H., *Hepatitis B virus and cancer prevention.* Recent Results Cancer Res, 2011. **188**: p. 75-84.
145. Kooreman, N.G., et al., *Autologous iPSC-Based Vaccines Elicit Anti-tumor Responses In Vivo.* Cell Stem Cell, 2018. **22**(4): p. 501-513 e7.
146. Melief, C.J., et al., *Therapeutic cancer vaccines.* J Clin Invest, 2015. **125**(9): p. 3401-12.
147. Galluzzi, L., et al., *Classification of current anticancer immunotherapies.* Oncotarget, 2014. **5**(24): p. 12472-508.
148. Liu, M.A., *A Comparison of Plasmid DNA and mRNA as Vaccine Technologies.* Vaccines (Basel), 2019. **7**(2).
149. Cintolo, J.A., et al., *Dendritic cell-based vaccines: barriers and opportunities.* Future Oncol, 2012. **8**(10): p. 1273-99.
150. Ilkow, C.S., et al., *From scourge to cure: tumour-selective viral pathogenesis as a new strategy against cancer.* PLoS Pathog, 2014. **10**(1): p. e1003836.
151. Ungerechts, G., et al., *Moving oncolytic viruses into the clinic: clinical-grade production, purification, and characterization of diverse oncolytic viruses.* Mol Ther Methods Clin Dev, 2016. **3**: p. 16018.
152. Russell, L., et al., *Oncolytic Viruses: Priming Time for Cancer Immunotherapy.* BioDrugs, 2019. **33**(5): p. 485-501.
153. Kaczorowski, A., et al., *Delivery of improved oncolytic adenoviruses by mesenchymal stromal cells for elimination of tumorigenic pancreatic cancer cells.* Oncotarget, 2016. **7**(8): p. 9046-59.
154. Gholami, S., et al., *A novel vaccinia virus with dual oncolytic and anti-angiogenic therapeutic effects against triple-negative breast cancer.* Breast Cancer Res Treat, 2014. **148**(3): p. 489-99.
155. Veinalde, R., et al., *Oncolytic measles virus encoding interleukin-12 mediates potent antitumor effects through T cell activation.* Oncoimmunology, 2017. **6**(4): p. e1285992.
156. Conry, R.M., et al., *Talimogene laherparepvec: First in class oncolytic virotherapy.* Hum Vaccin Immunother, 2018. **14**(4): p. 839-846.
157. Andtbacka, R.H., et al., *Talimogene Laherparepvec Improves Durable Response Rate in Patients With Advanced Melanoma.* J Clin Oncol, 2015. **33**(25): p. 2780-8.
158. Engeland, C.E., et al., *CTLA-4 and PD-L1 checkpoint blockade enhances oncolytic measles virus therapy.* Mol Ther, 2014. **22**(11): p. 1949-59.
159. Speck, T., et al., *Targeted BiTE Expression by an Oncolytic Vector Augments Therapeutic Efficacy Against Solid Tumors.* Clin Cancer Res, 2018. **24**(9): p. 2128-2137.
160. Campadelli-Fiume, G., et al., *Retargeting Strategies for Oncolytic Herpes Simplex Viruses.* Viruses, 2016. **8**(3): p. 63.
161. Berraondo, P., et al., *Cytokines in clinical cancer immunotherapy.* Br J Cancer, 2019. **120**(1): p. 6-15.
162. Aleynick, M., et al., *Pathogen Molecular Pattern Receptor Agonists: Treating Cancer by Mimicking Infection.* Clin Cancer Res, 2019. **25**(21): p. 6283-6294.
163. Harvey, J.B., et al., *CD73's Potential as an Immunotherapy Target in Gastrointestinal Cancers.* Front Immunol, 2020. **11**: p. 508.
164. Prendergast, G.C., et al., *Discovery of IDO1 Inhibitors: From Bench to Bedside.* Cancer Res, 2017. **77**(24): p. 6795-6811.
165. Genard, G., S. Lucas, and C. Michiels, *Reprogramming of Tumor-Associated Macrophages with Anticancer Therapies: Radiotherapy versus Chemo- and Immunotherapies.* Front Immunol, 2017. **8**: p. 828.
166. Zhou, J., et al., *Immunogenic cell death in cancer therapy: Present and emerging inducers.* J Cell Mol Med, 2019. **23**(8): p. 4854-4865.

167. Bipat, S., et al., *Ultrasonography, computed tomography and magnetic resonance imaging for diagnosis and determining resectability of pancreatic adenocarcinoma: a meta-analysis.* J Comput Assist Tomogr, 2005. **29**(4): p. 438-45.
168. Follen, M., et al., *Imaging in cervical cancer.* Cancer, 2003. **98**(9 Suppl): p. 2028-38.
169. Baskar, R., et al., *Cancer and radiation therapy: current advances and future directions.* Int J Med Sci, 2012. **9**(3): p. 193-9.
170. Ahmed, K.A., et al., *Altered fractionation schedules in radiation treatment: a review.* Semin Oncol, 2014. **41**(6): p. 730-50.
171. Begg, A.C., F.A. Stewart, and C. Vens, *Strategies to improve radiotherapy with targeted drugs.* Nat Rev Cancer, 2011. **11**(4): p. 239-53.
172. Citrin, D.E., *Recent Developments in Radiotherapy.* N Engl J Med, 2017. **377**(11): p. 1065-1075.
173. Palma, D.A., et al., *New developments in arc radiation therapy: a review.* Cancer Treat Rev, 2010. **36**(5): p. 393-9.
174. Verellen, D., et al., *Innovations in image-guided radiotherapy.* Nat Rev Cancer, 2007. **7**(12): p. 949-60.
175. Sterzing, F., et al., *Image-guided radiotherapy: a new dimension in radiation oncology.* Dtsch Arztebl Int, 2011. **108**(16): p. 274-80.
176. Lo, S.S., et al., *Stereotactic body radiation therapy: a novel treatment modality.* Nat Rev Clin Oncol, 2010. **7**(1): p. 44-54.
177. Schulz-Ertner, D. and H. Tsujii, *Particle radiation therapy using proton and heavier ion beams.* J Clin Oncol, 2007. **25**(8): p. 953-64.
178. Nickoloff, J.A., *Photon, light ion, and heavy ion cancer radiotherapy: paths from physics and biology to clinical practice.* Ann Transl Med, 2015. **3**(21): p. 336.
179. Jiang, G.L., *Particle therapy for cancers: a new weapon in radiation therapy.* Front Med, 2012. **6**(2): p. 165-72.
180. Wang, H. and Y. Wang, *Heavier ions with a different linear energy transfer spectrum kill more cells due to similar interference with the Ku-dependent DNA repair pathway.* Radiat Res, 2014. **182**(4): p. 458-61.
181. Nikjoo, H., et al., *Radiation track, DNA damage and response-a review.* Rep Prog Phys, 2016. **79**(11): p. 116601.
182. Hill, R.P., et al., *Hypoxia and Predicting Radiation Response.* Semin Radiat Oncol, 2015. **25**(4): p. 260-72.
183. Weyrather, W.K. and J. Debus, *Particle beams for cancer therapy.* Clin Oncol (R Coll Radiol), 2003. **15**(1): p. S23-8.
184. Hada, M. and A.G. Georgakilas, *Formation of clustered DNA damage after high-LET irradiation: a review.* J Radiat Res, 2008. **49**(3): p. 203-10.
185. Ogata, T., et al., *Particle irradiation suppresses metastatic potential of cancer cells.* Cancer Res, 2005. **65**(1): p. 113-20.
186. Shimokawa, T., et al., *The Future of Combining Carbon-Ion Radiotherapy with Immunotherapy: Evidence and Progress in Mouse Models.* Int J Part Ther, 2016. **3**(1): p. 61-70.
187. Baek, S.J., et al., *Cancer stem cells: The potential of carbon ion beam radiation and new radiosensitizers (Review).* Oncol Rep, 2015. **34**(5): p. 2233-7.
188. Sato, K., et al., *Repeated photon and C-ion irradiations in vivo have different impact on alteration of tumor characteristics.* Sci Rep, 2018. **8**(1): p. 1458.
189. Mohamad, O., et al., *Carbon Ion Radiotherapy: A Review of Clinical Experiences and Preclinical Research, with an Emphasis on DNA Damage/Repair.* Cancers (Basel), 2017. **9**(6).
190. Mizoe, J.E., et al., *Phase I/II clinical trial of carbon ion radiotherapy for malignant gliomas: combined X-ray radiotherapy, chemotherapy, and carbon ion radiotherapy.* Int J Radiat Oncol Biol Phys, 2007. **69**(2): p. 390-6.
191. Schulz-Ertner, D., et al., *Effectiveness of carbon ion radiotherapy in the treatment of skull-base chordomas.* Int J Radiat Oncol Biol Phys, 2007. **68**(2): p. 449-57.

192. Nikoghosyan, A.V., et al., *Randomised trial of proton vs. carbon ion radiation therapy in patients with low and intermediate grade chondrosarcoma of the skull base, clinical phase III study.* BMC Cancer, 2010. **10**: p. 606.
193. Malouff, T.D., et al., *Carbon Ion Therapy: A Modern Review of an Emerging Technology.* Front Oncol, 2020. **10**: p. 82.
194. Abraham, R.T., *Cell cycle checkpoint signaling through the ATM and ATR kinases.* Genes Dev, 2001. **15**(17): p. 2177-96.
195. Shen, T. and S. Huang, *The role of Cdc25A in the regulation of cell proliferation and apoptosis.* Anticancer Agents Med Chem, 2012. **12**(6): p. 631-9.
196. Reinhardt, H.C. and B. Schumacher, *The p53 network: cellular and systemic DNA damage responses in aging and cancer.* Trends Genet, 2012. **28**(3): p. 128-36.
197. Chen, J., *The Cell-Cycle Arrest and Apoptotic Functions of p53 in Tumor Initiation and Progression.* Cold Spring Harb Perspect Med, 2016. **6**(3): p. a026104.
198. Biau, J., et al., *Altering DNA Repair to Improve Radiation Therapy: Specific and Multiple Pathway Targeting.* Front Oncol, 2019. **9**: p. 1009.
199. Mahaney, B.L., K. Meek, and S.P. Lees-Miller, *Repair of ionizing radiation-induced DNA double-strand breaks by non-homologous end-joining.* Biochem J, 2009. **417**(3): p. 639-50.
200. Mariotti, L.G., et al., *Use of the gamma-H2AX assay to investigate DNA repair dynamics following multiple radiation exposures.* PLoS One, 2013. **8**(11): p. e79541.
201. Jasin, M. and R. Rothstein, *Repair of strand breaks by homologous recombination.* Cold Spring Harb Perspect Biol, 2013. **5**(11): p. a012740.
202. Galluzzi, L., et al., *Molecular mechanisms of cell death: recommendations of the Nomenclature Committee on Cell Death 2018.* Cell Death Differ, 2018. **25**(3): p. 486-541.
203. Maier, P., et al., *Cellular Pathways in Response to Ionizing Radiation and Their Targetability for Tumor Radiosensitization.* Int J Mol Sci, 2016. **17**(1).
204. Kalkavan, H. and D.R. Green, *MOMP, cell suicide as a BCL-2 family business.* Cell Death Differ, 2018. **25**(1): p. 46-55.
205. Singh, R., A. Letai, and K. Sarosiek, *Regulation of apoptosis in health and disease: the balancing act of BCL-2 family proteins.* Nat Rev Mol Cell Biol, 2019. **20**(3): p. 175-193.
206. Ogura, A., et al., *Redox regulation in radiation-induced cytochrome c release from mitochondria of human lung carcinoma A549 cells.* Cancer Lett, 2009. **277**(1): p. 64-71.
207. Orrenius, S., B. Zhivotovsky, and P. Nicotera, *Regulation of cell death: the calcium-apoptosis link.* Nat Rev Mol Cell Biol, 2003. **4**(7): p. 552-65.
208. Rahmanian, N., S.J. Hosseinimehr, and A. Khalaj, *The paradox role of caspase cascade in ionizing radiation therapy.* J Biomed Sci, 2016. **23**(1): p. 88.
209. Fulda, S. and K.M. Debatin, *Extrinsic versus intrinsic apoptosis pathways in anticancer chemotherapy.* Oncogene, 2006. **25**(34): p. 4798-811.
210. Chen, Z., et al., *Cellular senescence in ionizing radiation (Review).* Oncol Rep, 2019. **42**(3): p. 883-894.
211. Sia, J., et al., *Molecular Mechanisms of Radiation-Induced Cancer Cell Death: A Primer.* Front Cell Dev Biol, 2020. **8**: p. 41.
212. Walle, T., et al., *Radiation effects on antitumor immune responses: current perspectives and challenges.* Ther Adv Med Oncol, 2018. **10**: p. 1758834017742575.
213. Tang, C., et al., *Combining radiation and immunotherapy: a new systemic therapy for solid tumors?* Cancer Immunol Res, 2014. **2**(9): p. 831-8.
214. Idzko, M., D. Ferrari, and H.K. Eltzschig, *Nucleotide signalling during inflammation.* Nature, 2014. **509**(7500): p. 310-7.
215. Chao, M.P., et al., *Calreticulin is the dominant pro-phagocytic signal on multiple human cancers and is counterbalanced by CD47.* Sci Transl Med, 2010. **2**(63): p. 63ra94.
216. Golden, E.B., et al., *Radiation fosters dose-dependent and chemotherapy-induced immunogenic cell death.* Oncoimmunology, 2014. **3**: p. e28518.

217. Wang, L., et al., *Ionizing Radiation Induces HMGB1 Cytoplasmic Translocation and Extracellular Release.* Guo Ji Fang She Yi Xue He Yi Xue Za Zhi, 2016. **40**(2): p. 91-99.
218. Yang, D., et al., *High mobility group box-1 protein induces the migration and activation of human dendritic cells and acts as an alarmin.* J Leukoc Biol, 2007. **81**(1): p. 59-66.
219. Simmons, D.P., et al., *Type I IFN drives a distinctive dendritic cell maturation phenotype that allows continued class II MHC synthesis and antigen processing.* J Immunol, 2012. **188**(7): p. 3116-26.
220. Siemann, D.W., *The unique characteristics of tumor vasculature and preclinical evidence for its selective disruption by Tumor-Vascular Disrupting Agents.* Cancer Treat Rev, 2011. **37**(1): p. 63-74.
221. Klug, F., et al., *Low-dose irradiation programs macrophage differentiation to an iNOS(+)/M1 phenotype that orchestrates effective T cell immunotherapy.* Cancer Cell, 2013. **24**(5): p. 589-602.
222. Rodriguez-Ruiz, M.E., et al., *Intercellular Adhesion Molecule-1 and Vascular Cell Adhesion Molecule Are Induced by Ionizing Radiation on Lymphatic Endothelium.* Int J Radiat Oncol Biol Phys, 2017. **97**(2): p. 389-400.
223. Matsumura, S., et al., *Radiation-induced CXCL16 release by breast cancer cells attracts effector T cells.* J Immunol, 2008. **181**(5): p. 3099-107.
224. Yoon, M.S., et al., *Irradiation of breast cancer cells enhances CXCL16 ligand expression and induces the migration of natural killer cells expressing the CXCR6 receptor.* Cytotherapy, 2016. **18**(12): p. 1532-1542.
225. Burnette, B.C., et al., *The efficacy of radiotherapy relies upon induction of type i interferon-dependent innate and adaptive immunity.* Cancer Res, 2011. **71**(7): p. 2488-96.
226. Murata, M., et al., *A comparison of the antitumor effects of interferon-alpha and beta on human hepatocellular carcinoma cell lines.* Cytokine, 2006. **33**(3): p. 121-8.
227. Gerber, S.A., et al., *IFN-gamma mediates the antitumor effects of radiation therapy in a murine colon tumor.* Am J Pathol, 2013. **182**(6): p. 2345-54.
228. Lugade, A.A., et al., *Radiation-induced IFN-gamma production within the tumor microenvironment influences antitumor immunity.* J Immunol, 2008. **180**(5): p. 3132-9.
229. Zhang, B., et al., *Induced sensitization of tumor stroma leads to eradication of established cancer by T cells.* J Exp Med, 2007. **204**(1): p. 49-55.
230. Reits, E.A., et al., *Radiation modulates the peptide repertoire, enhances MHC class I expression, and induces successful antitumor immunotherapy.* J Exp Med, 2006. **203**(5): p. 1259-71.
231. Luce, A., et al., *Death receptor pathways mediate targeted and non-targeted effects of ionizing radiations in breast cancer cells.* Carcinogenesis, 2009. **30**(3): p. 432-9.
232. Gameiro, S.R., et al., *Radiation-induced immunogenic modulation of tumor enhances antigen processing and calreticulin exposure, resulting in enhanced T-cell killing.* Oncotarget, 2014. **5**(2): p. 403-16.
233. Nguyen, A.M., et al., *Upregulation of CD73 Confers Acquired Radioresistance and is Required for Maintaining Irradiation-selected Pancreatic Cancer Cells in a Mesenchymal State.* Mol Cell Proteomics, 2020. **19**(2): p. 375-389.
234. Keam, S., et al., *Enhancing the efficacy of immunotherapy using radiotherapy.* Clin Transl Immunology, 2020. **9**(9): p. e1169.
235. Moeller, B.J., et al., *Radiation activates HIF-1 to regulate vascular radiosensitivity in tumors: role of reoxygenation, free radicals, and stress granules.* Cancer Cell, 2004. **5**(5): p. 429-41.
236. Hammami, A., et al., *HIF-1alpha hampers dendritic cell function and Th1 generation during chronic visceral leishmaniasis.* Sci Rep, 2018. **8**(1): p. 3500.
237. Chen, B., et al., *HIF1A expression correlates with increased tumor immune and stromal signatures and aggressive phenotypes in human cancers.* Cell Oncol (Dordr), 2020. **43**(5): p. 877-888.

238. Shibuya, M., *Vascular Endothelial Growth Factor (VEGF) and Its Receptor (VEGFR) Signaling in Angiogenesis: A Crucial Target for Anti- and Pro-Angiogenic Therapies.* Genes Cancer, 2011. **2**(12): p. 1097-105.
239. Hovinga, K.E., et al., *Radiation-enhanced vascular endothelial growth factor (VEGF) secretion in glioblastoma multiforme cell lines--a clue to radioresistance?* J Neurooncol, 2005. **74**(2): p. 99-103.
240. Voron, T., et al., *VEGF-A modulates expression of inhibitory checkpoints on CD8+ T cells in tumors.* J Exp Med, 2015. **212**(2): p. 139-48.
241. Zhu, P., et al., *The role and significance of VEGFR2(+) regulatory T cells in tumor immunity.* Onco Targets Ther, 2017. **10**: p. 4315-4319.
242. Horikawa, N., et al., *Expression of Vascular Endothelial Growth Factor in Ovarian Cancer Inhibits Tumor Immunity through the Accumulation of Myeloid-Derived Suppressor Cells.* Clin Cancer Res, 2017. **23**(2): p. 587-599.
243. Kozin, S.V., et al., *Recruitment of myeloid but not endothelial precursor cells facilitates tumor regrowth after local irradiation.* Cancer Res, 2010. **70**(14): p. 5679-85.
244. Kalbasi, A., et al., *Tumor-Derived CCL2 Mediates Resistance to Radiotherapy in Pancreatic Ductal Adenocarcinoma.* Clin Cancer Res, 2017. **23**(1): p. 137-148.
245. Stafford, J.H., et al., *Colony stimulating factor 1 receptor inhibition delays recurrence of glioblastoma after radiation by altering myeloid cell recruitment and polarization.* Neuro Oncol, 2016. **18**(6): p. 797-806.
246. Chitu, V. and E.R. Stanley, *Colony-stimulating factor-1 in immunity and inflammation.* Curr Opin Immunol, 2006. **18**(1): p. 39-48.
247. Leblond, M.M., et al., *M2 macrophages are more resistant than M1 macrophages following radiation therapy in the context of glioblastoma.* Oncotarget, 2017. **8**(42): p. 72597-72612.
248. Liu, S., et al., *Effects of radiation on T regulatory cells in normal states and cancer: mechanisms and clinical implications.* Am J Cancer Res, 2015. **5**(11): p. 3276-85.
249. Vanpouille-Box, C., et al., *TGFbeta Is a Master Regulator of Radiation Therapy-Induced Antitumor Immunity.* Cancer Res, 2015. **75**(11): p. 2232-42.
250. Wennerberg, E., et al., *Barriers to Radiation-Induced In Situ Tumor Vaccination.* Front Immunol, 2017. **8**: p. 229.
251. Deng, L., et al., *Irradiation and anti-PD-L1 treatment synergistically promote antitumor immunity in mice.* J Clin Invest, 2014. **124**(2): p. 687-95.
252. Mole, R.H., *Whole body irradiation; radiobiology or medicine?* Br J Radiol, 1953. **26**(305): p. 234-41.
253. Hu, Z.I., H.L. McArthur, and A.Y. Ho, *The Abscopal Effect of Radiation Therapy: What Is It and How Can We Use It in Breast Cancer?* Curr Breast Cancer Rep, 2017. **9**(1): p. 45-51.
254. Postow, M.A., et al., *Immunologic correlates of the abscopal effect in a patient with melanoma.* N Engl J Med, 2012. **366**(10): p. 925-31.
255. Wersall, P.J., et al., *Regression of non-irradiated metastases after extracranial stereotactic radiotherapy in metastatic renal cell carcinoma.* Acta Oncol, 2006. **45**(4): p. 493-7.
256. Abuodeh, Y., P. Venkat, and S. Kim, *Systematic review of case reports on the abscopal effect.* Curr Probl Cancer, 2016. **40**(1): p. 25-37.
257. Yamazaki, T., et al., *Mitochondrial DNA drives abscopal responses to radiation that are inhibited by autophagy.* Nat Immunol, 2020. **21**(10): p. 1160-1171.
258. Vanpouille-Box, C., et al., *DNA exonuclease Trex1 regulates radiotherapy-induced tumour immunogenicity.* Nat Commun, 2017. **8**: p. 15618.
259. Demaria, S., et al., *Ionizing radiation inhibition of distant untreated tumors (abscopal effect) is immune mediated.* Int J Radiat Oncol Biol Phys, 2004. **58**(3): p. 862-70.
260. Rodriguez-Ruiz, M.E., et al., *Brachytherapy attains abscopal effects when combined with immunostimulatory monoclonal antibodies.* Brachytherapy, 2017. **16**(6): p. 1246-1251.
261. Twyman-Saint Victor, C., et al., *Radiation and dual checkpoint blockade activate non-redundant immune mechanisms in cancer.* Nature, 2015. **520**(7547): p. 373-7.

262. Demaria, S., et al., *Immune-mediated inhibition of metastases after treatment with local radiation and CTLA-4 blockade in a mouse model of breast cancer.* Clin Cancer Res, 2005. **11**(2 Pt 1): p. 728-34.
263. Kang, J., S. Demaria, and S. Formenti, *Current clinical trials testing the combination of immunotherapy with radiotherapy.* J Immunother Cancer, 2016. **4**: p. 51.
264. Dewan, M.Z., et al., *Fractionated but not single-dose radiotherapy induces an immune-mediated abscopal effect when combined with anti-CTLA-4 antibody.* Clin Cancer Res, 2009. **15**(17): p. 5379-88.
265. Dovedi, S.J., et al., *Acquired resistance to fractionated radiotherapy can be overcome by concurrent PD-L1 blockade.* Cancer Res, 2014. **74**(19): p. 5458-68.
266. Golden, E.B., et al., *Local radiotherapy and granulocyte-macrophage colony-stimulating factor to generate abscopal responses in patients with metastatic solid tumours: a proof-of-principle trial.* Lancet Oncol, 2015. **16**(7): p. 795-803.
267. van Meir, H., et al., *Impact of (chemo)radiotherapy on immune cell composition and function in cervical cancer patients.* Oncoimmunology, 2017. **6**(2): p. e1267095.
268. Casey, A.E., W.R. Laster, Jr., and G.L. Ross, *Sustained enhanced growth of carcinoma EO771 in C57 black mice.* Proc Soc Exp Biol Med, 1951. **77**(2): p. 358-62.
269. Howlader, N., et al., *Differences in Breast Cancer Survival by Molecular Subtypes in the United States.* Cancer Epidemiol Biomarkers Prev, 2018. **27**(6): p. 619-626.
270. Soliman, N.A. and S.M. Yussif, *Ki-67 as a prognostic marker according to breast cancer molecular subtype.* Cancer Biol Med, 2016. **13**(4): p. 496-504.
271. Johnstone, C.N., et al., *Functional and molecular characterisation of EO771.LMB tumours, a new C57BL/6-mouse-derived model of spontaneously metastatic mammary cancer.* Dis Model Mech, 2015. **8**(3): p. 237-51.
272. Le Naour, A., et al., *EO771, the first luminal B mammary cancer cell line from C57BL/6 mice.* Cancer Cell Int, 2020. **20**: p. 328.
273. Yang, Y., et al., *Immunocompetent mouse allograft models for development of therapies to target breast cancer metastasis.* Oncotarget, 2017. **8**(19): p. 30621-30643.
274. Scrimieri, F., et al., *Murine leukemia virus envelope gp70 is a shared biomarker for the high-sensitivity quantification of murine tumor burden.* Oncoimmunology, 2013. **2**(11): p. e26889.
275. Zhu, L., et al., *TSC1 controls macrophage polarization to prevent inflammatory disease.* Nat Commun, 2014. **5**: p. 4696.
276. Shaul, M.E., et al., *Dynamic, M2-like remodeling phenotypes of CD11c+ adipose tissue macrophages during high-fat diet--induced obesity in mice.* Diabetes, 2010. **59**(5): p. 1171-81.
277. Chen, E.Y., et al., *Enrichr: interactive and collaborative HTML5 gene list enrichment analysis tool.* BMC Bioinformatics, 2013. **14**: p. 128.
278. Kuleshov, M.V., et al., *Enrichr: a comprehensive gene set enrichment analysis web server 2016 update.* Nucleic Acids Res, 2016. **44**(W1): p. W90-7.
279. Neukirch, L., et al., *Adenovirus based virus-like-vaccines targeting endogenous retroviruses can eliminate growing colorectal cancers in mice.* Oncotarget, 2019. **10**(14): p. 1458-1472.
280. Huang da, W., B.T. Sherman, and R.A. Lempicki, *Systematic and integrative analysis of large gene lists using DAVID bioinformatics resources.* Nat Protoc, 2009. **4**(1): p. 44-57.
281. Walker, L.S., *Treg and CTLA-4: two intertwining pathways to immune tolerance.* J Autoimmun, 2013. **45**: p. 49-57.
282. Huang, C., et al., *Immune checkpoint molecules. Possible future therapeutic implications in autoimmune diseases.* J Autoimmun, 2019. **104**: p. 102333.
283. Howard, M., et al., *Characterization of relative biological effectiveness for conventional radiation therapy: a comparison of clinical 6 MV X-rays and 137Cs.* J Radiat Res, 2017. **58**(5): p. 608-613.
284. Suzuki, M., et al., *Relative biological effectiveness for cell-killing effect on various human cell lines irradiated with heavy-ion medical accelerator in Chiba (HIMAC) carbon-ion beams.* Int J Radiat Oncol Biol Phys, 2000. **48**(1): p. 241-50.

285. Durante, M. and J.S. Loeffler, *Charged particles in radiation oncology.* Nat Rev Clin Oncol, 2010. **7**(1): p. 37-43.
286. Franken, N.A., et al., *Clonogenic assay of cells in vitro.* Nat Protoc, 2006. **1**(5): p. 2315-9.
287. Franken, N.A., et al., *Cell survival and radiosensitisation: modulation of the linear and quadratic parameters of the LQ model (Review).* Int J Oncol, 2013. **42**(5): p. 1501-15.
288. Hojo, H., et al., *Difference in the relative biological effectiveness and DNA damage repair processes in response to proton beam therapy according to the positions of the spread out Bragg peak.* Radiat Oncol, 2017. **12**(1): p. 111.
289. Hagiwara, Y., et al., *3D-structured illumination microscopy reveals clustered DNA double-strand break formation in widespread gammaH2AX foci after high LET heavy-ion particle radiation.* Oncotarget, 2017. **8**(65): p. 109370-109381.
290. Furusawa, Y., et al., *Inactivation of aerobic and hypoxic cells from three different cell lines by accelerated (3)He-, (12)C- and (20)Ne-ion beams.* Radiat Res, 2000. **154**(5): p. 485-96.
291. Schroter, P., et al., *Radiation-induced alterations in immunogenicity of a murine pancreatic ductal adenocarcinoma cell line.* Sci Rep, 2020. **10**(1): p. 686.
292. Hartmann, L., et al., *Photon versus carbon ion irradiation: immunomodulatory effects exerted on murine tumor cell lines.* Sci Rep, 2020. **10**(1): p. 21517.
293. Maeda, J., et al., *Intrinsic Radiosensitivity and Cellular Characterization of 27 Canine Cancer Cell Lines.* PLoS One, 2016. **11**(6): p. e0156689.
294. Banath, J.P., S.H. Macphail, and P.L. Olive, *Radiation sensitivity, H2AX phosphorylation, and kinetics of repair of DNA strand breaks in irradiated cervical cancer cell lines.* Cancer Res, 2004. **64**(19): p. 7144-9.
295. Taneja, N., et al., *Histone H2AX phosphorylation as a predictor of radiosensitivity and target for radiotherapy.* J Biol Chem, 2004. **279**(3): p. 2273-80.
296. Todorovic, V., et al., *Mechanisms of different response to ionizing irradiation in isogenic head and neck cancer cell lines.* Radiat Oncol, 2019. **14**(1): p. 214.
297. Zhao, Y. and S. Chen, *Targeting DNA Double-Strand Break (DSB) Repair to Counteract Tumor Radio-resistance.* Curr Drug Targets, 2019. **20**(9): p. 891-902.
298. Shim, G., et al., *Comparison of Individual Radiosensitivity to gamma-Rays and Carbon Ions.* Front Oncol, 2016. **6**: p. 137.
299. Karagiannis, T.C. and A. El-Osta, *Double-strand breaks: signaling pathways and repair mechanisms.* Cell Mol Life Sci, 2004. **61**(17): p. 2137-47.
300. Kobayashi, D., et al., *Mitotic catastrophe is a putative mechanism underlying the weak correlation between sensitivity to carbon ions and cisplatin.* Sci Rep, 2017. **7**: p. 40588.
301. Ghorai, A., et al., *Radiosensitivity and Induction of Apoptosis by High LET Carbon Ion Beam and Low LET Gamma Radiation: A Comparative Study.* Scientifica (Cairo), 2014. **2014**: p. 438030.
302. Tsuboi, K., et al., *Cytotoxic effect of accelerated carbon beams on glioblastoma cell lines with p53 mutation: clonogenic survival and cell-cycle analysis.* Int J Radiat Biol, 1998. **74**(1): p. 71-9.
303. Tsuboi, K., et al., *Cell cycle checkpoint and apoptosis induction in glioblastoma cells and fibroblasts irradiated with carbon beam.* J Radiat Res, 2007. **48**(4): p. 317-25.
304. Hoffmann, P.R., et al., *Interaction between phosphatidylserine and the phosphatidylserine receptor inhibits immune responses in vivo.* J Immunol, 2005. **174**(3): p. 1393-404.
305. Steinman, R.M., et al., *The induction of tolerance by dendritic cells that have captured apoptotic cells.* J Exp Med, 2000. **191**(3): p. 411-6.
306. Ferguson, T.A., et al., *Uptake of apoptotic antigen-coupled cells by lymphoid dendritic cells and cross-priming of CD8(+) T cells produce active immune unresponsiveness.* J Immunol, 2002. **168**(11): p. 5589-95.
307. Casares, N., et al., *Caspase-dependent immunogenicity of doxorubicin-induced tumor cell death.* J Exp Med, 2005. **202**(12): p. 1691-701.

308. Obeid, M., et al., *Calreticulin exposure is required for the immunogenicity of gamma-irradiation and UVC light-induced apoptosis.* Cell Death Differ, 2007. **14**(10): p. 1848-50.
309. Gorin, J.B., et al., *Antitumor immunity induced after alpha irradiation.* Neoplasia, 2014. **16**(4): p. 319-28.
310. Li, G., X. Liang, and M.T. Lotze, *HMGB1: The Central Cytokine for All Lymphoid Cells.* Front Immunol, 2013. **4**: p. 68.
311. Frey, B., et al., *Combined treatment of human colorectal tumor cell lines with chemotherapeutic agents and ionizing irradiation can in vitro induce tumor cell death forms with immunogenic potential.* J Immunotoxicol, 2012. **9**(3): p. 301-13.
312. Yoshimoto, Y., et al., *Carbon-ion beams induce production of an immune mediator protein, high mobility group box 1, at levels comparable with X-ray irradiation.* J Radiat Res, 2015. **56**(3): p. 509-14.
313. Chen, X., et al., *Radiotherapy-induced cell death activates paracrine HMGB1-TLR2 signaling and accelerates pancreatic carcinoma metastasis.* J Exp Clin Cancer Res, 2018. **37**(1): p. 77.
314. Liao, Y., et al., *HMGB1 in Radiotherapy: A Two Headed Signal Regulating Tumor Radiosensitivity and Immunity.* Onco Targets Ther, 2020. **13**: p. 6859-6871.
315. Martins, I., et al., *Molecular mechanisms of ATP secretion during immunogenic cell death.* Cell Death Differ, 2014. **21**(1): p. 79-91.
316. Garg, A.D., et al., *Extracellular ATP and P(2)X(7) receptor exert context-specific immunogenic effects after immunogenic cancer cell death.* Cell Death Dis, 2016. **7**: p. e2097.
317. Orriss, I.R., et al., *Hypoxia stimulates vesicular ATP release from rat osteoblasts.* J Cell Physiol, 2009. **220**(1): p. 155-62.
318. Obeid, M., et al., *Calreticulin exposure dictates the immunogenicity of cancer cell death.* Nat Med, 2007. **13**(1): p. 54-61.
319. Andocs, G., et al., *Upregulation of heat shock proteins and the promotion of damage-associated molecular pattern signals in a colorectal cancer model by modulated electrohyperthermia.* Cell Stress Chaperones, 2015. **20**(1): p. 37-46.
320. Garg, A.D., et al., *Molecular and Translational Classifications of DAMPs in Immunogenic Cell Death.* Front Immunol, 2015. **6**: p. 588.
321. Wan, S., et al., *Chemotherapeutics and radiation stimulate MHC class I expression through elevated interferon-beta signaling in breast cancer cells.* PLoS One, 2012. **7**(3): p. e32542.
322. Garcia-Lora, A., I. Algarra, and F. Garrido, *MHC class I antigens, immune surveillance, and tumor immune escape.* J Cell Physiol, 2003. **195**(3): p. 346-55.
323. Lhuillier, C., et al., *Radiation therapy and anti-tumor immunity: exposing immunogenic mutations to the immune system.* Genome Med, 2019. **11**(1): p. 40.
324. Lhuillier, C., et al., *Radiotherapy-exposed CD8+ and CD4+ neoantigens enhance tumor control.* J Clin Invest, 2021.
325. Derer, A., et al., *Chemoradiation Increases PD-L1 Expression in Certain Melanoma and Glioblastoma Cells.* Front Immunol, 2016. **7**: p. 610.
326. Mimura, K., et al., *PD-L1 expression is mainly regulated by interferon gamma associated with JAK-STAT pathway in gastric cancer.* Cancer Sci, 2018. **109**(1): p. 43-53.
327. Pistillo, M.P., et al., *IFN-gamma upregulates membranous and soluble PD-L1 in mesothelioma cells: potential implications for the clinical response to PD-1/PD-L1 blockade.* Cell Mol Immunol, 2020. **17**(4): p. 410-411.
328. Garcia-Diaz, A., et al., *Interferon Receptor Signaling Pathways Regulating PD-L1 and PD-L2 Expression.* Cell Rep, 2017. **19**(6): p. 1189-1201.
329. Sato, H., et al., *DNA double-strand break repair pathway regulates PD-L1 expression in cancer cells.* Nat Commun, 2017. **8**(1): p. 1751.
330. Tsukui, H., et al., *CD73 blockade enhances the local and abscopal effects of radiotherapy in a murine rectal cancer model.* BMC Cancer, 2020. **20**(1): p. 411.

331. Valitutti, S., et al., *Different responses are elicited in cytotoxic T lymphocytes by different levels of T cell receptor occupancy.* J Exp Med, 1996. **183**(4): p. 1917-21.
332. Garnett, C.T., et al., *Sublethal irradiation of human tumor cells modulates phenotype resulting in enhanced killing by cytotoxic T lymphocytes.* Cancer Res, 2004. **64**(21): p. 7985-94.
333. Gameiro, S.R., et al., *Tumor Cells Surviving Exposure to Proton or Photon Radiation Share a Common Immunogenic Modulation Signature, Rendering Them More Sensitive to T Cell-Mediated Killing.* Int J Radiat Oncol Biol Phys, 2016. **95**(1): p. 120-130.
334. Garg, A.D., et al., *Danger signalling during cancer cell death: origins, plasticity and regulation.* Cell Death Differ, 2014. **21**(1): p. 26-38.
335. Dettmering, T., et al., *Increased effectiveness of carbon ions in the production of reactive oxygen species in normal human fibroblasts.* J Radiat Res, 2015. **56**(1): p. 67-76.
336. Lopez Perez, R., et al., *DNA damage response of clinical carbon ion versus photon radiation in human glioblastoma cells.* Radiother Oncol, 2019. **133**: p. 77-86.
337. Nguemgo Kouam, P., et al., *The increased adhesion of tumor cells to endothelial cells after irradiation can be reduced by FAK-inhibition.* Radiat Oncol, 2019. **14**(1): p. 25.
338. Lee, S.H., et al., *Regulation of ionizing radiation-induced adhesion of breast cancer cells to fibronectin by alpha5beta1 integrin.* Radiat Res, 2014. **181**(6): p. 650-8.
339. Behrends, U., et al., *Ionizing radiation induces human intercellular adhesion molecule-1 in vitro.* J Invest Dermatol, 1994. **103**(5): p. 726-30.
340. Basler, L., et al., *Abscopal effects of radiotherapy and combined mRNA-based immunotherapy in a syngeneic, OVA-expressing thymoma mouse model.* Cancer Immunol Immunother, 2018. **67**(4): p. 653-662.
341. Park, S.S., et al., *PD-1 Restrains Radiotherapy-Induced Abscopal Effect.* Cancer Immunol Res, 2015. **3**(6): p. 610-9.
342. Fujinami, N., et al., *Enhancement of antitumor effect by peptide vaccine therapy in combination with anti-CD4 antibody: Study in a murine model.* Biochem Biophys Rep, 2016. **5**: p. 482-491.
343. Stark, F.C., M.J. McCluskie, and L. Krishnan, *Homologous Prime-Boost Vaccination with OVA Entrapped in Self-Adjuvanting Archaeosomes Induces High Numbers of OVA-Specific CD8(+) T Cells that Protect Against Subcutaneous B16-OVA Melanoma.* Vaccines (Basel), 2016. **4**(4).
344. Maloy, K.J., et al., *Induction of mucosal and systemic immune responses by immunization with ovalbumin entrapped in poly(lactide-co-glycolide) microparticles.* Immunology, 1994. **81**(4): p. 661-7.
345. Garulli, B., et al., *Primary CD8+ T-cell response to soluble ovalbumin is improved by chloroquine treatment in vivo.* Clin Vaccine Immunol, 2008. **15**(10): p. 1497-504.
346. Habets, T.H., et al., *Fractionated Radiotherapy with 3 x 8 Gy Induces Systemic Anti-Tumour Responses and Abscopal Tumour Inhibition without Modulating the Humoral Anti-Tumour Response.* PLoS One, 2016. **11**(7): p. e0159515.
347. Baba, K., et al., *Experimental model for the irradiation-mediated abscopal effect and factors influencing this effect.* Am J Cancer Res, 2020. **10**(2): p. 440-453.
348. Rodriguez-Ruiz, M.E., et al., *Abscopal Effects of Radiotherapy Are Enhanced by Combined Immunostimulatory mAbs and Are Dependent on CD8 T Cells and Crosspriming.* Cancer Res, 2016. **76**(20): p. 5994-6005.
349. Zhang, X. and G. Niedermann, *Abscopal Effects With Hypofractionated Schedules Extending Into the Effector Phase of the Tumor-Specific T-Cell Response.* Int J Radiat Oncol Biol Phys, 2018. **101**(1): p. 63-73.
350. Yoo, G.S., et al., *Radiation-induced abscopal effect and its enhancement by programmed cell death 1 blockade in the hepatocellular carcinoma: A murine model study.* Clin Mol Hepatol, 2021. **27**(1): p. 144-156.
351. Overwijk, W.W. and N.P. Restifo, *B16 as a mouse model for human melanoma.* Curr Protoc Immunol, 2001. **Chapter 20**: p. Unit 20 1.

352. Reilley, M.J., et al., *TLR9 activation cooperates with T cell checkpoint blockade to regress poorly immunogenic melanoma.* J Immunother Cancer, 2019. **7**(1): p. 323.
353. Kato, R., et al., *Nintedanib promotes antitumour immunity and shows antitumour activity in combination with PD-1 blockade in mice: potential role of cancer-associated fibroblasts.* Br J Cancer, 2020.
354. Hu, Z., et al., *Combined SEP and anti-PD-L1 antibody produces a synergistic antitumor effect in B16-F10 melanoma-bearing mice.* Sci Rep, 2018. **8**(1): p. 217.
355. Crosby, E.J., et al., *Complimentary mechanisms of dual checkpoint blockade expand unique T-cell repertoires and activate adaptive anti-tumor immunity in triple-negative breast tumors.* Oncoimmunology, 2018. **7**(5): p. e1421891.
356. Chen, I.X., et al., *A bilateral tumor model identifies transcriptional programs associated with patient response to immune checkpoint blockade.* Proc Natl Acad Sci U S A, 2020. **117**(38): p. 23684-23694.
357. Gao, M., et al., *Therapy With Carboplatin and Anti-PD-1 Antibodies Before Surgery Demonstrates Sustainable Anti-Tumor Effects for Secondary Cancers in Mice With Triple-Negative Breast Cancer.* Front Immunol, 2020. **11**: p. 366.
358. O'Melia, M.J., M.P. Manspeaker, and S.N. Thomas, *Tumor-draining lymph nodes are survival niches that support T cell priming against lymphatic transported tumor antigen and effects of immune checkpoint blockade in TNBC.* Cancer Immunol Immunother, 2021.
359. Ebner, D.K., et al., *The Immunoregulatory Potential of Particle Radiation in Cancer Therapy.* Front Immunol, 2017. **8**: p. 99.
360. Takamori, S., et al., *Combination Therapy of Radiotherapy and Anti-PD-1/PD-L1 Treatment in Non-Small-cell Lung Cancer: A Mini-review.* Clin Lung Cancer, 2018. **19**(1): p. 12-16.
361. Sharma, R.A., et al., *Clinical development of new drug-radiotherapy combinations.* Nat Rev Clin Oncol, 2016. **13**(10): p. 627-42.
362. Jagodinsky, J.C., P.M. Harari, and Z.S. Morris, *The Promise of Combining Radiation Therapy With Immunotherapy.* Int J Radiat Oncol Biol Phys, 2020. **108**(1): p. 6-16.
363. Buchbinder, E.I. and A. Desai, *CTLA-4 and PD-1 Pathways: Similarities, Differences, and Implications of Their Inhibition.* Am J Clin Oncol, 2016. **39**(1): p. 98-106.
364. Selby, M.J., et al., *Anti-CTLA-4 antibodies of IgG2a isotype enhance antitumor activity through reduction of intratumoral regulatory T cells.* Cancer Immunol Res, 2013. **1**(1): p. 32-42.
365. Simpson, T.R., et al., *Fc-dependent depletion of tumor-infiltrating regulatory T cells co-defines the efficacy of anti-CTLA-4 therapy against melanoma.* J Exp Med, 2013. **210**(9): p. 1695-710.
366. Sharma, A., et al., *Anti-CTLA-4 Immunotherapy Does Not Deplete FOXP3(+) Regulatory T Cells (Tregs) in Human Cancers.* Clin Cancer Res, 2019. **25**(4): p. 1233-1238.
367. Ha, D., et al., *Differential control of human Treg and effector T cells in tumor immunity by Fc-engineered anti-CTLA-4 antibody.* Proc Natl Acad Sci U S A, 2019. **116**(2): p. 609-618.
368. McClanahan, F., et al., *PD-L1 checkpoint blockade prevents immune dysfunction and leukemia development in a mouse model of chronic lymphocytic leukemia.* Blood, 2015. **126**(2): p. 203-11.
369. Yoshida, K., et al., *Anti-PD-1 antibody decreases tumour-infiltrating regulatory T cells.* BMC Cancer, 2020. **20**(1): p. 25.
370. Younes, A.I., et al., *Addition of TLR9 agonist immunotherapy to radiation improves systemic antitumor activity.* Transl Oncol, 2021. **14**(2): p. 100983.
371. Pilones, K.A., et al., *Converging focal radiation and immunotherapy in a preclinical model of triple negative breast cancer: contribution of VISTA blockade.* Oncoimmunology, 2020. **9**(1): p. 1830524.
372. Young, K.H., et al., *Optimizing Timing of Immunotherapy Improves Control of Tumors by Hypofractionated Radiation Therapy.* PLoS One, 2016. **11**(6): p. e0157164.

373. Teitz-Tennenbaum, S., et al., *Radiotherapy potentiates the therapeutic efficacy of intratumoral dendritic cell administration.* Cancer Res, 2003. **63**(23): p. 8466-75.
374. Grapin, M., et al., *Optimized fractionated radiotherapy with anti-PD-L1 and anti-TIGIT: a promising new combination.* J Immunother Cancer, 2019. **7**(1): p. 160.
375. Philippou, Y., et al., *Impacts of combining anti-PD-L1 immunotherapy and radiotherapy on the tumour immune microenvironment in a murine prostate cancer model.* Br J Cancer, 2020. **123**(7): p. 1089-1100.
376. Takahashi, Y., et al., *Carbon ion irradiation enhances the antitumor efficacy of dual immune checkpoint blockade therapy both for local and distant sites in murine osteosarcoma.* Oncotarget, 2019. **10**(6): p. 633-646.
377. Helm, A., et al., *Reduction of Lung Metastases in a Mouse Osteosarcoma Model Treated With Carbon Ions and Immune Checkpoint Inhibitors.* Int J Radiat Oncol Biol Phys, 2021. **109**(2): p. 594-602.
378. Clement-Colmou, K., et al., *Influence of Radiotherapy Fractionation Schedule on the Tumor Vascular Microenvironment in Prostate and Lung Cancer Models.* Cancers (Basel), 2020. **12**(1).
379. Kelada, O.J., et al., *High Single Doses of Radiation May Induce Elevated Levels of Hypoxia in Early-Stage Non-Small Cell Lung Cancer Tumors.* Int J Radiat Oncol Biol Phys, 2018. **102**(1): p. 174-183.
380. Jani, A., et al., *High-Dose, Single-Fraction Irradiation Rapidly Reduces Tumor Vasculature and Perfusion in a Xenograft Model of Neuroblastoma.* Int J Radiat Oncol Biol Phys, 2016. **94**(5): p. 1173-80.
381. Park, H.J., et al., *Radiation-induced vascular damage in tumors: implications of vascular damage in ablative hypofractionated radiotherapy (SBRT and SRS).* Radiat Res, 2012. **177**(3): p. 311-27.
382. Marciscano, A.E., et al., *Elective Nodal Irradiation Attenuates the Combinatorial Efficacy of Stereotactic Radiation Therapy and Immunotherapy.* Clin Cancer Res, 2018. **24**(20): p. 5058-5071.
383. Dovedi, S.J., et al., *Fractionated Radiation Therapy Stimulates Antitumor Immunity Mediated by Both Resident and Infiltrating Polyclonal T-cell Populations when Combined with PD-1 Blockade.* Clin Cancer Res, 2017. **23**(18): p. 5514-5526.
384. Persa, E., et al., *The effect of ionizing radiation on regulatory T cells in health and disease.* Cancer Lett, 2015. **368**(2): p. 252-61.
385. Barcellos-Hoff, M.H., et al., *Transforming growth factor-beta activation in irradiated murine mammary gland.* J Clin Invest, 1994. **93**(2): p. 892-9.
386. Jobling, M.F., et al., *Isoform-specific activation of latent transforming growth factor beta (LTGF-beta) by reactive oxygen species.* Radiat Res, 2006. **166**(6): p. 839-48.
387. Arina, A., et al., *Tumor-reprogrammed resident T cells resist radiation to control tumors.* Nat Commun, 2019. **10**(1): p. 3959.
388. Du, H., et al., *The co-expression characteristics of LAG3 and PD-1 on the T cells of patients with breast cancer reveal a new therapeutic strategy.* Int Immunopharmacol, 2020. **78**: p. 106113.
389. Alam, M.S., et al., *CD73 is expressed by human regulatory T helper cells and suppresses proinflammatory cytokine production and Helicobacter felis-induced gastritis in mice.* J Infect Dis, 2009. **199**(4): p. 494-504.
390. Hernandez-Mir, G. and M.J. McGeachy, *CD73 is expressed by inflammatory Th17 cells in experimental autoimmune encephalomyelitis but does not limit differentiation or pathogenesis.* PLoS One, 2017. **12**(3): p. e0173655.
391. Capone, M., et al., *Frequency of circulating CD8+CD73+T cells is associated with survival in nivolumab-treated melanoma patients.* J Transl Med, 2020. **18**(1): p. 121.
392. Kong, Y., et al., *Downregulation of CD73 associates with T cell exhaustion in AML patients.* J Hematol Oncol, 2019. **12**(1): p. 40.
393. Chan, D.V., et al., *Differential CTLA-4 expression in human CD4+ versus CD8+ T cells is associated with increased NFAT1 and inhibition of CD4+ proliferation.* Genes Immun, 2014. **15**(1): p. 25-32.

394. Dawicki, W. and T.H. Watts, *Expression and function of 4-1BB during CD4 versus CD8 T cell responses in vivo.* Eur J Immunol, 2004. **34**(3): p. 743-751.
395. Chow, J., et al., *Radiation induces dynamic changes to the T cell repertoire in renal cell carcinoma patients.* Proc Natl Acad Sci U S A, 2020. **117**(38): p. 23721-23729.
396. Tu, M.M., et al., *Immunosurveillance and Immunoediting of Breast Cancer via Class I MHC Receptors.* Cancer Immunol Res, 2017. **5**(11): p. 1016-1028.
397. Stoth, M., et al., *Splenectomy reduces lung metastases and tumoral and metastatic niche inflammation.* Int J Cancer, 2019. **145**(9): p. 2509-2520.
398. Goto, T., *Radiation as an In Situ Auto-Vaccination: Current Perspectives and Challenges.* Vaccines (Basel), 2019. **7**(3).
399. Ruhland, M.K., et al., *Visualizing Synaptic Transfer of Tumor Antigens among Dendritic Cells.* Cancer Cell, 2020. **37**(6): p. 786-799 e5.
400. Tokunaga, R., et al., *CXCL9, CXCL10, CXCL11/CXCR3 axis for immune activation - A target for novel cancer therapy.* Cancer Treat Rev, 2018. **63**: p. 40-47.
401. Josephs, S.F., et al., *Unleashing endogenous TNF-alpha as a cancer immunotherapeutic.* J Transl Med, 2018. **16**(1): p. 242.
402. Bai, X., et al., *Blocking TGF-beta Signaling To Enhance The Efficacy Of Immune Checkpoint Inhibitor.* Onco Targets Ther, 2019. **12**: p. 9527-9538.
403. Shan, C., X. Li, and J. Zhang, *Progress of immune checkpoint LAG-3 in immunotherapy.* Oncol Lett, 2020. **20**(5): p. 207.
404. Vijayakumaran, R., et al., *Regulation of Mutant p53 Protein Expression.* Front Oncol, 2015. **5**: p. 284.
405. Li, J., et al., *The expression of costimulatory molecules CD80 and CD86 in human carcinoma cell lines: its regulation by interferon gamma and interleukin-10.* Cancer Immunol Immunother, 1996. **43**(4): p. 213-9.
406. Tirapu, I., et al., *Low surface expression of B7-1 (CD80) is an immunoescape mechanism of colon carcinoma.* Cancer Res, 2006. **66**(4): p. 2442-50.
407. Sun, Q., et al., *Phototherapy and anti-GITR antibody-based therapy synergistically reinvigorate immunogenic cell death and reject established cancers.* Biomaterials, 2021. **269**: p. 120648.
408. de Jong, M. and T. Maina, *Of mice and humans: are they the same?--Implications in cancer translational research.* J Nucl Med, 2010. **51**(4): p. 501-4.
409. Fares, J., et al., *Molecular principles of metastasis: a hallmark of cancer revisited.* Signal Transduct Target Ther, 2020. **5**(1): p. 28.
410. Verhaegen, F., et al., *ESTRO ACROP: Technology for precision small animal radiotherapy research: Optimal use and challenges.* Radiother Oncol, 2018. **126**(3): p. 471-478.
411. Pulaski, B.A. and S. Ostrand-Rosenberg, *Mouse 4T1 breast tumor model.* Curr Protoc Immunol, 2001. **Chapter 20**: p. Unit 20 2.
412. Schenkel, J.M. and D. Masopust, *Tissue-resident memory T cells.* Immunity, 2014. **41**(6): p. 886-97.

# Acknowledgements

An dieser Stelle möchte ich mich bei all den Personen bedanken, die mich bei der Anfertigung dieser Doktorarbeit unterstützt haben.

Mein herzlicher Dank gilt:

Prof. Dr. Stefan Eichmüller, für die Möglichkeit in seinem Team an diesem Projekt zu arbeiten. Danke für die konstante Unterstützung, die wissenschaftliche Betreuung, das Vertrauen in meine Fähigkeiten und die Förderung meiner persönlichen Entwicklung.

Dr. Wolfram Osen, für die zahlreichen wissenschaftlichen Diskussionen und den fachlichen Input. Besonders dankbar bin ich für seine Unterstützung beim Schreiben dieser Arbeit.

Prof. Dr. Stefan Rieken, für die Einblicke in die Welt der Strahlentherapie, die wissenschaftliche Unterstützung und die zahlreichen motivierenden Gespräche zu Beginn des Projektes.

Prof. Dr. Martin Müller und Prof. Dr. Dr. Christine Engeland, die als Mitglieder meines TAC-Komitees stetiges Interesse an meinem Projekt zeigten und mir mit konstruktiven wissenschaftlichen Beiträgen zur Seite standen.

Prof Dr. Ana Martin-Villalba und Prof. Dr. Viktor Umansky, für die Bereitschaft als Mitglieder meiner Prüfungskommission mich bei dem letzten Schritt zur Erlangung der Doktorwürde zu unterstützen.

Dr. Dr. Amir Abdollahi, Dr. Mahmoud Moustafa, und Dr. Stephan Brons, für die nächtelange Unterstützung bei der Kohlenstoffionenbestrahlung am HIT und den wertvollen wissenschaftlichen Austausch.

Dr. Ina Kurth, Dr. Peter Häring, Armin Runze, und Clemens Lang, ohne deren Einsatz die Photonenbestrahlung von Maustumoren nicht möglich gewesen wäre.

Den Mitarbeitern des zentralen Tierlabors und der FACS Core Facility, die den reibungslosen Ablauf zentraler Experimente meiner Doktorarbeit ermöglichten.

Jessica, die mir ihren wohlverdienten Posterpreis (ScioCD-Analyse) geschenkt hat und mir dadurch diese spannenden Analysen ermöglichte.

Elke, ohne die diese Doktorarbeit nicht möglich gewesen wäre. Vielen Dank für die zahlreichen Stunden, die du mit mir bei den Mäusen verbracht hast und in denen du meine wilden Mäuse gezähmt hast. Danke, dass du immer ein offenes Ohr für mich hattest, mir mit gutem Rat beiseite standst und mich aufgebaut hast, wenn ich einmal nicht weiterwusste. Es hat mir große Freude bereitet deine Sitznachbarin zu sein und mit dir zusammenzuarbeiten.

Meinen lieben Kollegen und Freunden David, Toni, Theresa, Krishna, Miriam, Julia, Luisa und Spencer, die mich während der Doktorarbeit wissenschaftlich und persönlich begleitet haben. Danke, dass ihr mich vom ersten Tag an so herzlich in die Laborgemeinschaft aufgenommen habt, für den wissenschaftlichen Austausch, und die zahlreichen Aktivitäten außerhalb des Labors.

Philipp, für die großartige Zusammenarbeit an diesem neuen und herausfordernden Projekt. Wir haben gemeinsam viel Neues über die Strahlentherapie gelernt und es ist schön zu sehen, was wir am Ende erreicht haben.

Adriane, für den Anstoß zu diesem Projekt. Danke, dass du immer ein offenes Ohr für mich hattest und für die vielen guten Ratschläge.

Den Auszubildenden Marie-Luise, Jana und Paula, für die tatkräftige Unterstützung bei meinen Experimenten.

Allen Kollegen aus dem GMP-Team und der Peptidsynthese (Claudia, Rainer, Wolfgang, Mario, Andrea), für die Schaffung einer tollen Arbeitsatmosphäre und eure Hilfsbereitschaft.

Meinen lieben Heidelberger Freuden, vor allem Ines, Jessica, Lena und Ronja, die für den Ausgleich zum stressigen Laboralltag sorgten. Danke, für die Wein & Käse-Abende, Frankreich-Wochenenden, Bauch-Beine-Po-Sessions und Feierabendbiere im Botanik. Ich bin froh mit euch Freunde fürs Leben gefunden zu haben.

Meinen Eltern Elke und Hermann, meiner Schwester Stefanie, und meiner Tante Karola, die die beste Familie sind, die man sich wünschen kann. Ich bin unglaublich dankbar, dass ihr mich auf all meinen Wegen unterstützt habt, immer an mich geglaubt habt und ich mich stets auf euch verlassen kann.